Université de Liège

Faculté des Sciences Appliquées

Collège de doctorat en Électricité, Électronique et Informatique

Model Order Reduction: Application to Electromagnetic Problems

Doctoral Dissertation presented by

Yannick Paquay

in fulfilment of the requirements for the degree of

Docteur en Sciences de l'Ingénieur

— December 2017 —

Abstract

With the increase in computational resources, numerical modeling has grown exponentially these last two decades. From structural analysis to combustion modeling and electromagnetics, discretization methods–in particular the finite element method–have had a tremendous impact. Their main advantage consists in a correct representation of dynamical and nonlinear behaviors by solving equations at local scale, however the spatial discretization inherent to such approaches is also its main drawback. Indeed, it usually leads to (very) large systems of equations—requiring abundance of computational resources, usually far too much for quasi-real time simulations.

In this dissertation, model order reduction of numerical models from finite element discretization is analyzed to efficiently and accurately downsize the number of degrees of freedom in static and dynamic, linear and nonlinear electromagnetic applications. In particular, an in-depth review of state of the art model order reduction methods is performed in view of the aforementioned problems. To this end, the proper orthogonal decomposition is considered to limit the number of unknowns in the resolution process. Nonlinear sampling methods such as: the missing point estimation approach and discrete empirical interpolation method, are compared to reduce the assembly phase. The parametric dependencies are taken into account by resorting to global reduced basis and nonlinear interpolation on manifolds techniques. Finally, a novel decoupled approach for the reduction of a coupled nonlinear magnetodynamic three-phase energy converter with external electric circuits is proposed and analyzed by combining all the aforementioned methods—impressively reducing the computational cost by 95%.

This dissertation is genuinely geared towards the application of *a priori* known methods on a variety of different numerical models of electromagnetic devices. Additional automatic algorithms which eliminate the arbitrary choices of numerical reduction parameters are proposed and compared to reference methods proposed in the literature. The following applications have been considered: a 2D inductor-core system to first illustrate and provide understanding of the proposed methods, a 2D single phase transformer, a 2D three-phase transformer and a 3D microwave antenna.

Résumé

Avec l'augmentation des puissances de calcul informatique au cours des deux dernières décénnies, la modélisation numérique s'est développée de manière exponentielle. De l'analyse structurelle en passant par la modélisation des réactions de combustions jusqu'à l'études des lois électromagnétiques, les méthodes de discrétisation–en particulier celle des éléments finis–ont eu un impact majeur. Leur avantage principal consiste en une représentation correcte des comportements dynamique et non linéaire en résolvant les équations au niveau local; cependant l'inhéherente discrétisation spatiale obtenue par ces méthodes représente leur principal désavantage. En effet, elle mène habituellement à des systèmes d'équations (très) larges—nécessitant d'importantes ressources de calcul, habituellement bien trop élévées pour des résolutions en temps (quasi) réel.

Dans cette dissertation, la réduction d'ordre de modèles numériques obtenus après discrétisation par la méthode des éléments finis est analysée pour diminuer de manière efficace et précise le nombre de degrés de liberté dans les cas électromagnetiques statiques et dynamiques, linéaires et non linéaires. En particulier, une étude approfondie de l'état de l'Art est proposée en regards des problèmes énoncés. A cette fin, la *proper orthogonal decomposition* est utilisée pour limiter le nombre d'inconnues lors de la résolution du problème. Ensuite, les méthodes d'échantillonage non linéaires telles que *missing point estimation* et *discrete empirical interpolation method* sont comparées pour réduire la phase d'assemblage des matrices. Les dépendences paramétriques sont prises en compte selon deux méthodes: la construction d'une base globale et l'interpolation non linéaire sur variétés. Finalement, une nouvelle approche découplée pour la réduction d'un transformateur triphasé couplé à des circuits électriques externes est proposée et analysée en combinant toutes les méthodes précitées—permettant une réduction de 95% des coûts originaux.

Cette dissertation est délibéremment orientée vers l'utilisation des méthodes *a priori* connues sur un ensemble de différents modèles numériques décrivant des applications électromagnétiques. Des algorithmes automatiques éliminants les choix arbitraires des paramètres de réduction sont proposés et comparés aux méthodes de références proposées dans la litérature. Les applications suivantes ont été considérées: un système noyau-inducteur 2D en premier lieu pour l'illustration et la compréhension des méthodes, ensuite un transformateur monophasé 2D, un transformateur triphasé 2D et une antenne micro-ondes 3D.

Contents

Introduction

Since the understanding of electromagnetism–formulated in equations by Maxwell between 1860 and 1871–a tremendous vast variety of advanced devices have been engineered based on those principles and have profoundly changed mankind's lifestyle: i.e. from first dynamo and radio in 19th century to the latest very efficient electric drives, cars and smartphones in 21st century.

To understand and improve these applications, mathematical models have been developed and studied in both academia and industry. In the mid-20th century, equivalent models based on simple electric equations were investigated. Those equivalent models were often tuned by hand and did not present sufficient robustness. At the end of the 20th century, the emergence of the computer sciences changed the modeling process rapidly. As a consequence to the growth in computational power, numerical models can be constructed to solve increasingly larger systems of equations. Since then, the number of transistors in CPUs and GPUs has continuously increased, following Moore's law and allowing an outstanding development of available computational resources. Along with it came detailed models that rely on Maxwell's equations at the local scale instead of equivalent electric circuits. Those numerical models are more accurate than the original ones. However, the time required to solve them may not have decreased throughout the years by considering more complex models that require more computational power.

In this work, we are interested in providing models that are approximately as accurate as the detailed ones while maintaining a computational speed comparable to the equivalent ones. In order to achieve this particular aim, we are investigating the topic of Model Order Reduction (MOR) for electromagnetic applications. For the last two decades, researchers have been developing reduction techniques in numerous areas such as chemical reactions, structural analysis and fluid dynamics—leading to real-time simulations. Lately, those methods have been applied in electromagnetics and showed very promising results in linear and static cases. As the logical next step, we are interested in reducing nonlinear, dynamic and coupled models of such electromagnetic applications, some of them are considered in this dissertation by including an inductor-core system, 2D single-phase and three-phase transformers and a microwave antenna.

Dissertation goals

This work contributes to the development and investigation of model order reduction techniques for (practical) applications which involve nonlinear, dynamical and coupled conditions. The work is mainly focused on the following topics:

- *Understanding previously developed model order reduction techniques*

  An extensive number of reduction techniques have been developed during the last three decades. Integrating these methods is one of the main components of this work and will determine the development of alternative approaches for the considered applications. This first part is crucial for the correct use of model order reduction techniques, and for understanding their limitations.

- *Automating the reduction procedure for linear electromagnetic applications*

  Model order reduction of linear electromagnetic problems has been partially treated in the literature. Indeed, some parts of the reduction process still require human expertise and do not lead to automatic reduction. We are interested in providing concrete methods and/or procedures to deal with linear applications. One of them consists in proposing algorithms that automate the reduction process which is still often based on arbitrary user-defined parameters.

- *Developing robust reductions of nonlinear magnetodynamic systems*

  Based on the work developed for linear applications, we consider the nonlinear magnetodynamic problem, which describes most low frequency electromagnetic power conversion applications. This is a very active research area, as no single "silver bullet" solution has yet been found. Here, we explore ideas from other research fields (e.g. thermodynamics and aerodynamics) that present the same kind of mathematical or numerical structures for which solutions or reduction procedures have been proposed.

- *Dealing with reduction strategies of parametrized problems*

  Similarly to the situation described for nonlinear applications, model order reduction of parametric problems has hardly been investigated in electromagnetism, whereas the mechanical community already developed robust solutions. In this work, we are interested in considering those methods in the electromagnetic research area.

- *Constructing a general approach for a practical application coupled to external electric circuits*

  Being able to reduce a real application such as a three-phase power transformer and integrate it in an electric network simulator is of great interest for both industry and academia. To conclude this dissertation, this practical application is considered as the final demonstrator of our model order reduction investigation.

Dissertation outline

This dissertation is divided into six chapters that follow a logical sequence by adding additional features. The same philosophy is applied to the chosen applications, as the same models are reused and complexified accordingly.

After this introduction, the first chapter introduces numerical modeling techniques for electromagnetic problems. It contains a review of both equivalent circuit approaches

and high fidelity modeling and presents the problem statement leading to the original large systems of equations that we will eventually try to reduce.

In chapter 2, we present an in-depth review of the model order reduction methods considered during our investigation. For all of them, a theoretical description and an academic example are presented to help the reader grasp the different concepts. The differentiation between linear and nonlinear problems is explained and the general procedures to adopt in such cases are explained. A particular attention is also given to the separation of online and offline stages that are characteristic of model order reduction techniques. Finally, a more refined outline is proposed according to the choice of the model order reduction technique for each of the following chapters.

Chapter 3 deals with linear electromagnetic problems in both time and frequency domain. In this first application chapter, linear model order reduction is illustrated on simple and real applications such as transformers and antennas. Several algorithms are proposed to automate the reduction processes and are validated on the aforementioned applications.

Then, in chapter 4, nonlinear permeability of magnetic materials is introduced to better depict the actual behavior of real devices. The linear and nonlinear methods are investigated and results show the difficulty to find robust methods for dynamic problems. In this section, a three-phase power transformer is considered as an application.

In chapter 5, the nonlinear problems are parametrized by considering multiple inputs and outputs which actively affect the system dynamics. Two intrinsically different strategies are investigated to efficiently reduce an inductor-core system.

Then, the coupling between the reduced order model of a nonlinear parameterized three-phase transformer with external electric coupling is detailed in chapter 6. A novel decoupled procedure is proposed to stabilize the overall reduced system.

Finally, general conclusions are drawn and future prospects are pointed out.

Original contributions

Hereafter is a list of contributions (including collaborative works) that we consider to be (at least partly) original:

1. The elaboration of three automatic reduction algorithms based on local and global quantities for quasi-linear applications in frequency domain (particular application to a 3D finite element model of a microwave antenna), in section 3.3.1.3.

2. The development of an automatic reduction algorithm in time domain based on local and global quantities for linear magnetodynamic applications (particular utilization on a 2D finite element model of a transformer), in section 3.3.1.4.

3. The comparison between Proper Orthogonal Decomposition method and Krylov-based approaches for magnetodynamic devices in the frequency domain using uniform selection or using the aforementioned algorithmic detection of snapshots (application to a 2D finite element model of a transformer), in section 3.3.1.4.

4. The review of resolution and assembling reductions for nonlinear magnetodynamic applications and external circuit coupling, in chapters 4 and 6.

5. The nonlinear interpolation of parametric reduced bases using manifold theory in magnetodynamics (application to a 2D finite element model of an inductor-core system), in section 5.4.

6. A novel decoupled approach between local and global quantities in coupling of nonlinear magnetodynamic devices and external electric circuits using Proper Orthogonal Decomposition and Missing Point Estimation, in section 6.8.

These contributions have been presented in the following peer-reviewed journals and conference proceeding.

Journals

- Yannick Paquay, Olivier Brüls, and Christophe Geuzaine. "Model Order Reduction of Nonlinear Eddy Current Problems with Parametric Electric Circuit Coupling.", *International Journal for Numerical Methods in Engineering*, In review (2017).

- Yannick Paquay, Olivier Brüls, and Christophe Geuzaine. "Nonlinear Interpolation on Manifold of Reduced-Order Models in Magnetodynamic Problems." *IEEE Transactions on Magnetics* 52.3 (2016): 7204804.

- Yannick Paquay, Christophe Geuzaine, Md. Rokibul Hasan, and Ruth V. Sabariego. "Reduced-Order Model Accounting for High-Frequency Effects in Power Electronic Components." *IEEE Transactions on Magnetics* 52.3 (2016): 7202904.

Proceedings

- Yannick Paquay, Olivier Brüls, and Christophe Geuzaine. "Model Order Reduction of Nonlinear Eddy Current Problems using Missing Point Estimation." *Model Reduction of Parametrized Systems*. Springer, Cham, 2017. 439-454.

- Yannick Paquay, Olivier Brüls, and Christophe Geuzaine. "Nonlinear Reduced Order Model of a 3-Phase Transformer for Electric Network Simulator Coupling." *Proceedings of 17th Biennal Conference on Electromagnetic Field Computations*, USA (2016).

- Yannick Paquay, Olivier Brüls, and Christophe Geuzaine. "Coupling Reduced Order Models of Electrical Devices with Electrical Network Simulators." *Proceedings of 10th International Symposium on Electric and Magnetic Fields*, France (2016).

- Yannick Paquay, Kevin Jacques, Christophe Geuzaine, and Johan Gyselinck. "Comparing Physics-Based and Automatic Model Order Reduction Techniques for Nonlinear Magnetostatic Systems." *Proceedings of 10th International Symposium on Electric and Magnetic Fields*, France (2016).

- Md. Rokibul Hasan, Ruth V. Sabariego, Christophe Geuzaine, and Yannick Paquay. "Proper orthogonal decomposition versus Krylov subspace methods in reduced-order energy-converter models." *Energy Conference (ENERGYCON), IEEE International*, Belgium (2016).

- Yannick Paquay, Olivier Brüls, and Christophe Geuzaine. "Model Order Reduction of Nonlinear Magnetodynamics with Interpolation on Grassmann Manifold." *Proceedings of Workshop Reduced basis, POD and PGD Model Reduction Techniques*, France (2015).

- Yannick Paquay, Olivier Brüls, and Christophe Geuzaine. "Model Order Reduction of Nonlinear Magnetodynamics with Manifold Interpolation." *Proceedings of 3rd Edition of Model Order Reduction of Parametrized Systems (MoRePaS III)*, Italy (2015).

- Yannick Paquay, Olivier Brüls, and Christophe Geuzaine. "Nonlinear Interpolation on Manifold of Reduced-Order Models in Magnetodynamic Problems." *Proceedings of 20th International Conference on the Computation of Electromagnetic Fields*, Canada (2015).

- Yannick Paquay, Christophe Geuzaine, Md. Rokibul Hasan, and Ruth V. Sabariego. "Reduced-Order Model Accounting for High-Frequency Effects in Power Electronic Components." *Proceedings of 20th International Conference on the Computation of Electromagnetic Fields*, Canada (2015).

Problem statement

1.1 Introduction

In this work, we investigate the model order reduction of numerical models of electromagnetic devices. Those models can originally be constructed in several manners following different philosophies. In this chapter, the numerical modeling of such applications is discussed. Two general (*a priori*) opposite methodologies are presented to model such systems. First, in section 1.2, Maxwell's equations are presented and derived to form very detailed and accurate models with a local description of the underlying physics—conducting to the *high fidelity modeling* method. Then, contrary to first method, in section 1.3, an equivalent circuit is determined thanks to the global observation of the system where comparable parameters are chosen to fit the expected results—leading to the so called *lumped parameter modeling* method. In section 1.4, the advantages and limitations of both approaches are listed and a choice is made on the philosophy to adopt for the modeling of electromagnetic devices in this dissertation. Finally, in section 1.5, the technical objectives of the present work are adjusted according to the chosen modeling method and its inherent limitations.

1.2 Electromagnetic equations

In this section, the developments of electromagnetic formulations (*i.e.* magnetostatic, magnetodynamic and full wave equations) in both time and frequency domains are derived. Since 1980s, computational resources have increasingly emerged—allowing the resolution of the aforementioned discretized equations at local scale with numerous degrees of freedom (e.g. millions of spatial points). By solving Maxwell's equations, very detailed models–later denoted High Fidelity Models (HFMs)–characterizing the underlying physical phenomena are obtained.

1.2.1   Continuous formulations

Let us consider Maxwell's equations [135]:

$$
\begin{cases}
\mathbf{curl}\ \underline{\mathbf{h}} &=& \underline{\mathbf{j}} + \partial_t \underline{\mathbf{d}}, \\
\mathbf{curl}\ \underline{\mathbf{e}} + \partial_t \underline{\mathbf{b}} &=& 0, \\
\mathrm{div}\ \underline{\mathbf{b}} &=& 0, \\
\mathrm{div}\ \underline{\mathbf{d}} &=& \underline{\mathbf{q}},
\end{cases}
\tag{1.1}
$$

where $\underline{\mathbf{h}}, \underline{\mathbf{e}}, \underline{\mathbf{b}}, \underline{\mathbf{d}}$ are the vectors of magnetic field, the electric field, the magnetic flux density and the electric flux density respectively. The source term vectors are the current density $\underline{\mathbf{j}}$ and the electric charge density $\underline{\mathbf{q}}$. These relations represent the generalized forms of the Ampère's law, Faraday's law, the magnetic Gauss's law and the electric Gauss's law and compose a mathematical representation of the electromagnetic field [104, 194]. For an isotropic medium, system (1.1) is uniquely determined at any time [32, 56] by choosing proper initial values for $\underline{\mathbf{h}}$ and $\underline{\mathbf{e}}$, boundary conditions and including the following constitutive relations

$$
\begin{cases}
\underline{\mathbf{j}} &=& \sigma \underline{\mathbf{e}} + \underline{\mathbf{j}}_s, \\
\underline{\mathbf{d}} &=& \epsilon \underline{\mathbf{e}}, \\
\underline{\mathbf{h}} &=& \nu \underline{\mathbf{b}},
\end{cases}
\tag{1.2}
$$

where σ, ϵ and ν are the conductivity, permittivity and the inverse of the permeability respectively. $\underline{\mathbf{j}}_s$ is the imposed current source.

1.2.1.1   Magnetostatic formulation

First, at low frequency and when no dynamic (*i.e.* no variation in time) occurs in the magnetic domain, systems (1.1) and (1.2) form the mathematical formulation

$$
\begin{cases}
\mathbf{curl}\ \underline{\mathbf{h}} &=& \underline{\mathbf{j}}, \\
\mathbf{curl}\ \underline{\mathbf{e}} &=& 0, \\
\mathrm{div}\ \underline{\mathbf{b}} &=& 0, \\
\underline{\mathbf{h}} &=& \nu \underline{\mathbf{b}},
\end{cases}
\tag{1.3}
$$

that ensures a unique determination at any time instant. Here, $\underline{\mathbf{j}} = \underline{\mathbf{j}}_s$. Since div $\underline{\mathbf{b}} = 0$, the magnetic flux density can be derived from a vector potential $\underline{\mathbf{a}}$ such that

$$
\underline{\mathbf{b}} = \mathbf{curl}\ \underline{\mathbf{a}}.
\tag{1.4}
$$

and then leads to the magnetostatic equation

$$
\mathbf{curl}\ \left(\nu\, \mathbf{curl}\ \underline{\mathbf{a}} \right) = \underline{\mathbf{j}}_s.
\tag{1.5}
$$

Considering a finite domain Ω with boundary Γ, the solution $\underline{\mathbf{a}} \in \mathbf{H}(\mathbf{curl}\ , \Omega) \triangleq \{\underline{\mathbf{a}} \in \mathbf{L}^2(\Omega);\ \mathbf{curl}\ \underline{\mathbf{a}} \in \mathbf{L}^2(\Omega)\}$ has to fulfill equation (1.5) in Ω and the boundary relation

$$
\underline{\mathbf{a}} \times \mathbf{n} = 0
\tag{1.6}
$$

along Γ where $\mathbf{n}$ is the outer unit normal vector.

1.2.1.2 Magnetodynamic formulation

Once conductivity is present in the domain, the magnetostatic equation (1.5) is no longer appropriate to accurately formulate the electromagnetic phenomena. Now, systems (1.1) and (1.2) form the mathematical formulation

$$\begin{cases} \mathbf{curl}\ \underline{\mathbf{h}} &=& \underline{\mathbf{j}}, \\ \mathbf{curl}\ \underline{\mathbf{e}} + \partial_t \underline{\mathbf{b}} &=& 0, \\ \operatorname{div}\ \underline{\mathbf{b}} &=& 0, \\ \underline{\mathbf{h}} &=& \nu \underline{\mathbf{b}}, \\ \underline{\mathbf{j}} &=& \sigma \underline{\mathbf{e}} + \underline{\mathbf{j}}_s. \end{cases} \tag{1.7}$$

Injecting (1.4) into the second equation of (1.7) implies

$$\mathbf{curl}\ \left(\underline{\mathbf{e}} + \partial_t \underline{\mathbf{a}}\right) = 0 \tag{1.8}$$

which defines the electric field $\underline{\mathbf{e}}$ as

$$\underline{\mathbf{e}} = -\partial_t \underline{\mathbf{a}} - \mathbf{grad}\ \nu \tag{1.9}$$

where ν is a scalar electric potential. Then, the magnetodynamic system is obtained by respecting

$$\operatorname{div}\ \left[-\sigma\left(\partial_t \underline{\mathbf{a}} + \mathbf{grad}\ \nu\right)\right] = 0, \tag{1.10}$$

$$\sigma\left(\partial_t \underline{\mathbf{a}} + \mathbf{grad}\ \nu\right) + \mathbf{curl}\ \left(\nu\,\mathbf{curl}\ \underline{\mathbf{a}}\right) = \underline{\mathbf{j}}_s \tag{1.11}$$

and the modified magnetic vector potential formulation [71, 112]:

$$\sigma \partial_t \underline{\mathbf{a}} + \mathbf{curl}\ \left(\nu\,\mathbf{curl}\ \underline{\mathbf{a}}\right) = \underline{\mathbf{j}}_s \tag{1.12}$$

by setting the scalar electric potential to zero as an implicit gauge.

1.2.1.3 Full wave formulation

Once the frequency f is sufficiently important (*i.e.* when the wave number $\lambda = c/f$ is much lower than the skin depth $\delta = \sqrt{\nu/\pi f \sigma}$), the electromagnetic system (1.1) cannot be simplified anymore. Introducing the constitutive relations from (1.2) into first equation of system (1.1) gives

$$\mathbf{curl}\ \left(\nu \underline{\mathbf{b}}\right) = \left(\sigma + \partial_t \epsilon\right) \underline{\mathbf{e}} + \underline{\mathbf{j}}_s. \tag{1.13}$$

Replacing $\underline{\mathbf{b}}$ with expression (1.4) and $\underline{\mathbf{e}}$ with relation (1.9) leads to the "$\underline{\mathbf{a}} - \nu$" formulation:

$$\operatorname{div}\ \left[-\sigma\left(\partial_t \underline{\mathbf{a}} + \mathbf{grad}\ \nu\right)\right] = 0, \tag{1.14}$$

$$\mathbf{curl}\ \left(\nu\,\mathbf{curl}\ \underline{\mathbf{a}}\right) + \sigma\mathbf{grad}\ \nu + \sigma\partial_t\underline{\mathbf{a}} + \partial_t\epsilon\mathbf{grad}\ \nu + \partial_t^2\epsilon\underline{\mathbf{a}}\ \ =\ \ \underline{\mathbf{j}}_s. \tag{1.15}$$

1.2.2   Spatial discretization

The continuous equations cannot be solved exactly on arbitrary domains Ω and has to be spatially discretized. In this work we choose a discretization based on the Finite Element Method (FEM) [55, 59, 110], which is well suited for problems that involve complex geometrical structures and nonlinear materials. Other discretization methods like the Finite Difference Method (FDM) [120, 139, 196] or the Finite Volume Method (FVM) [166, 199] could be used as well, which would not change the overall structure of the developments below.

1.2.2.1   Magnetostatic formulation

The weak formulation of (1.5) is obtained by multiplying it with appropriate test functions $\underline{\mathbf{a}}'$ and by integrating by parts over the integration domain Ω [64]:

$$\left(\nu\mathbf{curl}\ \underline{\mathbf{a}}, \mathbf{curl}\ \underline{\mathbf{a}}'\right)_\Omega + \left\langle\mathbf{n}\times\nu\mathbf{curl}\ \underline{\mathbf{a}}, \underline{\mathbf{a}}'\right\rangle_\Gamma = \left(\underline{\mathbf{j}}_s, \underline{\mathbf{a}}'\right)_\Omega \tag{1.16}$$

with $\underline{\mathbf{a}}' \in \mathbf{H}_0(\mathbf{curl}\ ,\Omega) \triangleq \left\{\underline{\mathbf{a}} \in \mathbf{H}(\mathbf{curl}\ ,\Omega); \underline{\mathbf{a}}' \times \mathbf{n} = 0\big|_\Gamma\right\}$. Applying the standard Galerkin FEM [79] using Whitney edge elements [31, 204, 215], the continuous field $\underline{\mathbf{a}}$ is expressed by a weighted sum of basis functions ϕ_i, associated to the mesh of Ω, as

$$\underline{\mathbf{a}} = \sum_i a_i\phi_i. \tag{1.17}$$

The coefficients a_i form the unknown vector $\mathbf{a} \in \mathbb{R}^{n_a \times 1}$ and the matrix form of (1.16) follows

$$\mathbf{Sa} = \mathbf{v} \tag{1.18}$$

where $\mathbf{S}$, $\mathbf{v}$ correspond to the stiffness matrix (*i.e.* representing the **curl** operator) and the source term (*i.e.* the imposed current) respectively.

1.2.2.2   Magnetodynamic formulation

Similarly with the continuous magnetodynamic equation (1.12), its weak formulation is directly obtained by

$$\left(\sigma\partial_t\underline{\mathbf{a}}, \underline{\mathbf{a}}'\right)_\Omega + \left(\nu\mathbf{curl}\ \underline{\mathbf{a}}, \mathbf{curl}\ \underline{\mathbf{a}}'\right)_\Omega + \left\langle\mathbf{n}\times\nu\mathbf{curl}\ \underline{\mathbf{a}}, \underline{\mathbf{a}}'\right\rangle_\Gamma = \left(\underline{\mathbf{j}}_s, \underline{\mathbf{a}}'\right)_\Omega \tag{1.19}$$

and the corresponding matrix form follows

$$\mathbf{M}\partial_t\mathbf{a} + \mathbf{Sa} = \mathbf{v} \tag{1.20}$$

where $\mathbf{M}$ corresponds to the mass matrix (*i.e.* representing the dynamics).

1.2.2.3 Full wave formulation

Similarly to magnetostatic and magnetodynamic weak formulations, after integration by parts (1.14), the "$\underline{\mathbf{a}} - v$" weak formulation is obtained as
Find $\underline{\mathbf{a}} - v$ so that

$$\left(v\mathbf{curl}\ \underline{\mathbf{a}},\mathbf{curl}\ \underline{\mathbf{a}}'\right)_{\Omega} + \partial_t^2\left(\epsilon\underline{\mathbf{a}},\underline{\mathbf{a}}'\right)_{\Omega} + \partial_t\left(\sigma\underline{\mathbf{a}},\underline{\mathbf{a}}'\right)_{\Omega_c} \tag{1.21}$$

$$+ (\partial_t\epsilon + \sigma)\left(\mathbf{grad}\ v,\underline{\mathbf{a}}'\right)_{\Omega} = \left(\underline{\mathbf{j}}_s,\underline{\mathbf{a}}'\right)_{\Omega_s},$$

$$\partial_t\left(\epsilon\,\mathbf{grad}\ v,\mathbf{grad}\ v'\right)_{\Omega} + \partial_t^2\left(\epsilon\underline{\mathbf{a}},\mathbf{grad}\ v'\right)_{\Omega} = 0, \tag{1.22}$$

holds for every $\underline{\mathbf{a}}'$ and v' in a suitable function space (*i.e.* defined by edge and nodal elements). To accurately treat wave propagation, an absorbing boundary condition [72, 143] has to be imposed on the external boundary of the domain (e.g. a Silver-Muller one). Equivalently, a perfect match layer [26] can be considered. The matrix form is written as

$$\mathbf{M}_1\partial_t^2\mathbf{x} + \mathbf{M}_2\partial_t\mathbf{x} + \mathbf{M}_3\mathbf{x} = \mathbf{v} \tag{1.23}$$

where $\mathbf{M}_1,\mathbf{M}_2,\mathbf{M}_3$ come from the terms in double time derivative, simple time derivative and time invariant respectively. Note that since two different unknowns are linked together (*i.e.* the magnetic vector potential and the scalar electric potential), the unknown vector is denoted $\mathbf{x}$.

1.2.3 Time domain

In order to solve a time dependent matrix form on a computer, it is further discretized in time. We are only considering the magnetodynamic formulation in time domain in this work. No time discretization is required for magnetostatic formulation and full wave electromagnetic equation is not usually meant to be solved in time. By defining

$$\mathbf{f}(\mathbf{a}, t) = \mathbf{M}^{-1}\left(\mathbf{Sa} - \mathbf{v}\right), \tag{1.24}$$

equation (1.20) can be written as

$$\partial_t\mathbf{a} + \mathbf{f}(\mathbf{a}, t) = 0. \tag{1.25}$$

Using a simple finite difference approximation of $\dot{\mathbf{a}}$, *i.e.*

$$\partial_t\mathbf{a} = \frac{\mathbf{a}_{k+1} - \mathbf{a}_k}{\Delta t}, \tag{1.26}$$

where $\Delta t = t_{k+1} - t_k$ is the time step (*i.e.* the time discretization size) and $\mathbf{a}_k = \mathbf{a}(t_k)$ is the value of vector $\mathbf{a}$ at time instant $t_k = k\Delta t$, leads to the standard θ-scheme:

$$\frac{\mathbf{a}_{k+1} - \mathbf{a}_k}{\Delta t} + [\theta\mathbf{f}(\mathbf{a}_{k+1}, t_{k+1}) + (1 - \theta)\mathbf{f}(\mathbf{a}_k, t_k)] = 0, \tag{1.27}$$

where θ is a parameter (see Table 1.1). In this dissertation, the unconditionally stable implicit backward Euler scheme is chosen (*i.e.* $\theta = 1$) and a new time iterate $\mathbf{a}_{k+1}$ is

Table 1.1: Time-stepping schemes according to implicitness parameter θ.

θ	Scheme	Type
0	Forward Euler	Explicit
1/2	Crank-Nicholson	Implicit
1	Backward Euler	Implicit

determined by solving

$$\left[\frac{\mathbf{M}_{k+1}}{\Delta t} + \mathbf{S}_{k+1} \right] \mathbf{a}_{k+1} = \mathbf{v}_{k+1} + \frac{\mathbf{M}_{k+1}}{\Delta t} \mathbf{a}_k, \tag{1.28}$$

where $\mathbf{M}_{k+1} = \mathbf{M}(t_{k+1})$ (analogously with $\mathbf{S}$ and $\mathbf{v}$) and may be changing in time. In the particular case (as it is also considered in this work) where the conductivity (respectively the reluctivity) does not vary in time, then matrix $\mathbf{M}$ (respectively $\mathbf{S}$) does not change and the subscripts can be omitted (*i.e.* $\mathbf{M} = \mathbf{M}_k$). Equation (1.28) then becomes

$$\left[\frac{\mathbf{M}}{\Delta t} + \mathbf{S} \right] \mathbf{a}_{k+1} = \mathbf{v}_{k+1} + \frac{\mathbf{M}}{\Delta t} \mathbf{a}_k. \tag{1.29}$$

Nonlinearities   While the conductivity and reluctivity do not (generally) change in time, they may vary according to the (induction) magnetic field—leading to nonlinear behaviors.

First, in this work we will always assume isotropic materials with a scalar conductivity. While in practical applications it will depend on the temperature, the variation takes place at a time scale much larger than the electromagnetic time scale we are interested in.

Second, in most of the energy conversion applications we are interested in, magnetic materials are used to channel the magnetic flux. In this work, anhysteretic materials are considered and exhibit nonlinear reluctivity which depends on the flux density **b** as depicted in Fig. 1.1(b) for a typical magnetic medium. Physically, at saturation, the medium cannot store additional magnetic energy—leading to a drastic increase in the reluctivity and consequently in the reluctance of the magnetic circuit (see eq. (1.37)). In this case, the stiffness matrix $\mathbf{S}$ varies with the solution and a linearization scheme (*i.e.* Newton-Raphson approach [163]) is required at each time step to solve equation (1.29). However, in general, we tend to limit the magnetic field to the linear region of the b/h curve where the reluctivity remains constant (as shown in Fig. 1.1(a)). Both situations occur in energy conversion applications and therefore are considered worth investigating in this work.

1.2.4 Frequency domain

In the frequency domain, both magnetodynamic and full wave formulations can be derived using the Laplace transform which is defined for a time domain function $f \in L^1$

(a) Linear reluctivity.

(b) Nonlinear reluctivity.
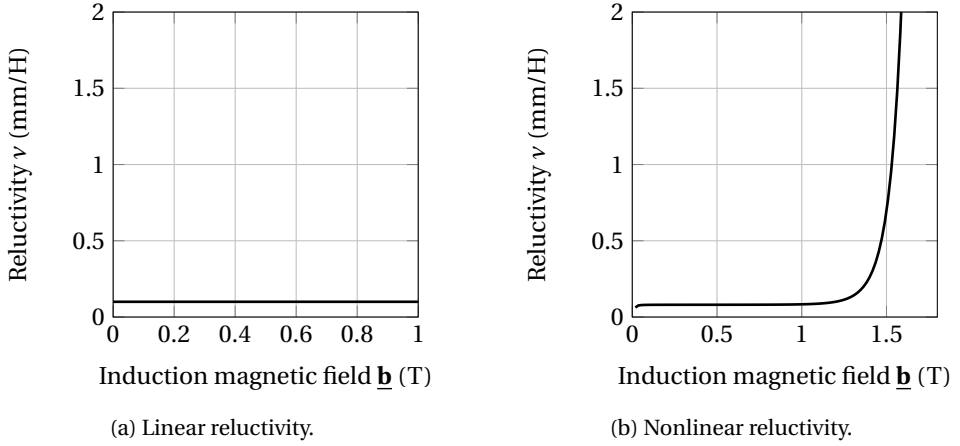
Figure 1.1: Two permittivity of linear and nonlinear materials.

as

$$\mathcal{L} : f \mapsto F, \quad F(s) := \mathcal{L}\{f(t)\}(s) := \int_0^\infty e^{-st} f(t) dt, \quad s \in \mathbb{C}. \tag{1.30}$$

Note that $s = \iota\omega$ where $\iota = \sqrt{-1}$ and $\omega = 2\pi f$ is the pulsation.

1.2.4.1 Magnetodynamic formulation

From matrix form (1.20), the discretized equation in complex formalism is

$$\left(\iota\omega\hat{\mathbf{M}} + \hat{\mathbf{S}}\right)\hat{\mathbf{a}} = \hat{\mathbf{v}}. \tag{1.31}$$

1.2.4.2 Full wave formulation

Similarly to the full wave formulation (1.23), the matrix form in frequency domain becomes

$$\left(-\omega^2\hat{\mathbf{M}}_1 + \iota\omega\hat{\mathbf{M}}_2 + \hat{\mathbf{M}}_3\right)\hat{\mathbf{x}} = \hat{\mathbf{v}}. \tag{1.32}$$

1.2.5 Global quantities

The aforementioned formulations in magnetostatics, magnetodynamics and full wave scenarios only take into account local quantities such as the magnetic vector potential **a** or the scalar electric potential v. Additional coupling can integrate global quantities **w**[1] into the discretized models (1.18), (1.29), (1.31) and (1.32) (e.g. imposing a global current in a wire or a global voltage as the excitation source term of the FE model) [66, 67, 69]. The determination of the coupling matrices from local to global quantities is described in [68, 78]. Equations are then solved, within an FE tool (e.g. GetDP [65]),

---

[1] Note **w** refers to the usual global quantities linked to the windings in energy conversion applications (e.g. transformer).

together by assembling all unknowns, global quantities (e.g. $\mathbf{w}$) and local ones (e.g. $\mathbf{a}$) into a unique unknown vector $\mathbf{x}$ (respectively the right hand term $\mathbf{v}$ becomes $\mathbf{y}$ by concatenating local and global sources).

In this work, four different situations are investigated and synthesized hereafter:

1. Magnetostatic formulation defined by

$$\mathbf{Sx} = \mathbf{y}. \tag{1.33}$$

Note that when no global quantity is assembled in the formulation, (1.33) is equal to (1.18).

2. Magnetodynamic formulation in time domain defined by

$$\left[\frac{\mathbf{M}}{\Delta t} + \mathbf{S}\right] \mathbf{x}_{k+1} = \mathbf{y}_{k+1} + \frac{\mathbf{M}}{\Delta t}\mathbf{x}_k. \tag{1.34}$$

Once more, when no global quantity is linked to the local ones, (1.34) is equivalent to (1.29).

3. Magnetodynamic formulation in frequency domain defined by

$$\left(\imath\omega\hat{\mathbf{M}} + \hat{\mathbf{S}}\right)\hat{\mathbf{x}} = \hat{\mathbf{y}}. \tag{1.35}$$

4. Full wave formulation in frequency domain expressed by (1.32).

1.3 Lumped parameter modeling

The lumped parameter modeling refers to the original definition of a model. According to Oxford dictionary, a model is described as "a simplified description, especially a mathematical one, of a system or process, to assist calculations and predictions". Before the emergence of computational power, researchers and engineers have investigated modeling (electro-)magnetodynamic devices at macro level without solving Maxwell's equation at micro-scale. To this end, electric or magnetic equivalent circuits–or Lumped Parameter Models (LPMs)–were elaborated to mimic their behaviors and/or observations. This approach presents multiple advantages such as keeping a physical interpretation of the macro observance of the systems or limiting the complexity of the models. Such models can be very precise according to the original problem complexity. To illustrate it, let us consider an academic magnetic circuit without losses as depicted in Fig. 1.2(a). Applying Ampère's law along the magnetic path Γ gives

$$\oint_{\Gamma} \underline{\mathbf{h}} \cdot \mathbf{dl} = h_{\Gamma} l_{\Gamma} = n_1 i_1 + n_2 i_2 \tag{1.36}$$

where h_{Γ}, l_{Γ}, n_x, i_x are the magnetic field in the core along Γ, the length of Γ, the number of turns of winding x and the current in winding x respectively. Considering a

(a) Ideal magnetic circuit.　　　　　(b) Equivalent electric circuit.
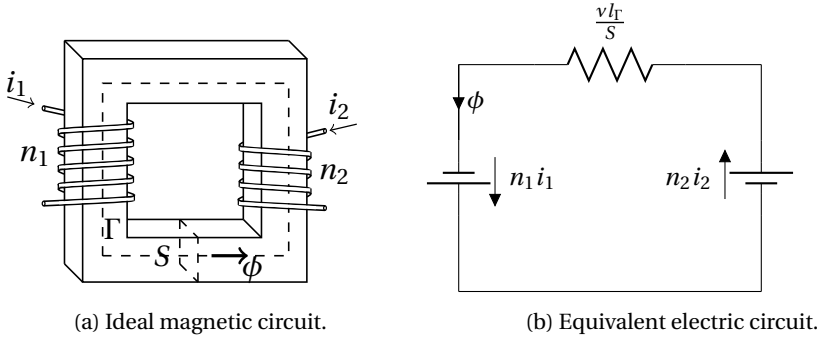
Figure 1.2: Lumped parameter modeling on a simple magnetic circuit.

perpendicular cross-section S, the magnetic flux ϕ is related to the magnetic field h by

$$\phi = \frac{h_\Gamma S}{v} = (n_1 i_1 + n_2 i_2)\frac{S}{v l_\Gamma} = \frac{(n_1 i_1 + n_2 i_2)}{\mathcal{R}} \tag{1.37}$$

with v is the inverse of the magnetic permeability of the magnetic medium and $\mathcal{R} = \frac{v l_\Gamma}{S}$ is an equivalent magnetic resistance (e.g. similar to the expression of an electric resistance from Pouillet's law), called the reluctance. Given equation (1.37), an equivalent electric circuit (see Fig. 1.2(b))–respecting similarly Ohm's law–can be constructed where the current would be the magnetic flux ϕ, the voltage supplies would be the magnetomotive forces from the windings $n_x i_x$ and the reluctance $\mathcal{R}$ (depending on magnetic and geometry properties). This simple example is the key for more complex descriptions of applications such as single and multi-phases transformers [180], dynamical electromechanical devices [208], rotating machines [131, 165, 214], actuators [44, 80], electromechanical transducers [197] or even multi-physics coupled problems [137].

1.4 Advantages and limitations of both approaches

While both methods have vastly been investigated during these last decades, their advantages and/or limitations determine the scope of possible model order reduction applications. Since we may be interested in designing and simulating models in large electric network simulators, four key issues have to be discussed:

- Computational cost. Reducing it is the main objective of this dissertation.

- Dealing with nonlinearities. As real applications present nonlinear behaviors, reduced models should accurately take them into account.

- Parameter dependencies. In case where actual device is modified, the reduced model should remain intact (or be easily changed). In particular for design and optimization stages, the electromagnetic device may not be physically built and modifications in the model must easily be performed. A second consideration lies

in the representation of multiple parameter values in the model. Is it necessary to have multiple models for each parameter?

- Coupling with external models. While standalone models of electromagnetic devices are useful, their integration as part of system-level models is very often the ultimate goal. By coupling those models with external ones, consistent systems can be studied and analyzed.

1.4.1   Computational cost

As the computational time and costs are at the center of this work, it consists in the first key question to look at. By its philosophy of macro observation of the system or extraction of FE type models, LPMs naturally present a smaller number of unknowns than those from local-based models derived by the high fidelity discretization approaches. Indeed, the latter often deals from thousands to millions of unknowns where the former only contains a few hundreds of them. Actually, the LPMs can be seen as Reduced Order Models (ROMs) of HFMs in case the parameters are deduced from the latter. Within this idea of combining the accuracy of the detailed models to the rapidity of the other, [179, 187] showed LPMs where the values of the parameters are derived from Finite Element (FE) simulations. However, determining the structure of the LPMs is not (yet) performed by automatic algorithms and still require researchers' knowledge—representing the major drawback/issue of the LPM approach.

1.4.2   Nonlinear parameters

Both approaches deal with the nonlinearities in the same way: a linearization procedure is employed at each time step (e.g. a Newton-Raphson scheme) which substantially increases the required time to solve the problem compared to a similar linear case. Indeed, each iteration requires the (re)evaluation of the matrix terms. In the micro approach, those matrices are particularly larger then those from the lumped parameter modeling and directly impact the computational time. However, determining the nonlinear behaviors (values) of equivalent parameters in LPMs is not an easy task (merely cumbersome when multiple physics are taken into account). On the other hand, since the HFMs intrinsically describe the physics in detail, the nonlinear data are much more easily obtained and implemented. Those models are usually more precise in nonlinear cases and are thus usually recommended.

1.4.3   Parameters dependency

At first glance, the parameter dependency leads to the same conclusions as for nonlinear parameters. However, it is more general as it includes all types of changes in the models. To answer the question if models can easily be modified when the parameters change, one would look for them to be determined by functions of the parameters. Even though the LPMs are derived from geometrical expressions, one may not know *a priori* the relation between the physical and lumped parameters. It requires new evaluations (e.g. tests) of the systems to establish new LPMs. In a HFM, the parameters are intrinsically

encapsulated in its formulation (and CAD description). This concern is particularly important when the electromagnetic devices are under development (e.g. during design and optimization stages in R&D units) as a considerable number of changes is often expected.

1.4.4 Coupling with external models

Finally, the integration of the models in large electric simulators by coupling them with other models is crucial for practical engineering problems. On the first hand, since LPMs are basically represented by electric circuits, their coupling with others is therefore trivial. On the other hand, the coupling of HFMs with external circuit requires a bit more care, but is nowadays practice (see e.g. [78]).

1.5 Objectives

As a conclusion, we are looking for the flexibility and accuracy of HFMs with the size and computational efficiency of LPMs without predefining any mathematical structure of the ROMs. As [179, 187] identified lumped parameter values from FE simulations, our goal is to compute ROMs from large HFMs (*i.e.* FE ones) with the following particular and ultimate objective in mind: the practical integration of parametric electromagnetic models in electric circuit simulators.

As a road map for this dissertation, the following list summarizes our four main objectives:

1. Deriving ROMs from nonlinear magnetodynamic HFMs.

2. Having flexibility, accuracy and robustness of HFMs.

3. Having size and computational requirements of LPMs.

4. Integrating ROMs into external electric networks.

CHAPTER 2

Fundamentals in model order reduction

In the 1960's, model order reduction techniques emerged in structural engineering fields. They were first designed to assemble reduced models of subparts of large model to be able to simulate the entire dynamics of the whole applications [54, 89, 108]. These methods were originally geared towards the analysis of internal modes or energy.

In conversion energy applications, we are more interested in the transfer function between the input and the output rather than studying the local components. From the 1980's, model order reduction methods have then been developed to minimize the number of equations in linear time invariant (LTI) systems [10, 11]. Since then, numerous reduction techniques have been investigated to tackle time variant and nonlinear problems [12, 25, 183]. Such complex time variant and nonlinear systems are largely studied in engineering fields from chemical reactions [113–115] to MEMS analysis [127, 128, 185] to structural vibrations optimization [28, 211] for example.

The general form of an LTI system is given by

$$\begin{cases} \mathbf{E}\dot{\mathbf{x}} & = & \mathbf{A}\mathbf{x} + \mathbf{B}\mathbf{u}, \\ \mathbf{y} & = & \mathbf{C}\mathbf{x} + \mathbf{D}\mathbf{u}, \end{cases} \tag{2.1}$$

where $\mathbf{A} \in \mathbb{R}^{n \times n}$ is the system or stiffness matrix, $\mathbf{E} \in \mathbb{R}^{n \times n}$ is the (so-called) mass matrix, $\mathbf{B} \in \mathbb{R}^{n \times m}$ is an input matrix, $\mathbf{u} \in \mathbb{R}^{m \times 1}$ is the input signal (m excitations), $\mathbf{C} \in \mathbb{R}^{l \times n}$ is the system output matrix, $\mathbf{D} \in \mathbb{R}^{l \times m}$ is an input matrix, $\mathbf{y} \in \mathbb{R}^{l \times 1}$ is the system output signal (l observations), and $\mathbf{x} \in \mathbb{R}^{n \times 1}$ is the state-space variable vector (n states).

Whereas the state variable $\mathbf{x}$ may be very large (*i.e.* $n \gg 1$), the output signal $\mathbf{y}$ usually contains relatively few components (*i.e.* $l \approx \mathcal{O}(1)$) or at least is much smaller than the number of state variables (*i.e.* $l \ll n$). As a consequence, one is highly interested in reducing the state-space relation in system (2.1) since most of the computational time and resources are spent on an excessively larger problem than the required or observed one.

Given formulation (2.1), the general model order reduction consists in projecting the high dimensional state-space vector $\mathbf{x}$ onto a reduced subspace with a much smaller
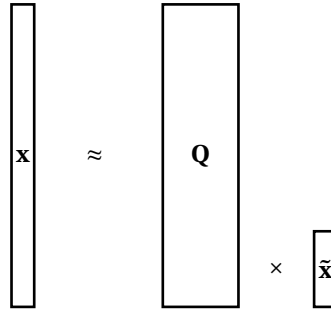
Figure 2.1: High fidelity vector $\mathbf{x}$ expressed by reduced vector $\tilde{\mathbf{x}}$ via the mapping basis $\mathbf{Q}$.

number of dimensions (*i.e.* $r \ll n$) and defining a corresponding reduced order state-space vector $\tilde{\mathbf{x}} \in \mathbb{R}^{r \times 1}$. Such a projection (illustrated in Fig. 2.1) is often expressed by a linear combination of $\mathbf{x}$ and is called the projection matrix $\mathbf{Q} \in \mathbb{R}^{n \times r}$ verifying

$$\mathbf{x} \approx \mathbf{Q}\tilde{\mathbf{x}}. \tag{2.2}$$

According to the choice of $\mathbf{Q}$ (and the related method), the approximation in (2.2) can be excellent or very poor. In most methods, error (upper) bounds can be determined and provide information on the aforementioned deviation between the reduced and high fidelity vectors.

Replacing $\mathbf{x}$ by its approximated form $\mathbf{Q}\tilde{\mathbf{x}}$ in (2.1) gives rise to an over-determined system with n equations for $r \leq n$ unknowns. Then, system (2.1) is left projected on a second subspace $\mathbf{P} \in \mathbb{R}^{n \times r}$. After projecting on the subspace spanned by the columns of $\mathbf{P}$, system (2.1) is reduced to formulation

$$\begin{cases} \tilde{\mathbf{E}}\dot{\tilde{\mathbf{x}}} & = & \tilde{\mathbf{A}}\tilde{\mathbf{x}} + \tilde{\mathbf{B}}\mathbf{u}, \\ \mathbf{y} & = & \tilde{\mathbf{C}}\tilde{\mathbf{x}} + \mathbf{D}\mathbf{u}, \end{cases} \tag{2.3}$$

with reduced matrices $\tilde{\mathbf{E}} = \mathbf{P}^{\mathbf{T}}\mathbf{E}\mathbf{Q} \in \mathbb{R}^{r \times r}$, $\tilde{\mathbf{A}} = \mathbf{P}^{\mathbf{T}}\mathbf{A}\mathbf{Q} \in \mathbb{R}^{r \times r}$, $\tilde{\mathbf{B}} = \mathbf{P}^{\mathbf{T}}\mathbf{B} \in \mathbb{R}^{r \times m}$, $\tilde{\mathbf{C}} = \mathbf{C}\mathbf{Q} \in \mathbb{R}^{l \times r}$. It is a Galerkin projection when the reduced matrices are equal to each other (*i.e.* $\mathbf{P} = \mathbf{Q}$).

In the next sections we review state-of-the-art model reduction techniques, which lead to different left and right projection matrices $\mathbf{P}$ and $\mathbf{Q}$.

Similarly to the previous chapter where modeling techniques followed different philosophies based on global or local description of the systems, model order reduction techniques can similarly be organized in several categories. In section 2.1, existing reduction methods are listed and explained. First, a set of methods equivalent to *model-based reduction techniques*, where the resulted ROMs are directly derived from the equations of the HFMs, are presented. Secondly, at the opposite of the first philosophy, reduced order models are derived from observations of the HFMs—being similar to the macro description of LPMs method regarding the modeling aspects. These methods could be denoted as *observation-based reduction techniques*. Lastly, alternative and efficient formulations can be derived when solutions allow a separable representation.

Then in section 2.2, the question regarding the treatment of nonlinearities is tackled. Due to the additional linearization scheme at each time step, the computational cost highly grows in nonlinear problems—requiring supplementary reductions considerations. Particular to model order reduction, the differentiation between online and offline phases is explained in section 2.3.1. Completing the requirements defined in previous chapter, the two distinct philosophies in the model order reduction community are presented to tackle parametric problems in section 2.3.2. Lastly, in section 2.3.3 we present the choice of the methods we will further consider for reducing HFMs, and we provide a more refined outline of the work which suggests the considered strategies for the studied applications—from simple linear magnetic devices to fully integrated parametric nonlinear applications with external electric circuits.

2.1 Model- and observation-based reduction techniques

In this section, we first present methods where the left and right subspaces are determined from the mathematical structure or properties of the HFM (2.1): the Schur complement approach, the balanced truncation method and the Krylov-based technique. Then methods where observations of the system are used to determine the projection matrices or to construct a black-box model are then reviewed: the Proper Orthogonal Decomposition and machine learning approaches. Lastly, the Proper Generalized Decomposition approach is described, where the dimension of the original system is reduced through a separable representation of the solution.

2.1.1 Schur complement approach

One of the oldest methods to deal with model reduction is the Schur complement approach, or static linear condensation [20, 89, 206]. It relies on eliminating the unwanted variables in a large system by inverting its corresponding block matrix. To illustrate it, let us consider the general system (2.4) where one is only interested in the vector $\mathbf{x_1}$ which is coupled to another vector $\mathbf{x_2}$ via the matrix $\mathbf{B}$. This coupling increases the overall system size which is unnecessary for the only observation of $\mathbf{x_1}$:

$$\left[\begin{array}{cc} \mathbf{A} & \mathbf{B} \\ \mathbf{C} & \mathbf{D} \end{array} \right] \left[\begin{array}{c} \mathbf{x_1} \\ \mathbf{x_2} \end{array} \right] = \left[\begin{array}{c} \mathbf{w_1} \\ \mathbf{w_2} \end{array} \right]. \tag{2.4}$$

By developing the system (2.4) into

$$\begin{cases} \mathbf{A}\mathbf{x_1} + \mathbf{B}\mathbf{x_2} &=& \mathbf{w_1}, \\ \mathbf{C}\mathbf{x_1} + \mathbf{D}\mathbf{x_2} &=& \mathbf{w_2}, \end{cases} \tag{2.5}$$

one can directly express $\mathbf{x_2}$ in terms of $\mathbf{x_1}$ as

$$\mathbf{x_2} = \mathbf{D}^{-1} \left(\mathbf{w_2} - \mathbf{C}\mathbf{x_1} \right) \tag{2.6}$$

if $\mathbf{D}$ is invertible. By injecting this expression into the first row of system (2.5), $\mathbf{x_1}$ becomes independent of $\mathbf{x_2}$ as

$$\mathbf{Ax_1} + \mathbf{Bx_2} \quad = \quad \mathbf{Ax_1} + \mathbf{BD}^{-1}(\mathbf{w_2} - \mathbf{Cx_1}) \tag{2.7}$$

$$= \quad (\mathbf{A} - \mathbf{BD}^{-1}\mathbf{C})\mathbf{x_1} + \mathbf{BD}^{-1}\mathbf{w_2}. \tag{2.8}$$

Rewriting this equation in conventional form, one finds the canonical equation

$$(\mathbf{A} - \mathbf{BD}^{-1}\mathbf{C})\mathbf{x_1} = \mathbf{w_1} - \mathbf{BD}^{-1}\mathbf{w_2} \tag{2.9}$$

which only implies vector $\mathbf{x_1}$. Contrary to the original system dimension that equals the sum of both the size of $\mathbf{x_1}$ and $\mathbf{x_2}$, this formulation results in a smaller dimension as it only contains the unknown $\mathbf{x_1}$. A direct solution of $\mathbf{x_1}$ is given by

$$\mathbf{x_1} = (\mathbf{A} - \mathbf{BD}^{-1}\mathbf{C})^{-1}(\mathbf{w_1} - \mathbf{BD}^{-1}\mathbf{w_2}). \tag{2.10}$$

Several issues appear with this approach, in particular when $\mathbf{x_1}$ is expressed by equation (2.10). The main problem comes from the direct inversion of matrices (*i.e.* $\mathbf{D}$ and $(\mathbf{A} - \mathbf{BD}^{-1}\mathbf{C})$). This operation may not be suitable if $\mathbf{D}$ is not invertible, is large or constantly changing. From Gauss-Jordan elimination technique [136, 159] to optimized inversion algorithms [77, 126], inverting a matrix of size $n \times n$ has a complexity between $\mathcal{O}(n^2)$ and $\mathcal{O}(n^3)$ and may lead to huge computational time and operations. In addition, if $\mathbf{D}$ is changing, one has to recompute its inverse multiple times—leading to an even more impractical method. Iterative linear solvers like preconditioned conjugate gradient methods [29, 52, 53, 117, 186] can be used instead of inverting the matrix blocs explicitly, but this still leads to very expensive methods in practice.

Even if the Schur complement method does not seem at first glance to provide a reduced system of the general form (2.3), a simple reverse-engineering analysis permits the identification of the left and right projection matrices. First, the right projection matrix $\mathbf{Q}$ is trivially determined by eliminating $\mathbf{x_2}$ from the high fidelity vector $\mathbf{x}$. Since one must satisfy

$$\mathbf{Qx_1} = \begin{bmatrix} \mathbf{Q_1} \\ \mathbf{Q_2} \end{bmatrix} \mathbf{x_1} = \begin{bmatrix} \mathbf{x_1} \\ \mathbf{x_2} \end{bmatrix}, \tag{2.11}$$

then

$$\mathbf{Q} = \begin{bmatrix} \mathbf{I} \\ \mathbf{x_2}/\mathbf{x_1} \end{bmatrix} = \begin{bmatrix} \mathbf{I} \\ \mathbf{D}^{-1}(\mathbf{w_2} - \mathbf{Cx_1})/\mathbf{x_1} \end{bmatrix}. \tag{2.12}$$

Considering the left projection matrix $\mathbf{P}$, since

$$\mathbf{P}^T\mathbf{w} = \begin{bmatrix} \mathbf{P_1}^T & \mathbf{P_2}^T \end{bmatrix} \begin{bmatrix} \mathbf{w_1} \\ \mathbf{w_2} \end{bmatrix} = \mathbf{w_1} - \mathbf{BD}^{-1}\mathbf{w_2}. \tag{2.13}$$

then

$$\mathbf{P} = \begin{bmatrix} \mathbf{I} \\ (-\mathbf{BD}^{-1})^T \end{bmatrix} = \begin{bmatrix} \mathbf{I} \\ -\mathbf{D}^{-T}\mathbf{B}^T \end{bmatrix}. \tag{2.14}$$
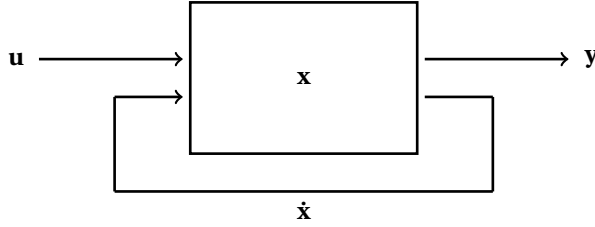
Figure 2.2: General representation of a LTI system.

2.1.2 Balanced truncation

Considering the LTI formulation in time domain (2.1), one is generally interested in the input-output relationship only. Graphically, the system is modeled by a black-box as depicted in Fig. 2.2. As one acts on the input $\mathbf{u}$, the output $\mathbf{y}$ changes and is the only variable of interest. This relation is usually defined in frequency domain as the transfer function $\mathbf{G}(s)$. By considering the Laplace transformation of system (2.1) with no initial condition as

$$\begin{cases} s\mathbf{E}\mathbf{x}(s) &=& \mathbf{A}\mathbf{x}(s) + \mathbf{B}\mathbf{u}(s), \\ \mathbf{y}(s) &=& \mathbf{C}\mathbf{x}(s) + \mathbf{D}\mathbf{u}(s). \end{cases} \tag{2.15}$$

the derivative of $\mathbf{x}$ is eliminated and the definition of the transfer function $\mathbf{G}(s)$, the relation between the input and the output, is further defined by

$$\mathbf{y}(s) = \left[\mathbf{C}(s\mathbf{E} - \mathbf{A})^{-1}\mathbf{B} + \mathbf{D} \right] \mathbf{u}(s) \tag{2.16}$$

$$= \mathbf{G}(s)\mathbf{u}(s). \tag{2.17}$$

If one defines a reduced model of (2.1) by (2.3), the aim is to provide a relatively close reduced output $\tilde{\mathbf{y}}$ to the original full size output $\mathbf{y}$ such that

$$\left\| \mathbf{y} - \tilde{\mathbf{y}} \right\| = \left\| \mathbf{G}\mathbf{u} - \tilde{\mathbf{G}}\mathbf{u} \right\| \leq \left\| \mathbf{G} - \tilde{\mathbf{G}} \right\| \cdot \left\| \mathbf{u} \right\| \leq \varepsilon \cdot \left\| \mathbf{u} \right\|, \tag{2.18}$$

where ε is an arbitrary tolerance bounding the error of the reduced output compared to the input excitation. From a different point of view, reducing the system is similar to the minimisation problem (while respecting $r \ll n$)

$$\min_{\text{rank}(\mathbf{G}) \leq r} \left\| \mathbf{G} - \tilde{\mathbf{G}} \right\|_{\infty} \tag{2.19}$$

The balanced truncation has the objective to eliminate the state-space variables of a balanced system that have minimal contribution in the transfer function by verifying equation (2.19) [141, 142]. System (2.1) is balanced if the controllability and observability Gramians (respectively $\mathbf{W_c}$ and $\mathbf{W_o}$) satisfy

$$\mathbf{W_c} = \mathbf{W_o} = diag(\xi_1, \cdots, \xi_n) \tag{2.20}$$

with $\xi_1 \geq \xi_2 \geq \cdots \geq \xi_n > 0$ their Hankel singular values in decreasing order. Those Gramians are the solutions of generalized Lyapunov equations [18, 132, 195]:

$$\mathbf{AW_cE}^T + \mathbf{EW_cA}^T \quad = \quad -\mathbf{BB}^T, \tag{2.21}$$

$$\mathbf{A}^T\tilde{\mathbf{W}}_o\mathbf{E} + \mathbf{E}^T\tilde{\mathbf{W}}_o\mathbf{A} \quad = \quad -\mathbf{C}^T\mathbf{C}, \quad \mathbf{W_o} = \mathbf{E}^T\tilde{\mathbf{W}}_o\mathbf{E}. \tag{2.22}$$

Any arbitrary system (2.1) (which is not balanced) can be transformed in a balanced one ($\tilde{\mathbf{E}}$, $\tilde{\mathbf{A}}$, $\tilde{\mathbf{B}}$, $\tilde{\mathbf{C}}$, $\tilde{\mathbf{D}}$) via a state-space transformation $\mathbf{T}$ such that

$$\begin{cases} \tilde{\mathbf{E}} & = & \mathbf{TET}^{-1}, \\ \tilde{\mathbf{A}} & = & \mathbf{TAT}^{-1}, \\ \tilde{\mathbf{B}} & = & \mathbf{TB}, \\ \tilde{\mathbf{C}} & = & \mathbf{CT}^{-1}, \\ \tilde{\mathbf{D}} & = & \mathbf{D}. \end{cases} \tag{2.23}$$

The discarded states are truncated after the reduced size r. A practical method allowing the direct balancing and truncation of an arbitrary system [86, 141, 212] is the following:

1. Compute controllability and observability Gramians $\mathbf{W_c}$ and $\mathbf{W_o}$ by solving generalized Lyapunov equations (2.21) and (2.22).

2. Compute the decomposition factors $\mathbf{S}$ and $\mathbf{R}$ of the Gramians according to one of the two methods:

   a) Compute the Cholesky factors $\mathbf{W_c} = \mathbf{S}^T\mathbf{S}$ and $\mathbf{W_o} = \mathbf{R}^T\mathbf{R}$.

   b) Compute the Singular Value Decomposition (SVD) of the Gramians: $\mathbf{W}. = \mathbf{U}.\mathbf{\Xi}.\mathbf{V}.^T$. The factors are given by $\mathbf{S} = \left(\mathbf{U_o\Xi_o^{1/2}}\right)^T$ and $\mathbf{R} = \left(\mathbf{U_c\Xi_c^{1/2}}\right)^T$.

3. Compute the SVD of $\mathbf{SR}^T$ in order to sort the Hankel singular values ξ_i:

$$\mathbf{SR}^T = \mathbf{U\Xi V}^T = \begin{bmatrix} \mathbf{U_1U_2} \end{bmatrix} \begin{bmatrix} \mathbf{\Xi_1} & \\ & \mathbf{\Xi_2} \end{bmatrix} \begin{bmatrix} \mathbf{V_1}^T \\ \mathbf{V_2}^T \end{bmatrix} \tag{2.24}$$

   with $\mathbf{\Xi} = diag(\xi_1, \cdots, \xi_n)$.

4. By truncating at rth singular value ξ_r (such that $1 \leq r \leq n$), the discarded states are the $n - r$ last ones and correspond to block matrices $\mathbf{U_2}$, $\mathbf{\Xi_2}$ and $\mathbf{V_2}$. The left and right projection matrices are given by

$$\begin{cases} \mathbf{P}^T & = \mathbf{\Xi_1}^{-1/2}\mathbf{V_1}^T\mathbf{RE}^{-1}, \\ \mathbf{Q} & = \mathbf{S}^T\mathbf{U_1}\mathbf{\Xi_1}^{-1/2}, \end{cases} \tag{2.25}$$

   and the reduced model follows the general reduction formulation (2.3).

Two major advantages come with this method:

1. Stability is preserved when it is applied on a stable system [158].
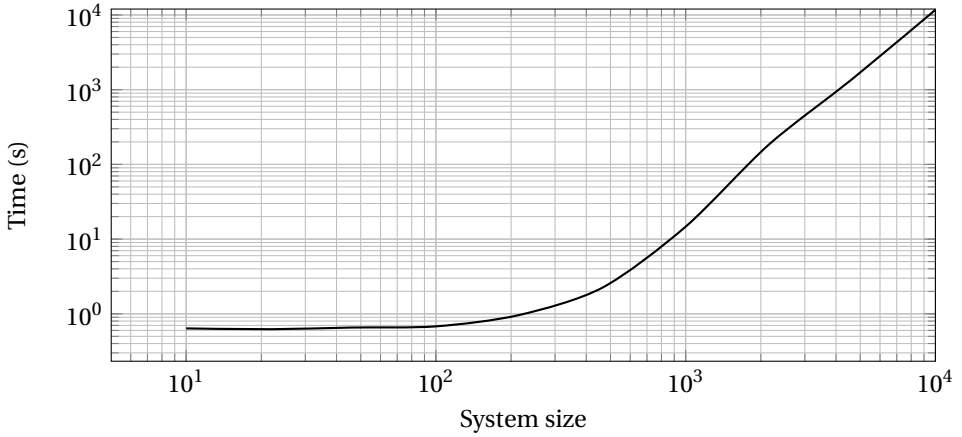
Figure 2.3: Time required to process the balanced truncation method with regard to to the system size.

2. An error bound is provided in [73]. By keeping the r first Hankel singular values $\xi_1, \cdots, \xi_r$, the error bound is defined as

$$\left\| \mathbf{y} - \tilde{\mathbf{y}} \right\| \leq 2 \left\| \mathbf{u} \right\| \sum_{k=r+1}^{n} \xi_k. \tag{2.26}$$

However, the main disadvantages of this method are large storage $\mathcal{O}(n^2)$ and high computational complexity $\mathcal{O}(n^3)$ as it requires dense matrix factorizations (the resolution time with respect to system size is depicted in Fig. 2.3 on a typical laptop). To alleviate these issues, novel approximate balanced reduction methods are being developed to efficiently apply this method [87, 156, 157, 193]. In addition, its main limitation consists in its application to LTI systems only. Limited studies investigated balanced truncation applied to nonlinear system [181].

Example Let us illustrate this method on the following small problem

$$\begin{cases} \begin{bmatrix} \dot{\mathbf{x}}_1 \\ \dot{\mathbf{x}}_2 \end{bmatrix} = \begin{bmatrix} -1 & 1 \\ 0 & -1 \end{bmatrix} \begin{bmatrix} \mathbf{x}_1 \\ \mathbf{x}_2 \end{bmatrix} + \begin{bmatrix} 1 \\ \delta \end{bmatrix} u, \\ \mathbf{y} = \begin{bmatrix} 1 & 1 \end{bmatrix} \begin{bmatrix} \mathbf{x}_1 \\ \mathbf{x}_2 \end{bmatrix}, \end{cases} \tag{2.27}$$

where δ is a parameter. Depending on the parameter value, the state $\mathbf{x}_2$ is controllable (*i.e.* $\delta \gg 1$) or not (*i.e.* $\delta \ll 1$). Based on the previous developments, if a state is not controllable (or observable), it may be eliminated by applying the balanced truncation method. In this case, the system would be reduced from size 2 down to 1. This observation can easily be done by deriving the transfer function $\mathbf{G}(s)$ using relation (2.16)

Table 2.1: Illustration of balanced truncation of system (2.27) by eliminating the second variable.

	$\delta = 10^{-2}$	$\delta = 1$	$\delta = 10^{2}$
$\mathbf{W_c}$	$\begin{bmatrix} 0.5050 & 0.005 \\ 0.005 & 5e-5 \end{bmatrix}$	$\begin{bmatrix} 1.25 & 0.75 \\ 0.75 & 0.5 \end{bmatrix}$	$\begin{bmatrix} 2550.5 & 2550 \\ 2550 & 5000 \end{bmatrix}$
$\mathbf{W_o}$	$\begin{bmatrix} 0.5 & 0.75 \\ 0.75 & 1.25 \end{bmatrix}$	$\begin{bmatrix} 0.5 & 0.75 \\ 0.75 & 1.25 \end{bmatrix}$	$\begin{bmatrix} 0.5 & 0.75 \\ 0.75 & 1.25 \end{bmatrix}$
ξ_i	$\begin{bmatrix} 0.51 \\ 1.22e-5 \end{bmatrix}$	$\begin{bmatrix} 1.5406 \\ 0.0406 \end{bmatrix}$	$\begin{bmatrix} 106.3754 \\ 5.8754 \end{bmatrix}$
$\mathbf{Q} = \mathbf{P}$	$\begin{bmatrix} -0.9951 \\ -0.0099 \end{bmatrix}$	$\begin{bmatrix} -0.8891 \\ -0.5623 \end{bmatrix}$	$\begin{bmatrix} -4.1880 \\ -6.6741 \end{bmatrix}$
$\tilde{\mathbf{A}}$	-0.9902	-0.6838	-0.5546
$\tilde{\mathbf{B}}$	-1.0050	-1.4515	-10.8621
$\tilde{\mathbf{C}}$	-1.0050	-1.4515	-10.8621

as

$$\mathbf{G}(s) = \frac{1}{s+1} + \delta \left(\frac{s+2}{(s+1)^2} \right), \tag{2.28}$$

where it is approximated by a 1-pole transfer function in case $\delta \ll 1$. Table 2.1 shows the balanced truncation of system (2.27) by only keeping the first variable. By looking at the Hankel singular values and the error criterion (2.26), the reduction only makes sense in the first case (*i.e.* $\delta = 10^{-2}$). As the parameter acts on matrix $\mathbf{B}$, only the controllability Gramian changes with it significantly. The Bode diagrams are depicted in Fig. 2.4 for $\delta = 10^{-2}$ and $\delta = 10^{2}$. On the first hand, with $\delta = 10^{-2}$, the balanced truncated model significantly matches the full model response. On the other hand, with $\delta = 10^{2}$, both models do no longer align to each other in amplitude and phase (even though the approximations remain quite good).

2.1.3   Krylov-based methods

Considering the case where $\mathbf{B}$ is a vector, one can derived its Taylor expansion around zero, using the transfer function described in (2.16), as

$$\mathbf{G}(s) = -\mathbf{C}\mathbf{A}^{-1}\mathbf{B} + \mathbf{D} - \mathbf{C}\left(\mathbf{A}^{-1}\mathbf{E}\right)\mathbf{A}^{-1}\mathbf{B}s - \cdots - \mathbf{C}\left(\mathbf{A}^{-1}\mathbf{E}\right)^{i}\mathbf{A}^{-1}\mathbf{B}s^{i} - \cdots \tag{2.29}$$

$$= \mathbf{D} - \sum_{i=0}^{\infty} \mathbf{C}\left(\mathbf{A}^{-1}\mathbf{E}\right)^{i}\mathbf{A}^{-1}\mathbf{B}s^{i} \tag{2.30}$$

$$= \mathbf{D} + \sum_{i=0}^{\infty} \mathbf{M}_{i} s^{i} \tag{2.31}$$

where $\mathbf{M}_i = -\mathbf{C}\left(\mathbf{A}^{-1}\mathbf{E}\right)^{i}\mathbf{A}^{-1}\mathbf{B}$ is called the ith moment around zero. Similarly, the moments and the transfer function can be determined around any arbitrary expansion point $s_{exp} \neq 0$. Translating the transfer function gives

$$\mathbf{G}(s) = \mathbf{C}\left[(s - s_{exp})\mathbf{E} - \left(\mathbf{A} - s_{exp}\mathbf{E}\right)\right]^{-1}\mathbf{B} + \mathbf{D} \tag{2.32}$$
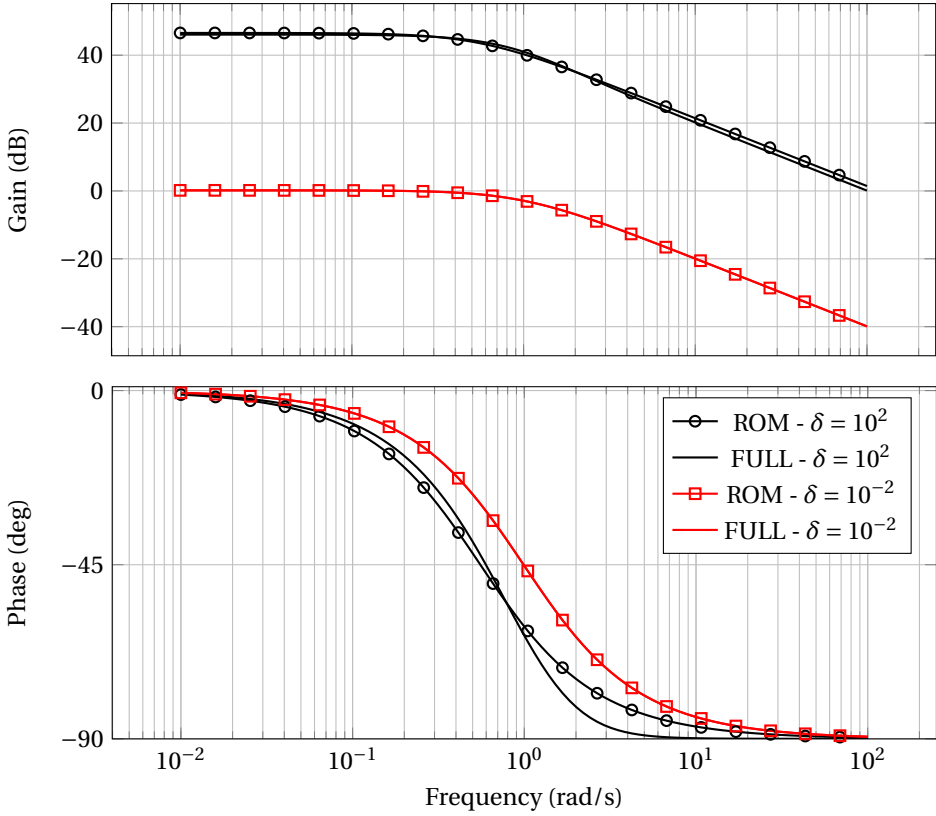
Figure 2.4: Comparison of full and balanced truncated systems of (2.27) with one mode.

where the moments around s_{exp} can be retrieved by substituting $\mathbf{A}$ by $(\mathbf{A} - s_{exp}\mathbf{E})$ in (2.29). As the moments define the transfer function, the reduced model (2.3) should share the same moments—leading to the usually called *moment matching* method.

Let us define the Krylov subspace of rank r by

$$\mathcal{K}_r(\mathbf{A}, \mathbf{B}) = span\left\{\mathbf{B}, \mathbf{AB}, \mathbf{A^2B}, \cdots, \mathbf{A^{r-1}B}\right\}, \tag{2.33}$$

with $\mathbf{A} \in \mathbb{R}^{n \times n}$ and $\mathbf{B} \in \mathbb{R}^n$. The vectors $\mathbf{B}, \mathbf{AB}, \mathbf{A^2B}, \cdots$ are usually called the basis vectors. It can be shown that if $\mathbf{Q}$ is a basis of Krylov subspace

$$\mathcal{K}_r\left((\mathbf{A} - s_{exp}\mathbf{E})^{-1}\mathbf{E}, (\mathbf{A} - s_{exp}\mathbf{E})^{-1}\mathbf{B}\right)$$

and $\mathbf{P}$ is chosen to preserve $\tilde{\mathbf{A}}$ nonsingular (e.g. $\mathbf{P} = \mathbf{Q}$), then the first r moments around expansion point $\mathbf{s}_{exp}$ for both full and reduced systems match [75]—leading to the Krylov-based reduction methods. For the sake of simplicity, the demonstration around $s_{exp} = 0$ is shown hereafter using the recursive theorem. From (2.31), the first moment

of the reduced model is given by

$$\tilde{\mathbf{M}}_0 = -\tilde{\mathbf{C}}\tilde{\mathbf{A}}^{-1}\tilde{\mathbf{B}} = \mathbf{C}\mathbf{Q}\left(\mathbf{P}^T\mathbf{A}\mathbf{Q}\right)^{-1}\mathbf{P}^T\mathbf{B}. \tag{2.34}$$

Since $\mathbf{A}\mathbf{A}^{-1} = \mathbf{I}$ and basis vector $\mathbf{A}^{-1}\mathbf{B}$ is part of the Krylov subspace $\mathcal{K}_r(\mathbf{A}^{-1}\mathbf{E}, \mathbf{A}^{-1}\mathbf{B})$ (*i.e.* basis vector is a linear combination of the subspace and $\exists \mathbf{v}_0 \in \mathbb{R}^r : \mathbf{A}^{-1}\mathbf{B} = \mathbf{Q}\mathbf{v}_0$), one can verify the moment matching between full and reduced model as

$$\begin{aligned}
\tilde{\mathbf{M}}_0 &= -\mathbf{C}\mathbf{Q}\left(\mathbf{P}^T\mathbf{A}\mathbf{Q}\right)^{-1}\mathbf{P}^T\mathbf{A}\mathbf{A}^{-1}\mathbf{B} \tag{2.35}\\
&= -\mathbf{C}\mathbf{Q}\left(\mathbf{P}^T\mathbf{A}\mathbf{Q}\right)^{-1}\mathbf{P}^T\mathbf{A}\mathbf{Q}\mathbf{v}_0 \tag{2.36}\\
&= -\mathbf{C}\mathbf{Q}\mathbf{v}_0 \tag{2.37}\\
&= -\mathbf{C}\mathbf{A}^{-1}\mathbf{B} \tag{2.38}\\
&= \mathbf{M}_0. \tag{2.39}
\end{aligned}$$

Considering the second moment $\mathbf{M}_1$, the following equalities can be derived

$$\begin{aligned}
\tilde{\mathbf{M}}_1 &= -\tilde{\mathbf{C}}\tilde{\mathbf{A}}^{-1}\tilde{\mathbf{E}}\tilde{\mathbf{A}}^{-1}\tilde{\mathbf{B}} \tag{2.40}\\
&= -\mathbf{C}\mathbf{Q}\left(\mathbf{P}^T\mathbf{A}\mathbf{Q}\right)^{-1}\left(\mathbf{P}^T\mathbf{E}\mathbf{Q}\right)\left(\mathbf{P}^T\mathbf{A}\mathbf{Q}\right)^{-1}\mathbf{P}^T\mathbf{B} \tag{2.41}\\
&= -\mathbf{C}\mathbf{Q}\left(\mathbf{P}^T\mathbf{A}\mathbf{Q}\right)^{-1}\left(\mathbf{P}^T\mathbf{E}\right)\mathbf{Q}\mathbf{v}_0 \tag{2.42}\\
&= -\mathbf{C}\mathbf{Q}\left(\mathbf{P}^T\mathbf{A}\mathbf{Q}\right)^{-1}\left(\mathbf{P}^T\mathbf{E}\right)\mathbf{A}^{-1}\mathbf{B} \tag{2.43}\\
&= -\mathbf{C}\mathbf{Q}\left(\mathbf{P}^T\mathbf{A}\mathbf{Q}\right)^{-1}\left(\mathbf{P}^T\mathbf{A}\mathbf{A}^{-1}\mathbf{E}\right)\mathbf{A}^{-1}\mathbf{B} \tag{2.44}\\
&= -\mathbf{C}\mathbf{Q}\left(\mathbf{P}^T\mathbf{A}\mathbf{Q}\right)^{-1}\mathbf{P}^T\mathbf{A}\mathbf{Q}\mathbf{v}_1 \tag{2.45}\\
&= -\mathbf{C}\mathbf{Q}\mathbf{v}_1 \tag{2.46}\\
&= -\mathbf{C}\mathbf{A}^{-1}\mathbf{E}\mathbf{A}^{-1}\mathbf{B} \tag{2.47}\\
&= \mathbf{M}_1 \tag{2.48}
\end{aligned}$$

since $\mathbf{A}^{-1}\mathbf{E}\mathbf{A}^{-1}\mathbf{B}$ is the second basis vector of the Krylov subspace $\mathcal{K}_r(\mathbf{A}^{-1}\mathbf{E}, \mathbf{A}^{-1}\mathbf{B})$ and can be written, as previously, by a linear combination of $\mathbf{Q}$ such as $\exists \mathbf{v}_1 \in \mathbb{R}^r : \mathbf{A}^{-1}\mathbf{E}\mathbf{A}^{-1}\mathbf{B} = \mathbf{Q}\mathbf{v}_1$. The following $(r-1)$ moments can be inferred with the same approach.

It may be worth knowing the special selection of $\mathbf{P}$ in the Krylov subspace

$$\mathcal{K}_r\left(\left(\mathbf{A} - s_{exp}\mathbf{E}\right)^{-T}\mathbf{E}^T, \left(\mathbf{A} - s_{exp}\mathbf{E}\right)^{-T}\mathbf{B}^T\right)$$

allows $2r$ moments matching between full and reduced models—usually called the two-sided Krylov method [84, 175].

The determination of the basis matrices $\mathbf{P}$ and $\mathbf{Q}$ are often handled by the Lanczos or Arnoldi algorithms in such subspaces [10, 176]. Krylov subspace reduction has been vastly investigated [16, 109, 174]—in particular the error bounds [148].

Example   Using the same example (2.27) as with the balanced truncation method, a single expansion Krylov reduction is shown in Table 2.2 and Fig. 2.5 in order to reduce the original size from two to one. Using the Arnoldi algorithm to determine the Krylov

Table 2.2: Illustration of 1 expansion point Krylov reduction of system (2.27) using Arnoldi algorithm.

	$\delta = 10^{-2}$	$\delta = 1$	$\delta = 10^2$
Q = P		$\begin{bmatrix} 0.01 \\ 1 \end{bmatrix}$	
$\tilde{\mathbf{A}}$		-0.9902	
$\tilde{\mathbf{B}}$	1	-1.4142	100.005
$\tilde{\mathbf{C}}$		1.0099	
$\mathbf{M}_0$	-1.03	-4	-301
$\tilde{\mathbf{M}}_0$	-1.03	-8	-103

subspace $\mathcal{K}_r(\mathbf{A}, \mathbf{B})$ with a single expansion point, the reduction basis $\mathbf{Q}$ contains one vector and is unique for all values of δ. As with the balanced truncation method, the lower δ, the better the reduced model. It is directly observed by the comparison of the first moment $\mathbf{M}$ and its reduced counterpart $\tilde{\mathbf{M}}_0$ in Table 2.2. The lower δ, the better the moments match to each others which leads to an accurate reduced model as described in Fig. 2.5.

2.1.4 Proper Orthogonal Decomposition

Instead of constructing the projection bases $\mathbf{P}$ and $\mathbf{Q}$ algebraically from the model (*i.e.* the large matrices $\mathbf{A}$, $\mathbf{B}$, ... in (2.1)), they can also be determined using the information contained in multiple observations of the state-space vector $\mathbf{x}$, by identifying a smaller dimensional subspace from high fidelity observations [116]. It consists in reducing a large number of correlated variables to a smaller number of interdependent ones. Let us consider N_t observations of $\mathbf{x} \in \mathbb{R}^{n \times 1}$ of a dynamical system as in (2.1), the snapshot matrix $\mathbf{X}$ is defined as the concatenation of all solutions $\mathbf{x}_i$ with $i = 1, \cdots, N_t$:

$$\mathbf{X} = \begin{bmatrix} \mathbf{x}_1, \cdots, \mathbf{x}_{N_t} \end{bmatrix} \in \mathbb{R}^{n \times N_t}. \tag{2.49}$$

Having a large snapshot matrix, the POD aims at finding a small orthogonal subspace containing the same information. Therefore, the high dimensional snapshot matrix can be expressed by a linear combination of the orthogonal vectors as

$$\mathbf{X} \approx \mathbf{Q}\tilde{\mathbf{X}} \tag{2.50}$$

which is similar to eq. (2.2) and where $\mathbf{Q} = \begin{bmatrix} q_1, \cdots, q_r \end{bmatrix} \in \mathbb{R}^{n \times r}$ and $\tilde{\mathbf{X}} = \begin{bmatrix} \tilde{\mathbf{x}}_1, \cdots, \tilde{\mathbf{x}}_{N_t} \end{bmatrix} \in \mathbb{R}^{r \times N_t}$. The determination of $\mathbf{Q}$ can be performed by either of three classical tools: the singular value decomposition (SVD) [57, 81, 201], the Principal Component Analysis (PCA) [111, 188, 207] or the Karhunen-Loeve Decomposition (KLD) [76, 118, 200]. Those three methods are equivalent as shown in [128]. By defining the error matrix as

$$\mathbf{E} = \mathbf{X} - \mathbf{Q}\tilde{\mathbf{X}}, \tag{2.51}$$
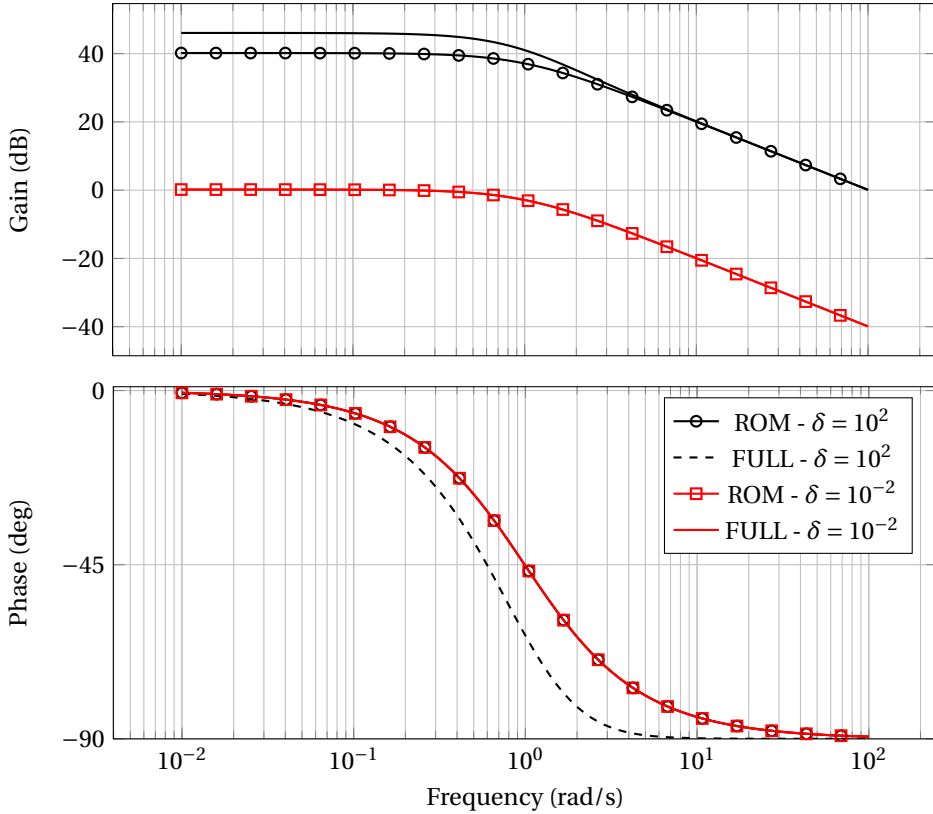
Figure 2.5: Comparison of full and Krylov reduced systems (using Arnoldi algorithm) of (2.27) around one expansion point.

the SVD finds the optimal approximation of $\mathbf{X} = \mathbf{U}\mathbf{\Xi}\mathbf{V^T}$ such that $\|\mathbf{E}\|$ is minimum for a given value of r. Note that $\mathbf{U} \in \mathbb{R}^{n \times n}$ and $\mathbf{V} \in \mathbb{R}^{N_t \times N_t}$ are orthogonal matrices and $\mathbf{\Xi} \in \mathbb{R}^{n \times N_t}$ is a diagonal matrix containing all singular values in decreasing order. By identification with eq. (2.2), one could consider $\mathbf{Q} = \mathbf{U} \in \mathbb{R}^{n \times n}$ and $\mathbf{\tilde{X}} = \mathbf{\Xi}\mathbf{V^T} \in \mathbb{R}^{n \times N_t}$. In this case, no reduction is performed and both left and right hand sides of (2.50) are equal to each other. The low rank approximation is obtained by truncating the size of the representation by taking r first columns of $\mathbf{Q} = [\mathbf{u}_1, \cdots, \mathbf{u}_r] \in \mathbb{R}^{n \times r}$. By doing so, it can be shown that the error (2.51) is minimized to the sum of next $n - r$ eigenvalues:

$$\varepsilon_r = \min \sum_i \|\mathbf{e}_i\|^2 = \min \sum_i \left\|\mathbf{x}_i - \mathbf{Q}\mathbf{\tilde{x}}_i\right\|^2 = \sum_{i=r+1}^{n} \sigma_i \tag{2.52}$$

where $\sigma_i = \xi_i^2$ is the ith singular value of $\mathbf{X}$. In the case $n \geq N_t$, performing a full SVD is time consuming and computationally expensive. Two approaches can solve the dependency on the size of the problem:
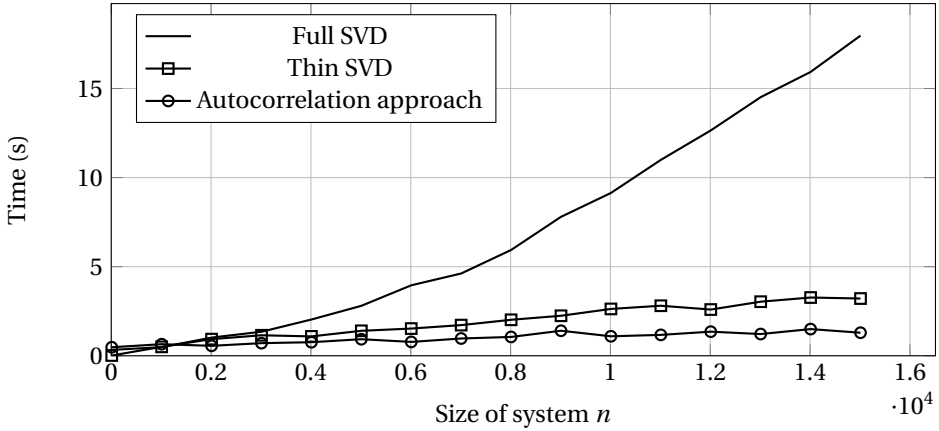
Figure 2.6: Required time to compute the projection basis from 1000 snapshots.

1. Computing the eigenvalue decomposition of the autocorrelation matrix $\mathbf{X^T X} \in \mathbb{R}^{N_t \times N_t}$ [102].

2. Computing a thin SVD which only computes the first non-zero singular values.

Fig. 2.6 shows the required time to compute the projection basis for the three different approaches according to the size n of random snapshot matrix $\mathbf{X}$ containing 1000 snapshots. It can be seen that the full SVD computation is the worst algorithm.

The main disadvantage of this method is the robustness of the Proper Orthogonal Decomposition (POD) approximation which is only valid with the snapshots for which it has been computed. As a consequence, to accurately reduce a dynamical system such as (2.1) with a good approximation, one has to correctly train the model with appropriate inputs $\mathbf{u}$ to generate relevant observations $\mathbf{x}_i$.

Example   To illustrate the POD, let us consider the original (and famous) picture of Lena (Fig. 2.9(a)). As an image is just a set of rows and columns made of pixels values, it represents a valid snapshot matrix $\mathbf{X}$ (i.e. the columns are the snapshots). One could have taken the rows as snapshots. The POD is applied on it to reduce its size. The numerical results are provided in Table 2.3 and graphically shown in Figs. 2.9(b), 2.9(c) and 2.9(d) with errors (ε) of 0.1%, 1% and 5% respectively. The original picture is 512 × 512 (as the rank). According to the error criteria, the lower the error, the larger the POD size. The POD sizes are 115, 21 and 4 respectively. With an error of 0.1%, the difference is hard to detect and the POD achieves a mathematical reduction factor of 4 (based on the order of the matrix representation) and 60% reduction in the jpg file. Note that jpg format also introduces an additional compression on the reconstructed matrix. Even if Fig. 2.9(c) (1% error) is blurred compared to the original picture, one can still recognize the model. It allows a further reduction down to a rank of 21 (96% reduction) and 70% reduction for the jpg file size. Finally, last picture in Fig. 2.9(d) with 5% error is totally

Table 2.3: Sizes [in kB] of the SVD matrices for all reductions in Fig. 2.9.

	Original	$\varepsilon = 0.1\%$	$\varepsilon = 1\%$	$\varepsilon = 5\%$
U	2000	452	83	16
Ξ	32	2	0.45	0.215
V	18100	1400	248	47
order	512	115	21	4
jpg file	98	39	29	19

Table 2.4: Illustration of POD reduction of system (2.27) using one mode.

	$\delta = 10^{-2}$	$\delta = 1$	$\delta = 10^2$
Ξ	$\begin{bmatrix} 35672 \\ 9 \end{bmatrix}$	$\begin{bmatrix} 76345 \\ 4272 \end{bmatrix}$	$\begin{bmatrix} 4.84 \cdot 10^7 \\ 6.74 \cdot 10^6 \end{bmatrix}$
ε_1	$6.36 \cdot 10^{-8}$	0.003	0.013
Q = P	$\begin{bmatrix} -1 \\ -0.0099 \end{bmatrix}$	$\begin{bmatrix} -0.8877 \\ -0.4586 \end{bmatrix}$	$\begin{bmatrix} -0.6897 \\ -0.7121 \end{bmatrix}$
Ã	-0.9901	-0.5912	-0.4916
B̃	-1	-1.3463	-71.8966
C̃	-1.099	-1.3463	-1.4017

blurred and does not allow the reader to identify the original source. This last example is shown to demonstrate the limitation of the POD reconstruction.

As a second example in the continuity of what was presented with all the previous methods, the academic example (2.27) is reduced to a single unknown system. As the POD requires snapshots **x**, system (2.27) is solved for 100 different frequencies using its Laplace transform system (2.15). The frequencies (in rad/s) are logarithmically distributed from 10^{-2} to 10^2. The details are presented in Table 2.4 and Bode diagrams are shown in Fig. 2.7 for $\delta = 10^{-2}$ and $\delta = 10^2$. As with the previous methods, the POD offers better results with lower δ values. However, general results are more accurate than with the balanced truncation or Krylov methods in this simple academic case.

2.1.5 Machine (deep) learning

Fully embracing the observation-based model order reduction strategy, the representation of the reduced model can bypass (2.3). Since the 1980's, the machine learning community has developed generic manners to create a learning machine capable of determining a high dimensional function $f(\mathbf{u})$ from the general problem $\mathbf{y} = f(\mathbf{u})$ by providing numerous inputs **u**. If the correct outputs are not given, the process is called "unsupervised" learning. On the contrary, when the outputs are provided, it is logically called "supervised" learning.

In the machine learning research fields, one of the current hot topic is the artificial neural network (ANN) [88, 191]. Multiple techniques have been explored to simplify or intensify ANNs but the philosophy remains intact and is briefly introduced in this overview. By acquiring more and more computational power, researchers try to develop
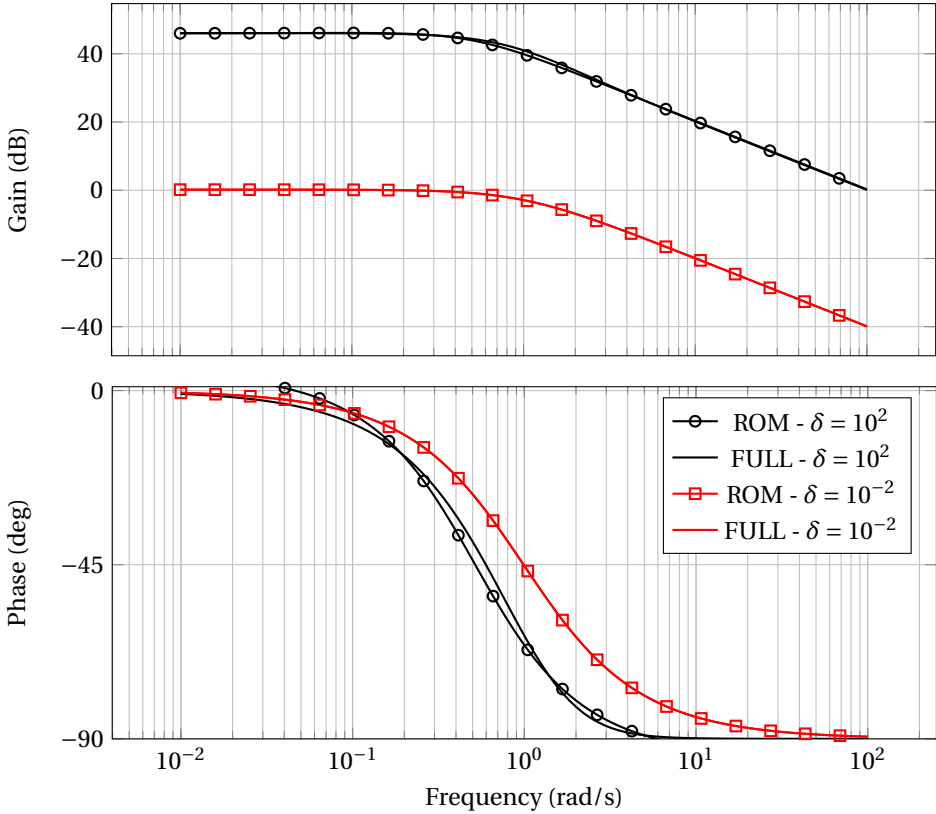
Figure 2.7: Comparison of full and POD reduced systems of (2.27) with one mode.

fully automated ANNs. An illustration of their concept is depicted in Fig. 2.8. Each neurone i of layer j represents a weighted sum of all the neurones of the previous layer $j-1$ and is mathematically described as

$$\forall i,j \quad \mathbf{x}_{ij} = \sum_i w_{i(j-1)}\mathbf{x}_{i(j-1)}, \quad \mathbf{x}_{i,0} = \mathbf{u}. \tag{2.53}$$

Note that the neurons of the first layer equal the inputs. Considering n layers, the outputs are described by $\mathbf{y} = \mathbf{x}_{i,n} = f(\mathbf{x}_{i,0}) = f(\mathbf{u})$ and the implicit (nonlinear) function $f(\mathbf{u})$ is determined by the collection of the weights w_{ij} in the ANN. When $n > 1$, this machine learning process is called "deep learning" as each layer captures a higher dimensional representation of the previous one [23, 124].

Deep learning methods are well suited for two purposes:

1. Classification: the objective is to label the inputs into categories. A direct example is the recognition of hand written digits. The model is trained with a classical database of digits from 0 to 9 [123]—meaning the weights w_{ij} are being determined. Then, a new (unknown) digit is provided as an input and the model has

to determine the value. Given this database, the best error rate is 0.23% using advanced machine learning concepts (e.g. convolutional nets) [50].

2. Prediction: the objective is to predict the next item[1]. A common example is the Google autocompletion during an internet research. Given the previous words and requests, Google predicts what would (logically) be the next word you will type in its search bar.

Example   Let us consider the picture in Fig. 2.9(a) to illustrate the learning in the different layers. The first layer takes the visible pixels as inputs. The second layer, by combining the first layer, would detect the edges in the picture. The third layer would assemble those edges to construct (and identify) curves. The fourth layer combines those curves to detect objects (e.g. the hat, the face or the feather). Finally, the last layer performs the classification of the picture by considering the object(s) in the picture (e.g. a woman with a hat and a feather on it). In this example, the layers have a practical meaning but it is no longer the case when complex structures (automatically generated) with hundreds of layers and millions of neurones are considered. Nowadays, a typical machine learning problem requires thousands of CPUs to correctly train the ANN in a respectable short time (couples of days or weeks). In October 2015, the AlphaGo distributed version was using 1202 CPUs and 176 GPUs [189].

As it can be deduced from this brief description, the main issues with this approach are:

1. The more complex the (nonlinear) function $f(\mathbf{u})$, the larger the training set. In the typical handwriting recognition, the training set comprises 30 thousands pictures [123]. In the AlphaGo challenge, more than 30 millions observations of Go games have been used to train the ANN [189]. This leads to two computationally consuming operations:

    a) Generating enough high fidelity solutions to train the ANN.

    b) Learning the solutions.

2. Even if the model is trained, it should perform faster than the original high fidelity system—which is not guaranteed by looking at the AlphaGo challenge statistics. This problem may be solved by creating a small ANN that mimics the behaviour of the large, originally trained, ANN. This technique is called the distillation [105] but is not guaranteed to fulfill sufficiently small error and high success rate.

3. The loss of structure of the general reduced system formulation (2.3). As the reduced model does no longer rely on a mathematical model based on Maxwell's equations, it entirely acts as a black box without any concrete meaning. Indeed, inner variables in ANNs consist in abstracted items.

---

[1]Voluntary vague as the neurone networks can deal with different type of objects.
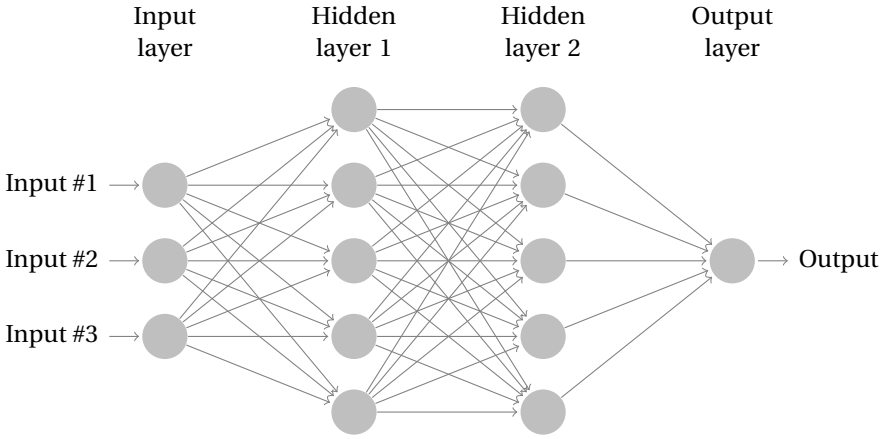
Figure 2.8: Artificial Neurone Network.

2.1.6 Proper Generalized Decomposition

Both model- and observation-based model order reduction techniques may suffer from the so-called "curse of dimensionality" where the accuracy of the solution depends exponentially on the dimensionality of the problem (noted D). In this context, the brute force approach may not work and other techniques have to be investigated in order to explore the whole space. In particular the case in quantum mechanics where Nobel Prize winner R.B. Laughlin famously declared that no computer would ever exist to crack the barriers of the Schrödinger equation in multi-particle systems [122]. By considering a general domain $\Omega \in \mathbb{R}^D$ which is discretized with n elements in each dimension, the number of degrees of freedom of a problem defined in such a space is n^D. Consequently, the classical computation methodology can be seen as a brute force approach and is impracticable for D and n relatively large. Three methodologies allow overcoming this problem:

1. Use different grids. As the discretisation in each direction may be different, one would adapt the sampling rate. However, this first naive approach is limited to simple problems.

2. Use sparse grids which involve $\mathcal{O}(n(\log n)D - 1)$ degrees of freedom instead of n^D [41]. However when the space dimension remains too large (e.g. $D \geq 20$), this approach becomes intractable [1].

3. Use separate variable decomposition. If one decomposes the D dimensions, the total number of evaluations becomes nD instead of n^D. The Proper Generalized Decomposition (PGD) falls in this category [3, 48, 49, 121, 145].

Hereafter we describe the general methodology of the PGD. Considering the general unknown $\mathbf{x} = \mathbf{x}(\mu_1, \cdots, \mu_D)$ depending on D parameters μ_i with $i = 1, \cdots, D$, the PGD

(a) Original picture.

(b) Reduced picture with 0.1% error.

(c) Reduced picture with 1% error.
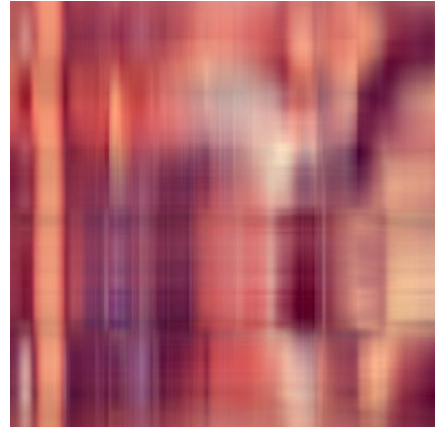
(d) Reduced picture with 5% error.

Figure 2.9: Comparison of POD reduction on a picture.

aims at finding r modes of the product of D separated representations $F_i^j(\mu_i)$:

$$\mathbf{x}(\mu_1, \cdots, \mu_D) \approx \sum_{j=1}^{r} \prod_{i=1}^{D} F_i^j(\mu_i). \tag{2.54}$$

Given the general problem

$$\mathcal{L}(\mathbf{x}) = \mathcal{G} \tag{2.55}$$

and boundary conditions, the solution $\mathbf{x}(\mu_1, \cdots, \mu_D)$ is determined through an enrichment process satisfying the representation (2.54). At the rth iteration of that process, the $r-1$ modes are known and the rth mode is determined. Relation (2.54) can be

written as

$$\mathbf{x}(\mu_1, \cdots, \mu_D) \approx \sum_{j=1}^{r-1} \prod_{i=1}^{D} F_i^j(\mu_i) + \prod_{i=1}^{D} F_i^r(\mu_i) \tag{2.56}$$

where the first part represents the first $r - 1$ modes and the second one is the new enrichment. Introducing this new expression (2.56) into the general formulation (2.55) leads to

$$\mathcal{L}\left(\sum_{j=1}^{r-1} \prod_{i=1}^{D} F_i^j(\mu_i) + \prod_{i=1}^{D} F_i^r(\mu_i)\right) = \mathcal{G} + \mathcal{R}^r \tag{2.57}$$

where $\mathcal{R}^r$ is the rth residual due to the approximation of the correct solution $\mathbf{x}$ by relation (2.54). By projecting eq. (2.57) onto each unknown function $F_i^r(\mu_i)$, the following system, with D equations, is obtained:

$$\int_{\Omega_i} \mathcal{L}\left(\sum_{j=1}^{r-1} \prod_{i=1}^{D} F_i^j(\mu_i) + \prod_{i=1}^{D} F_i^r(\mu_i)\right) \cdot F_i^r(\mu_i) \, d\mu_i = \int_{\Omega_i} \mathcal{G} \cdot F_i^r \, d\mu_i + \int_{\Omega_i} \mathcal{R}^r \cdot F_i^r \, d\mu_i \tag{2.58}$$

for $i = 1, \cdots, D$ and Ω_i is the parameter space of μ_i. By considering functions $F_i^r(\mu_i)$ orthogonal to the residual as the best choice [145], $\mathcal{R}^r$ vanishes. Then, a fixed point method is used to alternatively determine the functions F_i^r (fixing all F_j^r for $j \neq i$) until convergence is reached—leading to the representation of rth mode. The number of modes is progressively increased until the error ε defined as

$$\varepsilon = \left\| \mathcal{G} - \mathcal{L}\left(\sum_{j=1}^{r} \prod_{i=1}^{D} F_i^j(\mu_i)\right) \right\| \tag{2.59}$$

is sufficiently small lower than an arbitrary threshold ε_{max}.

The PGD method is perfectly suited for multidimensional systems whose solutions can be expressed by a separate representation of variables. An interesting survey of models can be found in [164].

Example   To illustrate the PGD, let us consider the classical (academic) parametric heat transfer equation:

$$\partial_t \mathbf{x} - \alpha \Delta \mathbf{x} = q \tag{2.60}$$

where α, q and $\mathbf{x}$ are the thermal diffusivity, the source term and the spatial temperature respectively–depending on $\mu_1 = \alpha$, $\mu_2 = t$ and $\boldsymbol{\mu_3}$ the spatial discretization ($\boldsymbol{\mu_3}$ could be subdivided in each spatial direction as $\boldsymbol{\mu_3} = \mathbf{e} = (x, y, z) = (\mu_4, \mu_5, \mu_6)$). Considering all these parameters as coordinates of the solution, a traditional resolution scheme would solve eq. (2.60) for all time values using a time stepping scheme and all thermal diffusivity values—leading to a cumbersome and computationally expensive approach. Therefore, one is looking for a separable representation of the solution as in eq. (2.54):

$$\mathbf{x}(t, \alpha, \mathbf{e}) \approx \sum_{j=1}^{r} F_1^j(t) F_2^j(\alpha) F_3^j(\mathbf{e}) \tag{2.61}$$

considering r modes. Using an FE method, the weak form of eq. (2.60) is used and leads to

$$\int_\Omega (\partial_t \mathbf{x} - \alpha \Delta \mathbf{x} - q) \mathbf{x}' \, \mathrm{d}\alpha \mathrm{dtd}\mathbf{e} = 0 \tag{2.62}$$

where $\Omega = \Omega_\alpha \times \Omega_t \times \Omega_\mathbf{e}$ is the union of all domain intervals of the variables and $\mathbf{x}'$ is the test function. The PGD proceeds as an enrichment method and therefore the $r - 1$ previous modes are known and one is looking for $F_1^r(t), F_2^r(\alpha), F_3^r(\mathbf{e})$ only. For the sake of simplicity, the superscript r is omitted. Introducing the approximation (2.61) into eq. (2.62) leads to

$$\int_\Omega (\partial_t F_1(t) F_2(\alpha) F_3(\mathbf{e}) - \alpha F_1(t) F_2(\alpha) \Delta F_3(\mathbf{e})) \mathbf{x}' \, \mathrm{d}\alpha \mathrm{dtd}\mathbf{e} = - \int_\Omega \mathcal{R}^{r-1} \mathbf{x}' \, \mathrm{d}\alpha \mathrm{dtd}\mathbf{e} \tag{2.63}$$

where

$$\mathcal{R}^{r-1} = \sum_{j=1}^{r-1} \partial_t F_1^j(t) F_2^j(\alpha) F_3^j(\mathbf{e}) - \alpha F_1^j(t) F_2^j(\alpha) \Delta F_3^j(\mathbf{e}) - q \tag{2.64}$$

is the residual at iteration $r - 1$.

To determine those three functions, a fixed point algorithm is used to alternatively solve equation (2.62) with appropriate test functions and ends up to the following loop (until convergence):

1. *Determining $F_1(t)$ ($F_2(\alpha)$ and $F_3(\mathbf{e})$ are known)*
   The test function is defined by

$$\mathbf{x}' = F_1'(t) F_2(\alpha) F_3(\mathbf{e}). \tag{2.65}$$

Introducing (2.65) in (2.63) leads to relation

$$\int_\Omega (\partial_t F_1 F_2 F_3 F_2 F_3 - \alpha F_1 F_2 \Delta F_3 F_2 F_3) F_1' \, \mathrm{d}\alpha \mathrm{dtd}\mathbf{e} \tag{2.66}$$

$$= - \int_\Omega \left(\sum_{j=1}^{r-1} \partial_t F_1^j F_2^j F_3^j F_2 F_3 - \sum_{j=1}^{r-1} \alpha F_1^j F_2^j \Delta F_3^j F_2 F_3 - q F_2 F_3 \right) F_1' \, \mathrm{d}\alpha \mathrm{dtd}\mathbf{e}.$$

But since both functions $F_2(\alpha)$ and $F_3(\mathbf{e})$ are known, their corresponding integrals (over Ω_α and $\Omega_\mathbf{e}$ respectively) can be computed. Let us define

$$\begin{cases} c_1 & = & \int_{\Omega_\alpha} F_2^2 \, \mathrm{d}\alpha \cdot \int_{\Omega_\mathbf{e}} F_3^2 \, \mathbf{de}, \\ c_2 & = & \int_{\Omega_\alpha} \alpha F_2^2 \, \mathrm{d}\alpha \cdot \int_{\Omega_\mathbf{e}} F_3 \Delta F_3 \, \mathbf{de}, \\ c_3^j & = & \int_{\Omega_\alpha} F_2^j F_2 \, \mathrm{d}\alpha \cdot \int_{\Omega_\mathbf{e}} F_3^j F_3 \, \mathbf{de}, \\ c_4^j & = & \int_{\Omega_\alpha} \alpha F_2^j F_2 \, \mathrm{d}\alpha \cdot \int_{\Omega_\mathbf{e}} F_3 \Delta F_3^j \, \mathbf{de}, \\ c_5 & = & \int_{\Omega_\alpha} F_2 \, \mathrm{d}\alpha \cdot \int_{\Omega_\mathbf{e}} F_3 \, \mathbf{de}, \end{cases} \tag{2.67}$$

then equation (2.66) becomes

$$\int_{\Omega_t} (\partial_t F_1 c_1 - F_1 c_2) F_1' \, \mathrm{dt} = - \int_{\Omega_t} \left(\sum_{j=1}^{r-1} \partial_t F_1^j c_3^j - \sum_{j=1}^{r-1} F_1^j c_4^j - q c_5 \right) F_1' \, \mathrm{dt} \tag{2.68}$$

and represents a classical weak form of an ODE (time evolution of F_1). It can be solved either in this weak form or directly in its strong form

$$\partial_t F_1 c_1 - F_1 c_2 = -\sum_{j=1}^{r-1} \partial_t F_1^j c_3^j + \sum_{j=1}^{r-1} F_1^j c_4^j + q c_5 \tag{2.69}$$

using time linearization scheme (e.g. finite differences). Solving equation (2.69) provides an updated solution $F_1(t)$.

2. *Determining $F_2(\alpha)$ ($F_1(t)$ and $F_3(\mathbf{e})$ are known)*
   Using a similar approach, the test function is defined by

   $$\mathbf{x}' = F_1 F_2' F_3. \tag{2.70}$$

   Introducing (2.70) in (2.63) leads to relation

   $$\int_{\Omega_\alpha} (c_6 F_2 - c_7 F_2) F_2' \, d\alpha = -\int_{\Omega_\alpha} \left(\sum_{j=1}^{r-1} F_2^j c_8^j - \sum_{j=1}^{r-1} F_2^j c_9^j - q c_{10} \right) F_2' \, d\alpha \tag{2.71}$$

   with the constants defined as

   $$\begin{cases} c_6 &= \int_{\Omega_t} F_1 \partial_t F_1 \, dt \cdot \int_{\Omega_\mathbf{e}} F_3^2 \, \mathbf{de}, \\ c_7 &= \int_{\Omega_t} F_1^2 \, dt \cdot \int_{\Omega_\mathbf{e}} F_3 \Delta F_3 \, \mathbf{de}, \\ c_8^j &= \int_{\Omega_t} \partial_t F_1^j F_1 \, dt \cdot \int_{\Omega_\mathbf{e}} F_3^j F_3 \, \mathbf{de}, \\ c_9^j &= \int_{\Omega_t} F_1^j F_1 \, dt \cdot \int_{\Omega_\mathbf{e}} F_3 \Delta F_3^j \, \mathbf{de}, \\ c_{10} &= \int_{\Omega_t} F_1 \, dt \cdot \int_{\Omega_\mathbf{e}} F_3 \, \mathbf{de}. \end{cases} \tag{2.72}$$

   As with equation (2.68), equation (2.71) can be solved using its strong form

   $$(c_6 - c_7) F_2 = -\sum_{j=1}^{r-1} F_2^j c_8^j + \sum_{j=1}^{r-1} F_2^j c_9^j + q c_{10} \tag{2.73}$$

   (as no differential operator is involved) to determine the updated solution $F_2(\alpha)$.

   As the original equation does not involve differential operators with respect to the heat diffusivity, the update equation (2.73) is a typical algebraic equation and shows the advantage of the PGD over a classical method.

3. *Determining $F_3(\mathbf{e})$ ($F_1(t)$ and $F_2(\alpha)$ are known)*
   Again, similarly to previous two update stages, the test function would be defined by

   $$\mathbf{x}' = F_1 F_2 F_3'. \tag{2.74}$$

   Introducing (2.74) in (2.63) leads to relation

   $$\int_{\Omega_\mathbf{e}} (c_{11} F_3 - c_{12} \Delta F_3) F_3' \, \mathbf{de} = -\int_{\Omega_\mathbf{e}} \left(\sum_{j=1}^{r-1} F_3^j c_{13}^j - \sum_{j=1}^{r-1} \Delta F_3^j c_{14}^j - q c_{15} \right) F_3' \, \mathbf{de} \tag{2.75}$$

with

$$\begin{cases} c_{11} &= \int_{\Omega_t} F_1 \partial_t F_1 \, dt \cdot \int_{\Omega_\alpha} F_2^2 \, d\alpha, \\ c_{12} &= \int_{\Omega_t} F_1^2 \, dt \cdot \int_{\Omega_\alpha} \alpha F_2^2 \, d\alpha, \\ c_{13}^j &= \int_{\Omega_t} \partial_t F_1^j F_1 \, dt \cdot \int_{\Omega_\alpha} F_2^j F_2 \, d\alpha, \\ c_{14}^j &= \int_{\Omega_t} F_1^j F_1 \, dt \cdot \int_{\Omega_\alpha} \alpha F_2 F_2^j \, d\alpha, \\ c_{15} &= \int_{\Omega_t} F_1 \, dt \cdot \int_{\Omega_\alpha} F_2 \, d\alpha. \end{cases} \tag{2.76}$$

Equation (2.75) is the weak form of an elliptic problem which can be solved using any spatial discretization technique (e.g. FEM). As it was shown for the two previous equations, its strong form is

$$c_{11} F_3 - c_{12} \Delta F_3 = -\sum_{j=1}^{r-1} c_{13}^j F_3^j + \sum_{j=1}^{r-1} c_{14}^j \Delta F_3^j + q c_{15}. \tag{2.77}$$

When the three functions have converged, the new rth mode is obtained. The number of modes increases and this process is repeated until the residual is sufficiently small (e.g. lower than 10^{-5}). Then, the solution is given by equation (2.61) for any value in time, space or heat diffusivity (as far as the system has been trained in its range). Electromagnetic examples using the PGD approach can be found in [98, 101].

2.2   Nonlinear extensions

Contrary to the exhaustive research carried out on linear model order reduction methods, nonlinear problems are still fairly open to further investigation. Indeed, each nonlinear situation is unique and it is hard to find either a general nonlinear reduction method or precise approximation of nonlinear states. To solve nonlinear problems, linearization techniques are used such as the Newton-Raphson scheme. Therefore, the current nonlinear reduction methods consist in using the previously described reduction techniques on the linearized problems. A complete survey of projection-based techniques is proposed in [25] and of nonlinear dynamical techniques in [138, 160].

From now on, we consider constituting matrices $\mathbf{A}$, $\mathbf{B}$, $\mathbf{C}$, $\mathbf{D}$ and $\mathbf{E}$ of system (2.1) that may depend on the state-space variable $\mathbf{x}$. The general problem becomes:

$$\begin{cases} \mathbf{E}(\mathbf{x})\dot{\mathbf{x}} &= \mathbf{A}(\mathbf{x})\mathbf{x} + \mathbf{B}(\mathbf{x})\mathbf{u}, \\ \mathbf{y} &= \mathbf{C}(\mathbf{x})\mathbf{x} + \mathbf{D}(\mathbf{x})\mathbf{u}. \end{cases} \tag{2.78}$$

2.2.1   Projection

To solve the nonlinear system (2.78), a linearization is performed (e.g. using a Picard method or a Newton-Raphson scheme) in order to determine the solution using an iterative process. This procedure requires a nonlinear loop where the system has to converge to a steady iterate . Given such a linear system, the previously described methods can be used to determine the reduction matrices $\mathbf{P}$ and $\mathbf{Q}$—such as illustrated by using the balanced truncation approach [133, 181] or the POD method [27, 190]. Applying the reduction methodology based on subspace representation (2.2) leads to a

similar reduced system as (2.3):

$$\begin{cases} \mathbf{P^T E(Q\tilde{x})Q\dot{\tilde{x}}} &= \mathbf{P^T A(Q\tilde{x})Q\tilde{x} + P^T B(Q\tilde{x})u}, \\ \mathbf{y} &= \mathbf{C(Q\tilde{x})Q\tilde{x} + D(Q\tilde{x})u}. \end{cases} \tag{2.79}$$

Its main drawback is that nonlinear terms still depend on a high dimensional state-space representation of $\mathbf{Q\tilde{x}}$. As a consequence, at each nonlinear iteration, the reduced solution must be projected back to its original size and a complete evaluation of the nonlinear matrices is required. This leads to two bottlenecks:

1. Because the reduced states have to be projected back at each nonlinear itera-tion, system (2.79) may not be solved at smaller computational costs (time and ressources) than with the original HFM (2.3) as it requires $\mathcal{O}(nr)$ multiplications.

2. Nowadays, numerical methods have replaced analytical analysis in most of engi-neer problems geared towards discretization techniques. Evaluating the nonlinear terms requires access to the numerical assembly of the original HFM at each it-eration—which may be an inconvenient procedure and lead to an even larger expense of computational time.

2.2.2 Element sampling methods

Projecting the entire state-space vector is theoretically correct (even though the high fidelity representation of reduced states may be different than actual solution). When the nonlinearities derive from material properties, as it is the case in electromagnetic applications, two scenarios (which are not antinomic) can be observed to reduce the size of the nonlinear evaluation:

1. The domain of interest is not only composed of nonlinear regions (see Fig. 2.10(a)).

2. Over the entire domain, only a limited region may enter in the nonlinear regime (see Fig. 2.10(b)).

In both cases, only the areas exhibiting nonlinear behaviors need to be reevaluated at each nonlinear iteration. When the problem is intrinsically nonlinear, the entire domain is considered nonlinear and the second scenario should be considered.

While the first scenario only depends on the application and can easily be handled by decoupling the linear and nonlinear materials, the second scenario is intrinsically more difficult as the *a priori* knowledge of the nonlinear regions is unknown. In this research area, multiple methods have been developed to determine the sampling region in general nonlinear domains [19, 42, 45, 46, 62, 74, 154, 171–173, 202, 205]. The same philosophy is shared by all these methods: sampling the nonlinear domain to accurately reconstruct the overall state-space vector with minimum entries—logically denoted as *element sampling methods*. Two of them are utilized in this work and are described hereafter.

First, the Discrete Empirical Interpolation Method (DEIM) [46] (or its continuous version EIM [19]) consists in projecting a reduced set of evaluations of a large vector (or matrix) onto a smaller mapping basis. By doing so, the assembly time originally
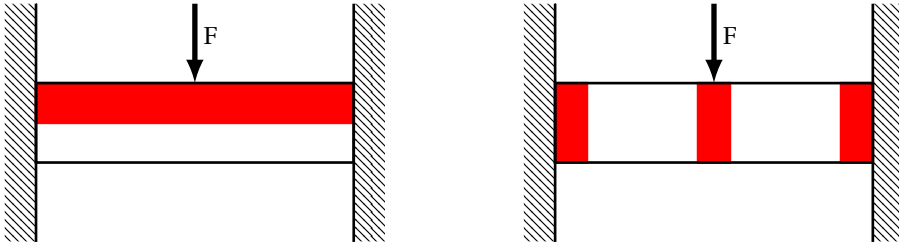
(a) Illustration of a double-sided clamped beam under central force F made of two different materials (red is nonlinear and white is linear).

(b) Illustration of nonlinear plasticity regions (red) for a double-sided clamped beam under central force F. White regions remain in linear states.

Figure 2.10: Illustration of the sampling methods in combined systems of linear and nonlinear regions.

required to generate the large vector (or matrix) is curtailed. Let us consider the large vector $\mathbf{f}(\boldsymbol{\mu}) \in \mathbf{R}^{n \times 1}$ depending on some parameters $\boldsymbol{\mu}$. One can construct the snapshot matrix $\mathbf{F}$ as:

$$\mathbf{F} = \begin{bmatrix} \mathbf{f}(\boldsymbol{\mu}_1), & \mathbf{f}(\boldsymbol{\mu}_2), & \cdots \end{bmatrix}. \tag{2.80}$$

To reduce the size of $\mathbf{f}(\boldsymbol{\mu})$, one would like to have a smaller representation similar to the one of the POD approach–$\bar{\mathbf{f}}(\boldsymbol{\mu})$:

$$\mathbf{f}(\boldsymbol{\mu}) \simeq \mathbf{U}\bar{\mathbf{f}}(\boldsymbol{\mu}) \tag{2.81}$$

where $\mathbf{U} \in \mathbf{R}^{n \times q}$ is a mapping basis and $\bar{\mathbf{f}}(\boldsymbol{\mu}) \in \mathbf{R}^{q \times 1}$ is a reduced representation of $\mathbf{f}(\boldsymbol{\mu})$ with $q \ll n$. As in section 2.1.4, the matrix $\bar{\mathbf{Q}}$ is obtained through the application of a thin SVD on the snapshot matrix $\mathbf{F}$ (and can be truncated):

$$[\mathbf{U}, \Xi, \mathbf{V}] = \text{thin SVD}(\mathbf{F}). \tag{2.82}$$

The DEIM expresses $\bar{\mathbf{f}}$ from the evaluation of only q components of $\mathbf{f}$:

$$\bar{\mathbf{f}}(\boldsymbol{\mu}) \simeq \left(\bar{\mathbf{P}}^T \mathbf{U}\right)^{-1} \bar{\mathbf{P}}^T \mathbf{f}(\boldsymbol{\mu}) \tag{2.83}$$

with $\bar{\mathbf{P}} \in \mathbf{R}^{n \times q}$ a selection matrix that picks q rows of $\mathbf{f}(\boldsymbol{\mu})^2$. The following procedure explains the sampling method:

1. Performing the selection of q rows to both sides of (2.81) leads to:

$$\bar{\mathbf{P}}^T \mathbf{f}(\boldsymbol{\mu}) \simeq \left(\bar{\mathbf{P}}^T \mathbf{U}\right)\bar{\mathbf{f}}(\boldsymbol{\mu}). \tag{2.84}$$

---

[2]In the general formulation of the reduced system (2.3), $\mathbf{P}$ reduces the overdetermination due to the excess of equations. Even though $\mathbf{P}$ is usually chosen equal to $\mathbf{Q}$, it could have been a selection matrix similar to $\bar{\mathbf{P}}$.

2. By inverting $\left(\bar{\mathbf{P}}^T \mathbf{U}\right)$, the expression of $\bar{\mathbf{f}}(\boldsymbol{\mu})$ (equation (2.83)) is obtained.

3. Finally, (2.81) can be written as:

$$\mathbf{f}(\boldsymbol{\mu}) \simeq \mathbf{U}\left(\bar{\mathbf{P}}^T \mathbf{U}\right)^{-1} \bar{\mathbf{P}}^T \mathbf{f}(\boldsymbol{\mu}) \tag{2.85}$$

where q components of $\mathbf{f}$ are generated and assembled using the selection matrix $\bar{\mathbf{P}}$ and projected on $\mathbf{U}$ to retrieve the full size vector $\mathbf{f}$.

Applying the DEIM methodology to the reduced order model (2.79), it becomes

$$\begin{cases} \mathbf{P}^T \check{\mathbf{U}}\bar{\mathbf{P}}^T \mathbf{E}(\mathbf{x})\mathbf{Q}\dot{\tilde{\mathbf{x}}} &= \mathbf{P}^T \check{\mathbf{U}}\bar{\mathbf{P}}^T \mathbf{A}(\mathbf{x})\mathbf{Q}\tilde{\mathbf{x}} + \mathbf{P}^T \check{\mathbf{U}}\bar{\mathbf{P}}^T \mathbf{B}(\mathbf{x})\mathbf{u}, \\ \mathbf{y} &= \check{\mathbf{U}}\bar{\mathbf{P}}^T \mathbf{C}(\mathbf{x})\mathbf{Q}\tilde{\mathbf{x}} + \check{\mathbf{U}}\bar{\mathbf{P}}^T \mathbf{D}(\tilde{\mathbf{x}})\mathbf{u}, \end{cases} \tag{2.86}$$

where $\check{\mathbf{U}} = \mathbf{U}\left(\bar{\mathbf{P}}^T \mathbf{U}\right)^{-1}$.

The main drawback of the DEIM is its dependency on the snapshots $\mathbf{f}(\boldsymbol{\mu})$ and their number. Contrary to the POD method where one looks for similar observations in the state-space vector, nonlinear vectors $\mathbf{f}$ may significantly vary with the parameters $\boldsymbol{\mu}$—leading to inaccurate representations and/or ill-conditioned systems based on too few observations.

Secondly, the Missing Point Estimation (MPE) [15] does not rely on a collection of nonlinear snapshots to determine the selection matrix $\bar{\mathbf{P}}$. In fact, the greedy algorithm selects q rows of the system such that $\check{\mathbf{Q}}^T \check{\mathbf{Q}} \approx \mathbf{I}$ with $\check{\mathbf{Q}} = \bar{\mathbf{P}}^T \mathbf{Q}$. In other words, the closer the condition number of $\check{\mathbf{Q}}^T \check{\mathbf{Q}}$ is to 1, the better. In the worst case, $q = n$ and no reduction is performed. Using this approach, the n nonlinear equations are sampled to a subset of q ones. Contrary to the DEIM, there is no mapping of the q equations onto a reduced basis (*i.e.* $\mathbf{U}\left(\bar{\mathbf{P}}^T \mathbf{U}\right)^{-1}$ in the DEIM), the reduced order model (2.79) is directly obtained by

$$\begin{cases} \check{\mathbf{P}}^T \bar{\mathbf{P}}^T \mathbf{E}(\mathbf{x})\check{\mathbf{Q}}\dot{\tilde{\mathbf{x}}} &= \check{\mathbf{P}}^T \bar{\mathbf{P}}^T \mathbf{A}(\mathbf{x})\check{\mathbf{Q}}\tilde{\mathbf{x}} + \check{\mathbf{P}}^T \bar{\mathbf{P}}^T \mathbf{B}(\mathbf{x})\mathbf{u}, \\ \mathbf{y} &= \check{\mathbf{P}}^T \bar{\mathbf{P}}^T \mathbf{C}(\mathbf{x})\check{\mathbf{Q}}\tilde{\mathbf{x}} + \check{\mathbf{P}}^T \bar{\mathbf{P}}^T \mathbf{D}(\mathbf{x})\mathbf{u}, \end{cases} \tag{2.87}$$

with $\check{\mathbf{P}} = \bar{\mathbf{P}}^T \mathbf{P}$ and $\check{\mathbf{Q}} = \bar{\mathbf{P}}^T \mathbf{Q}$. Complementary explanations can be found in [13–15].

The difference between DEIM and MPE methods lays in the expression of the full vector through its reduced set of entries and their determination. Whereas the MPE system (2.87) only evaluates and solves the system on those reduced number of entries, the DEIM projects the reduced entries of the large vector onto the mapping basis $\bar{\mathbf{Q}} \in \mathbf{R}^{n \times q}$ back into the high fidelity subspace.

Example   To illustrate the sampling nonlinear methods, an academic illustration of a reluctance equivalent electric circuit is chosen. Let us consider the parallel system illustrated in Fig. 2.11 where the currents $\mathbf{i}$ in all branches verify the vector formulation

$$\mathbf{v}(t) = \mathbf{L}\partial_t \mathbf{i} + \mathbf{R}(\mathbf{i})\mathbf{i} \tag{2.88}$$

with

$$\mathbf{L} = \begin{pmatrix} L_1 & 0 & 0 & \cdots & 0 \\ 0 & L_2 & 0 & \cdots & 0 \\ \vdots & \ddots & \ddots & \ddots & \vdots \\ 0 & 0 & 0 & \cdots & L_n \end{pmatrix}, \tag{2.89}$$

$$\mathbf{R} = \begin{pmatrix} R_1(i_1) & 0 & 0 & \cdots & 0 \\ 0 & R_2(i_2) & 0 & \cdots & 0 \\ \vdots & & \ddots & \ddots & \vdots \\ 0 & 0 & 0 & \cdots & R_n(i_n) \end{pmatrix}, \tag{2.90}$$

$$\mathbf{v} = \begin{pmatrix} v_1 \\ \vdots \\ v_n \end{pmatrix}, \tag{2.91}$$

$$\mathbf{i} = \begin{pmatrix} i_1 \\ \vdots \\ i_n \end{pmatrix}. \tag{2.92}$$

The parameter values are determined by the following set

$$\begin{cases} L_k & = & 10^{-15} & k \le 0.25n, \\ L_k & = & 10^4 & k > 0.25n, \\ R_k(i) & = & k \times 10^2 & k \le 0.25n, \\ R_k(i) & = & \exp(i) + k \times 10^2 & k > 0.25n \end{cases} \tag{2.93}$$

The voltage source is given as

$$v_k(t) = 500\sin(2\pi f t) \tag{2.94}$$

with $f = 50$Hz and a time discretization containing 40 time steps of $\Delta t = 1$ millisecond. Using an implicit Euler time scheme, equation (2.88) becomes

$$\left[\frac{\mathbf{L}}{\Delta t} + \mathbf{R}(\mathbf{i}_t) \right] \mathbf{i}_t = \mathbf{v} + \frac{\mathbf{L}}{\Delta t} \mathbf{i}_{t-1}. \tag{2.95}$$

The equation (2.95) can be linearized using a Newton-Raphson scheme where the iterative solution $\mathbf{i}_t^k$ updates accordingly to

$$f(\mathbf{i}_t^k) = 0 \approx f(\mathbf{i}_t^{k-1}) + \frac{\partial f(\mathbf{i}_t^k)}{\partial \mathbf{i}_t^k} \left(\mathbf{i}_t^k - \mathbf{i}_t^{k-1} \right) \tag{2.96}$$
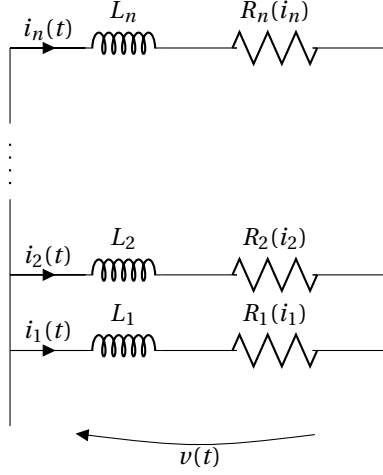
Figure 2.11: Parallel system of nonlinear branches.

with

$$f(\mathbf{i}_t^k) \quad = \quad \left[\frac{\mathbf{L}}{\Delta t} + \mathbf{R}(\mathbf{i}_t^k)\right]\mathbf{i}_t^k - \left[\mathbf{v} + \frac{\mathbf{L}}{\Delta t}\mathbf{i}_{t-1}\right],$$

$$\frac{\partial f(\mathbf{i}_t^k)}{\partial \mathbf{i}_t^k} \quad = \quad \left[\frac{\mathbf{L}}{\Delta t} + \mathbf{R}(\mathbf{i}_t^k)\right] + \underbrace{\left.\frac{\partial \mathbf{R}(\mathbf{i}_t^k)}{\partial \mathbf{i}}\right|_{\mathbf{i}_t^k} \mathbf{i}_t^k}_{\text{jacobian of } \mathbf{R}(\mathbf{i}_t^k)} . \tag{2.97}$$

In practice, the iterative increment $\delta\mathbf{i}_t^k$ is computed by solving

$$\underbrace{\frac{\partial f(\mathbf{i}_t^k)}{\partial \mathbf{i}_t^k}}_{\mathbf{J}(\mathbf{i}_t^k)}\delta\mathbf{i}_t^k = -\underbrace{f(\mathbf{i}_t^{k-1})}_{\mathbf{R}(\mathbf{i}_t^k)} \tag{2.98}$$

and the new iterate is obtained by

$$\mathbf{i}_t^{k+1} = \mathbf{i}_t^k + \delta\mathbf{i}_t^k. \tag{2.99}$$

Applying the aforementioned methods on equation (2.98), reduced order models can be built. To emphasise the need of sampling methods in nonlinear cases, a POD model without sampling is also generated and analyzed. In this POD case, the reduced unknown vector is projected back at each nonlinear iteration in order to evaluate the high fidelity nonlinear vector (*i.e.* $\mathbf{R}(\mathbf{i})$). The computational times are presented in

Table 2.5: Application of POD, DEIM and MPE on the system (2.88).

Size n	Time [s]			
	FULL	POD	DEIM	MPE
10	0.1236	0.0760	0.0687	0.0684
100	0.5506	0.1534	0.0580	0.0630
1000	4.7739	1.0126	0.0564	0.0664
10000	44.056	15.9980	0.0400	0.0466

Table 2.5 with a relative error below 10^{-8} for all models. As expected, the bigger the size of the system, the longer the time to solve it (column FULL). The POD method allows acceptable time reduction compared to the high fidelity resolution but it can be seen the computational time also increases with the size of the system as the nonlinear states have to be projected back to its full size. To handle this problem, the DEIM and MPE approaches have been implemented and the computational times are now independent of the original size n (e.g. computational time 1000x and 400x faster than the high fidelity model and POD model respectively with $n = 10000$). In particular, considering the largest size $n = 10000$, the POD method keeps four modes (to achieve an *a priori* error of 10^{-10}) and they are depicted in Fig. 2.12. The DEIM and MPE approaches sample the 10000 vector entries at the four points (2501, 1, 2500, 1133) and (470,71, 3806, 3970) respectively and are also shown on the POD modes in Fig. 2.12. The form of equation (2.88) is similar to those of the magnetodynamic problems of interest described by equation (1.34).

2.2.3   Polynomial approximation

Another way to solve the main issue of the back projection method consists in replacing the original nonlinear matrices by some reduced linearized expressions—the use of the Taylor expansion is a common approximation of a nonlinear function around an arbitrary point x_0 such as

$$f(x) = f(x_0) + \sum_{i=1}^{\infty} \frac{f^{(i)}(x)}{i!}(x - x_0)^i. \qquad (2.100)$$

This approach is only valid for nonlinear static time invariant functions. In particular, no memory effect is present in eq. (2.100) which cannot describe a previous state. The generalisation of the Taylor expansions are the Volterra series which can capture dynamics for time variant and nonlinear systems [170, 182]. It can also be seen as the generalization of the impulse response function of an LTI system $\mathbf{h}(t)$ if one defines the input-output relation as

$$\mathbf{y}(t) = \int_{-\infty}^{\infty} \mathbf{h}(\tau)\mathbf{u}(t - \tau)d\tau. \qquad (2.101)$$
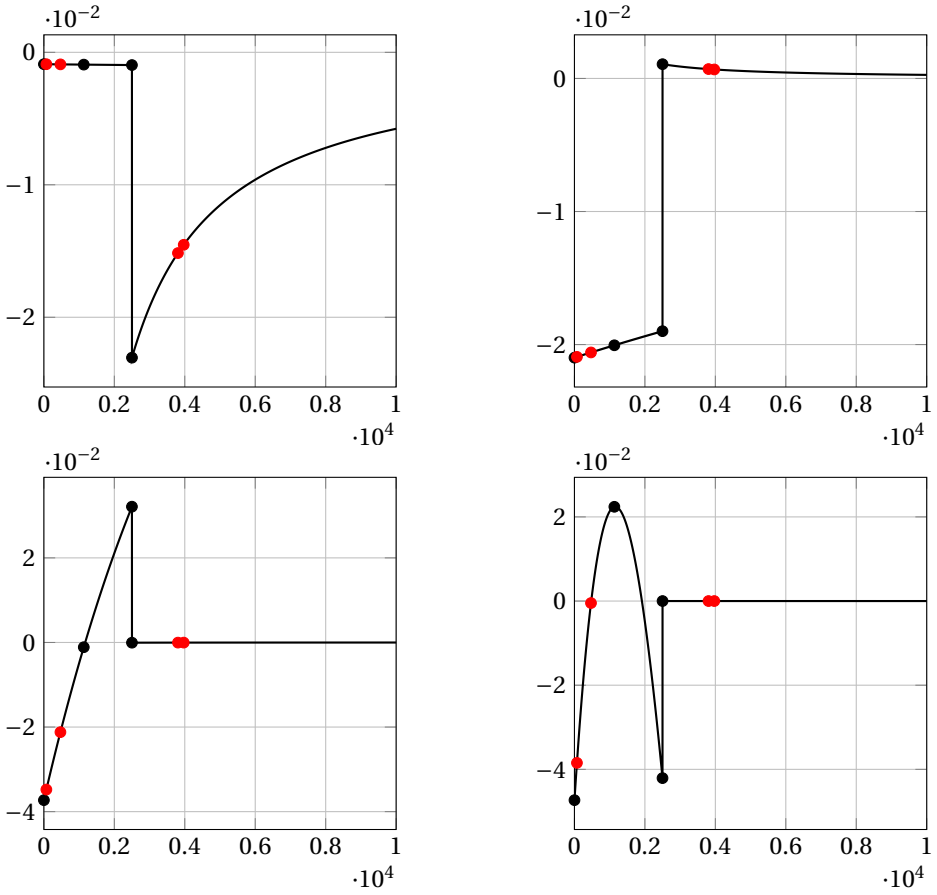
Figure 2.12: Four first POD modes of system 2.88 with $n = 10000$. 1st mode (up-left), 2nd mode (up-right), 3rd mode (down-left) and 4th mode (down-right). DEIM and MPE selection points in black and red respectively.

Indeed, one would write the input-output relation of a nonlinear system as the sum of multiple contributions depending of the input signal **u** as

$$\mathbf{y}(t) = \sum_{i=0}^{\infty} \mathbf{y}_i(t) = \sum_{i=0}^{\infty} \mathcal{H}_i[\mathbf{u}(t)] \tag{2.102}$$

where $\mathcal{H}_i[\mathbf{u}(t)]$ is referred to the ith order Volterra operator and defined by

$$\mathcal{H}_i[\mathbf{u}(t)] = \int_{\boldsymbol{\tau}_i \in \mathbb{R}^i} \mathbf{h}_i(\boldsymbol{\tau}_i) \prod_{j=1}^{i} \mathbf{u}(t - \boldsymbol{\tau}_j) d\boldsymbol{\tau}_i \quad (j = 1, 2, ...) \tag{2.103}$$

with $\boldsymbol{\tau}_i = [\tau_1, \cdots, \tau_i]^T$ a vector containing the i integration variables and the functions $\mathbf{h}_i$ the Volterra kernels. In particular, when $i = 1$, one finds the impulse response
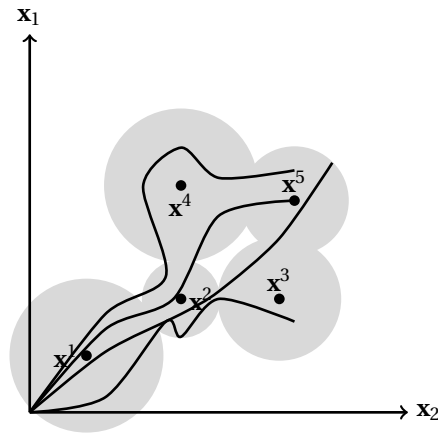
Figure 2.13: Trajectories in the state space $\mathbf{x}$ and clustering of the local reduction matrices.

function $\mathbf{h}(\tau) = \mathbf{h}_1(\boldsymbol{\tau}_1)$. The higher order multidimensional convolutional integrals take the multiple delays into account. Multiple research studies in engineering fields have been conducted using the Volterra series expansion [33, 35], in particular for dynamic problems in [37, 177, 178].

As a consequence, a nonlinear dynamical system is entirely defined by its Volterra kernels. As the basis functionals are correlated, determining the kernels is not an easy task. To estimate them, [34, 36] used the coefficients of the Wiener series (which are close to the Volterra series). More recently, [209] used artificial neural networks to learn and determine the kernels of an arbitrary dynamical nonlinear system.

However, due to memory usage and computational resources, the infinite sum in eq. (2.100) has to be truncated to the first terms and the nonlinear function $f(x)$ may be badly represented by its Taylor expansion. In addition, no efficient and accurate model order reduction methods can tackle the higher order terms. Multiple studies can be found in [17, 47, 61, 129, 210, 213].

2.2.4   Trajectory Piecewise Linear Models

Given multiple training inputs, the Trajectory Piece-Wise Linear (TPWL) [167] approximation designs a set of linear models around different expansion points which are then accurately weighted to represent the nonlinear behavior of the system. The procedure consists in five steps:

1. *Training.* For multiple inputs, the HFM is solved and the state-space vectors are retrieved (*i.e.* they are called trajectories)–see black lines in Fig. 2.13. This training must catch all the nonlinear behaviors and thus need to explore all states in the system. Determining the appropriate excitation signals and their number is crucial. In general, one cannot compute all the possible trajectories and would limit its computational resources to practical input signals.

2. *Expansion points.* Determining a set of key expansion points from the trajectories to build local linearized models. A simple greedy algorithm is used to determine the expansion points. Let us consider t as the number of expansion points, d an arbitrary distance and the initial state-space vector $\mathbf{x}_0$. Until the number of expansion points t is reached, the state-space vectors $\mathbf{x}_i$ that are too far from its closest expansion point $\mathbf{x}_j$ are added to the set of the expansion points $\mathcal{T}$ (see algorithm 2.1).

Algorithm 2.1: Selection of the expansion points in the TPWL method

---

Data: $\mathbf{x}_0$, t, s
Result: The set of expansion points $\mathcal{T}$
$\mathcal{T} = \{\mathbf{x}_0\}$; i = 1;
while $i \leq t$ **do**
    if $\min\limits_{\mathbf{x}_j \in \mathcal{T}} \dfrac{\|\mathbf{x}_i - \mathbf{x}_j\|}{\|\mathbf{x}_j\|} > d$ **then**
        $\mathcal{T} = \mathcal{T} \cup \{\mathbf{x}_i\}$;
    end
    i++;
end

---

3. *Linearization.* Linearizing the nonlinear models around the expansion points. One can linearize the nonlinear terms of system (2.78) by taking the first two terms of the approximation (2.100). At a given expansion point $\mathbf{x}_i$, each nonlinear term is written as

$$\mathbf{E}(\mathbf{x})\mathbf{x} = \mathbf{E}_i \mathbf{x}_i + \mathbf{J}_i^E (\mathbf{x} - \mathbf{x}_i) \tag{2.104}$$

where $\mathbf{J}_i^E \in \mathbb{R}^{n \times n}$ is the Jacobian of vector $\mathbf{E}(\mathbf{x})\mathbf{x}$ evaluated on $\mathbf{x}_i$.

4. *Model order reduction.* Applying the linear model order reduction methods onto the linearized models from system (2.78) for each expansion point $\mathbf{x}_i$ leads to

$$\begin{cases} \partial_t \left(\mathbf{P}_i^T \left[\mathbf{E}_i + \mathbf{J}_i^E (\mathbf{x} - \mathbf{x}_i) \right] \mathbf{Q}_i \tilde{\mathbf{x}} \right) &=& \mathbf{P}_i^T \left[\mathbf{A}_i + \mathbf{J}_i^A (\mathbf{x} - \mathbf{x}_i) \right] \mathbf{Q}_i \tilde{\mathbf{x}} + \mathbf{P}_i^T \mathbf{B} \mathbf{u}, \\ \mathbf{y} &=& \mathbf{C} \mathbf{Q}_i \tilde{\mathbf{x}} + \mathbf{D} \mathbf{u}. \end{cases} \tag{2.105}$$

System (2.105) only considers nonlinearities in matrices $\mathbf{E}$ and $\mathbf{A}$ as it is the most common case. However, the procedure is the same for the other terms. Two approaches can be used in the reduction stage. Either use the same bases $\mathbf{P}$ and $\mathbf{Q}$ for all expansion points or use specific $\mathbf{P}_i$ and $\mathbf{Q}_i$ for each linear system. The latter was the original philosophy of the TPWL as the weighted sum was first built–leading to a single linear model–before the reduction process. However, the former approach is more general. To determine the reduction matrices, studies include the use of POD [22, 82, 97], the moment-matching approach [30, 167] and the balanced truncation method [125].

5. *Weighting.* Defining appropriate weights to obtain an accurate model which consists in a weighted sum of all reduced linearized systems around the expansion points. By only considering the update equation of system (2.105) (for the sake of readiness), a weighted sum of all linearized reduced models would be written as

$$\partial_t \left(\sum_{i=1}^{t} w_i \mathbf{P}_i^T \left(\mathbf{E}_i + \mathbf{J}_i^E (\mathbf{x} - \mathbf{x}_i) \right) \mathbf{Q}_i \tilde{\mathbf{x}} \right) = \sum_{i=1}^{t} w_i \left(\mathbf{P}_i^T \left[\mathbf{A}_i + \mathbf{J}_i^A (\mathbf{x} - \mathbf{x}_i) \right] \mathbf{Q}_i \tilde{\mathbf{x}} + \mathbf{P}_i^T \mathbf{B} \mathbf{u} \right).$$

(2.106)

Two scenarios can be described to determine the weights w_i as a function of $\mathbf{x}$. First, when a full solution $\mathbf{x}$ at a given time instant equals one of the expansion points $\mathbf{x}_i$, the weighted coefficient w_i should, logically, be higher than all the others. Therefore the ith linearized model has more impact when $\mathbf{x} = \mathbf{x}_i$. Secondly, when $\mathbf{x} \neq \mathbf{x}_i$, the weights have to best describe the influence of all systems when linearized models are combined. A typical weight distribution is a Gaussian function as described in [167]. The procedure is the following:

a) Compute the distance d_i between the state-space vector $\mathbf{x}$ and all expansion points $\mathbf{x}_i$ (*i.e.* $d_i = \|\mathbf{x} - \mathbf{x}_i\|$ with $i = 1, ..., t$).

b) Normalise the distance based on the smallest one (*i.e.* $d_i = \frac{d_i}{\min(d_1, \cdots, d_t)}$).

c) By defining a standard deviation constant ϑ of the Gaussian function, the weight coefficients are computed as $w_i = e^{-d_i^2/2\vartheta^2}$ for $i = 1, \cdots, t$.

d) Normalise the coefficients.

Three main advantages of this method can be listed:

1. As with the other approaches, linearizing the nonlinear problem allows the use of the accurate and well-known linear reduction methods.

2. Combining multiple linearised models allows a better approximation of nonlinear behaviors.

3. Linearised systems reduce the size of the approximation—avoiding the exponential rise of the high order terms as in the Volterra/Taylor series.

Three disadvantages are intrinsically related to this method:

1. The results are strongly dependent on the training procedure.

2. Determining the number of linearization points with an accurate (a-priori) error criteria is not feasible.

3. No algorithm is proposed to generate the optimal weight coefficients.

Additional information and examples can be found in [2, 60, 168, 198].

Example   To illustrate the TPWL on a simple example, let us consider the 1D nonlinear function $f(x) = \tanh(x)$ with $x \in [0, 10]$. This function is chosen for two reasons. First, it is similar to a typical anhysteretic magnetic saturation curve in nonlinear core. Secondly, it is obviously piecewise linear. The function is linearized at the following seven linearization points $x_i = [0, 0.5, 1, 1.5, 2, 3, 5]$ with a deviation $\vartheta = 0.15$. The nonlinear function $f(x)$, linearized functions $l_i(x)$, weights $w_i(x)$ and relative error are shown in Fig. 2.14. One can observe a relative error lower than 2% for the entire domain (naturally bigger at small values of $f(x)$) and drops at the linearization points (as expected by the proper choice of the weights).

2.3   Other considerations

2.3.1   Online/Offline stages

To create a ROM, two different processes need to be described: the online and offline stages. Instinctively, a ROM has to be fast and accurate regarding the evaluation time but it is often forgotten to consider the time required to construct it. This distinction defines the separation between offline and online stages. The evaluation time (or runtime), when the model is actually used, is called the online stage. Considering the online stage as a theatre floor where excellent performance is requested, the offline step is the back stage where ROM is prepared and trained. This offline stage is often long and computational expensive. Depending on the utilized methods and the parametric problems, several training procedures are required to extract information from the HFMs and construct the ROMs—inducing substantial time during offline stages. In this dissertation, we are only interested in a tremendous reduction in the online stage whatever the offline step needs (*i.e.* long time and large computational power). Indeed, nowadays, large supercomputers can (in parallel) easily train HFMs and build corresponding ROMs before actual evaluations. The main focus is then geared towards runtime efficiency (speed and accuracy). Conversely, storage issues can be solved by using ROMs during the online stage. By determining such small models, they can actually be embedded in micro computers with a small amount of memory where the HFMs can simply not be stored.

2.3.2   Parametric problems

When dealing with parametric problems, model order reduction may not be easily adapted. Depending on the parameter space, the appropriate projection matrices **P** and **Q** may be difficult to determine. Considering reduced models as in eq. (2.3), two main manners exist to deal with parametric reduction:

1. Generating multiple local reduced bases in the parameter space and interpolating between them according to the actual parameter set [4, 5, 7, 8, 58, 150]. It consists in clustering the solutions in the parameter space based on multiple trajectories taken by the HFMs in that space as shown in Fig. 2.15. For each region around each value within each parameter (*i.e.* μ^i, $i \in [1, \cdots, 5]$), a small local basis is identified. The main difficulties are to correctly identify the clusters, the number
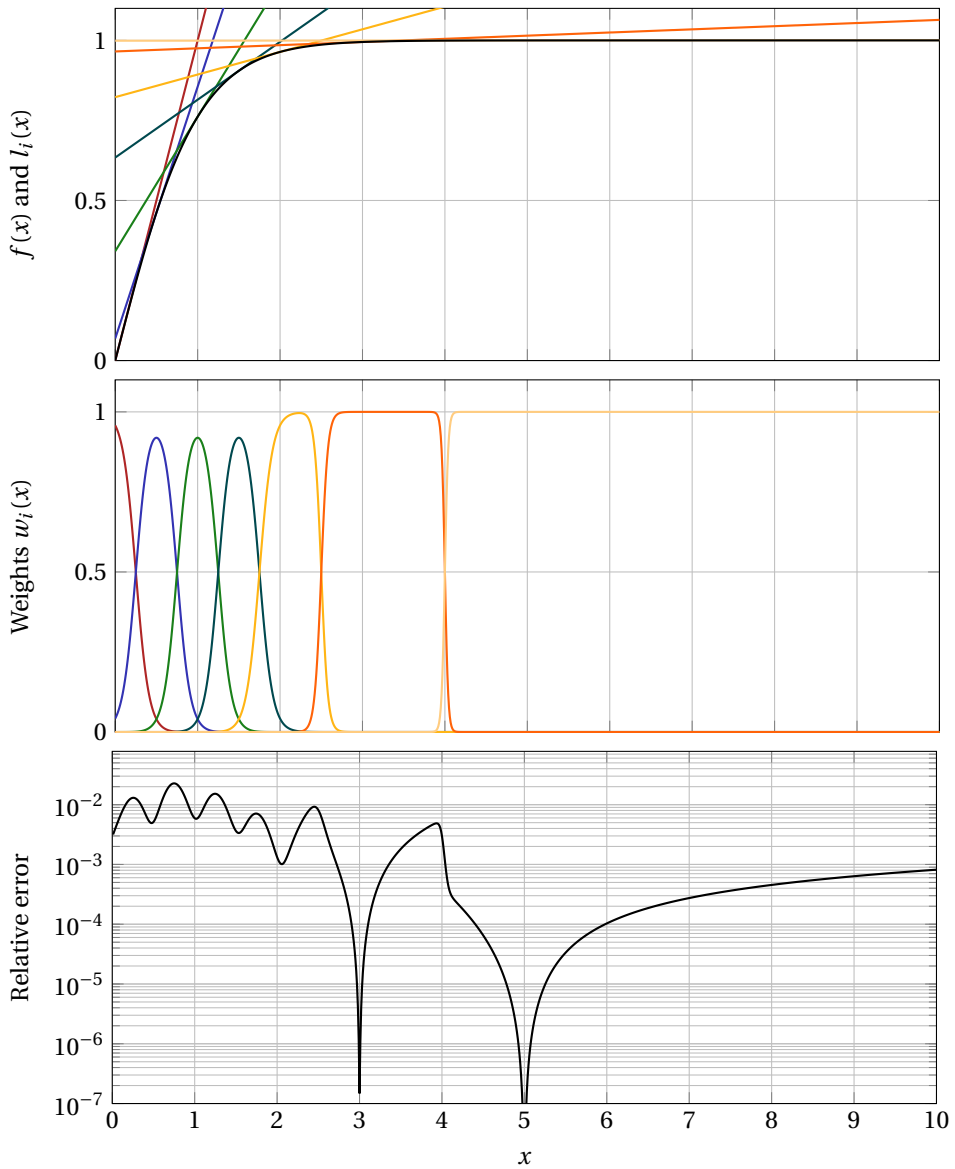
Figure 2.14: TPWL approximation of nonlinear function $f(x) = \tanh(x)$ at linearization points $x_i = [0, 0.5, 1, 1.5, 2, 3, 5]$. $f(x)$ in black up, linearized functions and corresponding weights according to the colours.
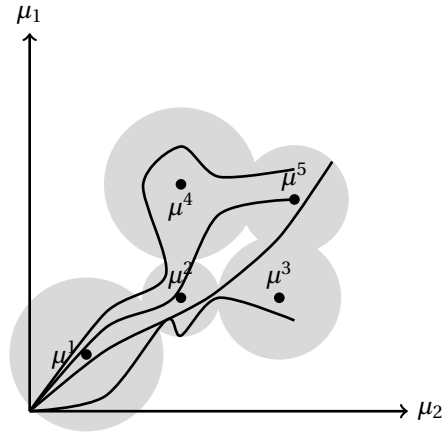
Figure 2.15: Trajectories in the parameter space μ and clustering of the local reduction matrices.

of local bases which may be large and the transition in the parameter space both online and offline taking into account the dynamical effects during the trainings. Then, for a new parameter set, the corresponding reduced basis is obtained by interpolating the predefined bases, e.g. using the manifold theory to preserve and ensure the same desired properties of reduced bases. An advanced review is made in [4].

2. Creating a single global basis by gathering all the information for all values within each parameter [99]. A naive approach would train the model with all possible values within each parameter range by exploring all the trajectories in the parameter space. However, [150] showed it is not the optimal choice in pure magnetodynamics (without coupling) as the training of the global basis only needs to explore the most stressful nonlinear states in which the reduced model may be in afterwards (during the online stage). In comparison with the former approach, the basis size tends to be larger than with local bases due to the need to catch and collect all the required information in a single place. Nevertheless, the basis size is often lower than the sum of all local bases as some redundancies may be eliminated with the model reduction techniques.

However, in unsteady problems, this global approach can lead to unstable reduced order models [96]. Another problem occurs when the modes from different parameter values are largely different and leads to a swap in the importance of the modes–leading to a truncation of important modes [85].

In addition to these intuitive explanations, a mathematically-rigorous survey of model order reduction techniques for dynamical parametric systems is proposed in [25].

2.3.3 Refined outline

The HFMs of nonlinear electromagnetic devices may contain a very large number of unknowns (e.g. millions)–preventing the use of reduction techniques such as the direct use of the Schur complement or the balanced truncation. As a corollary, and since a general engineer may directly use already defined FE models (as black-boxes), the reduction methods from the observations of the state-space vector are preferred such as the POD and PGD.

Considering the nonlinearities in the electromagnetic devices, polynomial approximations and TPWL approaches have already been investigated in previous work–inducing this dissertation towards the exploration of the correct usage of the element sampling methods in magnetodynamics.

Lastly, to take into account the parameter dependency of electromagnetic devices (e.g. the input excitations or the output loads for instance), both approaches (single and multiple reduced bases) are investigated in this dissertation as no previous investigation and comparison have been pursued so far.

Based on the descriptions of state-of-the-art reduced order model techniques and the objectives of the proposed work, a refined outline is proposed hereafter:

- Chapter 3 deals with linear electromagnetic problems and shows the application of the POD and the PGD. An academic inductor-core system is used as first example. A second test case consists in a frequency analysis of the impedance of a micro-antenna. Lastly, a time domain analysis of a 2D transformer is performed.

- In chapter 4, a nonlinear magnetic behavior is introduced in previously described linear problems—requiring the integration of the aforementioned sampling methods (*i.e.* MPE and DEIM approaches are considered and analysed). To this end, two examples are chosen: a simple inductor-core system and a three-phase power transformer.

- In chapter 5, the parametric dependencies are brought in the two nonlinear test cases by considering coupled formulations of local and global quantities in FE equations. The global training and nonlinear interpolation methods are investigated and compared on the inductor-core system.

- In chapter 6, an external electric circuit is added to the previously reduced system of the voltage-driven three-phase nonlinear transformer to demonstrate the proper future deployment in large electric network simulators of the obtained ROM. To this end, a decoupled approach of global and local quantities is proposed to determine robust, reliable, accurate and parametric ROM by considering the POD for the resolution reduction and the MPE for the assembly reduction.

3

Linear problems

3.1 Introduction

The aim of this chapter consists in setting the context of parametric model order reduction for linear magnetodynamics in time and frequency domains and linear electromagnetics in frequency domain as the basis for more complex situations to come in the following chapters.

In section 3.2, the reduction of the discretized magnetodynamics without global quantities using the POD and PGD methods with linear parameters is presented. As an application, a 2D inductor-core system is considered to illustrate the two reduction methods.

Then, in section 3.3, model order reduction of discretized full wave formulation is considered both in time and in frequency domains with global quantities. To this end, POD and Krylov-based methods are used to efficiently reduce the model of a 2D transformer and a 3D microwave antenna.

Finally, conclusions of the performance of these linear ROMs are presented in section 3.4.

3.2 Model order reduction of magnetodynamics without global quantities

To begin with the model order reduction of magnetodynamic systems, we initially consider the magnetodynamic equation (1.29) in time domain by using two model order reduction techniques: the POD and the PGD.

3.2.1 Proper Orthogonal Decomposition

Considering N_t time solutions $\mathbf{a}_i$, $i = 1, \cdots, N_t$ of equation (1.29), the snapshot matrix

$$\mathbf{A} = \begin{bmatrix} \mathbf{a}_1, \cdots, \mathbf{a}_{N_t} \end{bmatrix} \in \mathbf{R}^{n \times N_t} \tag{3.1}$$

is obtained. The determination of the reduced basis **Q** is achieved by the application of
an SVD on the snapshot matrix as

$$[\mathbf{U}, \mathbf{S}, \mathbf{V}] = \text{SVD}(\mathbf{A}) \tag{3.2}$$

and truncating **U** to its r first columns according to error criteria (2.52):

$$\mathbf{Q} = \mathbf{P} = [\mathbf{u}_1, \cdots, \mathbf{u}_r] \tag{3.3}$$

where $\mathbf{u}_i$ are the columns of **U** ($i = 1, \cdots, n$). The reduced form

$$\left[\frac{\tilde{\mathbf{M}}}{\Delta t} + \tilde{\mathbf{S}} \right] \tilde{\mathbf{a}}_{k+1} = \tilde{\mathbf{v}}_{k+1} + \frac{\tilde{\mathbf{M}}}{\Delta t} \tilde{\mathbf{a}}_k \tag{3.4}$$

with Δt the resolution, $\tilde{\mathbf{M}} = \mathbf{Q}^T \mathbf{M} \mathbf{Q}$ (respectively $\tilde{\mathbf{S}}$) and $\tilde{\mathbf{v}} = \mathbf{Q}^T \mathbf{y}$ is obtained by injecting
$\mathbf{a} \approx \mathbf{Q}\tilde{\mathbf{a}}$ into (1.29). Solving equation (3.4) for the desired N_t time steps $t_k = k\Delta t$ ($k = 1, ..., N_t$) provides the reduced snapshot matrix

$$\tilde{\mathbf{A}} = \left[\tilde{\mathbf{a}}_1, \cdots, \tilde{\mathbf{a}}_{N_t} \right] \in \mathbf{R}^{r \times N_t} \tag{3.5}$$

and high fidelity solutions are directly retrieved by applying relation (2.2).

Application to an inductor-core system   To illustrate this first model order reduction
technique, let us consider an academic inductor-core system as depicted in Fig. 3.1
where the current density source term **y** is directly imposed in the coil area as

$$\mathbf{y} = \frac{N_w}{S_c} I_{\text{peak}} \sin(2\pi f t) \mathbf{e}_z \tag{3.6}$$

where $N_w = 288$, $S_c = 27\text{mm}^2$, $I_{peak} = 1.41\text{A}$ ($I_{RMS} = 1\text{A}$), $f = 50\text{Hz}$ and $\mathbf{e}_z$ are the
number of turns, the total coil surface, the RMS input current, the frequency and the
unit vector along the z-axis respectively. Concerning the parameters of the model, a
core conductivity of 1000S/m and a linear relative permittivity of 2000 are chosen (*i.e.*
the reluctivity is the inverse of the permittivity and the core is 2000 times less reluctant
to magnetic field than vacuum or air). Then, equation (1.29) is solved for one period
with $N_t = 20$ time steps and time stepping $\Delta t = 1\text{ms}$. As this case is linear without any
coupling, only a single mode is sufficient to entirely describe the solutions for all time
steps. To illustrate this remark, the singular values of **A** are shown in Fig. 3.2. The decay
of the singular values is prominent in this case with first one close to 10^3 and second
one to 10^{-10}—leading to a drastic reduction of the size of the high fidelity subspace to
a unique dimensional space. The *a priori* POD error is negligible after the first mode.
The original size of the HFM consists of 973 unknowns (which is equivalent to the
reduction ratio in this case). It takes 0.34 second to solve the HFM and 0.0017 second
for the ROM—leading to a speedup of 200. It is important to note that the matrices
in (1.29) are only generated once in 6 seconds (from the FE tool). The generation
time is not taken into account in those numbers (which only correspond to the time
required to solve the 20 time steps). This deliberate choice is made to highlight the
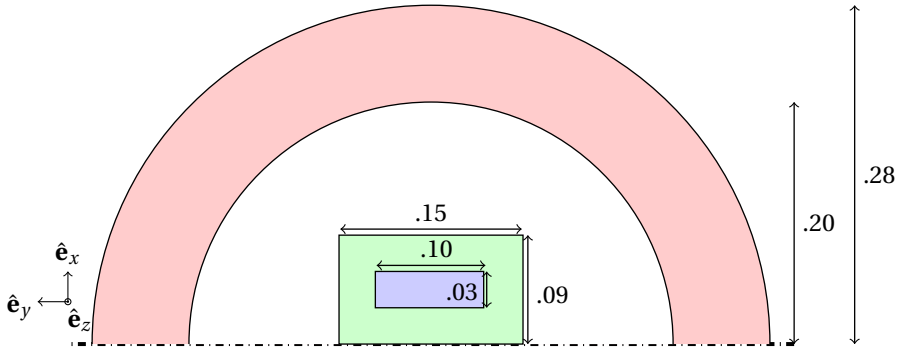
Figure 3.1: Axisymetric model of an inductor-core system. Blue is the coil, green is the core, white is the air and red is the infinite transformation. Dimensions in meters.
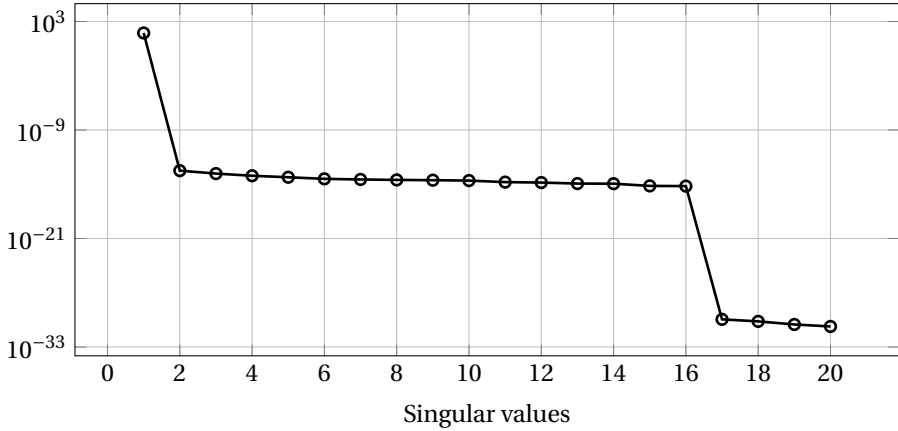
Figure 3.2: Singular values of **A**.

reduction in time by applying the POD. By considering the assembly time in the overall computational duration, the speedup settles down to 1.05 showing one of the further discussed issue—the assembly process may take as much time as the resolution one (if not more). The solutions for the 10 first time steps of the magnetic vector potential in the core (in z-direction) are depicted in Fig. 3.3 (the 10 last ones have similar behaviours). To illustrate the overall error in the considered time interval, the L^2 norm of the absolute and relative errors on the snapshot matrices (from HFM and ROM) is considered and defined by

$$\varepsilon_{absolute} \quad = \quad \left\| \mathbf{A} - \tilde{\mathbf{A}} \right\|_2, \tag{3.7}$$

$$\varepsilon_{relative} \quad = \quad \frac{\left\| \mathbf{A} - \tilde{\mathbf{A}} \right\|_2}{\left\| \mathbf{A} \right\|_2}. \tag{3.8}$$
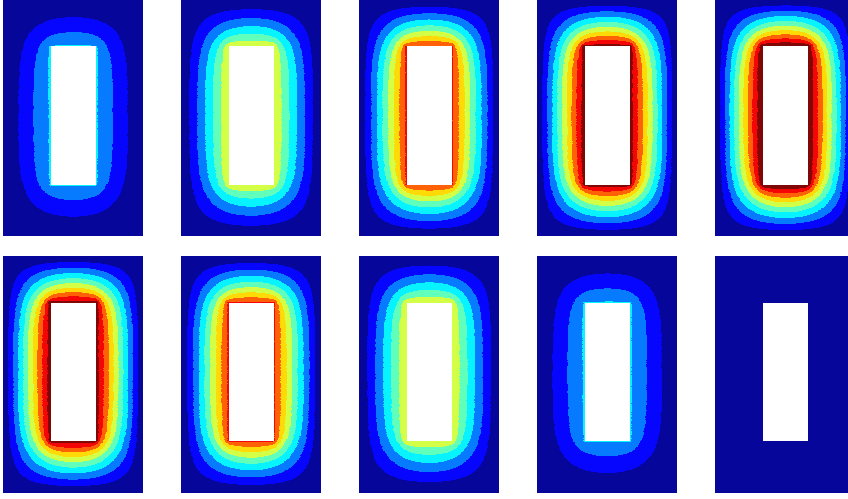
Figure 3.3: Z component of vector potential amplitude for the 10 first time steps of inductor-core system POD model. Legend: 0 (dark blue) to 0.1 (dark red) with a ten level linear-spaced graduation. (Vs/m)

In this application, the very small errors (*i.e.* $\varepsilon_{absolute} = 2.6 \cdot 10^{-11}$ and $\varepsilon_{relative} = 1.5 \cdot 10^{-12}$) show that the POD performs an outstanding reduction of the number of unknowns in the magnetodynamic inductor-core system while preserving an excellent accuracy with respect to the HFM. The absolute errors for the corresponding 10 first time steps are shown in Fig. 3.4. The direct observation of the time solutions in Fig. 3.3 intuitively shows the patterns of the single POD mode that is depicted in Fig. 3.5.

3.2.2 Proper Generalized Decomposition

In this section, the PGD formulation of magnetodynamic problems is presented. It first considers the general developments of separable magnetodynamic formulation by taking μ_i, $i = 1, \cdots, D$ variables. Then, the developments are particularized to a two-variable decomposition (in space and time) and a three-variable one (by adding the input current intensity). This two-step description illustrates one of the most important feature of the PGD: the hierarchical procedure of expansion with the number of separable variables. After the theoretical formulations, the PGD is applied on the same previously described 2D inductor-core system.

Let us assume **a** can be decomposed into μ_i, $i = 1, \cdots, D$ separable variables such that it can be written as

$$\mathbf{a}^r(\mu_1, \cdots, \mu_D) \approx \underbrace{\sum_{j=1}^{r-1} \prod_{i=1}^{D} F_i^j(\mu_i)}_{\mathbf{a}^{r-1}(\mu_1, \cdots, \mu_D)} + \prod_{i=1}^{D} F_i^r(\mu_i) \qquad (3.9)$$
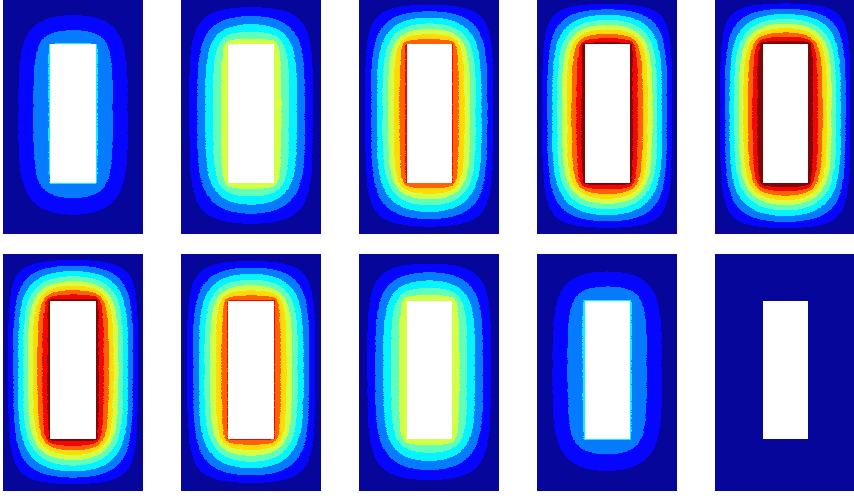
Figure 3.4: Absolute errors on the magnetic vector potential amplitude of 10 first time steps of inductor-core system POD model. Legend: 0 (dark blue) to 10^{-12} (dark red) with a ten level linear-spaced graduation. (Vs/m)
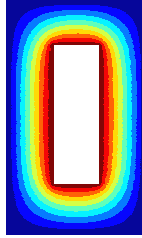
Figure 3.5: POD basis (1 mode) of the inductor-core system. Legend: 0 (dark blue) to 0.0186 (dark red) with a ten level linear-spaced graduation.

where $F_i^j(\mu_i)$ are the modes in the PGD decomposition. Injecting this PGD separated representation of $\mathbf{a}$ comprising r modes into the continuous magnetodynamic equation (1.12) leads to

$$\sigma\partial_t\left[\mathbf{a}^{r-1}+\prod_{i=1}^{D}F_i^r(\mu_i)\right]+\mathbf{curl}\left(\nu\,\mathbf{curl}\left[\mathbf{a}^{r-1}+\prod_{i=1}^{D}F_i^r(\mu_i)\right]\right)=\mathbf{j}_s. \qquad (3.10)$$

Following the enrichment procedure described in section 2.1.6, $\mathbf{a}^r(\mu_1,\cdots,\mu_D)$ is known and one is interested at finding the additional rth mode. Isolating the previously known solution $\mathbf{a}^{r-1}$ from the unknown modes $F_i^r(\mu_i)$, equation (3.10) becomes

$$\sigma\partial_t\prod_{i=1}^{D}F_i^r(\mu_i)+\mathbf{curl}\left(\nu\,\mathbf{curl}\,\prod_{i=1}^{D}F_i^r(\mu_i)\right)=\mathbf{j}_s-\sigma\partial_t\mathbf{a}^{r-1}-\mathbf{curl}\left(\nu\,\mathbf{curl}\,\mathbf{a}^{r-1}\right). \qquad (3.11)$$

In the first term (*i.e.* the derivative one), only the modes $F_i^r(\mu_i)$ depending on the time variable are impacted. By defining D_1 and D_2 two sets such that $F_i^j(\mu_i) \in D_1$ (D_2 respectively) is time independent (dependent respectively) and respecting $\prod_{i=1}^{D} F_i^r(\mu_i) = \prod_{i=1}^{D_1} F_i^r(\mu_i) \prod_{i=1}^{D_2} F_i^r(\mu_i)$ with $D = D_1 \cup D_2$, the time derivative terms become

$$\begin{cases} \sigma \partial_t \prod_{i=1}^{D} F_i^r(\mu_i) & = & \sigma \prod_{i=1}^{D_1} F_i^r(\mu_i) \partial_t \prod_{i=1}^{D_2} F_i^r(\mu_i), \\ \sigma \partial_t \mathbf{a}^{r-1} & = & \sigma \sum_{j=1}^{r-1} \left(\prod_{i=1}^{D_1} F_i^j(\mu_i) \partial_t \prod_{i=1}^{D_2} F_i^j(\mu_i) \right). \end{cases} \tag{3.12}$$

Conversely, the same separation can be performed with the **curl** operator by defining D_3 and D_4 two sets such that $F_i^j(\mu_i) \in D_3$ (D_4 respectively) is spatially independent (dependent respectively) and respecting $\prod_{i=1}^{D} F_i^r(\mu_i) = \prod_{i=1}^{D_3} F_i^r(\mu_i) \prod_{i=1}^{D_4} F_i^r(\mu_i)$ with $D = D_3 \cup D_4$. The **curl** terms can be rewritten as

$$\begin{cases} \mathbf{curl}\ \left(\nu\, \mathbf{curl}\ \prod_{i=1}^{D} F_i^r(\mu_i) \right) & = & \prod_{i=1}^{D_3} F_i^r(\mu_i) \mathbf{curl}\ \left(\nu \mathbf{curl}\ \prod_{i=1}^{D_4} F_i^r(\mu_i) \right), \\ \mathbf{curl}\ \left(\nu\, \mathbf{curl}\ \mathbf{a}^{r-1} \right) & = & \sum_{j=1}^{r-1} \prod_{i=1}^{D_3} F_i^j(\mu_i) \mathbf{curl}\ \left(\nu \mathbf{curl}\ \prod_{i=1}^{D_4} F_i^j(\mu_i) \right). \end{cases} \tag{3.13}$$

By injecting relations (3.12) and (3.13) into (3.11), the magnetodynamic equation becomes

$$\sigma \prod_{i=1}^{D_1} F_i^r(\mu_i) \partial_t \prod_{i=1}^{D_2} F_i^r(\mu_i) + \prod_{i=1}^{D_3} F_i^r(\mu_i) \mathbf{curl}\ \left(\nu \mathbf{curl}\ \prod_{i=1}^{D_4} F_i^r(\mu_i) \right) = \tag{3.14}$$

$$\mathbf{j}_s - \sigma \sum_{j=1}^{r-1} \left(\prod_{i=1}^{D_1} F_i^j(\mu_i) \partial_t \prod_{i=1}^{D_2} F_i^j(\mu_i) \right) - \sum_{j=1}^{r-1} \prod_{i=1}^{D_3} F_i^j(\mu_i) \mathbf{curl}\ \left(\nu \mathbf{curl}\ \prod_{i=1}^{D_4} F_i^j(\mu_i) \right).$$

Using FEM, the Partial Differential Equation (PDE) (3.14) is solved by means of its weak formulation obtained after multiplication by appropriate test functions $w^{'}$ in the form of $w^{'} = F_1^{'} F_2^r \cdots + F_1^r F_2^{'} \cdots + \cdots$ where $F_i^{'}$ is a test function in the same functional space than F_i^r and integration over the parameter space $\Omega_D = \Omega_{\mu_1} \times \Omega_{\mu_2} \times \cdots \times \Omega_{\mu_D}$. By doing so, equation (3.14) becomes

$$\int_{\Omega_D} \left[\sigma \prod_{i=1}^{D_1} F_i^r(\mu_i) \partial_t \prod_{i=1}^{D_2} F_i^r(\mu_i) \right] \cdot w^{'} \mathbf{d\mu} \tag{3.15}$$

$$+ \int_{\Omega_D} \left[\prod_{i=1}^{D_3} F_i^r(\mu_i) \mathbf{curl}\ \left(\nu \mathbf{curl}\ \prod_{i=1}^{D_4} F_i^r(\mu_i) \right) \right] \cdot w^{'} \mathbf{d\mu}$$

$$+ \int_{\Omega_D} \left[\sigma \sum_{j=1}^{r-1} \left(\prod_{i=1}^{D_1} F_i^j(\mu_i) \partial_t \prod_{i=1}^{D_2} F_i^j(\mu_i) \right) \right] \cdot w^{'} \mathbf{d\mu}$$

$$+ \int_{\Omega_D} \left[\sum_{j=1}^{r-1} \prod_{i=1}^{D_3} F_i^j(\mu_i) \mathbf{curl}\ \left(\nu \mathbf{curl}\ \prod_{i=1}^{D_4} F_i^j(\mu_i) \right) \right] \cdot w^{'} \mathbf{d\mu}$$

$$- \int_{\Omega_D} \left[\mathbf{j}_s \right] \cdot w^{'} \mathbf{d\mu} = 0.$$

Each integral term induces D equations by the application of the test function w'. In each of them, a single function F_i^r is tested by its corresponding test function F_i' while the other functions are known and form coefficients. At this point, due to the potentially large number of parameter D, further general developments are not relevant and the particularization to formulations involving two or three variables is then considered.

Formulation with two variables   First, the unknown is separated in two variables–space and time (*i.e.* $\mu_1 = \mathbf{x}$ and $\mu_2 = t$ with $D = 2$)–such that equation (3.9) becomes

$$\mathbf{a}^r(\mathbf{x}, t) = \mathbf{a}^{r-1} + \mathbf{S}^r(\mathbf{x})\mathbf{T}^r(t) \tag{3.16}$$

where $\mathbf{S}^r(\mathbf{x})$ and $\mathbf{T}^r(t)$ are the rth mode corresponding to the space and time variable respectively. By doing so, one verifies $D_1 = \{\mathbf{S}^i(\mathbf{x})\}$, $D_2 = \{\mathbf{T}^i(t)\}$, $D_3 = \{\mathbf{T}^i(t)\}$ and $D_4 = \{\mathbf{S}^i(\mathbf{x})\}$ for $i = 1, \cdots, r$. For the sake of readiness, dependencies are omitted and different notations than F_i^j are used (e.g. $\mathbf{S}^i = F_1^i$ and $\mathbf{T}^i = F_2^i$). With test functions $w' = \mathbf{S}'\mathbf{T}^r + \mathbf{S}^r\mathbf{T}'$, separated formulation of source term $\mathbf{j}_s = \mathbf{j_x}J_t$ and equation (3.16), (3.15) becomes

$$\int_{\Omega_D} \left[\sigma \mathbf{S}^r \partial_t \mathbf{T}^r\right] \cdot \left[\mathbf{S}'\mathbf{T}^r + \mathbf{S}^r\mathbf{T}'\right] \mathrm{dt}\mathbf{dx} \tag{3.17}$$

$$+ \int_{\Omega_D} \left[\mathbf{T}^r \, \mathbf{curl} \, \left(\nu \mathbf{curl} \, \mathbf{S}^r\right)\right] \cdot \left[\mathbf{S}'\mathbf{T}^r + \mathbf{S}^r\mathbf{T}'\right] \mathrm{dt}\mathbf{dx}$$

$$+ \int_{\Omega_D} \left[\sigma \sum_{j=1}^{r-1} \left(\mathbf{S}^j \partial_t \mathbf{T}^j\right)\right] \cdot \left[\mathbf{S}'\mathbf{T}^r + \mathbf{S}^r\mathbf{T}'\right] \mathrm{dt}\mathbf{dx}$$

$$+ \int_{\Omega_D} \left[\sum_{j=1}^{r-1} \mathbf{T}^j \mathbf{curl} \, \left(\nu \mathbf{curl} \, \mathbf{S}^j\right)\right] \cdot \left[\mathbf{S}'\mathbf{T}^r + \mathbf{S}^r\mathbf{T}'\right] \mathrm{dt}\mathbf{dx}$$

$$- \int_{\Omega_D} \left[\mathbf{j_x}J_t\right] \cdot \left[\mathbf{S}'\mathbf{T}^r + \mathbf{S}^r\mathbf{T}'\right] \mathrm{dt}\mathbf{dx} = 0.$$

By defining the following constants:

$$t_{jr} = \int_{\Omega_t} \left(\partial_t \mathbf{T}^j\right)\mathbf{T}^r \mathrm{dt}, \tag{3.18}$$

$$s_{jr} = \int_{\Omega_\mathbf{x}} \sigma \mathbf{S}^j \mathbf{S}^r \mathbf{dx}, \tag{3.19}$$

$$u_{jr} = \int_{\Omega_t} \mathbf{T}^j \mathbf{T}^r \mathrm{dt}, \tag{3.20}$$

$$v_{jr} = \int_{\Omega_\mathbf{x}} \mathbf{curl} \, \left(\nu \mathbf{curl} \, \mathbf{S}^j\right)\mathbf{S}^r \mathbf{dx}, \tag{3.21}$$

$$y_r = \int_{\Omega_t} \mathbf{j}_t \mathbf{T}^r \mathrm{dt}, \tag{3.22}$$

$$z_r = \int_{\Omega_\mathbf{x}} \mathbf{j_x}\mathbf{S}^r \mathbf{dx}, \tag{3.23}$$

equation (3.17) can be written in the more compact form

$$\int_{\Omega_{\mathbf{x}}} \left[\sum_{j=1}^{r} t_{jr}\sigma\mathbf{S}^j + u_{jr}\mathbf{curl}\left(\nu\mathbf{curl}\ \mathbf{S}^j\right) - y_r\mathbf{j_x} \right] \cdot \mathbf{S}'\mathbf{dx} \tag{3.24}$$

$$+ \int_{\Omega_t} \left[\sum_{j=1}^{r} s_{jr}\partial_t\mathbf{T}^j + v_{jr}\mathbf{T}^j - z_r\mathbf{j}_t \right] \cdot \mathbf{T}'\mathrm{dt} = 0.$$

Finally, equation (3.24) is solved by computing the two integral terms separately and updating the solutions until convergence. Decoupling (3.24) into two equations leads to the procedure described in algorithm 3.1 as explained in section 2.1.6.

Algorithm 3.1: PGD procedure to solve eq. (3.24)

Data: Initialized $S^0(\mathbf{x})$ and $T^0(t)$ (e.g. 0) and ROM error criteria ε_{max}
Result: The set of modes $S^j(\mathbf{x})$ and $T^j(t)$ with $j = 1, ..., r$
$\varepsilon_{rom} = 1$
r=1
$S_1^1 = S^0$ and $T_1^1 = T^0$
while $\varepsilon_{max} \leq \varepsilon_{rom}$ **do**
    $\varepsilon_{iter} = 1$
    i=1
    while $\varepsilon_{iter} \leq \varepsilon_{rom}$ **do**
        Find S_i^r by solving
        $\int_{\Omega_{\mathbf{x}}} \left[\sum_{j=1}^{r}\left(t_{jr}\sigma\mathbf{S}_i^j + u_{jr}\mathbf{curl}\left(\nu\mathbf{curl}\ \mathbf{S}_i^j\right)\right) - y_r\mathbf{j_x} \right] \cdot \mathbf{S}'\mathbf{dx} = 0$
        Find T_i^r by solving
        $\int_{\Omega_t} \left[\sum_{j=1}^{r}\left(s_{jr}\partial_t\mathbf{T}_i^j + v_{jr}\mathbf{T}_i^j\right) - z_r\mathbf{j}_t \right] \cdot \mathbf{T}'\mathrm{dt} = 0$
        Compute error ε_{iter} (e.g. L^2 norm between iterates S_i^r and S_{i-1}^r and T_i^r
         and T_{i-1}^r)
        i++
    end
    Iterative process converged and rth mode is obtained $S^r = S_i^r$ and $T^r = T_i^r$.
    Compute error ε_{rom} (see equation (2.59))
    r++
end
PGD model is obtained with modes $S^j(\mathbf{x})$ and $T^j(t)$ $(j = 1, ..., r)$.

Formulation with three variables   Since the PGD method simplifies a complex model into a separable representation of modes (corresponding to independent variables), additional parameters can easily be added to the formulation (3.16). As a second example and to illustrate this remark, the source current intensity is considered as a new parameter for the magnetodynamic problem. Now, the solution field **a** can be written as

$$\mathbf{a}^r(\mathbf{x}, t, i) = \mathbf{a}^{r-1} + \mathbf{S}^r(\mathbf{x})\mathbf{T}^r(t)\mathbf{I}^r(i) \tag{3.25}$$

where i is the peak current value in source term

$$\mathbf{j}(\mathbf{x}, t, i) = j_{\mathbf{x}}(\mathbf{x})\, j_t(t)\, j_i(i)\mathbf{e}_z. \tag{3.26}$$

By applying the same procedure as before, the PGD formulation (3.11) now consists in
solving the system of three separated equations

$$\begin{cases} \sum_{j=1}^{r} u_{jr} q_{jr} \mathbf{curl}\ \nu \mathbf{curl}\ S^j + t_{jr} q_{jr} S^j &=& y_r w_r j_{\mathbf{x}}, \\ \sum_{j=1}^{r} v_{jr} q_{jr} T^j + s_{jr} q_{jr} \mathrm{dt} T^j &=& z_r w_r j_t, \\ \sum_{j=1}^{r} \left(v_{jr} u_{jr} + s_{jr} t_{jr} \right) I^j &=& z_r y_r j_I, \end{cases} \tag{3.27}$$

with the six constants defined from (3.18) to (3.23) and the two additional ones

$$q_{jr} = \int_{\Omega_i} \mathbf{I}^j \mathbf{I}^r \mathrm{di}, \tag{3.28}$$

$$w_r = \int_{\Omega_i} \mathbf{j}_i \mathbf{I}^j \mathrm{di}. \tag{3.29}$$

System (3.27) is voluntary written in strong form (instead of weak one in (3.24)) for the
sake of conciseness and highlight the differentiation between the coefficients and the
unknowns.

The main advantage of the PGD formulation is directly observable by the hierarchi-
cal enrichment in modes and in number of variables (coming from the formulation with
two variables to three). This characteristic is derived from the separable representation
of independent variables. As they are independent one to each other, the same con-
stants can be reused in a richer formulation presenting more variables. As the method
is entirely centered around the enrichment of modes, one can observe the particular
enrichment in the formulation by adding one variable. Finally, system (3.27) is solved
using the same procedure as described in algorithm 3.1 but with three variables.

Application to an inductor-core system   Even though the PGD may seem compli-
cated with the previous formulations, applying it to the uncoupled linear inductor-core
system showed in Fig. 3.1 gives very intuitive results. Indeed, as the POD showed the
solutions in time only require a single mode, the separation of variables is trivial.

First, let us consider the same problem as described in the POD section with the
PGD formulation involving the separation in space and time (no separation in intensity
is taken into account first). As the source term is expressed by (3.6), it can be separated
as

$$\mathbf{v} = \mathbf{v}_{\mathbf{x}} \cdot v_t = \left(\frac{N_w}{S_c} I_{\mathrm{peak}} \mathbf{e}_z \right) \cdot \sin(2\pi f t). \tag{3.30}$$

The intuitive separate modes are shown in Fig. 3.6 with one spatial mode S^1 (similar
to the one observed in the POD formulation) and one time mode T^1 corresponding
to the sin expression in the source term. Given those two modes, one can retrieve a
particular value of the magnetic vector potential at any given coordinates in space
and time without the need to recompute the original problem (or the PGD modes).
Consequently, the speedup in time and curtailment in computational resources are
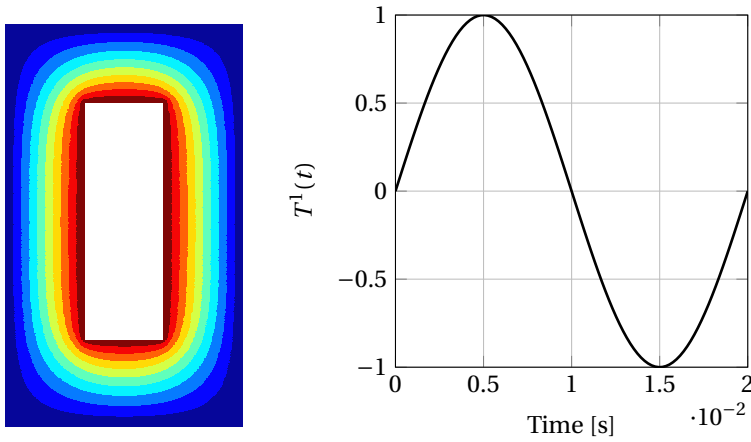
Figure 3.6: (Left) 1st mode in space. Legend: 0 (dark blue) to 0.1 (dark red) with a ten level linear-spaced graduation. (Right) 1st mode in time.

massively noticeable if the PGD modes are already defined. The time to determine those modes follows classical FE resolutions but can be large in case the fixed point algorithm 3.1 does not easily converge.

Because the PGD is aimed at dealing with numerous parameters, one may be interested in adding the conductivity, the permittivity or the RMS input current as parameters in the original problem. Let us consider the PGD formulation (3.27) with the input current I_{RMS} as a third parameter. Here, the source term can easily be separated in three terms as

$$\mathbf{v} = \mathbf{v_x} \cdot v_i \cdot v_t = \left(\frac{N_w}{S_c} \mathbf{e}_z \right) \cdot I_{\mathrm{peak}} \cdot \sin(2\pi f t). \tag{3.31}$$

The first current mode I^1 in the PGD formulation corresponds to a linear ramp as depicted in Fig. 3.7 and the space and time modes are the same as in the two-variable separation case (Fig. 3.6). The PGD method has been applied on a coupled formulation of a similar problem in [98].

3.3   Model order reduction of electromagnetics with global quantities

Here, in complement to the last section where the model order reduction methods have been presented for linear time domain magnetodynamics, MOR is introduced for linear magnetodynamic and full wave applications by integrating global quantities as described in section 1.2.5. Only the coupling between FE local and global quantities without external electric circuit is considered. Due to this coupling, multiple modes in the reduced order models are expected.

Two methods are considered –POD and Krylov-based approaches–in both time and frequency domains of two magnetodynamic applications: a 2D transformer and a 3D microwave antenna. Those results are parts of the research presented in [95, 151].
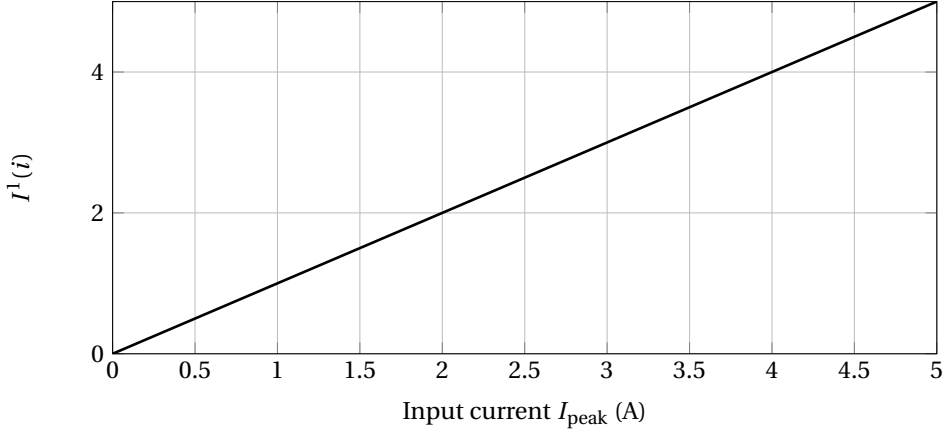
Figure 3.7: 1st mode in intensity.

3.3.1 Proper Orthogonal Decomposition

3.3.1.1 Reduced order model of magnetodynamic formulation

The POD acts similarly in this case as in the previous formulation which only comprised local quantities. From the general magnetodynamic equation in time (1.34), the reduced order model is directly obtained by

$$\mathbf{Q}^T \left[\frac{\mathbf{M}}{\Delta t} + \mathbf{S} \right] \mathbf{Q}\tilde{\mathbf{x}}_{k+1} = \mathbf{Q}^T \mathbf{y}_{k+1} + \mathbf{Q}^T \frac{\mathbf{M}}{\Delta t} \mathbf{Q}\tilde{\mathbf{x}}_k. \tag{3.32}$$

(reminding that $\mathbf{x}$ and $\mathbf{y}$ are the unknown and source vectors comprising both local and global relations in extension of $\mathbf{a}$ and $\mathbf{v}$ respectively).

Similarly, in frequency domain, (1.35) is projected onto the POD reduced basis $\hat{\mathbf{Q}}$ and gives the reduced model formulation

$$\hat{\mathbf{Q}}^T (\imath\omega\mathbf{M} + \mathbf{S}) \hat{\mathbf{Q}}\mathbf{x} = \hat{\mathbf{Q}}^T \mathbf{y} \tag{3.33}$$

where $\hat{\mathbf{Q}}$ (equivalently to $\mathbf{Q}$ in time domain) is generated through the application of the SVD onto the snapshot matrix, which is obtained by collecting and appending the solutions at given frequencies such as

$$\mathbf{X} = [\mathbf{x}_1, \cdots, \mathbf{x}_K] \in \mathbf{R}^{n \times K} \tag{3.34}$$

with $\mathbf{x}_i$ the solution of system (1.32) at frequency f_i with $i = 1, \cdots, K$ (equivalently at time t_i in time domain).
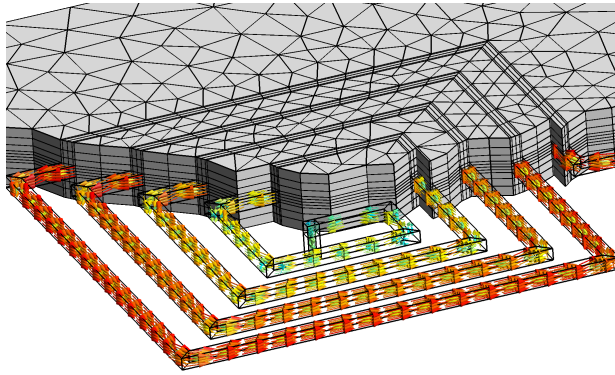
Figure 3.8: 3D model of the microwave antenna. [151]

3.3.1.2   Reduced order model of full wave formulation

Based on full wave equation (1.32), the reduced order model of full wave formulation using POD method is

$$\hat{\mathbf{Q}}^T \underbrace{\left(-\omega^2 \mathbf{M}_1 + \imath\omega \mathbf{M}_2 + \mathbf{M}_3\right)}_{\mathbf{A}} \hat{\mathbf{Q}} \mathbf{x} = \hat{\mathbf{Q}}^T \mathbf{y}. \tag{3.35}$$

3.3.1.3   Application to a 3D microwave antenna

To illustrate the POD on full wave coupled formulation, a 3D microwave antenna application is considered (and is depicted in Fig. 3.8). It is made of copper ($\sigma = 5.77 \cdot 10^7 \text{S/m}$) and has a $5 \times 5 \text{ mm}^2$ square section. Contrary to the previous application in time domain, a frequency analysis is performed to determine the input impedance $\mathbf{z}$ of the antenna in the frequency band $[0.01 - 100]$MHz—without the need to know the underlying local unknowns using (3.35). Here, the impedance corresponds to the global quantity of interest. It is important to notice that size of the system is directly linked to the number of elements in the mesh. Since the mesh discretization usually changes with the frequency (respecting the rule of thumb of minimum 10 elements per wavelength), the finest mesh is considered for all frequencies—leading to a constant size n of the system.

While the application of the POD on the simple case of magnetodynamics without global quantity only requires one snapshot (for one mode), two issues occur when global quantities are included:

1. The number of modes (and consequently the minimum number of snapshots) is unknown. This means that the HFM needs to be trained at multiple frequencies to generate enough snapshots to constitute **X** and obtain an appropriate POD basis.

2. The choice of the snapshots is not predetermined. This will induce an over-training of the HFM and generating dependent snapshots. As a consequence,

a loss of time is noticed and performing the reduce order modeling may not be as interesting as most of the high fidelity solutions may have already been computed.

To our knowledge, even if some reduced order modeling techniques effectively deal with parametric problems by stimulating (predefined) particular values of the parameters [83, 134, 152, 169], no algorithm has been developed to construct a representative snapshot matrix for the POD by determining the appropriate parameter values for which the system has to be trained. Even though, recent developments similar to the one presented here have been published in [38, 153].

In joint work [151], three greedy algorithms are proposed to adequately find the minimum number of high fidelity resolutions at given frequencies and obtain an accurate response over the entire frequency range thanks to the fast evaluation of the ROM:

1. **Algorithm** 3.2 stops the greedy search when the residual error on local quantities is smaller than the fixed tolerance τ. If it is not the case for all frequencies, the HFM is solved at the frequency corresponding to the highest error to enrich the POD basis. Both the convergence criterion and snapshot selection are based on local quantities. The main disadvantage is the need to project-back the solution to the full size subspace for all frequencies at each greedy iteration. However, it is still faster than solving the HFM for all frequencies.

2. **Algorithm** 3.3 uses the same philosophy as algorithm 3.2 except that the convergence criterion is based on the error made on the global quantity (*i.e.* the input impedance **z**). If the tolerance on the global quantity is not fulfilled for all frequencies, then the selection process for the next snapshot is the same as in previous algorithm.

3. **Algorithm** 3.4 is only based on the global quantity. Here, the convergence criterion is the same as in algorithm 3.3 but the selection of frequencies is based on numerical convergence of the global quantity. In other words, at a given iteration, it looks at the largest variation in the frequency domain of the global quantity. If it is sufficiently small (*i.e.* lower than tolerance τ) than the algorithm stops and the global quantity response is said to have converged over the entire domain; if not, than the HFM is solved for the frequency presenting the largest variation and the process loops back.

In practice, by forcing the current in the antenna, the input voltage is retrieved by integrating the electric field over a closed loop. Such an operation can be discretized and added as an additional equation in (1.32)—allowing a faster evaluation of the global quantity from reduced solution. Indeed, in this application, the voltage (and the input impedance since the input current is set to 1A) is placed to be the first unknown in **x**. Therefore, the evaluation of the input impedance is directly obtain by only evaluating the first row of the HFM such as

$$\mathbf{z} = \mathbf{A}[1,:]\hat{\mathbf{Q}}\tilde{\mathbf{x}} - \mathbf{y}[1]. \tag{3.36}$$

where $\mathbf{A}[1,:]$ is the first row of $\mathbf{A}$. Because the reduced solution still has to be projected back to high fidelity subspace, this operation mathematically shows the post-operation performed on local quantities to retrieve the global one. Two models of the antenna

---

Algorithm 3.2: Greedy algorithm based on local quantities (for snapshot selection and convergence criterion).

Data: $\mathcal{F}_k = \{f_k\}$ with $k = 1, \ldots, K$, tolerance τ
Result: $\hat{\mathbf{Q}}$, ROM for F_k
Choose an initial frequency f_1.
Solve full FE at f_1 and get initial snapshot $\mathbf{x}_1$.
t = 1
r = 1
while t **do**
    $\mathbf{X} = [\mathbf{x}_1]$, remove f_1 from $\mathcal{F}_k$, $r = 1$
    Generate $\hat{\mathbf{Q}}$ (from SVD on $\mathbf{X}$).
    for f_k *in* F_k **do**
        Compute reduce matrices for f_k.
        Solve reduced system and retrieve $\tilde{\mathbf{x}}$.
        Compute error on residual $\varepsilon_k = \|\mathcal{R}(\hat{\mathbf{Q}}\tilde{\mathbf{x}})\|$.
    end
    if $\varepsilon_{max} = \max(\varepsilon_k) > \tau, \forall k$ **then**
        Pick frequency $f_{\varepsilon_{max}}$ associated to ε_{max}.
        Solve full FE at $f_{\varepsilon_{max}}$ and obtain $\mathbf{x}_{\varepsilon_{max}}$.
        Add the new snapshot $\mathbf{X} = [\mathbf{X}, \mathbf{x}_{\varepsilon_{max}}]$.
        Remove $f_{\varepsilon_{max}}$ from $\mathcal{F}_k$, r++.
    else
        t=0
    end
    if $r=K$ **then**
        t=0
    end
end

---

are considered and present different impedance responses in order to test the greedy algorithms. The first one (later called "model 1") comprises two turns and a single resonance in the impedance response. It is made of 13420 prisms and 5360 hexahedra, yielding to 46563 complex unknowns. The second one (noted "model 2" later on) is made of four turns and presents multiple peak resonances in the impedance analysis. It has 15120 prisms and 6800 hexahedra, leading to 54826 complex unknowns. By considering 10000 frequencies in the sweep analysis, the computational time required to solve the HFM over the entire frequency range by the serial approach is 44 hours.

First, the three algorithms have been tested on the model 1 to determine which one is the most efficient (*i.e.* requiring the minimum time and number of snapshots to reach a given tolerance). The convergence rates of L^2 relative error on the input impedance with respect to the number of snapshots are shown in Fig. 3.9 for all three algorithms. All algorithms determine snapshots that guarantee to reach a prescribed tolerance τ. By

---

Algorithm 3.3: Greedy algorithm based on local quantities (snapshot selection) and global quantity (convergence criterion).

Data: $\mathcal{F}_k = \{f_k\}$ with $k = 1,\dots,K$, tolerance τ
Result: $\hat{\mathbf{Q}}$, ROM, $\mathbf{Z}$ for F_k
Choose an initial frequency f_1.
Solve full FE at f_1 and get initial snapshot $\mathbf{x}_1$.
Initialize $\mathbf{Z}_0^k \neq 0, \forall k$.
t = 1
r = 1
while t **do**

    $\mathbf{X} = [\mathbf{x}_1]$, remove f_1 from $\mathcal{F}_k$, $r = 1$
    Generate $\hat{\mathbf{Q}}$ (from SVD on $\mathbf{X}$).
    for f_k *in* F_k **do**

        Compute reduce matrices for f_k.
        Solve reduced system and retrieve $\tilde{\mathbf{x}}$.
        Evaluate ROM impedance $\mathbf{z}_r^k$.
        Compute numerical error on impedance $\varepsilon_{z,k} = \left\| \frac{\mathbf{z}_r^k - \mathbf{z}_{r-1}^k}{\mathbf{z}_{r-1}^k} \right\|$.

    end
    if $\varepsilon_{z,max} = \max(\varepsilon_{z,k}) > \tau, \forall k$ **then**

        for f_k *in* F_k **do**

            Compute reduce matrices for f_k.
            Solve reduced system and retrieve $\tilde{\mathbf{x}}$.
            Compute error on residual $\varepsilon_k = \|\mathcal{R}(\hat{\mathbf{Q}}\tilde{\mathbf{x}})\|$.

        end
        Pick frequency $f_{\varepsilon_{max}}$ associated to ε_{max}.
        Solve full FE at $f_{\varepsilon_{max}}$ and obtain $\mathbf{x}_{\varepsilon_{max}}$.
        Add the new snapshot $\mathbf{X} = [\mathbf{X}, \mathbf{x}_{\varepsilon_{max}}]$.
        Remove $f_{\varepsilon_{max}}$ from $\mathcal{F}_k$, r++.

    else
        t=0
    end
    if $r = K$ **then**
        t=0
    end

end

Algorithm 3.4: Greedy algorithm based on global quantity (for snapshot selection and convergence criterion).

Data: $\mathcal{F}_k = \{f_k\}$ with $k = 1, \ldots, K$, tolerance τ
Result: $\hat{\mathbf{Q}}$, ROM, $\mathbf{Z}$ for F_k
Choose an initial frequency f_1.
Solve full FE at f_1 and get initial snapshot $\mathbf{x}_1$.
Initialize $\mathbf{Z}_0^k \neq 0, \forall k$.
t = 1
r = 1
while t **do**
    $\mathbf{X} = [\mathbf{x}_1]$, remove f_1 from $\mathcal{F}_k$, $r = 1$
    Generate $\hat{\mathbf{Q}}$ (from SVD on $\mathbf{X}$).
    for f_k *in* F_k **do**
        Compute reduce matrices for f_k.
        Solve reduced system and retrieve $\tilde{\mathbf{x}}$.
        Evaluate ROM impedance $\mathbf{z}_r^k$.
        Compute numerical error on impedance $\varepsilon_{z,k} = \left\| \frac{\mathbf{z}_r^k - \mathbf{z}_{r-1}^k}{\mathbf{z}_{r-1}^k} \right\|$.
    end
    if $\varepsilon_{z,max} = \max(\varepsilon_{z,k}) > \tau, \forall k$ **then**
        Pick frequency $f_{\varepsilon_{max}}$ associated to $\varepsilon_{z,max}$.
        Solve full FE at $f_{\varepsilon_{z,max}}$ and obtain $\mathbf{x}_{\varepsilon_{z,max}}$.
        Add the new snapshot $\mathbf{X} = [\mathbf{X}, \mathbf{x}_{\varepsilon_{z,max}}]$.
        Remove $f_{\varepsilon_{z,max}}$ from $\mathcal{F}_k$, r++.
    else
        t=0
    end
    if r=K **then**
        t=0
    end
end

---

taking $\tau = 10^{-6}$, algorithm 3.4 needs 25 snapshots while algorithms 3.2 and 3.3 require 74 and 82 snapshots respectively. As algorithm 3.4 is 2.96 and 3.28 times more efficient than the two others, it is the preferred choice hereafter for the automatic reduction of both antenna models.

Model 1 Considering the first model with two turns, the impedance norms, angles and relative errors of POD models with four sizes (*i.e.* 2, 3, 6 and 12) are shown in Fig. 3.10 compared to the HFM—which means that the 46563 original unknowns are reduced to only a dozen ones. The first frequency is 0.01MHz as the lowest in the considered range. The second is the latest: 100MHz. The third one is the resonance frequency at 64.49MHz. With six modes (corresponding to frequencies [0.01, 0.1, 1, 30, 64, 49, 100]MHz), the relative error is close to 10^{-5} around the resonance frequency
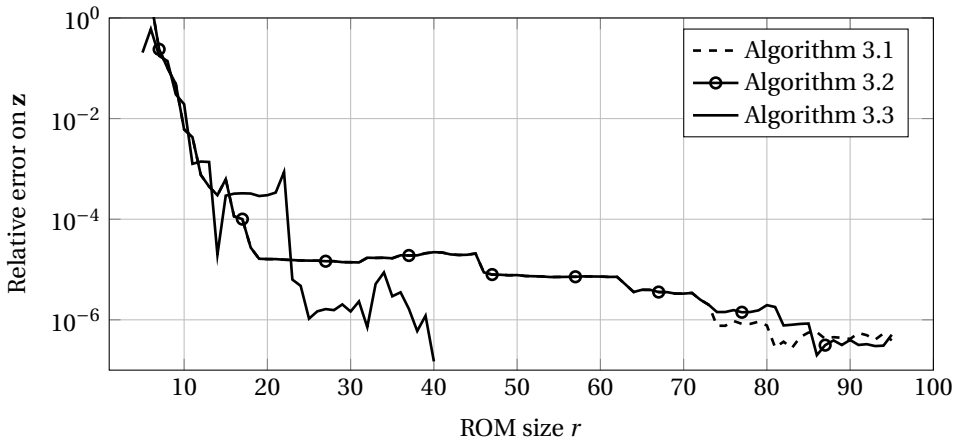
Figure 3.9: Convergence of the three algorithms vs the size of the ROM.

and $6.7 \cdot 10^{-4}$ over the entire frequency range. The reduction ratio is $46563/6 = 7760$. Considering twelve modes, the relative error is even smaller.

Two important conclusions can be derived from this first test case:

1. The algorithm detects the resonance peak quickly in the greedy process as it corresponds to the second chosen frequency.

2. The information given at the resonance notably improves the results in both impedance norm and phase. Identifying and training the HFM with well chosen input excitations is of great importance for the quality of the ROM.

Even though the results are obtained by algorithm 3.4, equivalent observations can be drawn with algorithms 3.2 and 3.3.

Model 2 A second application involves the POD reduction on antenna model 2 with four turns and presenting five resonance peaks (three high and two zeros). The impedance norms, phases and relative errors are shown in Fig. 3.11 in comparison to the HFM. As expected, the higher the number of modes, the smaller the relative error. Compared to the first test case (antenna model 1), the number of modes required to reach the same level of relative errors is bigger as the second model presents a more difficult impedance response between 0.01 and 100MHz. The average relative error is 2.59, $6.71 \cdot 10^{-3}$, $8.73 \cdot 10^{-4}$ for 5, 10 and 15 modes respectively. The 25 first selected frequencies are [0.01, 100, 1, 2, 80, 86, 21, 60, 51, 50, 35, 68, 17, 82, 97, 9, 12, 6, 67, 69, 66, 3, 4, 83, 81]MHz in the order of selection by the greedy algorithm whereas the resonant ones are 17, 50, 83MHz (up), 35 and 68MHz (down). One can observe that all resonant frequencies are present in the automatically selected ones. Even if one may only be interesting in the global quantities (e.g. the impedance), one can look at the errors of local fields. In Fig. 3.12 are shown the relative errors on the magnetic field **b** in the middle of the coil (in height) for the same four POD basis sizes: 5, 10, 15 and 25.
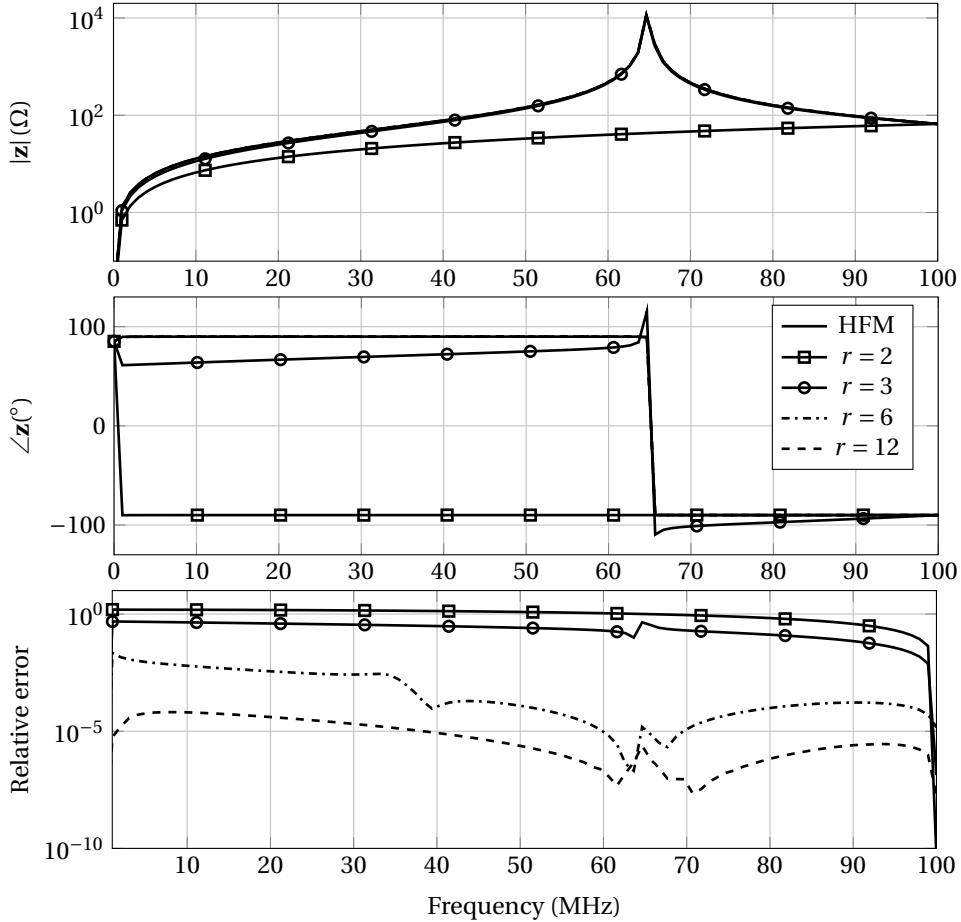
Figure 3.10: Results of ROMs for model 1. (Top) Impedance norm. (Middle) Impedance angle. (Bottom) Relative error of complex impedance from reduced model.

The relative errors are $1.04 \cdot 10^{-6}$, $5.95 \cdot 10^{-11}$, $3.77 \cdot 10^{-12}$ and $3.91 \cdot 10-14$ respectively. Respecting the computational time, solving 10000 frequencies with the classical serial HFM requires 44 hours, while the three proposed algorithms only need 4.5 hours, 3.5 hours and 19 minutes respectively—leading to respective speedups of 10, 13 and 140.

3.3.1.4 Application to a 2D transformer

In complement to the frequency analysis, a time domain approach is investigated as with the inductor-core system presented in section 3.2.1. Here, a 2D transformer is considered (depicted in Fig. 3.13) with the primary winding (358 turns) on the left and the secondary one (206 turns) on the right in open-circuit (both in copper with conductivity $\sigma = 5.77 \cdot 10^7 \, \text{S/m}$ and non magnetic behavior). The core is made of iron
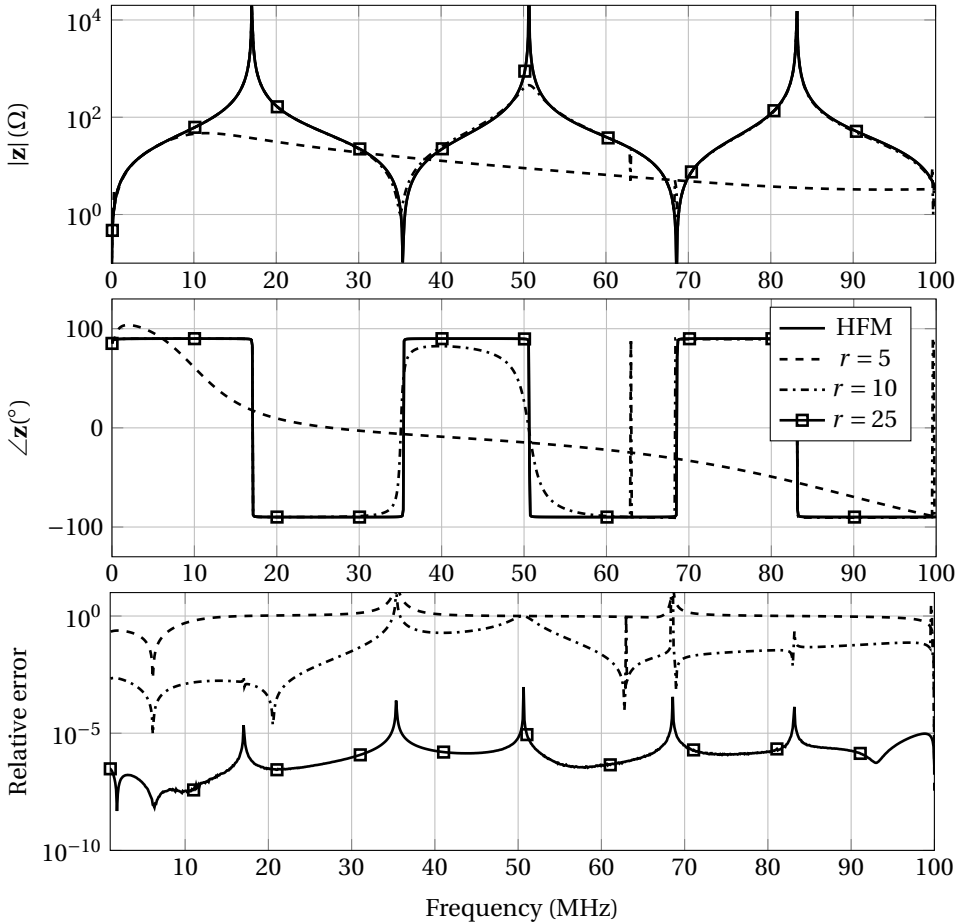
Figure 3.11: Results of ROMs for model 2. (Top) Impedance norm. (Middle) Impedance angle. (Bottom) Relative error of complex impedance from reduced model.

with linear magnetic behavior (*i.e.* $\nu = \frac{1}{1000}\nu_0$) and conductivity $\sigma = 3.72 \cdot 10^3 \text{S/m}$. The model comprises 8430 triangles, yielding to 4175 unknowns as the finest discretization in this application (and is kept constant).

The equations in time and frequency domains are given by (1.34) and (1.35) respectively and the POD reduced models correspond to (3.32) and (3.33) respectively.

In this example, the Joule losses are considered as the global quantity of interest. Due to the conductive core, the solution at time instant t_k depends on the solution at previous instant t_{k-1} which prohibits parallel computations to efficiently construct the required reduced basis. Indeed, the classical manner to deal with temporal scheme in model order reduction consists in deducing the basis from the resolution of the first N_s ($< N_t$) solutions [99, 161] with N_t the total number of time steps. Unfortunately, the choice of the number of snapshots N_s is arbitrary. To solve this issue in time domain,
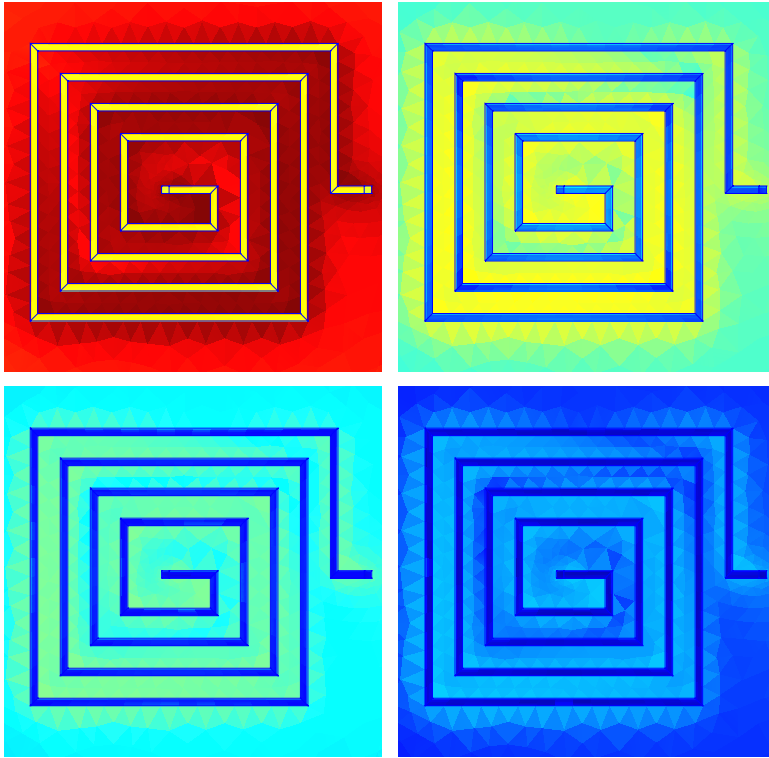
Figure 3.12: Cut (at coil center) of the absolute error of magnetic induction field **b** for $r = 5, 10, 15, 25$ snapshots (from up-left to down-right). Scale range: 10^{-16} (dark blue) to 10^{-5} (dark red). [151]

based on similar greedy ideology than algorithms 3.2, 3.3 and 3.4 in frequency domain, algorithm 3.5 is proposed and has the following philosophy: the HFM and ROM are solved in parallel for each time step until the error (of the local or global quantity) between HFM and ROM for nb time steps is lower than the tolerance τ. If a single test fails the error bound limitation, the counter is reset and a new basis is computed by using all the (high fidelity) snapshots computed so far. The higher the number of trials nb, the more predictive the ROM becomes[1].

Let us consider a frequency of 50Hz and a time interval of 1.5 periods with $N_t = 90$ time steps (60 per period). Using the algorithm 3.5 with a tolerance $\tau = 10^{-4}$ on the time discretized system gives the results depicted in Fig. 3.14. If too few bases are considered due to a small number of trials nb (e.g. $r \leq 4$), then the solution clearly diverges compared to the HFM. The error lowers when nb increases—forcing the ROM to capture more information from additional high fidelity snapshots. With ten modes, the L^2 relative error is below 1% for the entire time interval. The obtained reduction ratio is $4175/10 = 418$. Notice that the size of a POD basis r may not change with nb

---

[1]A similar algorithm has recently been proposed by [51].

Algorithm 3.5: Adaptive algorithm in time domain published in [95].

Data: Time steps $\{t_k\}$, $k \in [1, ..., K]$, $\mathbf{M}_k, \mathbf{S}_k, \mathbf{y}_k, \varepsilon_{max}, nb$
Result: Reduced solutions $\tilde{\mathbf{x}}_k$ and basis $\hat{\mathbf{Q}}$
$\hat{\mathbf{Q}} = \mathbf{0}_n$
$\mathbf{x}_0 = \mathbf{0}_n$
$\tilde{\mathbf{x}}_0 = 0$
count $= 0$
for $k \leftarrow 1$ **to** K **do**
$\quad$ Compute reduced matrices of equation (3.4) (e.g. $\tilde{\mathbf{M}}$).
$\quad$ Retrieve $\mathbf{x}_k$ by solving HFM (1.29).
$\quad$ Retrieve $\tilde{\mathbf{x}}_k$ by solving ROM (3.4).
$\quad$ Compute error ϵ (on local or global quantities) (e.g. $\epsilon = \left\| \mathbf{x}_k - \hat{\mathbf{Q}}\tilde{\mathbf{x}}_k \right\|_2 / \left\| \mathbf{x}_k \right\|_2$).
$\quad$ **if** $\max \epsilon \leq \varepsilon_{max}$ **then**
$\quad\quad$ count ++
$\quad$ **else**
$\quad\quad$ count $= 0$
$\quad$ **end**
$\quad$ **if** *count* $= nb$ **then**
$\quad\quad$ **for** $k \leftarrow 1$ **to** K **do**
$\quad\quad\quad$ Retrieve $\tilde{\mathbf{x}}_k$ by solving ROM (3.4).
$\quad\quad$ **end**
$\quad\quad$ break
$\quad$ **else if** *count* $= 0$ **then**
$\quad\quad$ Generate reduced basis $\hat{\mathbf{Q}}$ from full solutions.
$\quad\quad$ Compute reduced matrices of equation (3.4) (e.g. $\tilde{\mathbf{M}}$).
$\quad\quad$ Initialize $\tilde{\mathbf{x}}_0 = \mathbf{0}$
$\quad\quad$ **for** $i \leftarrow 1$ **to** k **do**
$\quad\quad\quad$ Retrieve $\tilde{\mathbf{x}}_i$ by solving ROM (3.4).
$\quad\quad$ **end**
$\quad$ **else**
$\quad\quad$ //Keep current reduced basis
$\quad$ **end**
end
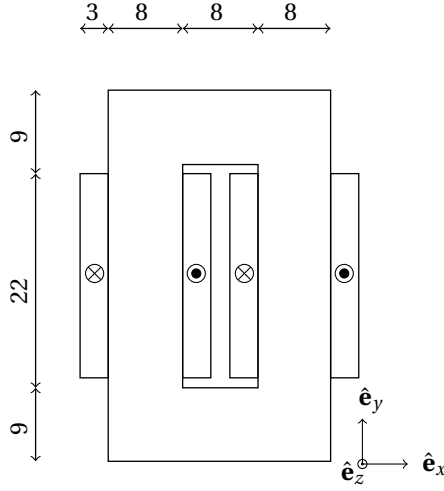
Figure 3.13: 2D model of the 1 phase transformer. Direction of the currents shown in windings by dot and cross symbols. Dimensions in cm. [95]

as it is truncated to its r most significant modes. Indeed, with $nb < 4$, the number of modes equals 6 and with $nb > 3$, it equals 10. This is the reason why the results are detailed according to r in order to appropriately compare this approach with others (showing the divergence issue at low ROM size). As a conclusion, the algorithm 3.5 gives the results for $r = 6$ and $r = 10$ with $nb < 4$ and $nb > 3$ respectively.

Conversely, the good convergence behavior is observed for local quantities (e.g. the magnetic flux density **b**) as the absolute error is depicted in Fig. 3.15 at 25ms with respect to the size of the ROM (*i.e.* $r = 4, 5, 6, 10$). At this time instant, the HFM has not been solved and no contribution to the POD basis can be related to it—showing the adequate results for further (untested) time simulations.

Even though algorithm 3.5 may solve time discretized systems, the choice of the number of trials nb remains an arbitrary one as N_s is in classical POD approaches. Moreover, the algorithm still relies on serial computations of the HFM until the number of trials is sufficient. To this end, generating the POD basis in the frequency domain to further use in the time domain would solve both issues. To do so, one has to verify that projectors in time and frequency domains can easily be interchanged. In steady state, the harmonic formalism verifies

$$\mathbf{x}_k = \|\hat{\mathbf{x}}\| \, e^{\imath \omega t_k} \tag{3.37}$$

at time instant t_k with $\mathbf{x}_k$ and $\hat{\mathbf{x}}$ the solutions in time and frequency domains respectively. Therefore, the full size vector $\mathbf{x}_k$ in time is linked to its reduced form $\tilde{\mathbf{x}}_k$ in frequency by

$$\mathbf{x}_k \quad \approx \quad \mathbf{Q}\tilde{\mathbf{x}}_k, \tag{3.38}$$
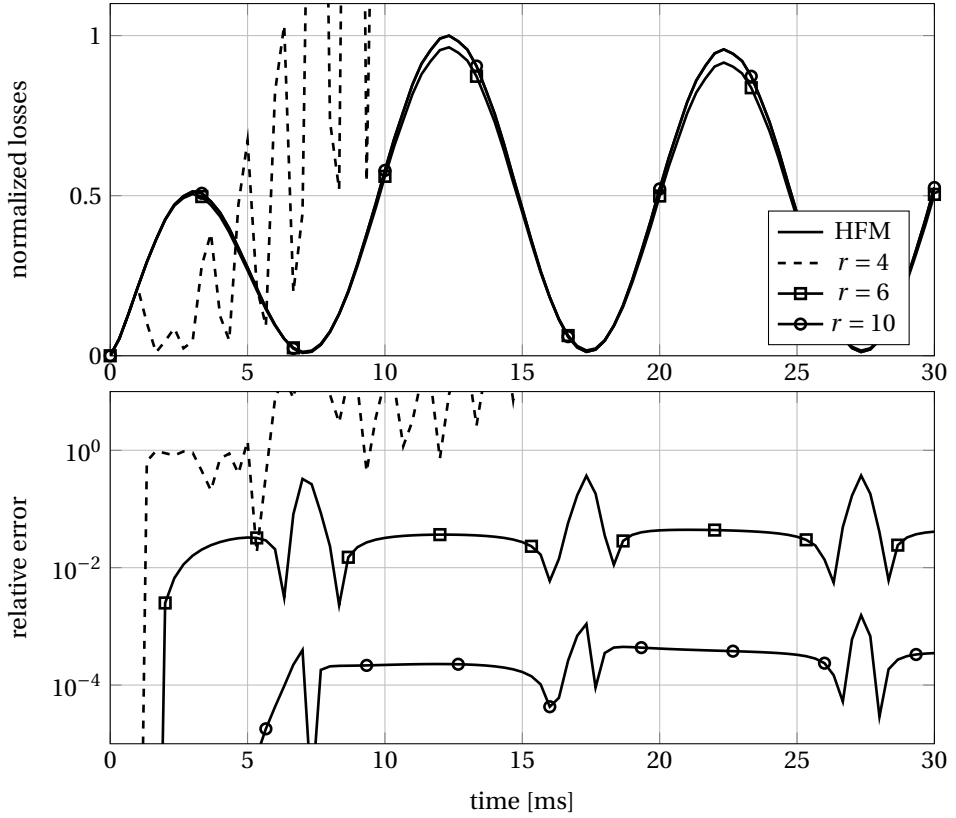
Figure 3.14: Greedy time algorithm. (Top) Normalized losses in the transformer core with POD. (Bottom) L^2-relative error.

$$= \mathbf{Q}\Re\left\{\left\|\tilde{\hat{\mathbf{x}}}\right\| e^{\iota\omega t_k}\right\}, \tag{3.39}$$

$$= \Re\left\{\mathbf{Q}\left\|\tilde{\hat{\mathbf{x}}}\right\| e^{\iota\omega t_k}\right\}, \tag{3.40}$$

$$= \Re\left\{\hat{\mathbf{Q}}\left\|\tilde{\hat{\mathbf{x}}}\right\| e^{\iota\omega t_k}\right\}, \tag{3.41}$$

with $\hat{\mathbf{Q}}$ the reduced basis in frequency domain. Equation (3.41) demonstrates the interchangeability of both bases. Further developments have been shown in [16].

Uniform selection First, as previously studied in [161], the POD basis is based on snapshots taken uniformly in the frequency range. Let us consider the frequency range [0,100]Hz to adequately center the frequency of interest (50Hz). The normalized losses from the ROMs and the relative errors in frequency domain are shown in Fig. 3.16 (first and third graphs). The relative error is above 1% with two modes whereas it is around 10^{-4} and 10^{-6} with four and six modes respectively. We considered a linearly spaced frequency set of r frequencies between 0 and 100Hz. In time domain, the
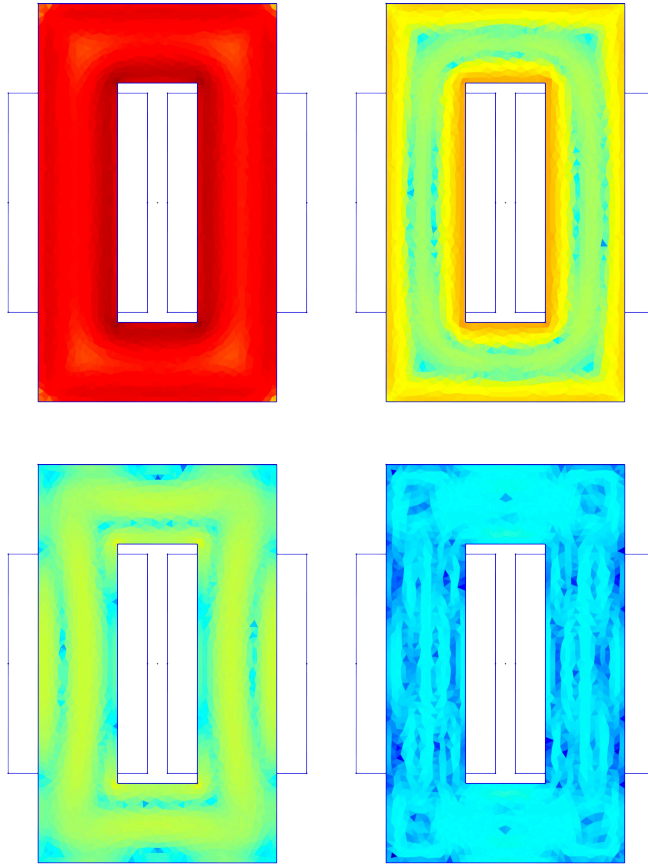
Figure 3.15: Cut (at coil center) of the absolute error of magnetic flux density (field) **b** for $r =$ 4, 5, 6, 10 at 25 ms (from up-left to down-right). Logarithmic scale range: 10^{-6} (dark blue), 10^{-3} (yellow) and 10^1 (dark red) [95]

transposition of the POD basis generated in frequency domain provides encouraging results as depicted in Fig. 3.16 (second and fourth graphs). As expected, two modes are not sufficient to adequately represent the system and the losses explodes after 2 milliseconds. Better results are obtained with four modes. However, some oscillations are present at the beginning from 2 to 4 milliseconds even though the rest of the time are rather good with relative error near 1%. Finally, six modes allow an error below 1% for all time instants.

Greedy algorithm selection   Even if the results are quite good with the uniform selection of frequencies, one may compare it to algorithm 3.4 that was developed to automatically detect resonant peaks in electromagnetic devices. The results are very similar to the uniform selection as they are depicted in Fig. 3.17. The frequencies de-
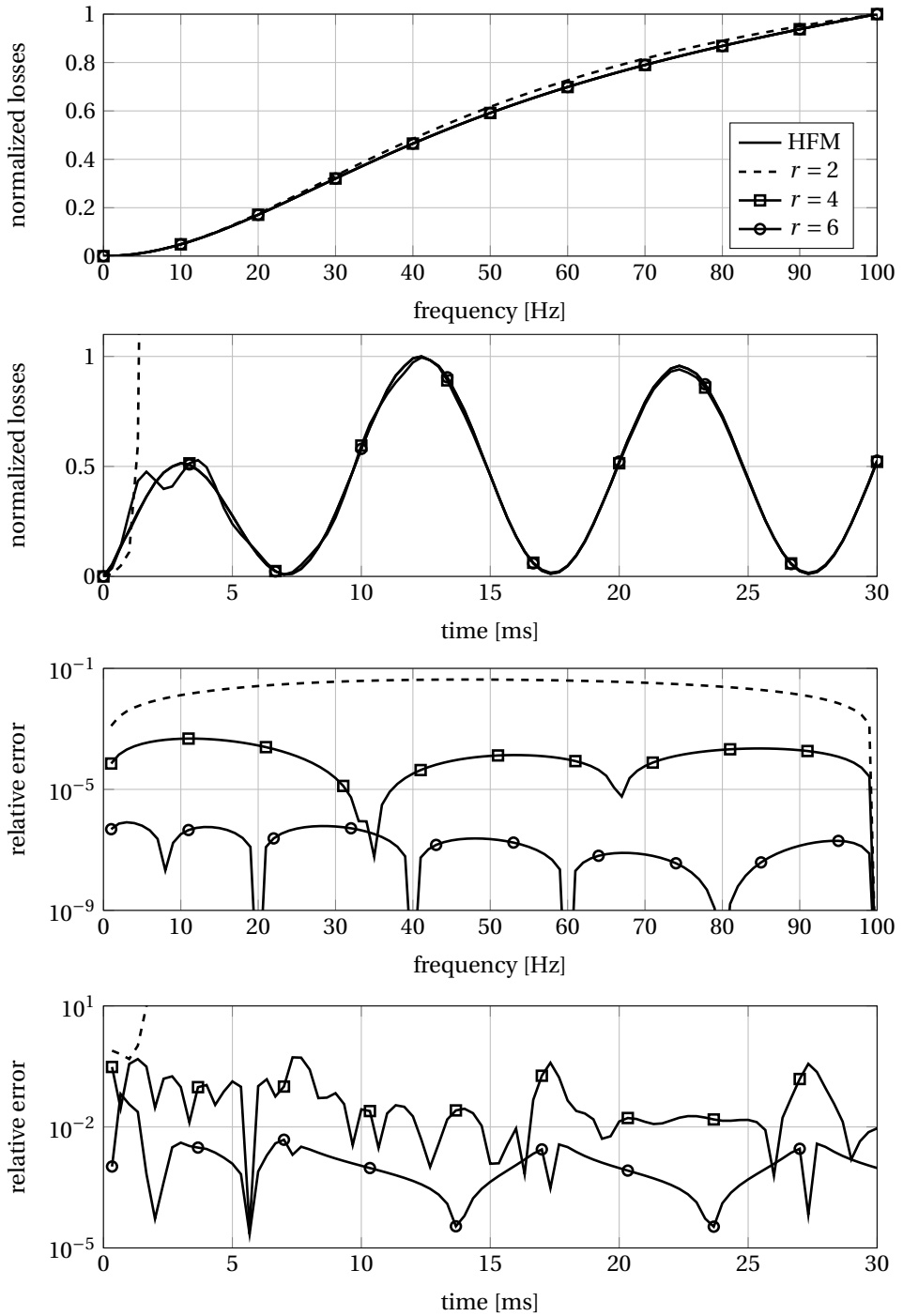
Figure 3.16: Uniform frequency algorithm. (Top) normalized losses in transformer core with POD. (Bottom) L^2-relative error.

termined by the greedy algorithm are ordered as [0, 100, 57, 33, 12, 11, 23, 72, 74]Hz and are very close to the one of uniform selection. The convergence rate of the greedy algorithm for this application is shown in Fig. 3.18. Except the beginning presenting a plateau for the first two modes, the POD convergence presents a logarithmic decrease with respect to the number of modes. The advantage of the greedy algorithm over the uniform selection approach are the absence of arbitrary choice concerning the number of snapshots and their determination (e.g. at which frequencies the HFM need to be solved).

3.3.2   Krylov-based method

In addition to the POD approach in time and frequency domains, an Arnoldi Krylov Subspace (AKS) method, described in section 2.1.3, is applied to reduce the same 2D transformer case.

Contrary to the POD, the AKS approach is only applicable in the frequency domain. Therefore, the results are to be compared with those of the POD based on the uniform selection and greedy algorithm methods. Similarly, the generated basis is used in both time and frequency domains. From equation (1.35) the transfer function reads

$$H(s) = (\mathbf{M}s + \mathbf{S})^{-1}\mathbf{y}. \tag{3.42}$$

Approximating the transfer function with a Padé expansion around the expansion point s_{exp} as in [161] leads to

$$H(s) = \sum_j H_j \left(s - s_{exp}\right)^j \tag{3.43}$$

with $H_j = (-(\mathbf{M}s_{exp} + \mathbf{S})^{-1}\mathbf{M})^j(\mathbf{M}s_{exp} + \mathbf{S})^{-1}\mathbf{y}$ for $j = 0, 1, ..., n - 1$. Thus, the Krylov subspace $\mathcal{K}_n(\alpha, \gamma)$ is defined by $\alpha = -(\mathbf{M}s_{exp} + \mathbf{S})^{-1}\mathbf{M}$ and $\gamma = (\mathbf{M}s_{exp} + \mathbf{S})^{-1}\mathbf{y}$. From the Krylov subspace $\mathcal{K}_n(\alpha, \gamma)$, the reduced basis $\hat{\mathbf{Q}}$ is obtained by the application of the Arnoldi algorithm with two moments for each expansion point [146]. Therefore, by using two moments, the reduced size r doubles compared to the POD one for an identical number of selected frequencies.

Uniform selection   First, the uniform selection of frequencies in the range [0,100]Hz is performed and leads to the results in frequency and time domains depicted in Fig. 3.19. Those results have to be compared to the ones shown in Fig. 3.16. They are very close to the POD observations with relative errors of 10^{-2}, 10^{-4}, 10^{-8} with $r = 4, 8, 12$ (corresponding to 2, 4, 6 frequencies respectively in POD case).

Greedy algorithm selection   Secondly, applying the greedy algorithm 3.4 to avoid the arbitrary choice of the number of snapshots to consider and construct the projection basis gives the results of Fig. 3.20 in frequency and time domains (to be compared with Fig. 3.17 for POD approach). Once again, the results are very similar to the POD ones except that the selected frequencies are different with [0,100,99,72,31,9,85,28,5]Hz (the first two remain identical in both situations and represents the extreme frequencies in the considered range). Overall, the AKS results are slightly better then POD ones.
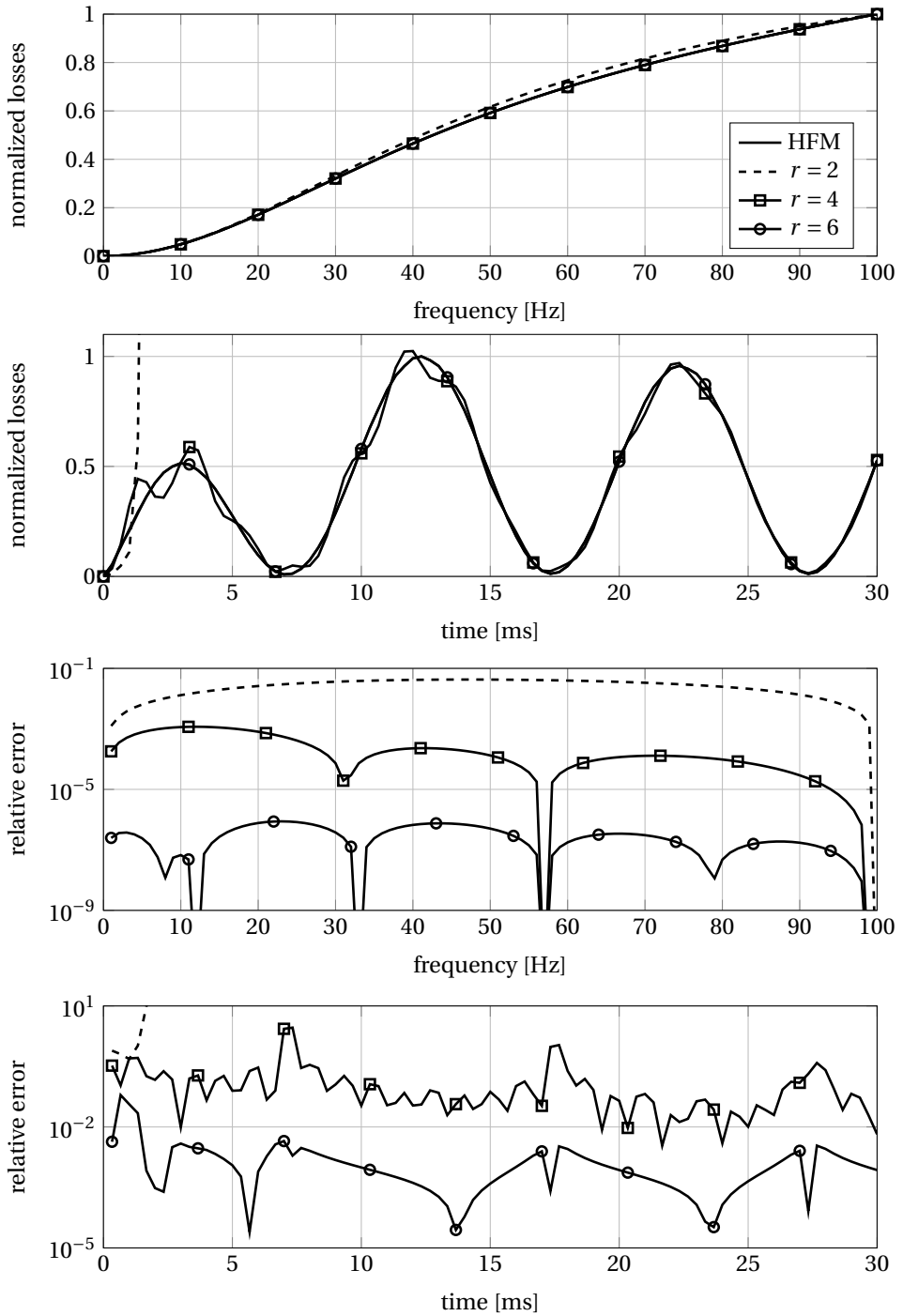
Figure 3.17: Greedy frequency algorithm. (Top) Normalized losses in transformer core with POD. (Bottom) L^2-relative error.
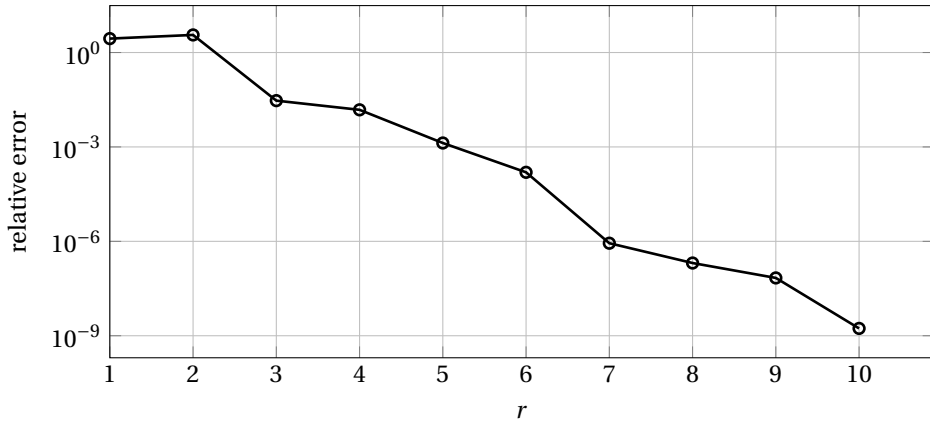
Figure 3.18: Convergence rate of greedy algorithms with POD.

Finally, the convergence rate of the AKS method by generating the projection basis in frequency domain in order to employ it in time domain is shown in Fig. 3.21. Excepting the two plateaus at the beginning, the AKS approach presents the similar logarithmic decay with the number of modes (twice as much as the POD method as two moments are considered per expansion points).

3.4 Conclusion

In this chapter, multiple model order reduction techniques have been applied in linear (electro)magnetodynamics. The PGD has been applied and detailed on a single unknown formulation without global quantity. The AKS method has been derived on a coupled multi-variable problem with local and global unknowns. The POD has been employed in both situations, in time and frequency domains, as it is one of the most versatile approach.

When the formulation only presents one local quantity in linear problems (which is a vector of numerous unknown components), a single mode is sufficient to entirely describe the dynamics—presenting the best reduction ratio. With multiple local and global quantities in a coupled formulation, several modes are required to accurately reduce the HFM. For these three methods, the number of modes cannot be chosen based on an *a priori* error estimate valid in the whole parameter range, so this number is usually fixed by trial and error.

Three automatic algorithms have been proposed to construct the snapshot matrix for the POD method by identifying the proper parameter values. They have been applied in different situations and showed excellent results in both time and frequency domains—with reduction of the resolution process above 99%. This method has been extended to the use of AKS reduction approach and results are very similar to the ones obtained with the POD.

Several applications have been detailed in this chapter such as an academic 2D inductor-core system with single variable formulation in magnetic vector potential, a
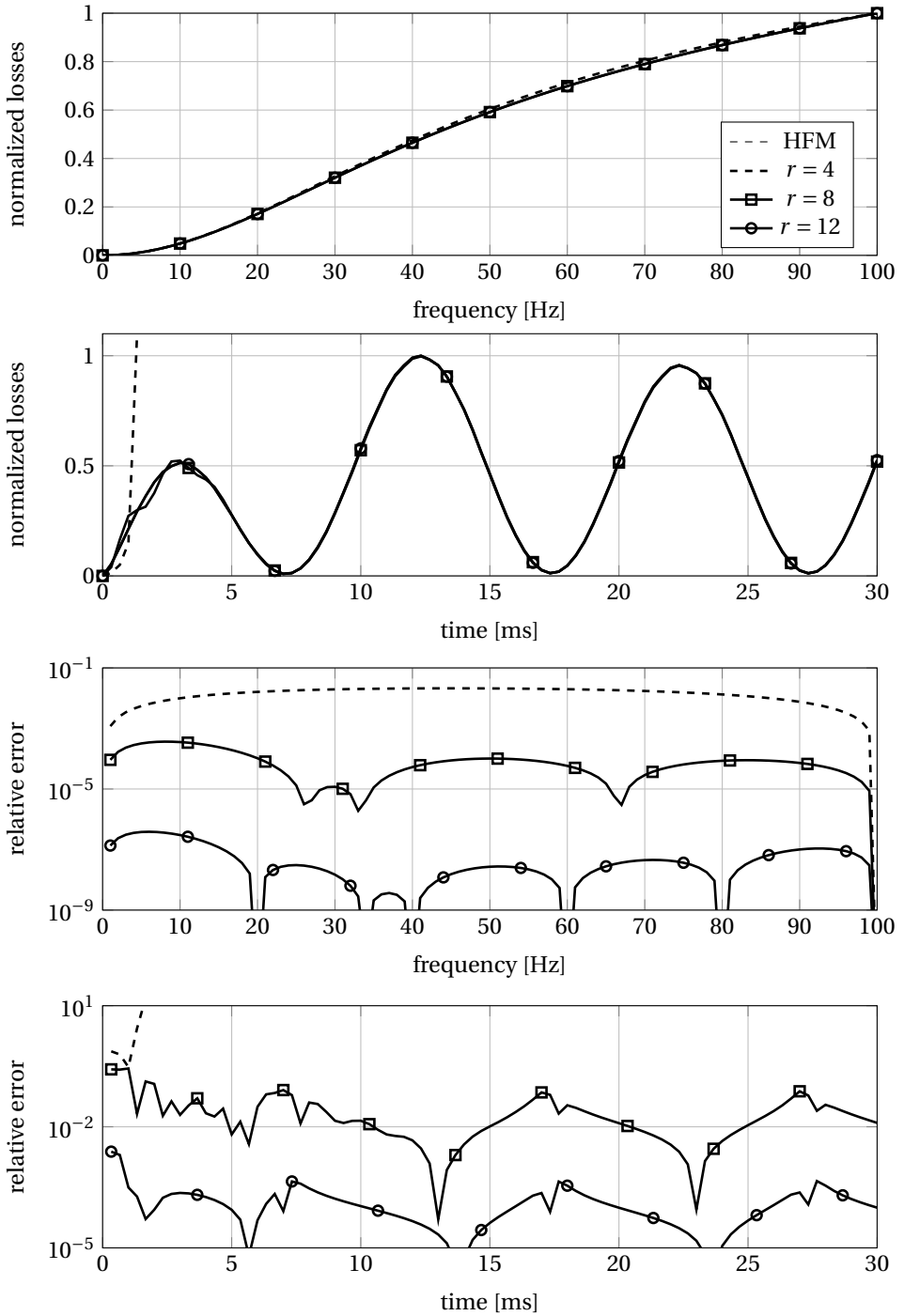
Figure 3.19: Uniform frequency algorithm. (Top) normalized losses in transformer core with AKS. (Bottom) L^2-relative error (down).
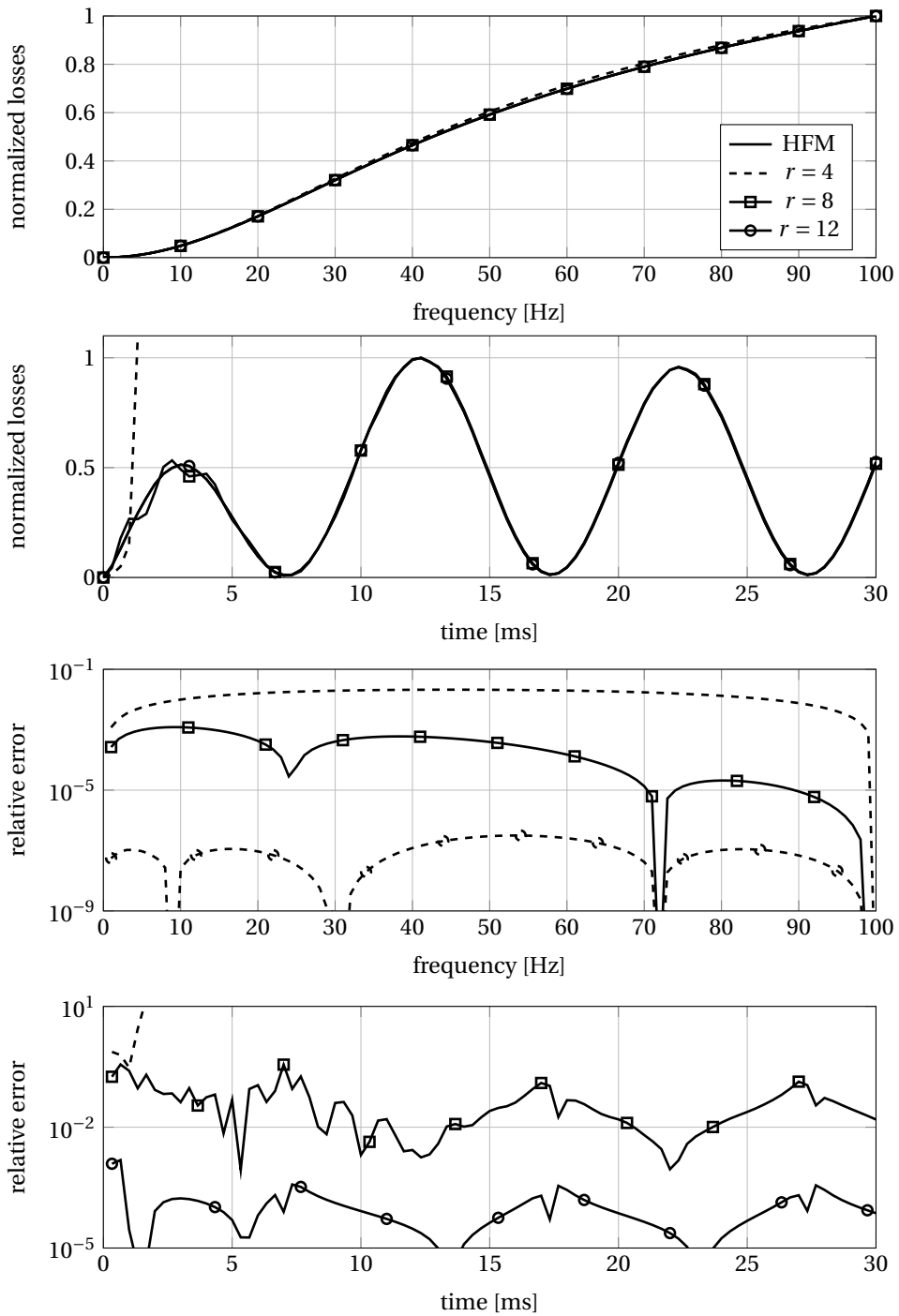
Figure 3.20: Greedy frequency algorithm. (Top) Normalized losses in transformer core with AKS. (Bottom) L^2-relative error.
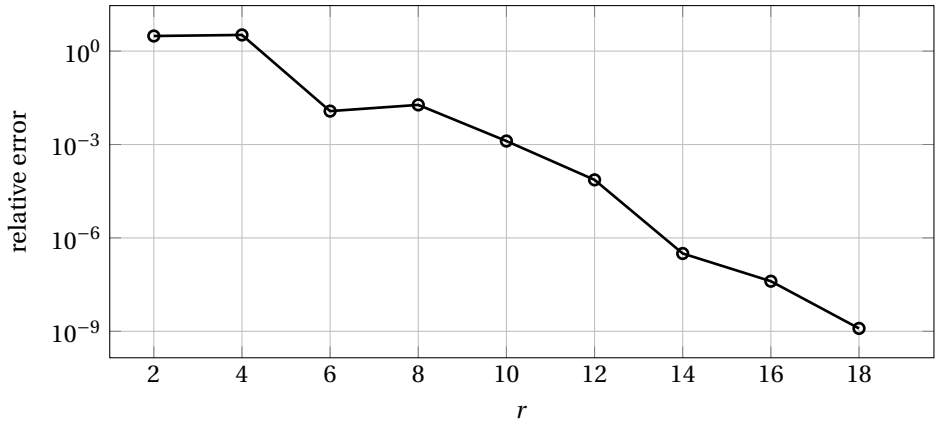
Figure 3.21: Convergence rate of greedy algorithm 3.5 with AKS.

2D transformer with coupled formulation and global quantities, and a 3D microwave antenna with full electromagnetic coupled formulation. All test cases showed drastic reductions by the application of the aforementioned MOR techniques.

This section paves the next developments for more complex situations involving nonlinearities, parameterized systems and external circuit coupling will further be involved.

CHAPTER 4

Nonlinear problems

4.1 Introduction

While the resolution process is obviously linked to the computational expenses, the assembly step may also be as time consuming as the resolution one. This observation is of great importance in nonlinear problems. Indeed, such problems are linearized (e.g. using a Newton-Raphson scheme) which implies an additional loop in the resolution procedure. Due to those new iterations, the time required in the assembly is critical to efficiently reduce nonlinear problems. In practice, applying the simple back-projection presented in section 2.2.1 does not lead to actual reduction in time as most of the time is spent in the generation of the nonlinear vectors and matrices.

To deal with such problems, element sampling methods have been developed in diverse engineering fields so that nonlinear operators of the ROM can be estimated from a reduced set of components of the HFM. In this chapter, two of them have been investigated in the context of magnetodynamic applications as described in section 2.2.2. First, the DEIM tends to approximate a general nonlinear vector from a reduced set of projected components onto a reduced basis. It is similar to the reduced approximation made so far except that the reduced states are the aforementioned reduced set of components. Secondly, the MPE is intrinsically linked to the POD method and limits the number of components in the projection matrix. Its idea consists in finding the most "useful" components in the projection matrix and restricts the assembly to them.

The chapter is organized as follows. In section 4.2 we present the nonlinear magnetodynamic formulation which is then, particularized by the application of the MPE and DEIM in sections 4.3 and 4.4 respectively. Two applications are considered: the previously described inductor-core system and a three-phase current-driven transformer.

4.2 Nonlinear formulation

In real applications, the magnetic cores do present nonlinear reluctivity (or permeability) depending on the magnetic flux density such that $v = v(\mathbf{b})$ (see Fig. 1.1(b)). Inserting

such a behavior in previously described linear general magnetodynamic reduced equation (3.32), one obtains the nonlinear relations

$$\mathbf{Q}^T \left[\frac{\mathbf{M}}{\Delta t} + \mathbf{S}(\mathbf{Q}\tilde{\mathbf{x}}_{k+1}) \right] \mathbf{Q}\tilde{\mathbf{x}}_{k+1} \quad = \quad \mathbf{Q}^T \mathbf{y}_{k+1} + \mathbf{Q}^T \frac{\mathbf{M}}{\Delta t} \mathbf{Q}\tilde{\mathbf{x}}_k, \tag{4.1}$$

$$\mathbf{x}_k \quad \approx \quad \mathbf{Q}\tilde{\mathbf{x}}_k, \tag{4.2}$$

where matrix $\mathbf{S}(\mathbf{x}_{k+1}) = \mathbf{S}(\mathbf{Q}\tilde{\mathbf{x}}_{k+1})$ now depends on the solution $\mathbf{x}_{k+1}$. Now, both $\tilde{\mathbf{x}}_{k+1}$ and $\mathbf{S}(\mathbf{x}_{k+1})$ are unknown at time instant t_{k+1} and a linearization scheme is used. Using a Newton-Raphson scheme, the solution is updated (i denotes the index of the nonlinear iteration) by

$$\tilde{\mathbf{x}}_{k+1}^{i+1} = \tilde{\mathbf{x}}_{k+1}^i + \boldsymbol{\delta}\tilde{\mathbf{x}}_{k+1}^{i+1} \tag{4.3}$$

where the increment $\boldsymbol{\delta}\tilde{\mathbf{x}}_{k+1}^{i+1}$ is the solution of

$$\mathbf{Q}^T \mathbf{J}\left(\mathbf{x}_{k+1}^i\right) \mathbf{Q}\, \boldsymbol{\delta}\tilde{\mathbf{x}}_{k+1}^{i+1} = -\mathbf{Q}^T \mathbf{r}\left(\mathbf{x}_{k+1}^i\right) \tag{4.4}$$

with $\mathbf{r}(\mathbf{x}_{k+1}^i) = \mathbf{r}(\mathbf{Q}\tilde{\mathbf{x}}_{k+1}^i)$ the residual defined by the difference between right and left hand sides in (1.34):

$$\mathbf{r}(\mathbf{x}_{k+1}^i) = \mathbf{y}_{k+1} + \frac{\mathbf{M}}{\Delta t}\mathbf{x}_k - \left(\left[\frac{\mathbf{M}}{\Delta t} + \mathbf{S}(\mathbf{x}_{k+1}^i) \right] \mathbf{x}_{k+1}^i \right) \tag{4.5}$$

and $\mathbf{J}$ the Jacobian of $\mathbf{r}(\mathbf{x}_{k+1}^i)$. This nonlinear loop is stopped at each time step once the increment or the residual is sufficiently small (*i.e.* $\left\| \boldsymbol{\delta}\tilde{\mathbf{x}}_{k+1}^{i+1} \right\| < 10^{-5}$ or $\left\| \mathbf{r}(\mathbf{Q}\tilde{\mathbf{x}}_{k+1}^i) \right\| < 10^{-5}$). Then, the solution is said to have converged and $\tilde{\mathbf{x}}_k = \tilde{\mathbf{x}}_k^i$.

4.3   Missing Point Estimation

Originally, the MPE method [13–15] has been developed for chemical reactions following the idea that the finite number of probes available limits the knowledge of the reactions at particular spots. Then, from those sampled probed areas, how can the information be inferred in the entire domain of interest? On the contrary, what are the particular positions to locate the probes and acquire all the information required to determine the solutions entirely?

With this philosophy, the MPE is intrinsically linked to the POD basis that extracts the maximum information from observations of the system. The MPE aims at sampling this basis $\mathbf{Q}$ to its q minimum number of rows while preserving a sufficiently low condition number of $\mathbf{Q}^T\mathbf{Q}$ to accurately solve the FE system. Similarly, different techniques have been developed, e.g. gappy POD [39] and hyper-reduction [171] and differ in the manner the selection matrix is determined.

Let us define $\bar{\mathbf{P}} \in \mathbb{R}^{n \times q}$ ($q \ll n$) a selection matrix of q components and the sampled expressions of the residual and Jacobian by

$$\bar{\mathbf{r}}(\mathbf{x}) \quad = \quad \bar{\mathbf{P}}^T \mathbf{r}(\mathbf{x}), \tag{4.6}$$

$$\bar{\mathbf{J}}(\mathbf{x}) \quad = \quad \bar{\mathbf{P}}^T \mathbf{J}(\mathbf{x}). \tag{4.7}$$

In the context of FEM, the coefficients on a given row of the original (sparse) matrix can be computed locally (e.g. for nodal finite elements, by considering all the mesh elements that share the corresponding node). This allows to generate the reduced set of q rows of the nonlinear matrices efficiently defined by $\bar{\mathbf{P}}$, by only considering a small subset of elements in the mesh [25, 144]. Since q rows are selected, only the corresponding q rows in the POD basis are useful and then kept with $\bar{\mathbf{Q}} = \bar{\mathbf{P}}^T \mathbf{Q} \in \mathbb{R}^{q \times r}$ computed once (or offline). Then, the application of the MPE sampling matrix $\bar{\mathbf{P}}$ on the Jacobian and residual of equation (4.4) leads to the linearized POD-MPE equation

$$\bar{\mathbf{Q}}^T \bar{\mathbf{J}} \mathbf{Q} \, \delta \tilde{\mathbf{x}} = -\bar{\mathbf{Q}}^T \bar{\mathbf{r}}. \tag{4.8}$$

The overall system is reduced to an r-dimensional subspace (with the application of the POD basis $\mathbf{Q}$) but only by considering q components of the FE model (using $\bar{\mathbf{P}}$) with $r, q \ll n$. Compared to the POD error criterion based on the singular values of the snapshot matrix, the MPE selection indices are obtained by increasing sequentially q with the most contributing rows of the POD basis according to the greedy (non hierarchical) algorithm [13, 15] that tends to verify

$$\bar{\mathbf{Q}}^T \bar{\mathbf{Q}} \approx I. \tag{4.9}$$

Equivalently, this condition can be interpreted as the decay of the condition number of $\bar{\mathbf{Q}}^T \bar{\mathbf{Q}}$ to 1 (the closest, the better). This procedure may be long and should only be done once during an offline stage. The MPE takes into account the initial n FE degrees of freedom to determine the reduced set of unknowns without depending on a number of snapshots. In the worst case, the reduced set of entries equals all of them (i.e. $q = n$) and no assembly reduction is performed.

4.4 Discrete Empirical Interpolation Method

Contrary to the direct element sampling method described with the MPE approach, the DEIM tends to project the sampled elements of the high fidelity size nonlinear vector/matrix onto a projection basis $\mathbf{U}$ (similar to the POD method). Given this projection matrix based on a singular value decomposition of nonlinear snapshots $\mathbf{Z}$ (cf. section 2.2.2), the greedy algorithm 4.1 determines the appropriate sampling matrix $\bar{\mathbf{P}}$. From our point of view based on [100], we did not use the snapshots $\mathbf{J}(\mathbf{x})\delta\mathbf{x}$—as it would apply the DEIM on the right hand side $\mathbf{r}(\mathbf{x})$. Here, the DEIM is applied on the whole system and tries to approximate $\mathbf{x}$. Thus, the nonlinear snapshots equal the complete ones, i.e. $\mathbf{x}_k$ ($k = 1, \cdots, N_t$) which effectively correspond to the correct sampling of the nonlinear unknowns $\mathbf{x}$. As a result, the nonlinear reduced basis $\mathbf{U}$ equals the POD projection basis $\mathbf{Q}$ of the overall system.

Considering the Jacobian and the residual as nonlinear matrices, their DEIM sampled expressions are given (as defined by (2.85)) by

$$\mathbf{J}(\mathbf{x}) \quad \simeq \quad \mathbf{Q} \left(\bar{\mathbf{P}}^T \mathbf{Q} \right)^{-1} \bar{\mathbf{P}}^T \bar{\mathbf{J}}(\mathbf{x}), \tag{4.10}$$

Algorithm 4.1: DEIM greedy algorithm. [45]

Data: Nonlinear reduced basis $\mathbf{U} = \begin{bmatrix}\mathbf{u}_1, \cdots, \mathbf{u}_q\end{bmatrix}$ given by the application of a
truncated SVD on nonlinear snapshot matrix $\mathbf{F} = [\mathbf{f}_1, \cdots]$
Result: Sampling matrix $\bar{\mathbf{P}}$
Find index with $[\sim, k] = \max(|\mathbf{u}_1|)$
Construct matrices with $\tilde{\mathbf{U}} = [\mathbf{u}_1]$ and $\bar{\mathbf{P}} = [\mathbf{e}_k]$
for $i = 2$ *to* q **do**
    Solve $\left(\bar{\mathbf{P}}^T \tilde{\mathbf{U}}\right)\mathbf{c} = \bar{\mathbf{P}}^T \mathbf{u}_i$
    Compute $\mathbf{r} = \mathbf{u}_i - \tilde{\mathbf{U}}\mathbf{c}$
    Find index with $[\sim, k] = \max(|\mathbf{r}|)$
    Enrich matrices with $\mathbf{U} \leftarrow \begin{bmatrix}\tilde{\mathbf{U}}\,\mathbf{u}_i\end{bmatrix}$ and $\bar{\mathbf{P}} \leftarrow \begin{bmatrix}\bar{\mathbf{P}}\,\mathbf{e}_k\end{bmatrix}$
end

$$\mathbf{r}(\mathbf{x}) \quad \simeq \quad \mathbf{Q}\underbrace{\left(\bar{\mathbf{P}}^T \mathbf{Q}\right)^{-1}}_{\bar{\mathbf{Q}}^{-1}} \bar{\mathbf{P}}^T \bar{\mathbf{r}}(\mathbf{x}). \tag{4.11}$$

Now, injecting (4.10) and (4.11) into original POD equation (4.4) leads to the POD-DEIM reduced equation

$$\bar{\mathbf{Q}}^{-1}\bar{\mathbf{J}}(\mathbf{x})\mathbf{Q}\,\delta\tilde{\mathbf{x}} = -\bar{\mathbf{Q}}^{-1}\bar{\mathbf{r}}(\mathbf{x}). \tag{4.12}$$

with $\bar{\mathbf{Q}}$, $\bar{\mathbf{J}}(\mathbf{x})$, $\bar{\mathbf{r}}(\mathbf{x})$ defined as in (4.6) and (4.7) respectively, which corresponds to the formulation in [99].

Naturally, the greedy algorithm considers the r POD modes to compute the selection matrix $\bar{\mathbf{P}}$ which may not lead to sufficient entries in order to correctly represent the nonlinear terms (as $q = r \ll n$)—pointing out the most critical issue of this approach.

Recently, a novel algorithm based on DEIM procedure (called DIME) that differently determines the sampling matrix $\bar{\mathbf{P}}$ by using a QR factorization with column pivoting is considered as a third sampling method. Extensive mathematical explanations can be found in [62].

4.5   Applications

In this section, two applications are considered to illustrate the reduction in the assembly stage with the POD-MPE and POD-DEIM/DIME approaches. First, the academic inductor-core system coupled with global current is reduced by the mean of the POD-MPE method. Secondly, a three-phase current-driven transformer (also coupled with global currents) is tested with POD-MPE and POD-DEIM/DIME methods. In addition, sensitivities in the core conductivity and dependencies in current intensities are also performed to test the stability of the reduction with regards to those parameters.

4.5.1 Inductor-core system

Using the same test case configuration as described in the chapter 3 (cf. Fig. 3.1) but with nonlinear permittivity depicted in Fig. 1.1(b) and following the Brauer's law:

$$\nu(|\mathbf{b}|) = \gamma + \alpha \exp(\beta |\mathbf{b}|^2) \qquad (4.13)$$

with $\gamma = 80.47$, $\alpha = 0.05$ and $\beta = 4.21$ (from core material V330-50A), the POD-MPE approach is considered with formulation (4.8). The inductor-core system is coupled with global input current and presents 981 unknowns.

Four input currents are considered [0.1,0.4,0.7,1.0]A in order to test the reduction efficiency and accuracy (as well as its sensitivity). Supplementary, four conductivity values for the core are considered $[0,10^2,10^4,10^6]$S/m to evaluate the performance from non conductive to very conductive core material. Since the parametric reduction order modeling is not yet considered in this chapter, the POD basis used for each test case has previously been computed for the same configuration. This allows the exact analysis of the MPE approach without considering errors from resolution reductions through an inappropriate POD usage. The POD basis comprises six modes for all cases.

In [15], the authors force a minimum number of indices in the MPE process in known critical regions and interfaces (notably with respect to the sources). This constraint is set to ensure the stability of the POD-MPE equation (e.g. without any source term, the solution is trivially zero). From our point of view, the greedy algorithm should automatically detect those regions as they would present the highest contributions in the determination of the lowest condition number. To test this hypothesis, Figs. 4.1, 4.2 and 4.3 show the errors (defined as in (3.8)) when no index, indices in the coil and indices in both coil and core are forced respectively. The conclusions from those results are:

1. For certain values of q, the reduced model does not converge when the proper indices are not forced (Fig. 4.1 and 4.2).

2. When no index is forced (Fig. 4.1), reaching a small error (*i.e.* 10^{-4}) requires 6% of the original elements for all input currents—leading to an assembly reduction of $1/0.06 = 16.6$.

3. When the coil indices are forced (Fig 4.2), the convergence is better with stabilized small error before 5% of the original number of elements—leading to an assembly reduction of 20.

4. When the coil and core indices are forced (Fig. 4.3), the results are way better than previously. The convergence rate is faster at a small relative error below 10^{-4} with roughly 3% of original elements—leading to an assembly reduction of 33.

5. Whatever the conductivity values or the input currents, the MPE reduction is fairly uniform with similar results throughout all experiments.

Even though forcing some (important) indices improves the results by lowering the relative errors, the observation is not as significant as expected or explained in [15]. The
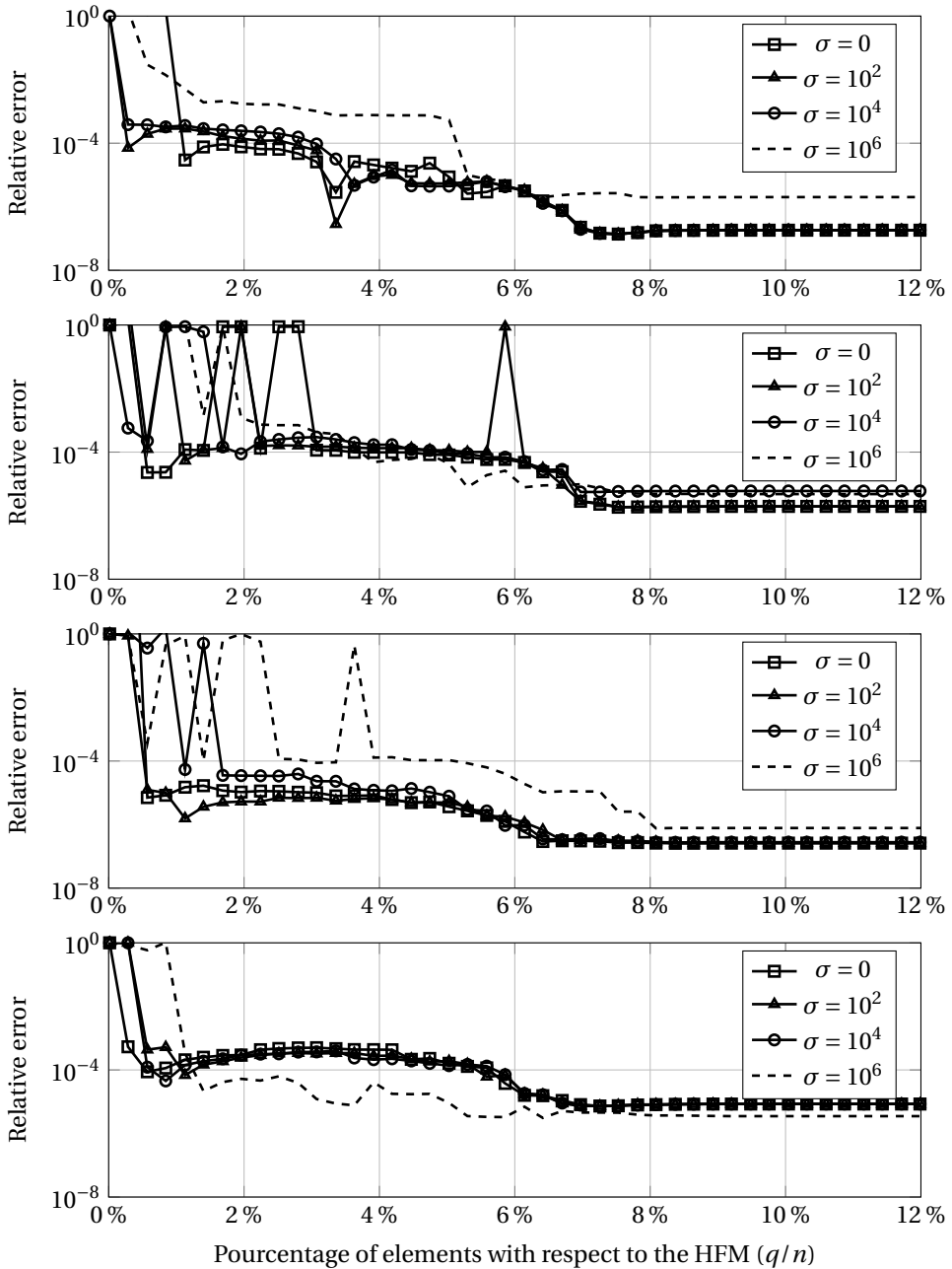
Figure 4.1: Relative errors of POD-MPE model of inductor-core system vs MPE size for different values of the core conductivity σ with input current 0.1, 0.4, 0.7 and 1.0A (from top to bottom). No forced indices.
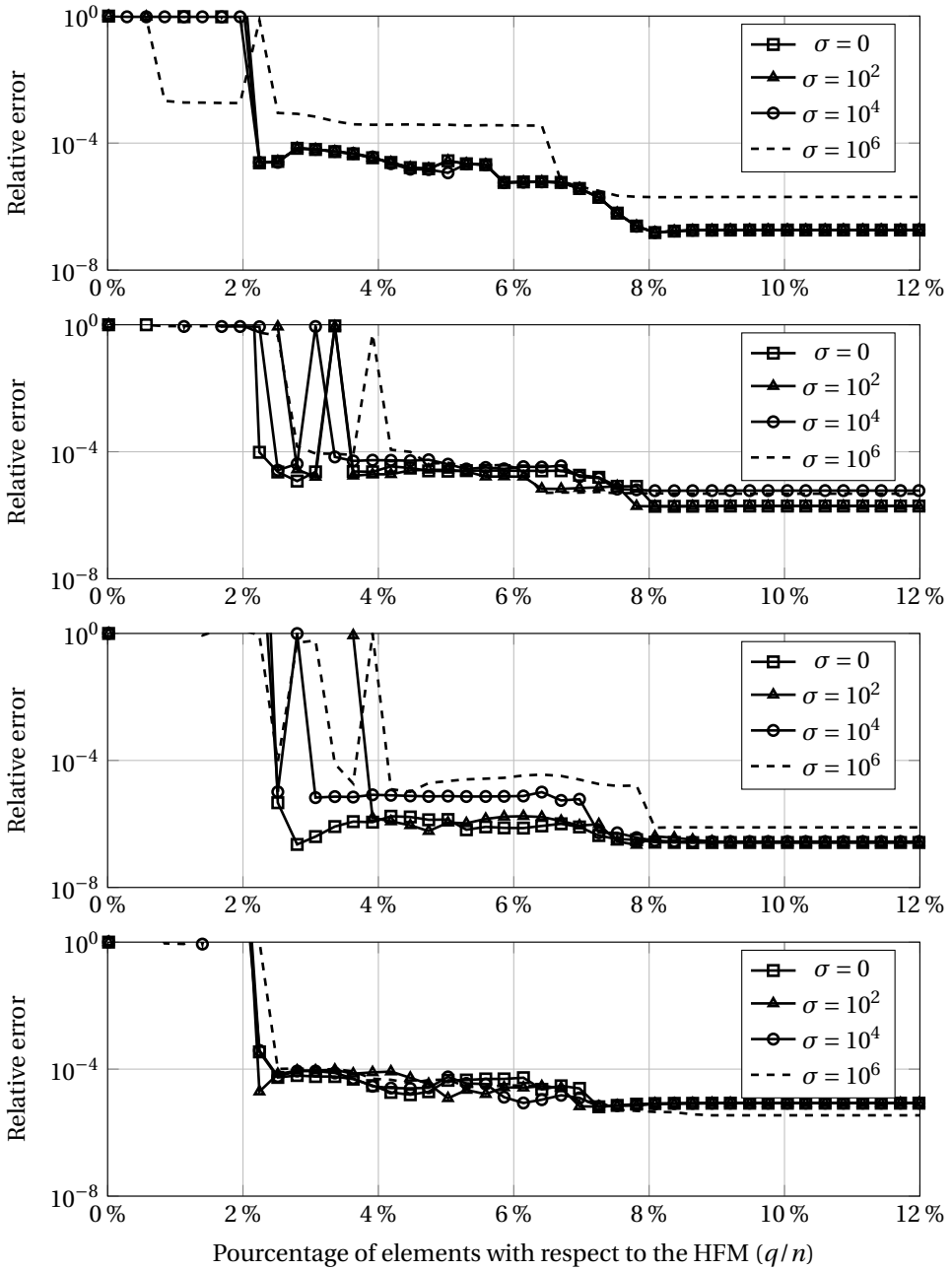
Figure 4.2: Relative errors of POD-MPE model of inductor-core system vs MPE size for different values of the core conductivity σ with input current 0.1, 0.4, 0.7 and 1.0A (from top to bottom). Coil indices are forced.
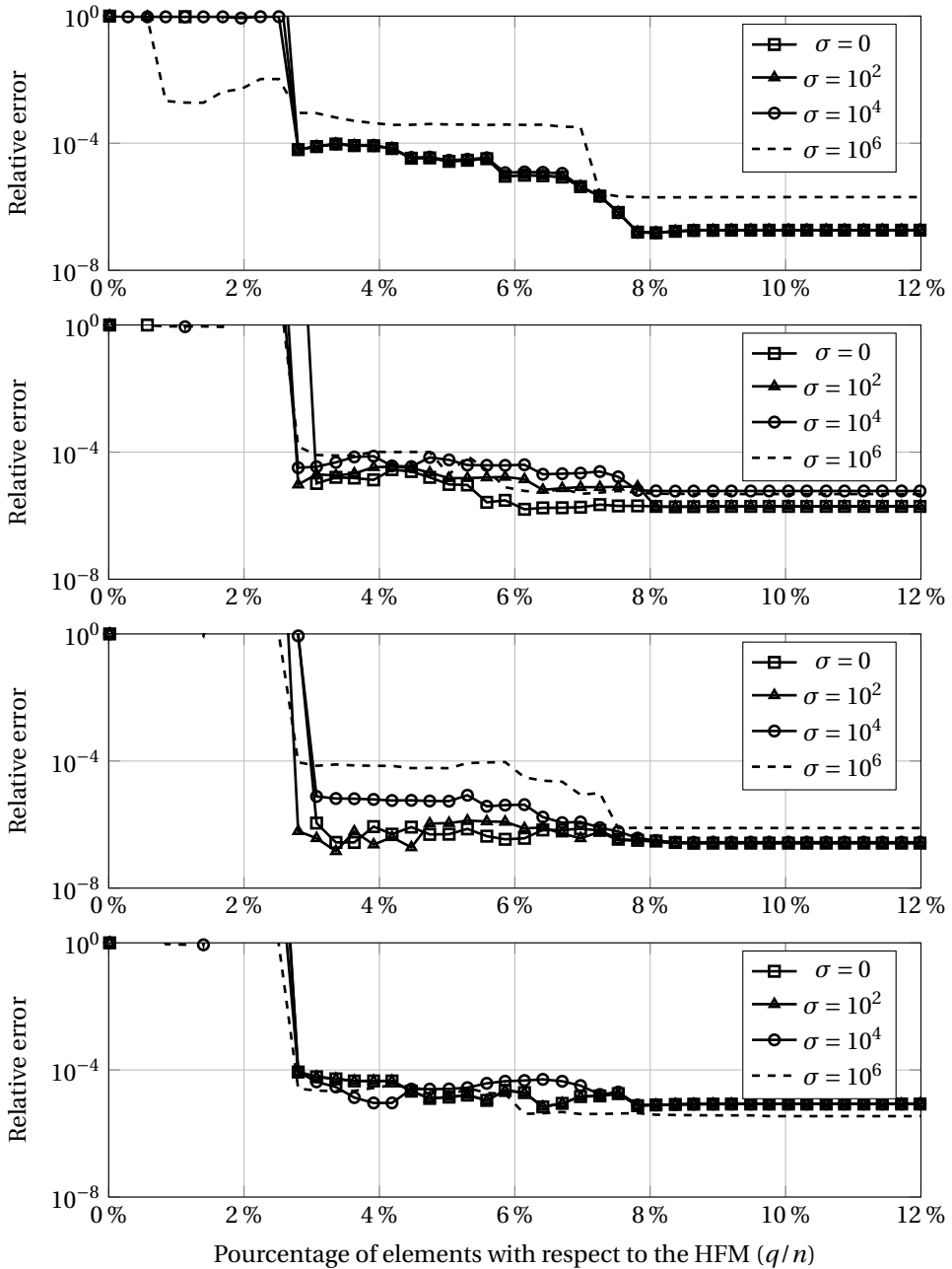
Figure 4.3: Relative errors of POD-MPE model of inductor-core system vs MPE size for different values of the core conductivity σ with input current 0.1, 0.4, 0.7 and 1.0A (from top to bottom). Coil and core indices are forced.
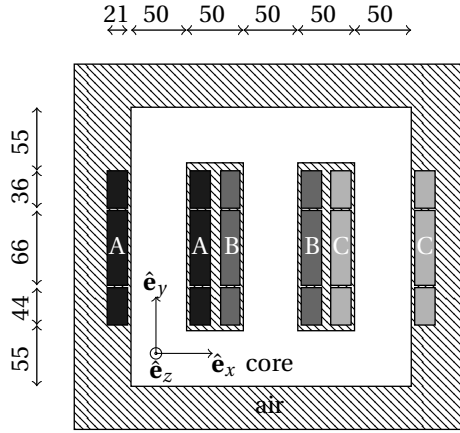
Figure 4.4: FE model of the 3-phase transformer. Description in Table 4.1. Dimensions in mm. [90]

automatic determination of the MPE points without forcing remains a valid approach in our experience.

4.5.2 Current-driven three-phase power transformer

As a more complex and realistic test case, a three-phase transformer is considered and depicted in Fig. 4.4 and Table 4.1. It contains one three-phased input in star configuration and two three-phased outputs (one in star and one in triangle configurations). The model has $n = 7300$ unknowns and is simulated at no load (similar to the inductor-core system). Without conductivity (non-conductive behavior), the nonlinear reluctivity follows the same Brauer's law as in (4.13). Here, as the core conductivity is also considered non zero (conductive behavior) for a laminated iron core, the constitutive law (1.2) is modified accordingly to [91] as

$$\mathbf{h} = \nu(|\mathbf{b}|)\mathbf{b} + \frac{d^2}{12}\sigma\partial_t\mathbf{b}, \tag{4.14}$$

where $d = 0.5$mm is the thickness of the laminations and $\sigma = 2\cdot10^7$S/m is the conductivity of iron. As with the academic inductor-core system, a single period at 50Hz (T=20ms) with N_t=20 time steps is considered with input current

$$\mathbf{I} = (-1)^\eta I_{peak}\cos(2\pi f t + \varphi_i)\hat{\mathbf{e}}_z \tag{4.15}$$

where $\eta = 0$ (resp. $\eta = 1$) for left (resp. right) part of the coil (representing the direction of the current), $I_{peak} \in [0.1, 0.3]$ A is the input peak current ($I_{peak} = 0.1$ A induces linear magnetic behaviour whereas $I_{peak} = 0.3$ A causes the core to saturate).

Table 4.1: Subdomains of the 3-phase transformer in Fig.4.4.

Domain	Region	Legend in Fig.4.4
$\Omega_c^{nl} \setminus \Omega_j$	core (if $\sigma \neq 0$)	white
Ω_{cc}^{l}	air	stripped
Ω_{cc}^{nl}	core (if $\sigma = 0$)	white
Ω_j	windings	filled
Phase	Delay φ_i [rad]	Legend in Fig.4.4
A	0	black
B	$4\pi/3$	gray
C	$2\pi/3$	light gray

Resolution reduction - POD   First, in order to verify that the POD can efficiently reduce this three-phase transformer, one has to observe the singular value decay. Given an input current of 0.25A, a single POD basis can achieve a small relative error (*i.e.* below 2%) for all input currents as it can be seen in Fig. 4.6(up) with the singular values depicted in Fig. 4.5. The POD basis is truncated after the 11 first modes to respect an a-priori error of 10^{-15} and leads to a theoretical speedup between 663 and 440000 [106, 107]. In Fig. 4.6(down) is shown the POD relative error for different core conductivities when using a basis generated with a core conductivity of 1S/m. As explained in [150], changing the conductivity modifies the distribution of the eddy currents that will prevent the use of a single basis. Therefore, the POD bases are generated with the same conductivity value than those of the (tested) reduced configurations.

Assembly reduction - DEIM/DIME   As explained in section 4.4, the choice of nonlinear snapshots may be crucial for the application of the DEIM. From our experiment, taking the residuals $\mathbf{r}(\mathbf{x})$ at different time instants as snapshots would not lead to appropriate DEIM projection basis as the singular values do not decrease as expected (see Fig. 4.5). Indeed, two possibilities are offered:

1. By taking the converged residuals, no correlation between them is expected as they should be as minimum as possible—leading to no proper reduced basis.

2. Taking all non-converged residuals would lead to a way greater snapshot matrix—leading to potential computational and storage issues.

As a consequence, the original full size solutions $\mathbf{X}$ are considered as snapshots for the DEIM method. However, the method considering the residuals as snapshots may be worth investigating and comparing with the proposed one (taking the solutions as snapshots). In [99], the POD-DEIM approach efficiently reduces a static 3D transformer with a relative error of 4% by considering 55 DEIM edges (representing 0.5% of the original number of nodes). Here, considering a conductive core directly impacts the stability of the POD-DEIM model as it becomes more and more dependent on *a priori* independent parameters (*i.e.* the number of time steps per period or the conductivity values) [140, 192]. As an alternative, the DIME algorithm is also investigated. However, similar results are observed in this eddy current problem ($I = 0.3A$ and
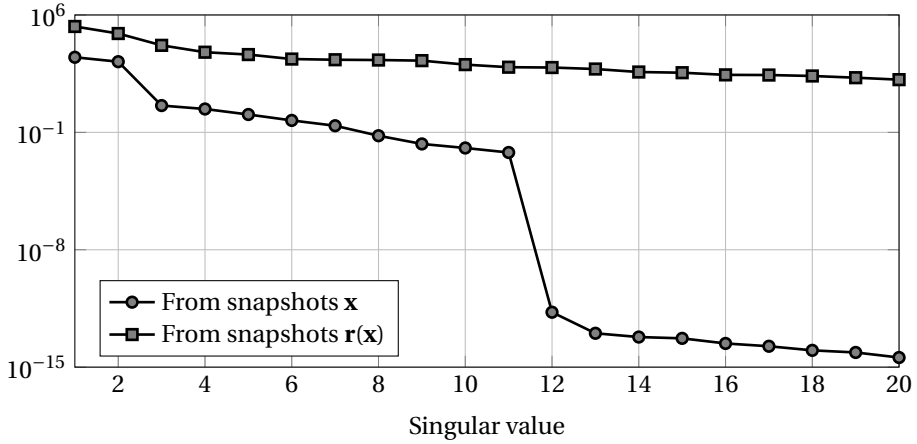
Figure 4.5: Singular values of snapshot matrices of **X** and right hand side **r(x)**.

$\sigma = 2 \cdot 10^7 \mathrm{S/m}$). These issues are depicted in Fig. 4.7 where the change in the number of time steps highly impacts the relative errors obtained with both POD-DEIM and POD-DIME models—whereas the POD-MPE method allows a quasi constant relative error. In Fig. 4.7(top) the basis for the DEIM/DIME algorithm is truncated to the 25 first modes—following the general truncation methodology as in POD. In Fig. 4.7(bottom), the basis for the DEIM algorithm is not truncated (in order to catch a sufficiently large number of elements in the FE assembly stage) and has consequently the same number of modes as the number of time steps. One would have expected better results in this second scenario with a bigger size for the basis. Considering more than 90 time steps per period does not influence the results. Due to these oscillations, the DEIM/DIME is not considered for further developments and applications.

Assembly reduction - MPE   Concerning the POD-MPE model, Fig. 4.7 shows a quasi-constant relative error with respect to the number of time steps per period (as expected). Similar results were obtained by varying the number of periods or the core conductivity values. Four scenarios are considered for the application of the POD-MPE approach. Either small ($I = 0.1$A) or large ($I = 0.3$A) current values and either no conductivity ($\sigma = 0$) or laminated iron core configuration ($\sigma = 2 \cdot 10^7 \mathrm{S/m}$). The condition numbers of covariance matrix of sampled projection basis **Q̄**–as the criterion of the MPE algorithm–are shown in Fig. 4.8(up) with an extremely fast decay to one. However, in this case, the relative error (depicted in Fig. 4.8(bottom)) with respect to the MPE size seems to be independent to this criterion. Indeed, a relative error of 0.1% is reached for a MPE sampling size q in the range [50,350] according to the configuration (core conductivity and input current intensity). Now, by applying the POD-MPE approach, the magneto-dynamic problem is solved with 11 unknowns through the application of the POD by only considering and assembling 350 elements/rows in the FE matrices (in case of the worst scenario) by the MPE sampling—leading to significant assembly reduction ratios between 99% and 95% compared to the original 7300 unknowns. Similarly to the global
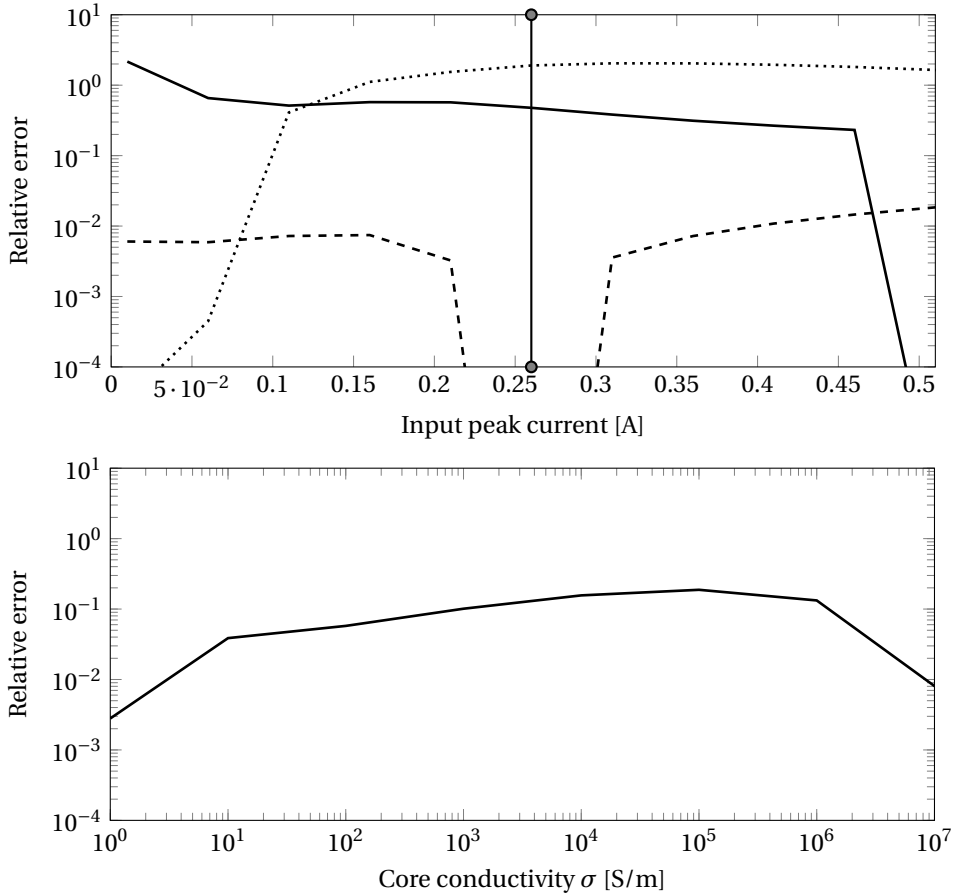
Figure 4.6: (Top) Relative error of POD model according to input peak current (basis generated with input current $I = 0.01$ A (dotted line), 0.25 A (dashed line), 0.5 A (solid line)). The vertical line represents the transition between linear and nonlinear regimes. (Bottom) Relative error of POD model according to core conductivity (basis generated with $\sigma = 1$ S/m).
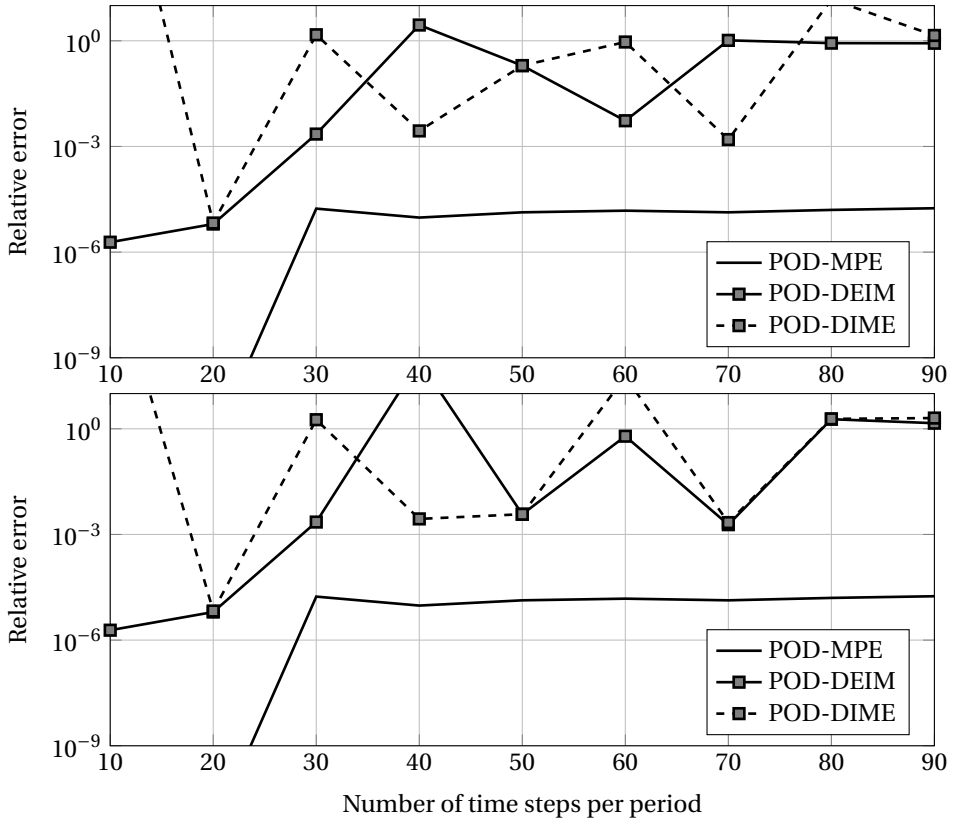
Figure 4.7: (Top) Relative errors with truncated basis (25 modes). (Bottom) Relative errors with untruncated basis.

quantities, the local fields (*i.e.* the magnetic flux density **b**) present small errors and are depicted in Fig. 4.9 for the four different configurations, i.e. $I = 0.1$ A (top) - $I = 0.3$ A (middle) and $\sigma = 0$ S/m (left) - $\sigma = 2 \cdot 10^7$ S/m (right) as well as the 50 first MPE selected points (bottom).

4.6 Conclusion

In this chapter, the combined approach of the POD and the MPE has been presented to efficiently and drastically reduce both nonlinear static and eddy current models of an inductor-core system and a three-phase current-driven power transformer. However, as illustrated with the transformer, the MPE condition number may not be the best criterion to predict the error of the sampled reduced model as it seems uncorrelated with the obtained results.

On the other hand, the combined POD-DEIM/DIME approach failed to reduce robustly the three-phase transformer as its stability becomes parameter-depend on the
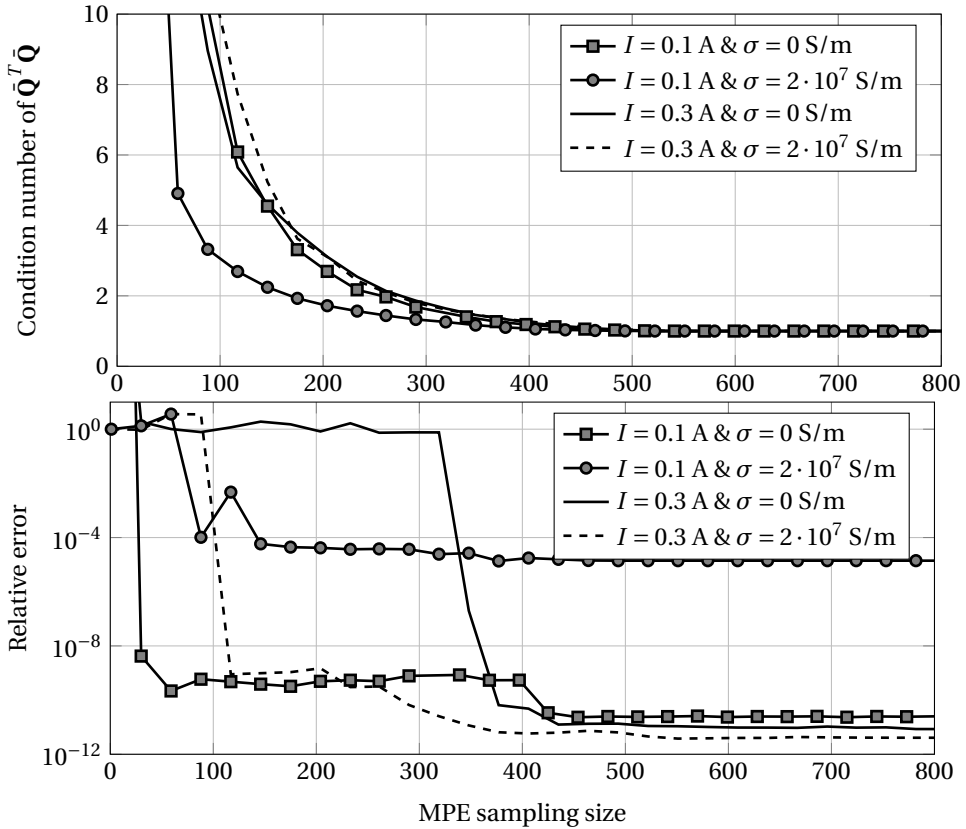
Figure 4.8: (Top) Condition number of the MPE selection process. (Bottom) Relative error of POD-MPE model of 3-phase current-fed transformer compared to HFM.

dynamic situation.

The POD-MPE approach is the preferred one for the coupling of nonlinear energy conversion devices with electric circuits such as presented in chapter 6. In addition, the important reduction ratios, above 95%, in the three-phase transformer are encouraging for the next test case involving electric network coupling in chapter 6.
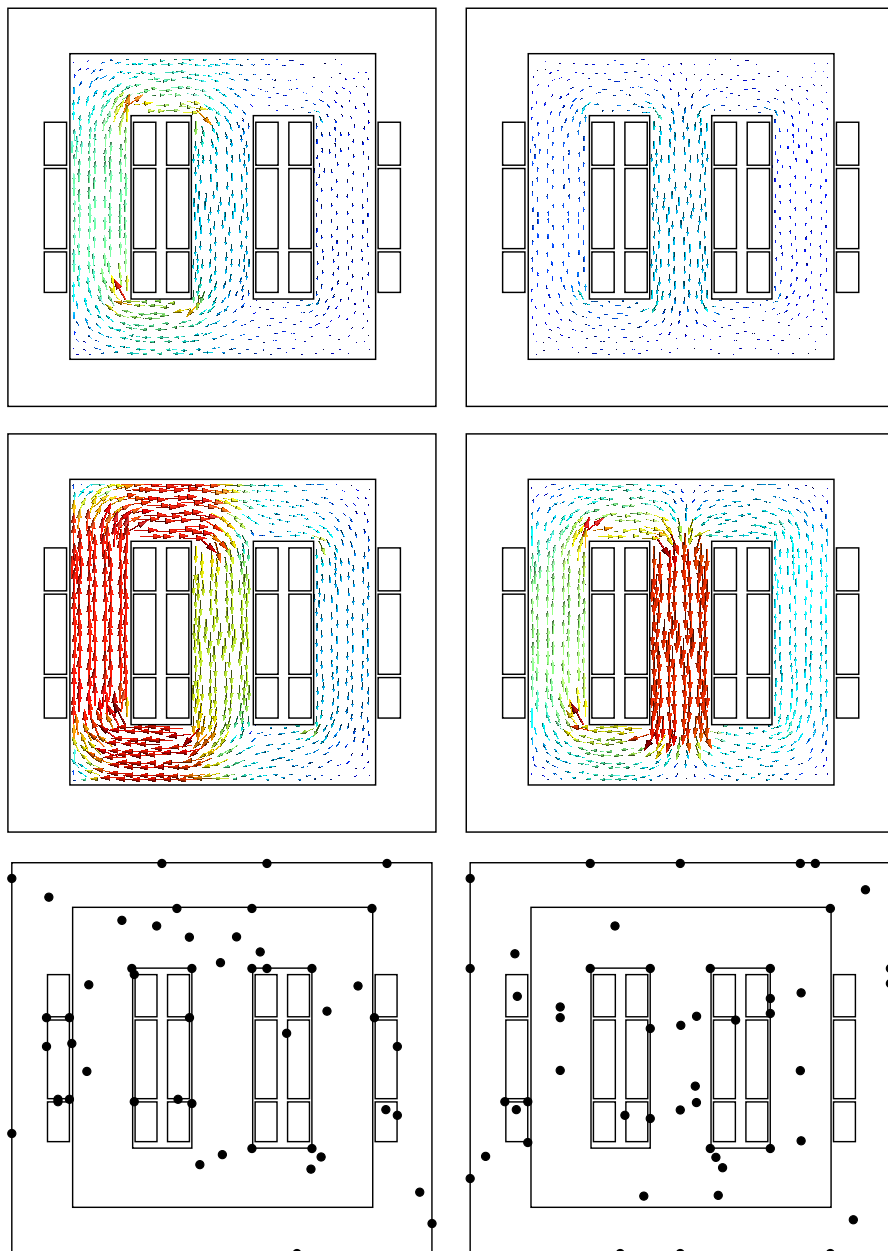
Figure 4.9: 20th time step of induction field for input current $I = 0.1$ A (top) - $I = 0.3$ A (middle) and core conductivity $\sigma = 0$ S/m (left) - $\sigma = 2 \cdot 10^7$ S/m (right). Legend : linear scale from 0 T (blue-small arrows) to 1.52 T (red-large arrows) . 50 first MPE points (bottom).

Nonlinear parametrised problems

5.1 Introduction

Creating reduced order models for given sets of parameter values for which they have been pre-computed is a great achievement, but creating reduced order models for multiple parameter values and being able to deal with parametrized problems is of greater interest.

In this chapter, nonlinear parametrized magnetodynamic problems are studied in the context of model order reduction to develop more generic reduced order models.

Two methodologies are presented. The first one consists in building a single basis for all values within the parameter values while the second one is based on the interpolation of multiple reduced bases created from different trainings (comprising different parameter values). This latter approach follows the principle of the interpolation on manifolds.

To illustrate those theories onto nonlinear parametrized problems, the academic inductor-core system is considered with different parameters as the intensity and the frequency of the input current.

5.2 Parameter sampling

Regarding the reduced order modeling techniques, the manner the parameter space is sampled is critical, e.g. using the POD, snapshots must be computed for appropriate sampled parameter values. In case of small number of parameters, a random or structured sampling may be sufficient (*i.e.* Latin hypercube or grid-based sampling). They constitute the simplest approach that will produce a rich and large dataset by covering the entire parameter space. When the number of parameters increases, those methods may lead to very large number of high fidelity simulations as the number of samples in a regular grid grows exponentially with the number of parameters. In case the number of parameters is very large, the number of points in the grid is intractable and more complex sampling methods have to be used, such as greedy adaptive search methods

[24, 40, 93], adaptive parameter sampling based on local sensitivity analysis [30] or optimal interpolation points [21] (only in the case there exists an affine parameter dependency in **B** and **C** and no dependency in **A** and **E** in general state-space formulation (2.1)).

In this dissertation, a small number of parameters is considered as they consist in the values that external excitations can have onto the magnetodynamic devices—in contrast with material values (e.g. permittivity, conductivity, ...) and shape parameters (e.g. geometrical dimensions) that are common in optimization processes and which can lead to large parameter spaces. To this end, a regular grid sampling is performed in the considered parameter space.

5.3   Parametrized reduced order model generation

In this section, based on the general description in section 2.3.2, the two different strategies for generating parametrized ROMs are detailed. Those philosophies are applicable (to our knowledge) with any of the reduction methods (especially those presented in chapter 2).

First, in section 5.3.1 is presented the generation of a single basis for POD reduced model of nonlinear magnetodynamic formulation (4.1). Then, in section 5.3.2, the multiple bases generation and manifold interpolation are detailed.

In further sections, the D parameters will be denoted by **p** which belongs to the unique domain $\Omega_p \in \mathbb{R}^D$. Recently, [9, 63, 70, 94, 154, 203] proposed to divide the parameter space Ω_p into multiple sub-domains to construct local bases. However, the two presented generation strategies remain valid within any partitioning of Ω_p.

5.3.1   Single basis model

From general nonlinear magnetodynamic equation (4.1), a global basis is determined by a unique projection matrix **Q** which is obtained by sampling the parameter space.

In the general case where the matrices **M**, **S** and **v** depend on the parameters **p**, the obtained ROM is inefficient and the computational gain (compared to the HFM) is mostly lost. Indeed, such problems are similar to the one exposed in chapter 4 and require sampling approaches such as the DEIM or MPE methods. However, in case of affine dependency, one can write

$$\mathbf{M}(\mathbf{p}) = \sum_i^k c_i(\mathbf{p})\mathbf{M}_i \tag{5.1}$$

where $\mathbf{M}_i$ does not depend on the parameters and $c_i(\mathbf{p})$ are general functions of **p**. Then, the reduced matrix $\tilde{\mathbf{M}}$ can be efficiently computed for all parameter values as

$$\tilde{\mathbf{M}}(\mathbf{p}) = \sum_i^k c_i(\mathbf{p})\underbrace{\mathbf{Q}^T\mathbf{M}_i\mathbf{Q}}_{\tilde{\mathbf{M}}_i} \tag{5.2}$$

and $\tilde{\mathbf{M}}_i$ are precomputed once.

In this dissertation, only the right hand side **y** is parameter-dependent—allowing the pre-computation of all other matrices. However, the projected (reduced) matrices still have to be adequately represented in the reduced subspace when a parameter change induces the solution to change (drastically). Two common methodologies to capture all the information related to the parameter space can be derived:

1. The global basis **Q** consists in the concatenation of local bases (*i.e.* $\mathbf{Q}^i$, $i = 1, \cdots, P$) generated for the P sampled parameter values (*i.e.* $\mathbf{p}^i$, $i = 1, \cdots, P$) such as

$$\mathbf{Q} = \left[\mathbf{Q}^1, \cdots, \mathbf{Q}^P \right]. \tag{5.3}$$

   But doing so, the resulting global basis may include redundant information due to potential similar local bases. One may perform an SVD [81] on **Q** to solve this issue.

2. The second manner intrinsically solves the aforementioned problem as the global basis **Q** is obtained from the SVD [81] of the concatenation of snapshots obtained for the sampled parameter values—such as

$$\mathbf{X} = \left[\mathbf{x}_1^1, \cdots, \mathbf{x}_{N_t}^1, \mathbf{x}_1^2, \cdots, \mathbf{x}_{N_t}^P \right], \tag{5.4}$$
$$\mathbf{Q} = \text{SVD}(\mathbf{X}). \tag{5.5}$$

   where $\mathbf{x}_k^p$ is the solution at time instant t_k with parameter values $\mathbf{p}^p$. Compared to the generation of the local bases in the first methodology from local snapshot matrices, the matrix **X** is importantly larger. However, all the snapshots have to be computed in both cases and performing the SVD directly on them is not more computationally expensive. An additional advantage consists in the observation of the singular values for all the snapshots in order to measure the extent the global parametrized model can be reduced onto a global POD basis. With this method, the standard POD *a priori* error criterion remains valid. Therefore, this latter approach is considered in this work.

5.3.2 Multiple bases model

Instead of constructing a single basis which is valid for all parameter values, one can consider generating multiple local bases (*i.e.* $\mathbf{Q}^i$, $i = 1, \cdots, P$) for the P sampled parameter values (*i.e.* $\mathbf{p}^i$, $i = 1, \cdots, P$) and interpolating them in case of a simulation involving a new (unexplored) parameter set $\mathbf{p}^* \in \Omega_p$.

Straightforward interpolation (*i.e.* Lagrange) of reduced bases may lead to an invalid basis. Let us consider the simple case with two local bases such as one is the opposite of the other (*i.e.* $\mathbf{Q}^1 = -\mathbf{Q}^2$) and new parameter is in the middle of respective parameter sets $\mathbf{p}^1$ and $\mathbf{p}^2$, then the interpolated quantity will be zero (which is not a basis). Therefore, one must not interpolate the bases directly but their underlying subspaces. To this end, the interpolation of such subspaces thanks to a projection onto a tangent space of the underlying manifold structure has been highlighted in [5]. Contrary to the straightforward interpolation among the bases that does not preserve the desired properties of the bases, the manifold structure does. As a note, one may observe that

the representation of a basis may be independent of the choice of coordinate representation as the importance is given to the subspace that is spanned by this basis. In [4], the definition of the Grassmann manifold is provided and matches the one of the projection bases detailed in section 2. Indeed, the Grassmann manifold $\mathcal{G}_{n,r}$ is the set of all r-dimensional subspaces of $\mathbb{R}^n$. As a particular case, the Stiefel manifold $\mathcal{S}_{n,r}$ is defined as the set of all r-dimensional orthonormal bases of $\mathbb{R}^n$, and correspond to the definition of a POD reduced basis. For the sake of generality, the interpolation on the Grassmann manifold is considered and further developed in this research. For more details, see [4].

   The procedure is described hereafter and is illustrated in Fig. 5.1:

1. Define a reference point. Let define $\mathcal{Q}^p$ the span of basis $\mathbf{Q}^p$ obtained with the parameter values $\mathbf{p}^p$. By definition, $\mathcal{Q}^p \in \mathcal{G}_{n,r}$. Let us consider $\mathcal{Q}^1$ as the reference point. Here, a tangent space $\mathcal{T}_\mathcal{S}(\mathcal{Q}^1)$ to the manifold $\mathcal{G}_{n,r}$ at $\mathcal{Q}^1$ can be defined.

2. Let us define $\mathcal{R}^p$ as the projection of $\mathcal{Q}^p$ for $p = 1, \cdots, P$ onto $\mathcal{T}_\mathcal{S}(\mathcal{Q}^1)$ using the logarithmic mapping

$$\mathcal{R}^p = \mathrm{Log}_{\mathcal{Q}^1}(\mathcal{Q}^p) \in \mathcal{T}_\mathcal{S}(\mathcal{Q}^1). \tag{5.6}$$

   In matrix form, the logarithm map on $\mathcal{G}_{n,r}$ is defined as

$$(\mathbf{I} - \mathbf{Q}^1\mathbf{Q}^{1,T})\mathbf{Q}^p\left(\mathbf{Q}^{1,T}\mathbf{Q}^1\right)^{-1} = \mathbf{U}^p\mathbf{\Sigma}^p\mathbf{V}^{p,T}, \tag{5.7}$$

$$\mathbf{R}^p = \mathbf{U}^p\tan^{-1}(\mathbf{\Sigma}^p)\mathbf{V}^{p,T}. \tag{5.8}$$

3. As all $\mathcal{R}^p$ lie onto the Euclidean space $\mathcal{T}_\mathcal{S}(\mathcal{Q}^1)$, an interpolation method (e.g. Lagrange) can be used to determine the matrix $\mathbf{R}^*$ that would have been obtained from the projection onto that space of the subspace $\mathcal{Q}^*$ spanned by the basis $\mathbf{Q}^*$ generated for a new parameter set $\mathbf{p}^*$. Thus,

$$\mathbf{R}^* = \sum_i^P l_i(\mathbf{p}^*)\mathbf{R}^i \tag{5.9}$$

   with $l_i(\mathbf{p}^*)$ the Lagrange coefficients. Now, $\mathbf{R}^*$ spans the subspace $\mathcal{R}^* \in \mathcal{T}_\mathcal{S}$.

4. Project subspace $\mathcal{R}^*$ back onto the manifold in $\mathcal{Q}^*$ using the exponential mapping

$$\mathcal{Q}^* = \mathrm{Exp}_{\mathcal{Q}^1}(\mathcal{R}^*) \in \mathcal{G}_{n,r}. \tag{5.10}$$

   In matrix form, the exponential map is obtained as

$$\mathbf{R}^* = \mathbf{U}^*\mathbf{\Sigma}^*\mathbf{V}^{p^*,T}, \tag{5.11}$$

$$\mathbf{Q}^* = \mathbf{Q}^1\mathbf{V}^{p^*,T}\cos(\mathbf{\Sigma}^*) + \mathbf{U}^*\sin(\mathbf{\Sigma}^*). \tag{5.12}$$

   where the interpolated basis $\mathbf{Q}^*$ spans $\mathcal{Q}^*$.

Considering this approach to determine the projection basis for any parameter values still requires the projection of the system original full size matrices (e.g. $\mathbf{M}$) onto it. In case of numerous changes in the parameter space requiring as many interpolations,
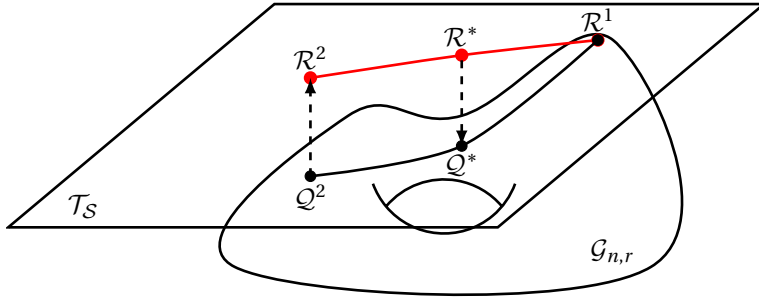
Figure 5.1: Interpolation of $\mathbf{Q}^*$ from $\mathbf{Q}^1$ and $\mathbf{Q}^2$ on the Grassmann manifold by considering $\mathbf{Q}^1$ as the reference point.

a significant time and computational resources may be lost in that operation. To overcome this issue, another approach would consists in interpolating the reduced matrices directly instead of the reduced bases. This philosophy has been investigated in [6, 7, 58, 130, 147] and mainly consists in determining a consistent representation of the reduced bases among all the parameters. This allows direct interpolation or manifold interpolation of the reduced matrices. This method has not been investigated in this dissertation (which may be one of the future works).

5.4   Application to a parametrized inductor-core system

In this section, the previously described academic inductor-core system is considered. The POD reduced nonlinear magnetodynamic formulation (4.4) without sampling method is used to highlight the choice of the POD basis. Two parameters are considered: the intensity and the frequency of the input current. This work has previously been published in [149, 150].

Input current intensity   In the first scenario where the intensity of the input current can be different than the one used to generate the POD basis, a single basis trained with the highest input current is sufficient to achieve very small error ($< 0.1\%$). Actually, the global training is inherent to the application of a sinusoidal input current (see equation (3.6)). Indeed, as the range of the sine function is $[-1, 1]$, the input current ranges in $[-I_{peak}, I_{peak}]$A. This type of excitation naturally performs a sampling in the parameter space for all lower values thanks to the time discretisation. In particular, when the basis is trained without a sufficiently high current (to enter in saturation), the reduced model cannot achieve a small error ($> 10\%$ are commonly observable). This observation is quite logical as the POD basis has only explored the linear behavior and does not have the information regarding the saturation states. As a conclusion, two observations can be derived:

1. The global basis is directly obtained by only simulating the HFM with the highest input current (peak value).

2. The choice of the training is crucial to retrieve maximum information and limit the number of high fidelity computations.

Input current frequency   As a second test case presenting different observations, the frequency of the input current is considered as a parameter and can be changed from the training stage to the online computations. This choice is interesting as it will directly impact the shape of eddy current distribution—*a priori* limiting the use of a single POD basis which spatially describes the fields at a given frequency.

First, to confirm the need of multiple POD bases in this example, let analyze the relative errors obtained with a single POD basis generated at a unique frequency over the frequency range [1,16000]Hz (see Fig. 5.2). Here, four results are depicted when the POD basis is generated at 15, 150, 1000 and 16000 Hz respectively and then use over the entire frequency range. Except for the same particular frequency where the relative error is small (as expected), all others are important with majority of them above 100%. This illustrates that the use of a single POD basis generated at a given frequency cannot be considered (to achieve small errors) for any another frequency. As the previous range may be very large, two detailed analyses are performed at 50 and 350Hz. In Fig. 5.3 is shown the same result as in Fig. 5.2 when the POD basis is generated at 50Hz. Contrary to the prior results, the POD basis can be used for another frequency as far as it is relatively close to the one used for the basis generation (e.g. 1% relative error remains achievable within a 30Hz difference). This means that a POD basis has to be computed each 60Hz. This limitation may be sufficient in real application but one may be interested in larger frequency bands—which prohibits the use of single POD basis. As the frequency range increases, the global basis and interpolation method are analyzed to limit the number of bases generation. In Fig. 5.4 are shown the relative error obtained at 50Hz with three approaches that combine the information retrieved at two neighbor frequencies. The global basis method concatenates the snapshots taken at (50-x) and (50+x) Hz (with x the distance between the frequencies and 50Hz), performs an SVD and truncates the basis respecting an *a priori* error of 10^{-15}. The Grassmann method follows the procedure described in section 5.3.2 with the POD bases generated at (50-x) and (50+x)Hz. Lastly, Lagrange method is tested to illustrate the incoherent results that are obtained from direct interpolation of the bases without taking into account the manifold theory. Naturally, the Lagrange method provides erroneous results and should not be taken as a valid approach. It is considered as illustrative in further results. One can see that the global POD basis is always better than the Grassmann interpolation with a maximum relative error of $2 \cdot 10^{-4}$ by combining the snapshots from 20 and 80Hz instead of 10^{-3} for the manifold interpolation. Two conclusions can be drawn:

1. By generating the POD bases each 60Hz as in the direct use of the POD basis, this method divides the relative error by 100.

2. By keeping the relative error criterion to 1%, the number of POD bases can be lowered—reducing the computational resolutions of HFMs[1].

---

[1]A precise value of the sampling number cannot be given due to the limited frequency analysis made in this work.
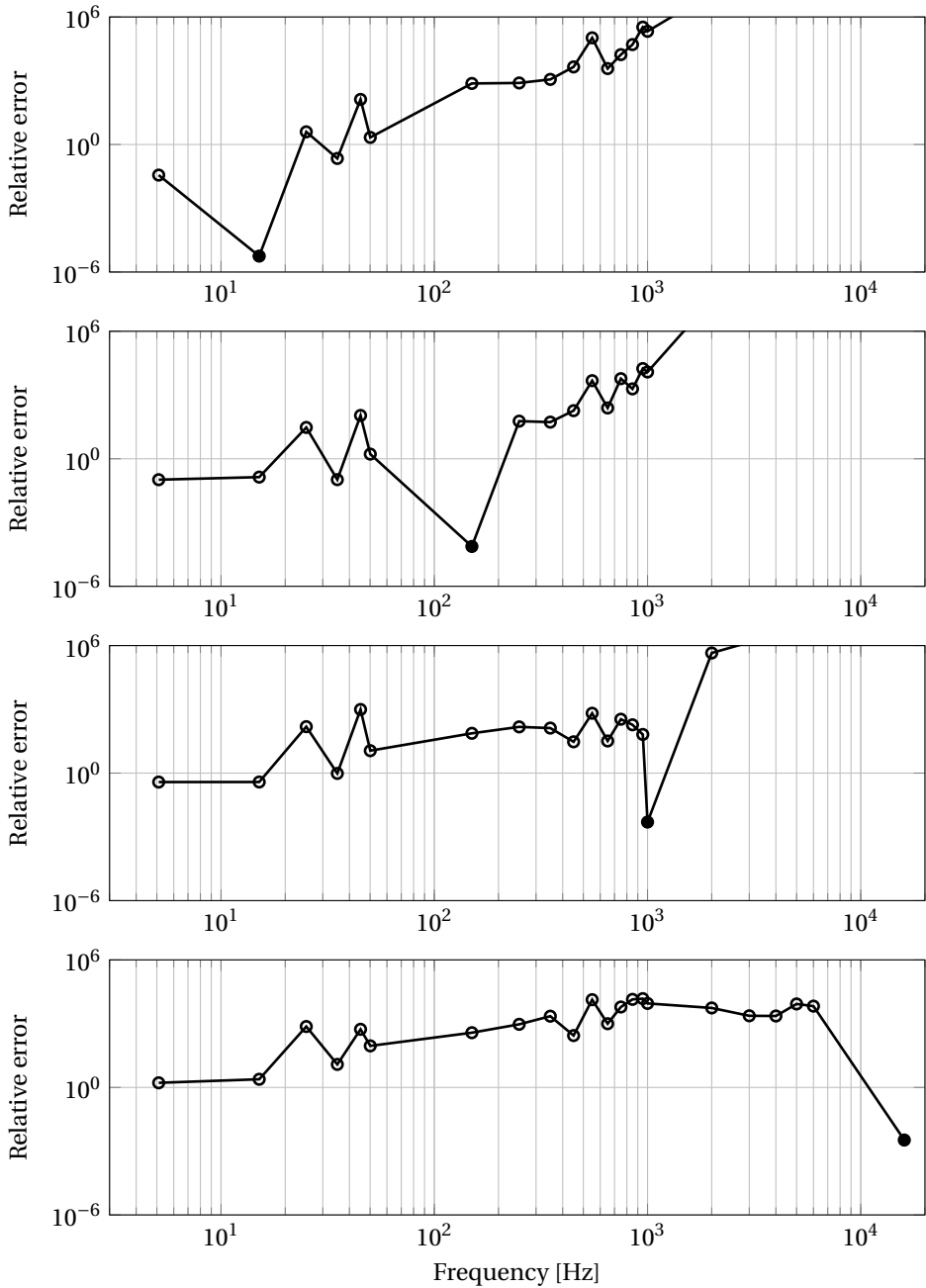
Figure 5.2: Relative errors of ROMs according to the frequency with the POD basis generated at frequency=15, 150, 1000, 16000Hz (from top to bottom). Filled circles correspond to the ROMs at same frequency than the one used for the construction of POD basis.
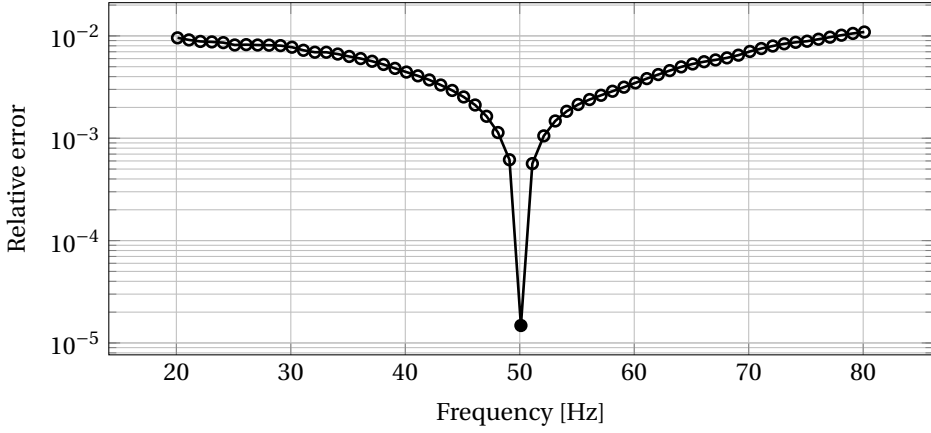
Figure 5.3: Relative error of ROMs according to the frequency with the POD basis generated at frequency=50Hz. Filled circle corresponds to the ROM at same frequency than the one used for the construction of POD basis.
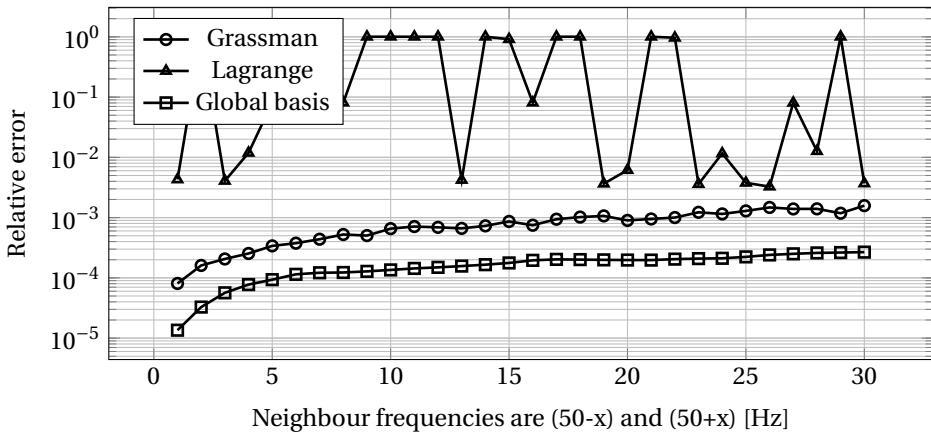
Figure 5.4: Relative errors of ROMs using Grassman or Lagrange interpolation with two bases generated at frequencies (50-x) and (50+x) Hz and global basis from snapshots at same frequencies.

Instead of moving the left and right "neighbours" at the same time, Fig. 5.5 shows the relative errors at 50Hz when the left frequency is fixed while the right one is changing for the generation of the local bases (or the snapshots for the global basis). From top to bottom, the left frequency is fixed at 20, 30, 40 and 49Hz. The right frequency is given by the x-axis. The results show the global POD basis remains a better suited approach then the Grassmann interpolation (for the considered frequency range). Logically, the errors lower when the left frequency get closer to 50Hz but not significantly. This is the main insight of these results. Indeed, if the error would have literally dropped instead of the slow decay, the previous results (with left and right neighbours generated at equidistant of the frequency of interest) would not be sufficient to limit the sampling of the POD bases. Here, as the relative error with the global basis is only divided by 3 (with right frequency at 51Hz) and 10 (with right frequency at 80Hz), increasing the number of POD would not significantly improve the relative errors. It is worth mentioning that contrary to the results from the global basis, the errors made by the Grassmann manifold interpolation flatten to the error at 51Hz when the left frequency is increased (no decrease as with the global basis is observed). This insight is quite logical since the projections of the bases (from 20 to 49Hz) become more and more equivalent to the projection of the basis at 51Hz and therefore set the same reference tangent space for all upper frequencies.

As another test case, the frequency 350Hz is considered. Similar results and conclusions can be made from the results in Fig. 5.6 (direct use of single POD basis generated at 350Hz), Fig. 5.7 with left and right frequencies at equidistant of 350Hz and Fig. 5.8 (with fixed left frequencies at 320, 330, 340 and 349Hz). However, the global basis gives even better results than the Grassmann manifold interpolation even though the relative errors are smaller than in the 50Hz case. This second example demonstrates the coherence of the results for two different frequency tests.

5.5 Conclusion

Dealing with parametric models, either at design or operational stages, is crucial for modern applications. Defining a corresponding accurate reduced model (or multiple of them) is the next question to answer. In this chapter, two methodologies to construct POD reduced model of nonlinear magnetodynamic inductor-core system are presented: the first one deals with a global reduced model whereas the second is based on the interpolation of multiple bases using manifold theory.

The results show great interest of those methods as the direct use of a single POD basis is limited to a tiny region in the parameter space. However, as certain parameters are inherently linked to appropriate training of the POD basis, such a proper procedure is therefore sufficient to accurately gather all required information.

Here, by considering a change in the frequency of the input current (leading to drastic change in the eddy current distribution), the global basis approach always provides better results than the methods that interpolate two bases. For that reason, this approach is preferred when the model only deals with a small number of parameters—allowing the generation of a single basis based on all trained snapshots.
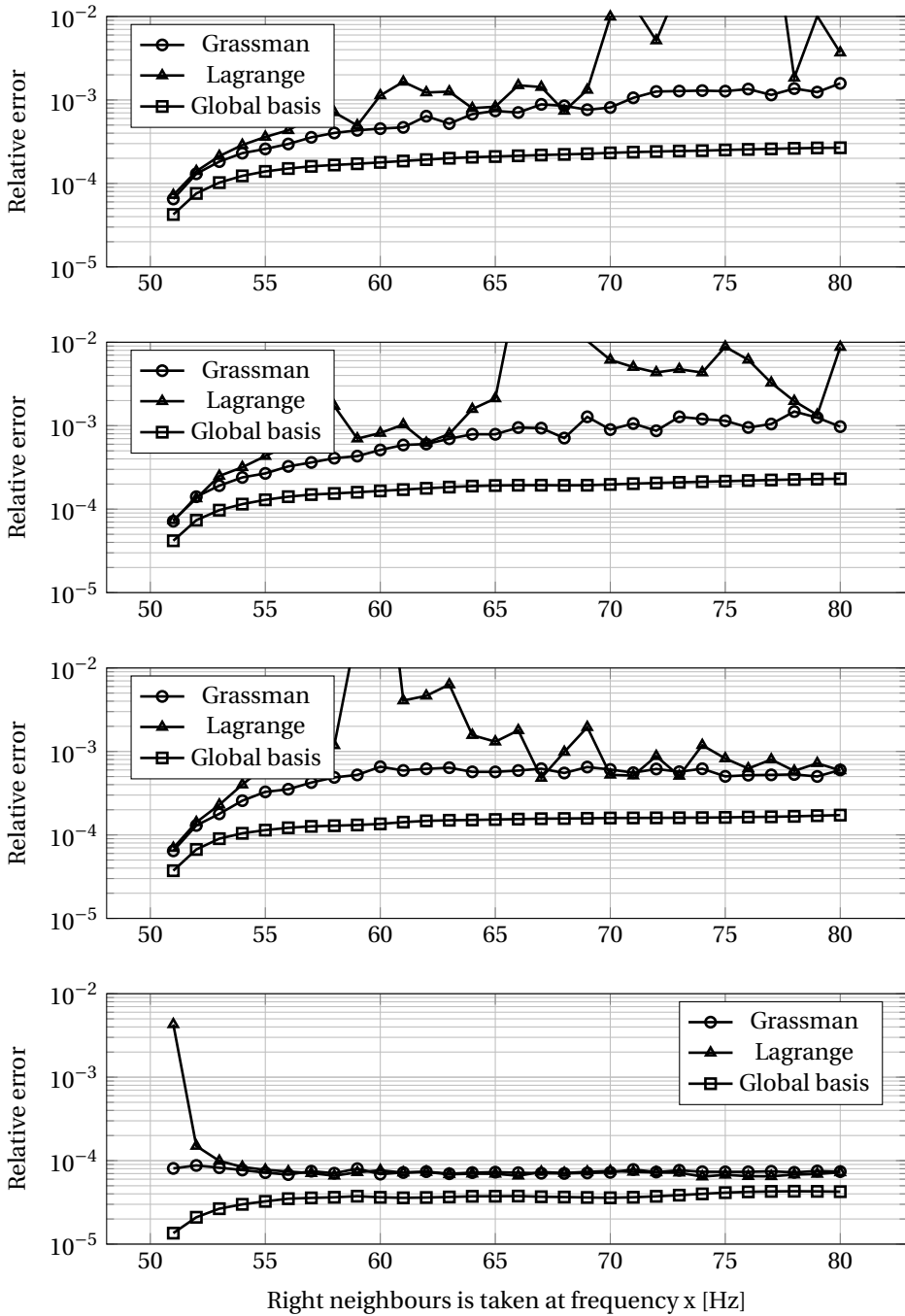
Figure 5.5: Relative errors of ROMs using Grassman or Lagrange interpolations with two bases generated at frequencies 20, 30, 40, 49 (from top to bottom) and x Hz and global basis from snapshots at same frequencies.
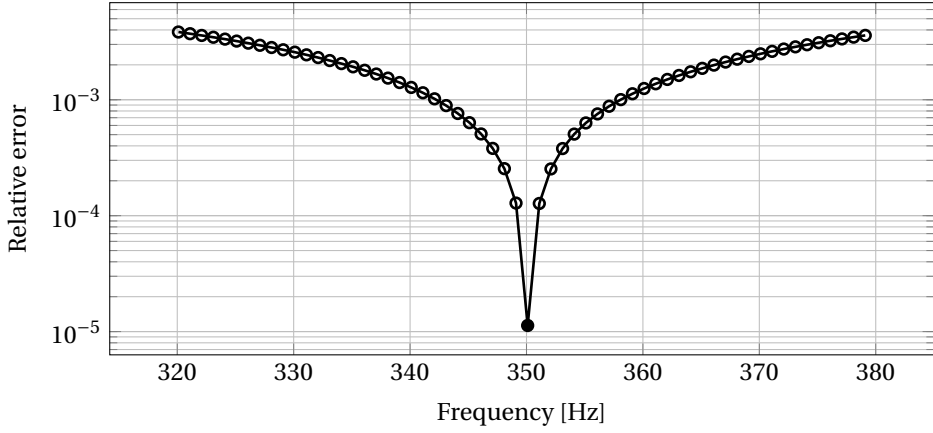
Figure 5.6: Relative error of ROMs according to the frequency with the POD basis generated at frequency=350Hz. Filled circles correspond to the ROM at same frequency than the one used for the construction of POD basis.
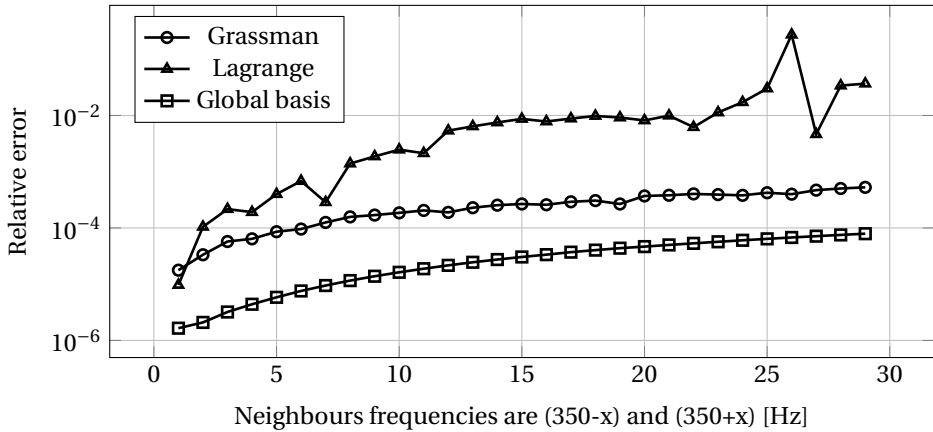
Figure 5.7: Relative error of ROMs using Grassman or Lagrange interpolation with two bases generated at frequencies (350-x) and (350+x) Hz and global basis from snapshots at same frequencies.
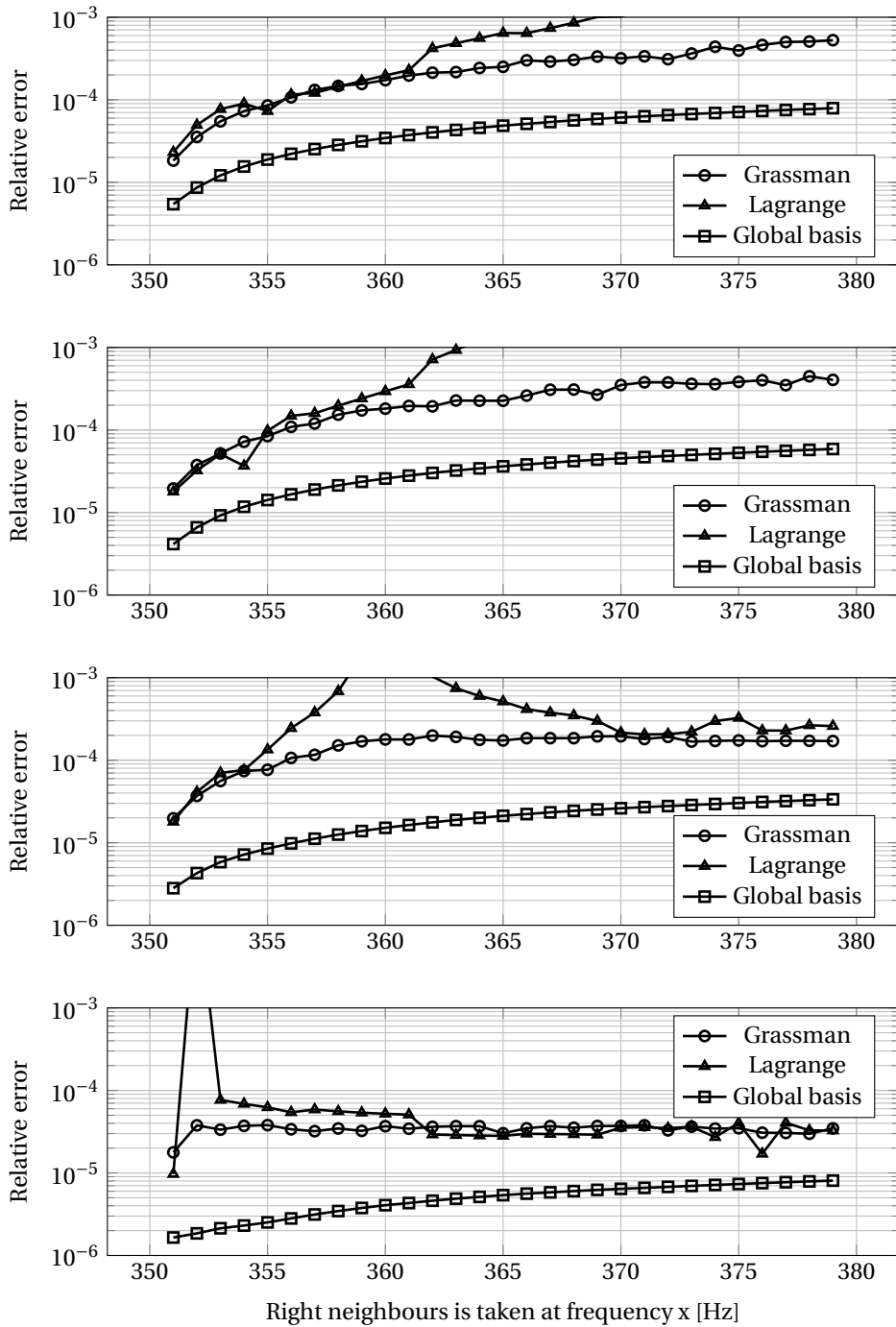
Figure 5.8: Relative error of ROMs using Grassman or Lagrange interpolation with two bases generated at frequencies 320, 330, 340, 349 Hz (from top to bottom) and x Hz and global basis from snapshots at same frequencies.

CHAPTER 6

Parametrized electric coupling with nonlinear magnetodynamic devices

6.1 Introduction

In this last chapter, the linear POD method, the nonlinear sampling approaches and the conclusions of the parametrized analysis using a global basis are used to efficiently and accurately reduce a 2D three-phase voltage-driven power transformer (previously described in section 4.5.2) coupled with external electric circuits.

It concludes the investigation of model order reduced modeling in electromagnetics by providing an example of practical application that can further be used in large network simulators.

First, a description of the nonlinear coupled FE model is provided and explained. Secondly, a decoupled formulation is proposed to adequately perform the reduction on local variables—keeping the external (global) quantities unchanged. Finally, results of this novel approach for magnetodynamic applications are substantially analyzed.

6.2 Nonlinear finite element model

The nonlinear FE formulation has been described in section 4.2 for a global input current. In this chapter, as in real applications, a voltage-driven transformer is considered and conducts to additional variables in the formulation (*i.e.* global input voltage).

From the time and spatial discretized magnetodynamic equation (1.34), separating the local and the global quantities leads to the bloc form (regardless the time discretization)

$$\left[\begin{array}{cc} \mathbf{A}_{aa} & \mathbf{A}_{aw} \\ \mathbf{A}_{wa} & \mathbf{A}_{ww} \end{array} \right] \left[\begin{array}{c} \mathbf{a} \\ \mathbf{w} \end{array} \right] = \left[\begin{array}{c} \mathbf{y}_a \\ \mathbf{y}_w \end{array} \right] \tag{6.1}$$

where $\mathbf{a}$ corresponds to the local unknowns and $\mathbf{w}$ represents the global quantities (at windings in this case).

Figure 6.1: single phase transformer with external electric circuit.

6.3   Network coupling

Once the FE model is obtained, one can integrate it in electric network simulators by coupling it with external circuit equations. As a simple example of the procedure, the coupling of a single phase transformer with input voltage and output resistance load is illustrated in Fig. 6.1 and further detailed. Based on the bloc matrix form (6.1), coupling external electric components is straightforward. Indeed, as the global quantities $\mathbf{w}$ correspond to the input and output currents I_{in} and I_{out} and voltages V_{in} and V_{out} (in Fig. 6.1), the additional currents and voltages in the external electric networks are directly obtained by adding the corresponding circuit equations (e.g. resistors, diodes, ...). Therefore, equation (6.1) becomes

$$
\begin{bmatrix}
\mathbf{A}_{aa} & \mathbf{A}_{aw} & \mathbf{0} \\
\mathbf{A}_{wa} & \mathbf{A}_{ww} & \mathbf{C}_{wc} \\
\mathbf{0} & \mathbf{C}_{cw} & \mathbf{C}_{cc}
\end{bmatrix}
\begin{bmatrix}
\mathbf{a} \\
\mathbf{w} \\
\mathbf{c}
\end{bmatrix}
=
\begin{bmatrix}
\mathbf{y}_a \\
\mathbf{y}_w \\
\mathbf{y}_c
\end{bmatrix}
\tag{6.2}
$$

with $\mathbf{a}$, $\mathbf{w}$ and $\mathbf{c}$ are the vectors of local FE unknowns, global FE unknowns and global external quantities (currents and voltages) in the external circuits respectively, $\mathbf{C}_{wc}$ and $\mathbf{C}_{cw}$ the coupling matrices from global quantities in the FE model and global quantities in the external circuits, $\mathbf{C}_{cc}$ the electric circuit matrix, and $\mathbf{y}_c$ the source term in the external circuits. As an illustration with the single phase transformer in Fig. 6.1, equation (6.2) would be in the form

$$
\left[
\begin{array}{c|cccc|cccc}
\mathbf{A}_{aa} & & \multicolumn{2}{c}{\mathbf{A}_{aw}} & & 0 & 0 & 0 & 0 \\
\hline
 & -1 & 0 & 0 & 0 & 1 & 0 & -R_{in} & 0 \\
 & 0 & -1 & 0 & 0 & 0 & 1 & 0 & 0 \\
\mathbf{A}_{wa} & 0 & 0 & 0 & 0 & 0 & 0 & 1 & 0 \\
 & 0 & 0 & 0 & 0 & 0 & 0 & 0 & 1 \\
\hline
0 & 0 & 0 & 0 & 0 & 1 & 0 & 0 & 0 \\
0 & 0 & 0 & 0 & 0 & 0 & -1 & 0 & R_{out} \\
0 & 0 & 0 & 1 & 0 & 0 & 0 & -1 & 0 \\
0 & 0 & 0 & 0 & 1 & 0 & 0 & 0 & -1
\end{array}
\right]
\begin{bmatrix}
\mathbf{a} \\
V_{in} \\
V_{out} \\
I_{in} \\
I_{out} \\
V_{gen} \\
V_R \\
I_{gen} \\
I_R
\end{bmatrix}
=
\begin{bmatrix}
\frac{\mathbf{M}}{\Delta t}\mathbf{a} \\
0 \\
0 \\
0 \\
0 \\
V_{gen} \\
0 \\
0 \\
0
\end{bmatrix}
\tag{6.3}
$$

where the source term is fixed by V_{gen}. Note that V_{gen} is present in the unknown vector for the sake of clarity (with respect to the separation between the global quantities from the FE model and external circuits). Naturally, one can group all global quantities $\mathbf{w}$ and $\mathbf{c}$ in a single variable $\mathbf{g} = [\mathbf{w}, \mathbf{c}]^T$ such that the coupled system (6.2) is in the form

$$\underbrace{\begin{bmatrix} \mathbf{A}_{aa}(\mathbf{a}) & \mathbf{A}_{ag} \\ \mathbf{A}_{ga} & \mathbf{A}_{gg} \end{bmatrix}}_{\mathbf{A}} \underbrace{\begin{bmatrix} \mathbf{a} \\ \mathbf{g} \end{bmatrix}}_{\mathbf{x}} = \underbrace{\begin{bmatrix} \mathbf{y}_a \\ \mathbf{y}_g \end{bmatrix}}_{\mathbf{y}}. \tag{6.4}$$

In case of large electric circuits where the definitions of electric components are not explicit (e.g. derived from equivalent models), one can couple a matrix form of the external networks to this FE model and obtain a general system similar to (6.4).

6.4 High fidelity coupled formulation

At each time step t_k, the system (6.4) has to be solved as a classic

$$\mathbf{A}_k(\mathbf{x}_k)\mathbf{x}_k = \mathbf{y}_k(\mathbf{x}_k) \tag{6.5}$$

equation. Reminding section 4.2, this remains a nonlinear equation and a Newton-Raphson scheme is employed to linearize it such that the solution $\mathbf{x}_k$ is obtained when the update

$$\mathbf{x}_k^{i+1} = \mathbf{x}_k^i + \delta\mathbf{x}_k^{i+1} \tag{6.6}$$

has converged. The increment $\delta\mathbf{x}_k^{i+1}$ is the solution of the classical Newton-Raphson equation

$$\mathbf{J}\left(\mathbf{x}_k^i\right) \delta\mathbf{x}_k^{i+1} = -\mathbf{r}\left(\mathbf{x}_k^i\right) \tag{6.7}$$

with $\mathbf{J}\left(\mathbf{x}_k^i\right)$ and $\mathbf{r}\left(\mathbf{x}_k^i\right)$ the Jacobian and the residual respectively. The solution is considered converged when the increment is sufficiently small (*i.e.* in this work, $\left\|\delta\mathbf{x}_k^{i+1}\right\| < 10^{-5}$ is used). Similarly, as previously introduced in section 4.2, the solution can also be considered converged when the error on the residual is sufficiently small.

6.5 Resolution reduction

6.5.1 Reduced formulation

The POD method is considered to reduce system (6.4) (and further linearized equation (6.7)). By applying the straightforward POD training, the snapshot matrix is given by

$$\mathbf{X} = \left[\mathbf{x}_0, \cdots, \mathbf{x}_{N_s}\right] = \begin{bmatrix} \mathbf{a}_0, \cdots, \mathbf{a}_{N_s} \\ \mathbf{g}_0, \cdots, \mathbf{g}_{N_s} \end{bmatrix} = \begin{bmatrix} \mathbf{X}_a \\ \mathbf{X}_g \end{bmatrix} \in \mathbf{R}^{n \times N_s} \tag{6.8}$$

when $N_s \le N_t$ snapshots are taken. As previously described in prior chapters, the POD basis is determined by truncating the result of the application of an SVD on the snapshot matrix. However, $\mathbf{a}$ and $\mathbf{g}$ represent intrinsically two types of unknowns

inducing a drastic difference in matrices $\mathbf{X}_a \in \mathbb{R}^{n_a \times N_s}$ and $\mathbf{X}_g \in \mathbb{R}^{n_g \times N_s}$. Due to this observation, applying an SVD on $\mathbf{X}$ may not lead to an optimal (or appropriate) reduced basis for both unknowns $\mathbf{a}$ and $\mathbf{g}$. This observation has already been presented in the coupled systems of mechanical and thermal physics [103]. Due to the different order in magnitude in the different quantities, determining a single basis to correctly represent both of them is not an easy task and often instabilities in the resolution scheme of the reduced system may occur. The authors proposed two solutions to this issue:

1. Applying a scaling factor to normalize the variables and define proper reduced basis. This method introduces an additional issue: the determination of the scaling factor represents a new problem that is not easy to solve.

2. Separating the variables and reducing them by using different bases (generated by snapshots of the separate variables). This latter method is considered in this dissertation.

Generally, the size of the global quantities is much smaller than the local ones in the FE model and may not need a particular reduction[1]. Therefore, the local unknowns are the only one requiring a reduction by using an appropriate reduced basis $\mathbf{Q}_a$ generated from the snapshot matrix $\mathbf{X}_a$. By doing so, the separated reduced system of (6.4) is

$$\left[\begin{array}{cc} \mathbf{Q}_a^T \mathbf{A}_{aa} \mathbf{Q}_a & \mathbf{Q}_a^T \mathbf{A}_{ag} \\ \mathbf{A}_{ga} \mathbf{Q}_a & \mathbf{A}_{gg} \end{array} \right] \left[\begin{array}{c} \tilde{\mathbf{a}} \\ \mathbf{g} \end{array} \right] = \left[\begin{array}{c} \mathbf{Q}_a^T \mathbf{y}_a \\ \mathbf{y}_g \end{array} \right]. \tag{6.9}$$

In our experience, the projection of the coupling matrix $\mathbf{A}_{ag}$ onto the reduced basis leads to unstable reduced POD system when the magnetodynamic system is driven with an imposed voltage and coupled to electric circuits instead of an imposed current source with no external interactions (as in the prior chapter). Indeed, global quantities and their coupling matrix are badly projected on the local basis on the local unknowns. To solve this problem, a decoupled formulation is sought in the form

$$\left[\begin{array}{cc} \tilde{\mathbf{A}}_{aa} & \mathbf{0} \\ \tilde{\mathbf{A}}_{ga} & \mathbf{A}_{gg} \end{array} \right] \left[\begin{array}{c} \tilde{\mathbf{a}} \\ \mathbf{g} \end{array} \right] = \left[\begin{array}{c} \tilde{\mathbf{y}}_a \\ \mathbf{y}_g \end{array} \right]. \tag{6.10}$$

From equation (6.4), the local quantities $\mathbf{a}$ can be decoupled from the global ones with

$$\mathbf{A}^* \mathbf{a} = \left(\mathbf{A}_{aa} - \mathbf{A}_{ag} \mathbf{A}_{gg}^{-1} \mathbf{A}_{ga} \right) \mathbf{a} = \mathbf{y}_a - \mathbf{A}_{ag} \mathbf{A}_{gg}^{-1} \mathbf{y}_g = \mathbf{y}^*. \tag{6.11}$$

Note that inverting matrix $\mathbf{A}_{gg}$ is feasible for three reasons:

1. It consists in differential-algebraic equations from electric relations and a minimal graph representation of the electric block matrix $\mathbf{A}_{gg}$ can be found [119].

2. It is relatively small compared to the other blocks—allowing fast evaluation.

---

[1] If this assumption would not be fulfilled, a separate reduction of the global quantities can be performed as detailed for local ones in this dissertation.

3. The external electric components change at a way smaller pace than the (electro)magnetodynamic ones–where that property is exploited in multi-rate coupling and co-simulation researches [155, 162, 184]–and can be considered constant (for a relatively long period of time at micro-scale).

Applying the POD reduced basis $\mathbf{Q}_a$ onto decoupled equation (6.11) leads to the reduced equation

$$\mathbf{Q}_a^T \mathbf{A}^* \mathbf{Q}_a \tilde{\mathbf{a}} = \mathbf{Q}_a^T \mathbf{y}^* \tag{6.12}$$

with $\mathbf{Q}_a \in \mathbb{R}^{n_a \times r}$ and unknown $\tilde{\mathbf{a}} \in \mathbb{R}^{r \times 1}$. Now, the coupled reduced system respecting the form (6.10) is

$$\begin{bmatrix} \mathbf{Q}_a^T \mathbf{A}^* \mathbf{Q}_a & \mathbf{0} \\ \mathbf{A}_{ga} \mathbf{Q}_a & \mathbf{A}_{gg} \end{bmatrix} \begin{bmatrix} \tilde{\mathbf{a}} \\ \mathbf{g} \end{bmatrix} = \begin{bmatrix} \mathbf{Q}_a^T \mathbf{y}^* \\ \mathbf{y}_g \end{bmatrix}. \tag{6.13}$$

Here, the size of the system (6.13) equals $r + n_g$ and is supposed to be much smaller than original one $n = n_a + n_g$.

6.5.2   Single vs multiple parameter models

Previously described in chapter 5, the global basis is the preferred approach to deal with slight parametric dependencies in the input and output excitations. Therefore, no nonlinear interpolation is considered in this section.

In particular, the correct training of such a basis is crucial. A global trajectory such that all nonlinear behaviours are encoutered in the magnetodynamic model in order to capture all the required information is mandatory.

This method is presented in details within the application section by comparing multiple training strategies.

6.6   Assembly reduction

This section refers to the methods detailed in chapter 4 by considering the MPE and DEIM approaches to curtail the generation of the entries in the nonlinear terms.

6.6.1   Missing Estimation Point

Only equation (6.12) has to be correctly sampled as the nonlinear terms are present in $\mathbf{A}_{aa}$. Indeed, one can see that the other block matrices in $\mathbf{A}$ do not depend in $\mathbf{a}$ as they are constituting the coupling between local and global quantities and expression of the external electric network.

Applying the definition of the MPE (as in (4.7)) onto (6.12) leads to

$$\bar{\mathbf{Q}}_a^T \bar{\mathbf{A}}^* \mathbf{Q}_a \tilde{\mathbf{a}} = \bar{\mathbf{Q}}_a^T \bar{\mathbf{y}}^* \tag{6.14}$$

where the reduction processes can intuitively be understood in detailed form

$$\underbrace{\left(\bar{\mathbf{P}}^T\mathbf{Q}_a\right)^T}_{constant}\left(\underbrace{\bar{\mathbf{P}}^T\mathbf{A}_{aa}}_{MPE}-\underbrace{\bar{\mathbf{P}}^T\mathbf{A}_{ag}\mathbf{A}_{gg}^{-1}\mathbf{A}_{ga}}_{constant}\right)\underbrace{\mathbf{Q}_a}_{POD}\tilde{\mathbf{a}}=\underbrace{\left(\bar{\mathbf{P}}^T\mathbf{Q}_a\right)^T}_{constant}\left(\underbrace{\bar{\mathbf{P}}^T\mathbf{y}_a}_{MPE}-\underbrace{\bar{\mathbf{P}}^T\mathbf{A}_{ag}\mathbf{A}_{gg}^{-1}\mathbf{y}_g}_{constant}\right). \quad (6.15)$$

The MPE terms are evaluated at each nonlinear iteration and come from the application of the selection matrix $\bar{\mathbf{P}}$ on the block decomposition of $\mathbf{A}$ (i.e. $\bar{\mathbf{P}}^T\mathbf{A}_{aa}$) and $\mathbf{y}$ ($\bar{\mathbf{P}}^T\mathbf{y}_a$ and $\bar{\mathbf{P}}^T\mathbf{A}_{ag}\mathbf{A}_{gg}^{-1}\mathbf{y}_g$).

6.6.2 Discrete Empirical Interpolation Method

Similarly to MPE sampling procedure, the DEIM formulation is obtained by

$$\left(\bar{\mathbf{P}}^T\mathbf{Q}_a\right)^{-1}\bar{\mathbf{A}}^*\mathbf{Q}_a\tilde{\mathbf{a}}=\left(\bar{\mathbf{P}}^T\mathbf{Q}_a\right)^{-1}\bar{\mathbf{y}}^* \quad (6.16)$$

following the scheme described in 2.2.2 and equation (4.12). In details, analogue to (6.15), equation (6.16) is written as

$$\underbrace{\left(\bar{\mathbf{P}}^T\mathbf{Q}_a\right)^{-1}}_{constant}\left(\underbrace{\bar{\mathbf{P}}^T\mathbf{A}_{aa}}_{DEIM}-\underbrace{\bar{\mathbf{P}}^T\mathbf{A}_{ag}\mathbf{A}_{gg}^{-1}\mathbf{A}_{ga}}_{constant}\right)\underbrace{\mathbf{Q}_a}_{POD}\tilde{\mathbf{a}}=\underbrace{\left(\bar{\mathbf{P}}^T\mathbf{Q}_a\right)^{-1}}_{constant}\left(\underbrace{\bar{\mathbf{P}}^T\mathbf{y}_a}_{DEIM}-\underbrace{\bar{\mathbf{P}}^T\mathbf{A}_{ag}\mathbf{A}_{gg}^{-1}\mathbf{y}_g}_{constant}\right). \quad (6.17)$$

6.7 General reduced order model

From both similar equations (6.15) and (6.17), a general equation with local and global quantities regardless the sampling method can be formulated. To obtain this global form, let us first define the projection operators

$$\Xi_{\mathbf{Y}}=\left[\begin{array}{cc}\mathbf{Y} & \mathbf{0}\\ \mathbf{0} & \mathbf{I}\end{array}\right]\in\mathbb{R}^{n\times n}\quad\text{and}\quad\Pi_{\mathbf{Y}}=\left[\begin{array}{c}\mathbf{Y}\\ \mathbf{0}\end{array}\right]\in\mathbb{R}^{n\times y_2} \quad (6.18)$$

with $\mathbf{Y}\in\mathbb{R}^{y_1\times y_2},\mathbf{I}\in\mathbb{R}^{(n-y_1)\times(n-y_2)}$ the identity matrix so that the full order unknown $\mathbf{x}$ is retrieved by

$$\mathbf{x}=\Xi_{\mathbf{Q}_a}\tilde{\mathbf{x}}. \quad (6.19)$$

Now, the general reduced system for all methods is written as

$$\left[\begin{array}{cc}\mathbf{C}_1\left(\Pi_{\bar{\mathbf{P}}}^T\mathbf{A}\Pi_{\mathbf{I}_{n_a}}-\bar{\mathbf{P}}^T\mathbf{A}_{ag}\mathbf{A}_{gg}^{-1}\mathbf{A}_{ga}\right)\mathbf{C}_2 & \mathbf{0}\\ \mathbf{A}_{ga}\mathbf{C}_2 & \mathbf{A}_{gg}\end{array}\right]\left[\begin{array}{c}\tilde{\mathbf{a}}\\ \mathbf{g}\end{array}\right]=\left[\begin{array}{c}\mathbf{C}_1\left(\Pi_{\bar{\mathbf{P}}}^T\mathbf{y}-\bar{\mathbf{P}}^T\mathbf{A}_{ag}\mathbf{A}_{gg}^{-1}\mathbf{y}_g\right)\\ \mathbf{y}_g\end{array}\right]$$
$$(6.20)$$

with the definition of the constants in Table 6.1. To solve system (6.20), one can derive a linearized Newton-Raphson equation as with (6.7). However, one can directly identify the matrices $\mathbf{A}$ and $\mathbf{y}$ to be the Jacobian $\mathbf{J}$ and the residual $\mathbf{r}$ respectively. While generating the left hand side with block decomposition of the Jacobian is simple, treating the residual may be more challenging (as it involves block decomposition of matrices $\mathbf{M}$

Table 6.1: Definition of constants of (6.20) for all reduction techniques.

Method	HFM	POD	MPE	DEIM/DIME
$\bar{\mathbf{P}}$	$\mathbf{I}_{n_a}$	$\mathbf{I}_{n_a}$	from algorithm	from algorithm
$\mathbf{C}_1 \in \mathbb{R}^{r \times q}$	$\mathbf{I}_{n_a}$	$\mathbf{Q}_a^T$	$\left(\bar{\mathbf{P}}^T\mathbf{Q}_a\right)^T$	$\left(\bar{\mathbf{P}}^T\mathbf{Q}_a\right)^{-1}$
$\mathbf{C}_2 \in \mathbb{R}^{n_a \times r}$	$\mathbf{I}_{n_a}$	$\mathbf{Q}_a$	$\mathbf{Q}_a$	$\mathbf{Q}_a$

and $\mathbf{S}$). For the sake of clarity, one can decompose the residual expression to

$$
\mathbf{r}_k^{i+1} = \left[\begin{array}{c} \mathbf{r}_{a,k}^{i+1} \\ \mathbf{r}_{g,k}^{i+1} \end{array} \right]
$$

$$
= \left[\begin{array}{cccc} \frac{\mathbf{M}_{aa}}{\Delta t}\mathbf{C}_2 & -\left(\frac{\mathbf{M}_{aa}}{\Delta t}+\mathbf{S}_{aa}\right)\mathbf{C}_2 & \mathbf{S}_{ag} & \mathbf{0} \\ \frac{\mathbf{M}_{ag}}{\Delta t}\mathbf{C}_2 & -\frac{\mathbf{M}_{ag}}{\Delta t}\mathbf{C}_2 & \mathbf{S}_{gg} & \mathbf{I} \end{array} \right] \left[\begin{array}{c} \tilde{\mathbf{a}}_{k-1} \\ \tilde{\mathbf{a}}_k^i \\ \mathbf{g}_k^i \\ \mathbf{v}_g \end{array} \right] \tag{6.21}
$$

to highlight how the resolution and assembly reductions will operate on it. Note that only the block matrix $\mathbf{S}_{aa}$ is nonlinear with $\mathbf{a}$ and needs to be updated whereas the rest is constant and can be precomputed once.

Practical implementation   Depending on the FE software, the initial $\mathbf{A}$ and $\mathbf{y}$ matrices (or sub-blocs $\mathbf{M}, \mathbf{S}, \mathbf{v}$) may be atomically generated (e.g. no specific access to $\mathbf{A}_{aa}$) and the MPE selection must directly be performed on them. Since $\mathbf{A}_{aa}$ can be written as $\mathbf{A}_{aa} = \mathbf{\Pi}_{\mathbf{I}_{n_a}}^T \mathbf{A}\mathbf{\Pi}_{\mathbf{I}_{n_a}}$ with $\mathbf{I}_{n_a}$ the identity matrix of size n_a, $\bar{\mathbf{P}}^T\mathbf{A}_{aa} = \bar{\mathbf{P}}^T\mathbf{\Pi}_{\mathbf{I}_{n_a}}^T\mathbf{A}\mathbf{\Pi}_{\mathbf{I}_{n_a}}$ and the term $\bar{\mathbf{P}}^T\mathbf{\Pi}_{\mathbf{I}_{n_a}}^T$ must be inverted to apply the MPE selection on the original $\mathbf{A}$ matrix. By applying block multiplication, one directly finds $\bar{\mathbf{P}}^T\mathbf{\Pi}_{\mathbf{I}_{n_a}}^T = \mathbf{\Pi}_{\bar{\mathbf{P}}}^T$ which is equivalent to simply expand the $\bar{\mathbf{P}}$ selection matrix to original full size (rows). In practice, as $\mathbf{A}_{aa}$ is the upper left block of $\mathbf{A}$, computing the q rows of $\mathbf{A}_{aa}$ is equivalent to computing the q first rows of $\mathbf{A}$–e.g.

$$
\bar{\mathbf{P}}^T\mathbf{A}_{aa} = \left[\begin{array}{cc} 0 & 1 \\ 0 & 0 \\ 1 & 0 \\ 0 & 0 \end{array} \right]^T \mathbf{A}_{aa} \quad \text{and} \quad \mathbf{\Pi}_{\bar{\mathbf{P}}}^T\mathbf{A} = \left[\begin{array}{cc} 0 & 1 \\ 0 & 0 \\ 1 & 0 \\ 0 & 0 \\ \hline x & x \\ x & x \end{array} \right]^T \mathbf{A} \tag{6.22}
$$

both correspond to the computations of 3rd and 1st rows of $\mathbf{A}$. Therefore, the block decomposition is implicitly performed by the implementation. Then, the columns can be truncated by applying $\mathbf{\Pi}_{\mathbf{I}_{n_a}}$ on the right side as

$$
\bar{\mathbf{P}}^T\mathbf{A}_{aa} = \mathbf{\Pi}_{\bar{\mathbf{P}}}^T\mathbf{A}\mathbf{\Pi}_{\mathbf{I}_{n_a}} \tag{6.23}
$$

$$= \begin{bmatrix} \bar{\mathbf{P}}^T & \mathbf{0} \end{bmatrix} \begin{bmatrix} \mathbf{A}_{aa} & \mathbf{A}_{ag} \\ \mathbf{A}_{ga} & \mathbf{A}_{gg} \end{bmatrix} \begin{bmatrix} \mathbf{I} \\ \mathbf{0} \end{bmatrix} \tag{6.24}$$

This truncation can also be directly implemented in the FE code. Indeed, only the indices of the columns lower than size n_a have to be computed. Considering the local influence of a degree of freedom in the FE method, most of the elements are null–which allows fast evaluations of non-zero elements using sparse format for the required q rows.

Concerning the **y**-term, the selection matrix $\bar{\mathbf{P}}$ naturally extends to full size $(n_a + n_g)$ and performs the selection on it as

$$\bar{\mathbf{P}}^T \mathbf{y}_a = \bar{\mathbf{P}}^T \Pi_{\mathbf{I}_{n_a}}^T \mathbf{y} = \Pi_{\bar{\mathbf{P}}}^T \mathbf{y}. \tag{6.25}$$

Finally, considering term $\bar{\mathbf{P}}^T \mathbf{A}_{ag} \mathbf{A}_{gg}^{-1} \mathbf{y}_g$, the matrix product $\mathbf{A}_{ag} \mathbf{A}_{gg}^{-1}$ does not allow any permutation with $\bar{\mathbf{P}}$. Even though, since $\bar{\mathbf{P}}$ selects q rows in the n_a first ones of **y** and $\mathbf{y}_g$ lies in the n_g last ones, $\mathbf{y}_g$ cannot be retrieved by applying a function of $\bar{\mathbf{P}}$ on **y**. However, $\bar{\mathbf{P}}^T \mathbf{A}_{ag} \mathbf{A}_{gg}^{-1} \in \mathbb{R}^{q \times n_g}$ is constant and small. As a result, from a computational point of view, it is allowed to generate the last $n_g \approx O(1)$ entries of **y** (i.e. $\mathbf{y}_g$) and store $\bar{\mathbf{P}}^T \mathbf{A}_{ag} \mathbf{A}_{gg}^{-1}$.

6.8   Application to a voltage-driven three-phase power transformer

In this section, the general coupled formulation (6.20) is used to solve the coupling between a three-phase voltage-driven transformer with external electric circuits.

6.8.1   Problem description

The three-phase power transformer introduced in section 4.5.2 is used. For this application, the conductivity does not act as a parameter and is taken into account with the modified constitutive law (4.14) ($\sigma = 2\,10^7 \mathrm{S/m}$) by considering an iron laminated core. In addition, the current input excitation is replaced by a voltage one that follows

$$V_i = s V_i^{RMS} \cos(2\pi f t + \varphi_i) \tag{6.26}$$

for phase i with φ_i the corresponding phase delay and s a soft-start limitation such that

$$\begin{cases} s & = & \frac{1}{2}\left[1 - \cos(\pi t)\right] & , & t < 1, \\ s & = & 1 & , & t \geq 1. \end{cases} \tag{6.27}$$

These quantities are shown in Fig. 6.2 in case of $V_a^{peak} = V_a^{RMS}\sqrt{2} = 220\sqrt{2}$. The input RMS voltage values V_i^{RMS} are taken in the set $[10, 80, 150, 220]\mathrm{V}$ in order to simulate both low and high excitations. Using the smooth soft-start limitation, the simulations are computed for 1.4 seconds corresponding to 70 periods at $f = 50\mathrm{Hz}$ ($T = 20$ ms) with $N_t = 1400$ time steps to avoid any transient disturbance.
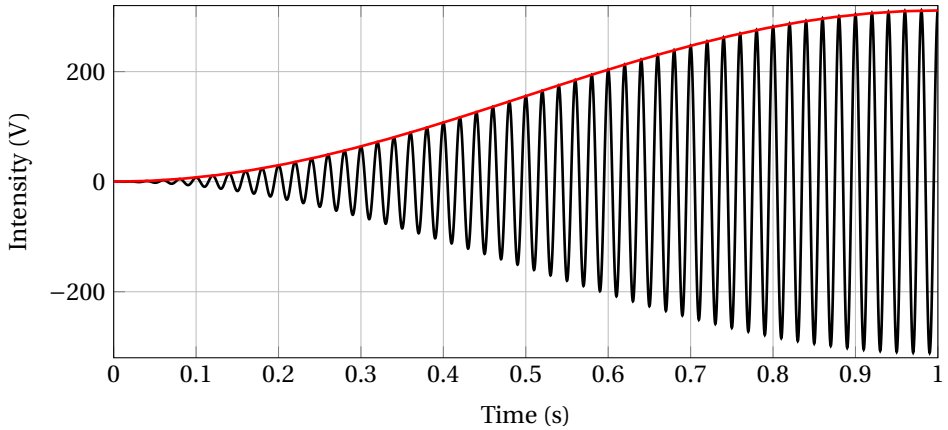
Figure 6.2: Input voltage V_a and soft-start limitation with $V_a^{RMS} = 220$V.
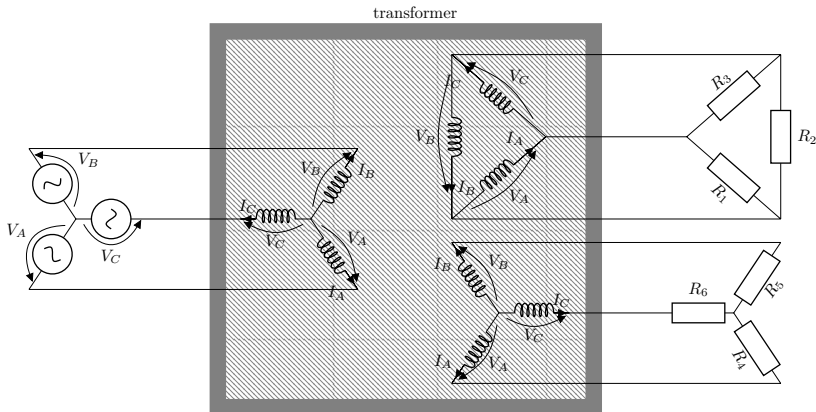
Figure 6.3: Setup - electric circuit

Concerning the external electric circuits, the voltage-driven transformer is connected to the balanced network of resistive loads–composed of two different configurations in star and triangle–depicted in Fig. 6.3. These loads vary in the range $R \in [0.1, 1, 10, 100]\,\Omega$ where lowest value simulates short-circuit and highest one corresponds to open-circuit configuration.

6.8.2 Resolution reduction

Changing the parameters (*i.e.* input voltage and output loads) values can significantly change the local fields (see magnetic flux density field for all extreme values in Fig. 6.4) and consequently represents a challenge for an appropriate global training. As with current input in section 5.4, the voltage source (6.26) ranges in $[-V_i^{RMS}, V_i^{RMS}]$ (see
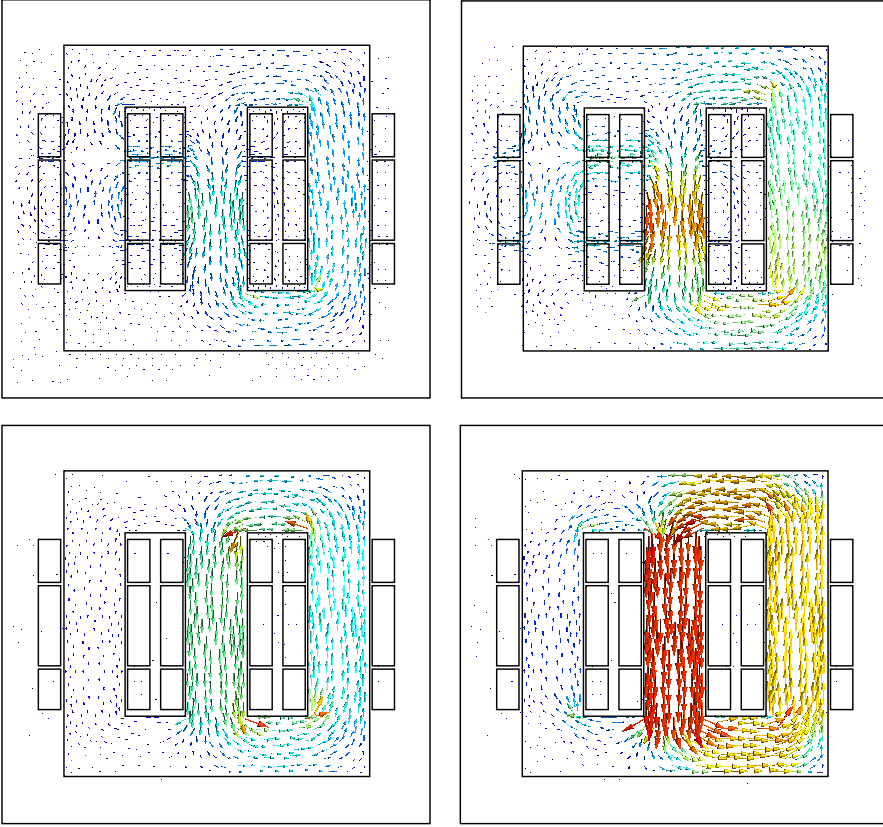
Figure 6.4: 1400th time step of induction field with input voltage $V = 10$ V (left) and $V = 220$ V (right) and output load $R = 0.1\Omega$ (up) and $R = 100\Omega$ (down) from top left to bottom right. Legend : linear scales from 0 T with blue-small arrows to 0.12 T (left) and 1.7 T (right) with red-large arrows.

Fig. 6.2) and using the highest peak voltage for the training stimulates all the nonlinear behaviors according to the magnetization curve depicted in Fig. 6.5. To illustrate this explanation with numerical data, Figs. 6.6 and 6.7 show the relative errors of the global quantities with POD bases generated at different voltages. No load is considered to stimulate the highest nonlinear states. Indeed, with no load connected in the secondaries, there is no output currents that limit the internal magnetic field (Faraday's law). In Fig. 6.6, the POD bases have been trained with input voltages $V_{training}^{RMS} = 10$V, 80V, 150V and 220V respectively and are used to reduce the nonlinear magnetodynamic formulation with input voltages $V_{live}^{RMS} = 10$V, 80V, 150V and 220V. These results validate the training strategy for three reasons:

1. Errors are small when the POD basis comes from a training with higher input voltage (i.e. $V_{training}^{RMS} \geq V_{live}^{RMS}$).

2. In the opposite situation with a training lower than the input test voltage (i.e.
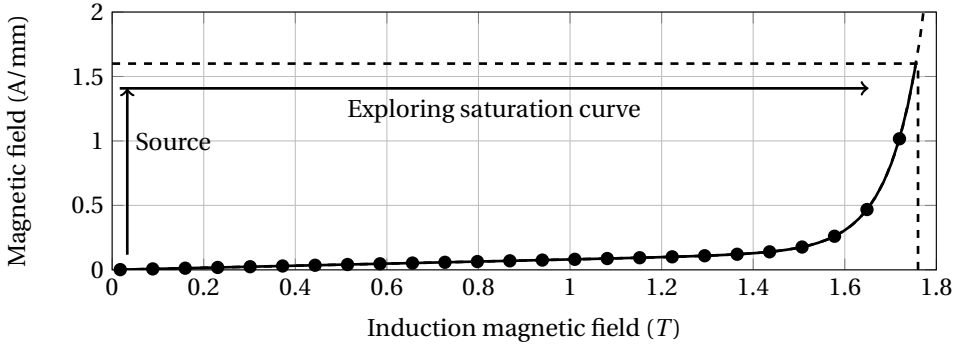
Figure 6.5: Saturation curve

Table 6.2: Setup of loads for the global training of the single reduced basis. The time row represents intervals from the last time instant till the described ones (e.g. the second column → 1.2 should be understood as the time interval $[1.0, 1.2[$).

Time [s]	0.0 → 1.0	→ 1.2	→ 1.4	→ 1.6	→ 1.8	→ 2.0	→ 2.2	→ 2.4	→ 2.6
$R_{1\rightarrow 6}[\Omega]$	100	50	10	5	2	1	0.5	0.2	0.1

$V_{training}^{RMS} < V_{live}^{RMS}$), errors stabilise at high values as the bases lack information from the non exploration of nonlinear states.

3. Errors are quasi similar for all input voltages when using the highest training voltage (i.e. $V_{training}^{RMS} = 220$V) for all input test voltages V_{live}^{RMS} (Fig. 6.7).

Now, to take into account the dependency in the output load, a similar varying procedure is considered by modifying their values from highest to lowest values. In practice, a single training is performed during 2.6 seconds (time step = 1ms) with the highest input voltage $V_{1,2,3}^{RMS} = 220$V respecting the load procedure defined in Table 6.2 to capture all dynamical and nonlinear behaviours.

With the 2600 snapshots, the single POD basis can be deduced by the application of the SVD if the singular values decay sufficiently fast—illustrating the possibility of projecting the HFM onto a reduced subspace (of size r). Indeed, the singular values are depicted in Fig. 6.8 and the POD relative error for all configurations[2] are shown in Fig. 6.9. Note that all configurations have been tested during 2.6 seconds to appropriately test the choice of the training procedure. As in previous chapter, the L^2 relative error defined in (3.8) is used. One can see that for an *a priori* POD error of 0.1% (which is considerable acceptable from an engineering point of view) the number of unknowns in the reduced system is only 50 (comparable to the original 7300). This drastic reduction leads to a curtailment ratio of 99% in both resources and computational time and a theoretical speedup comprised between 145 and 21,000 depending on the solver

---

[2]By configuration is meant a couple $[V,R]$ in the prescribed ranges. No distinction of a particular configuration is shown to illustrate the robustness of the proposed methods over the entire parameter space.
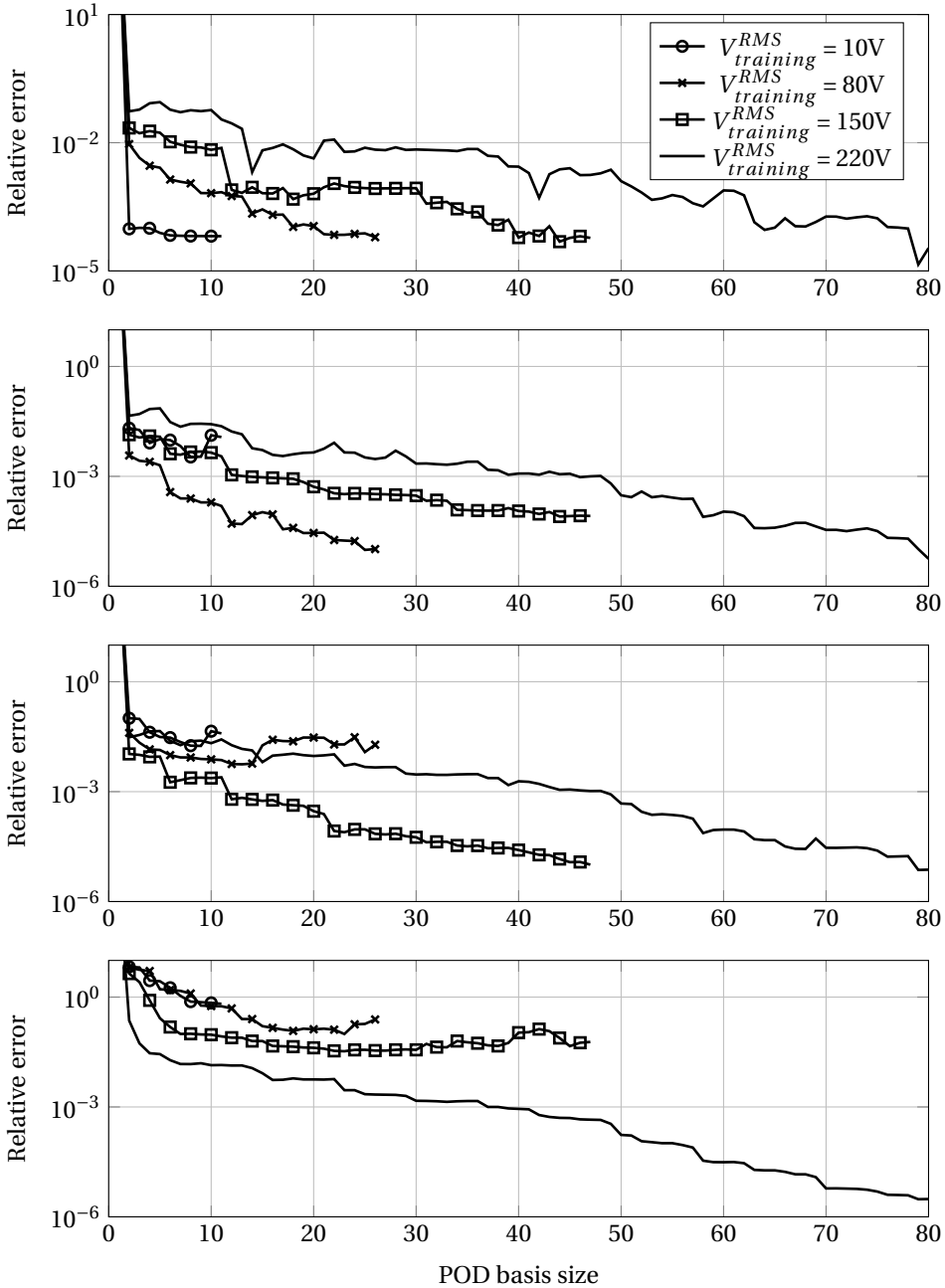
Figure 6.6: No load. (From top to bottom) POD relative error for input voltage $V_{live}^{RMS} = 10V$, V_{live}^{RMS} = 80V, V_{live}^{RMS} = 150V and V_{live}^{RMS} = 220V.
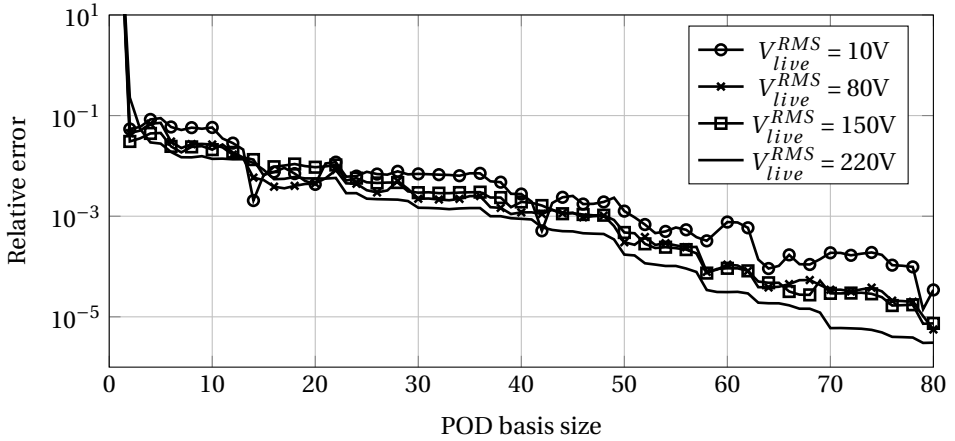
Figure 6.7: POD relative error for multiple input voltage V_{live}^{RMS} using POD basis generated with input voltage $V_{training}^{RMS}$ = 220V.

[106, 107]. Numerical results show better accuracy than predicted by the POD *a priori* error. From there (Fig. 6.9), three main conclusions can be made:

1. As expected, the larger the POD basis, the smaller the error.

2. All reduced models provide relatively the same relative errors given an *a priori* defined error (as awaited by results in global training shown in Fig. 6.7).

3. All errors are below the *a priori* error criterion which acts as an upper-bound in this problem.

In conclusion, from en empirical point of view, the resolution reduction can effectively be performed using a single POD approach on the coupled system with appropriate *a priori* error estimate.

6.8.3 Assembly reduction

6.8.3.1 Discrete Empirical Interpolation Method

Similarly to the first observations made with the input current in section 4.5.2, in this experiment with input voltage source, the POD-DEIM/DIME model (6.20) suffers from the same ill-conditioning problem. Indeed, condition number as high as 10^{20} have been encountered and thus leads to (very) non-robust solutions.

From the observations in both current and voltage mode of magnetodynamic problems, one may conclude that the POD-DEIM/DIME cannot efficiently and robustly be used.
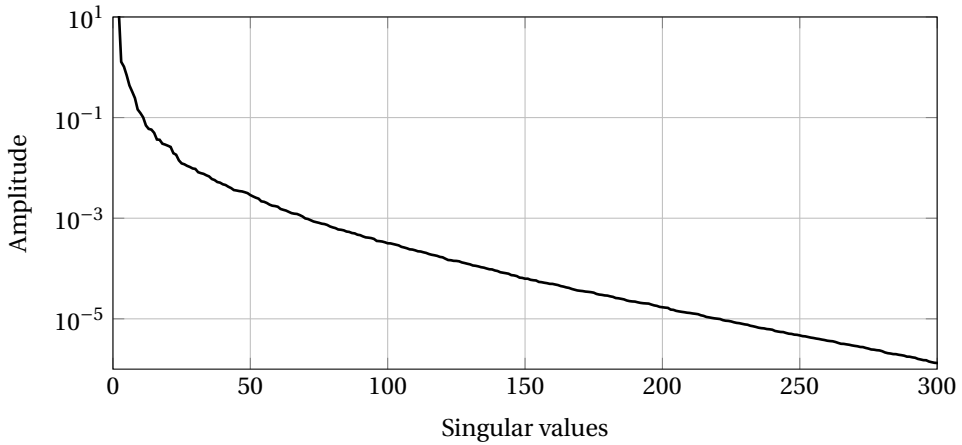
Figure 6.8: Amplitude of the singular values of the global training snapshot matrix.
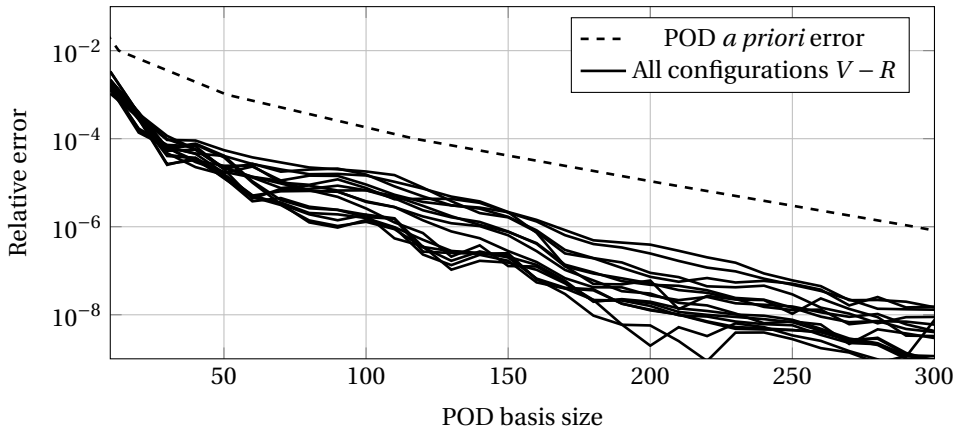
Figure 6.9: Relative error for all configurations vs POD size.

6.8.3.2   Missing Point Estimation

According to the results in Fig. 6.9, a POD basis of size 50 is chosen for two reasons. First, it drastically reduces the resolution complexity by 99%. Secondly, the *a priori* error of 0.1% and actual error of 1e-5 for all cases are fairly acceptable from an engineering point of view. The condition number of $\bar{\mathbf{Q}}_a^T \bar{\mathbf{Q}}_a$ is shown in Fig. 6.10(top) and decays as the number of elements increases. Naturally, the higher the number of entries in nonlinear terms the lower the error. Considering the full size, when no reduction is performed, the POD-MPE error tends to the POD error. As the condition number is described as a correlated indicator of the resulted error, multiplying it by the a-priori POD error provides an *a priori* MPE error. In the present problem, this indicator acts, similarly with the POD one, as an upper bound when the number of elements is

sufficiently large (satisfying the MPE conditioning criterion). In Fig. 6.10(middle) are also depicted the relative errors of POD-MPE model for all configurations by considering a POD size of 50. From a practical point of view, 200 elements satisfy a legitimate error criterion of 1%—allowing a reduction of 97% in the assembly process. However, the actual error is ten times lower at 0.1% in most cases. In Fig. 6.10, the errors show appropriate decaying behaviours regarding the condition number of the MPE process (200 elements correspond to a condition number of 7 from Fig. 6.10). In addition, the pivot value (around an MPE condition number of 10) does not fluctuate as the POD basis size changes. As explained in [15], the condition number has to be sufficiently small (defining this pivot value) to accurately reduce the assembly process otherwise non robust solutions emerge.

Directly related to the POD basis, the selection matrix $\bar{\mathbf{P}}$ has to be recomputed in case of a modification in the size of the basis. Similarly to the hierarchical generation of the POD basis, one may be interested in generating the MPE selection matrix regardless the POD size. Naturally, using the largest POD basis to determine the MPE selection matrix $\bar{\mathbf{P}}$ for any POD size is a logical choice. In Fig. 6.10(bottom) is depicted the relative errors made by the POD-MPE method using the selection matrix generated from the largest POD basis (i.e. 340 modes)–but still considering the truncated basis (50 modes) for the resolution reduction. The results are good (presenting low errors) but show a less robust convergence decay (i.e. some test cases do converge with a small number of elements equivalently to a large condition number, whereas others do not)–preventing the correct use of this approach. However, once the results have converged, they are similar to the ones previously obtained. As a consequence, the selection process may provide similar indices from both POD bases. Nonetheless, they are not entirely identical as the 200 first MPE selection points can be graphically seen in Fig. 6.11 for both bases (50-mode and 340-mode POD bases in black and in red respectively). Compared to the black points, the red ones are more concentrated on the edges where the saturation behaviours tend to emerge. Given that observation, one may investigate different point selections as an experienced user may know the most critical areas to take into consideration. Following this last observation on the dependency in the choice of the points in the MPE process, four different scenarios are studied:

1. Scenario 1: as the nonlinear behaviours mostly happen in the corners of the core and the global currents flowing in the coil are of great interest, the corresponding 95 first MPE indices are forced in those areas.

2. Scenario 2: more indices are added in the core in order to fully capture the nonlinear behaviours (i.e. the indices are chosen in the corners, in the middle of the E shape-core and uniformly distributed on the external boundary). These extra points lead to a total of 165 first forced indices in the MPE process.

3. Scenario 3: 7 extra points in the air region are added to those of the second scenario –obtaining 172 imposed indices.

4. Scenario 4: a random selection is used.
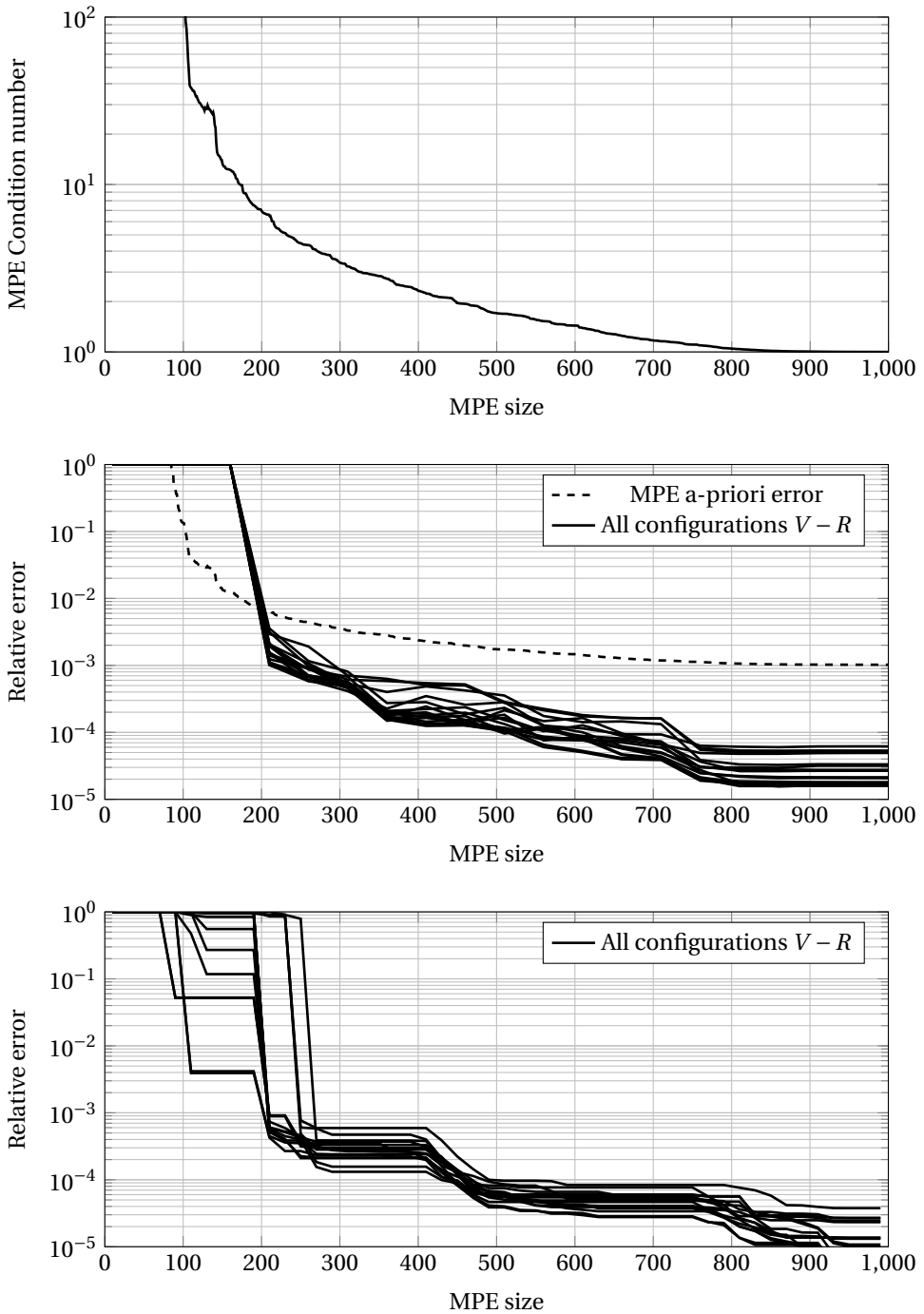
Figure 6.10: (Top) MPE size vs MPE condition number. (Middle) Relative error (all cases) vs MPE size (MPE indices determined from 50-mode POD basis). (Bottom) Relative error (all cases) vs MPE size (MPE indices determined from 340-mode POD basis)
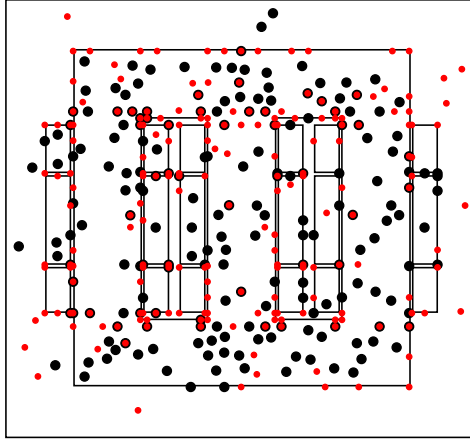
Figure 6.11: Comparison of 200 MPE first points based on 50-mode POD basis (black) and 340-mode POD basis (red).

All other indices are then determined using the MPE algorithm. The 200 first MPE points are shown in Fig. 6.12 for all four scenarios. The related results are shown in Fig. 6.13 and can be analyzed as follows:

1. Scenario 1: the decay is not monolithic and 1% is reached with 230 elements. This is 15% larger than with the automatic determination from Fig. 6.10.

2. Scenario 2: the results are very similar to those from the automatic determination by the MPE algorithm.

3. Scenario 3: similar to the observation of scenario 2. This insight induces two explanations. First, the extra points in the air, which is linear, do not add significant useful information as expected. Secondly, there is no need to specify critical regions first (e.g. with an experienced user), as the automatic determination from scratch using the MPE algorithm equally performs.

4. Scenario 4: at a first glance, the results are very similar to the one obtained with the automatic determination. However, two test configurations do not reach .1% relative error with less than 350 elements contrary to the previous test cases. In addition, the lack of an *a priori* MPE error bound represents also a disadvantage of choosing a random selection of points. In conclusion, random selection of the nonlinear indices may provide sufficiently good results but can be improved by using the MPE automatic algorithm without forcing any element in case of unknown nonlinear patterns [15, 171].

6.9 Conclusion

The coupling between numerical HFMs based on Maxwell's equations and external (differential) algebraic electric network equations is of great interest to eliminate the
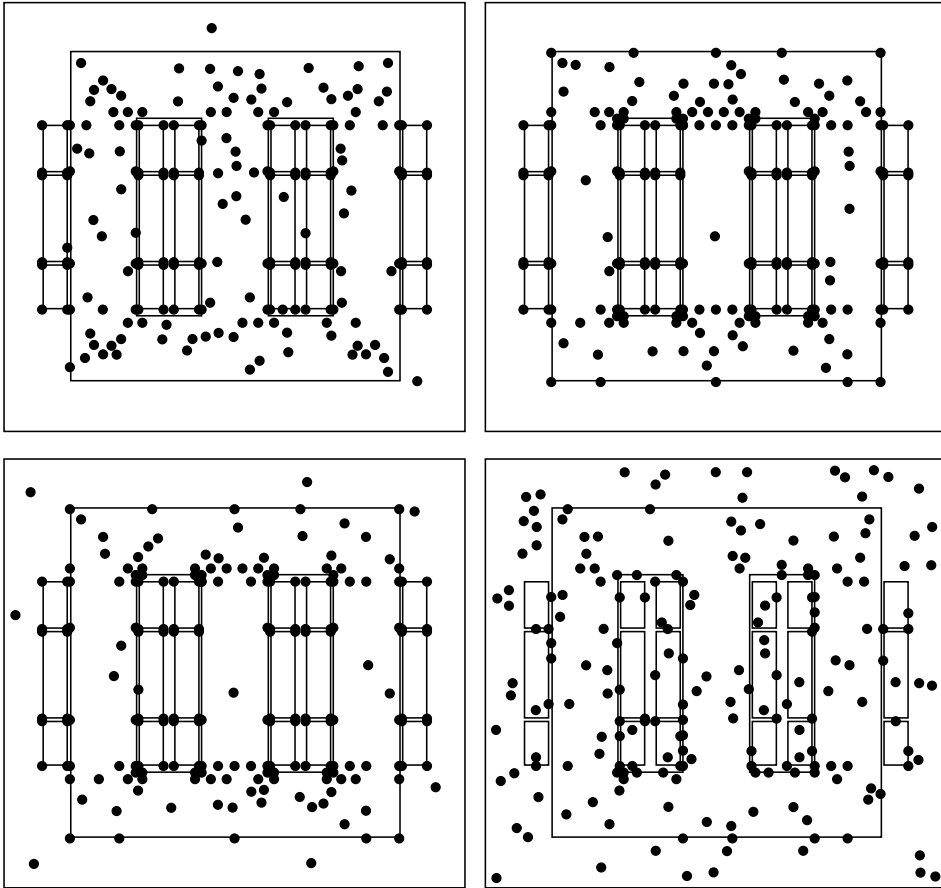
Figure 6.12: 200 first MPE indices in scenario 1 (top-left), 2 (top-right), 3 (bottom-left) and 4 (bottom-right). In scenario 1, 95 indices are forced in the coil. In scenario 2, 165 are forced in coil and core. In scenario 3, 172 are forced in coil, core and air. In scenario 4, random indices are chosen.
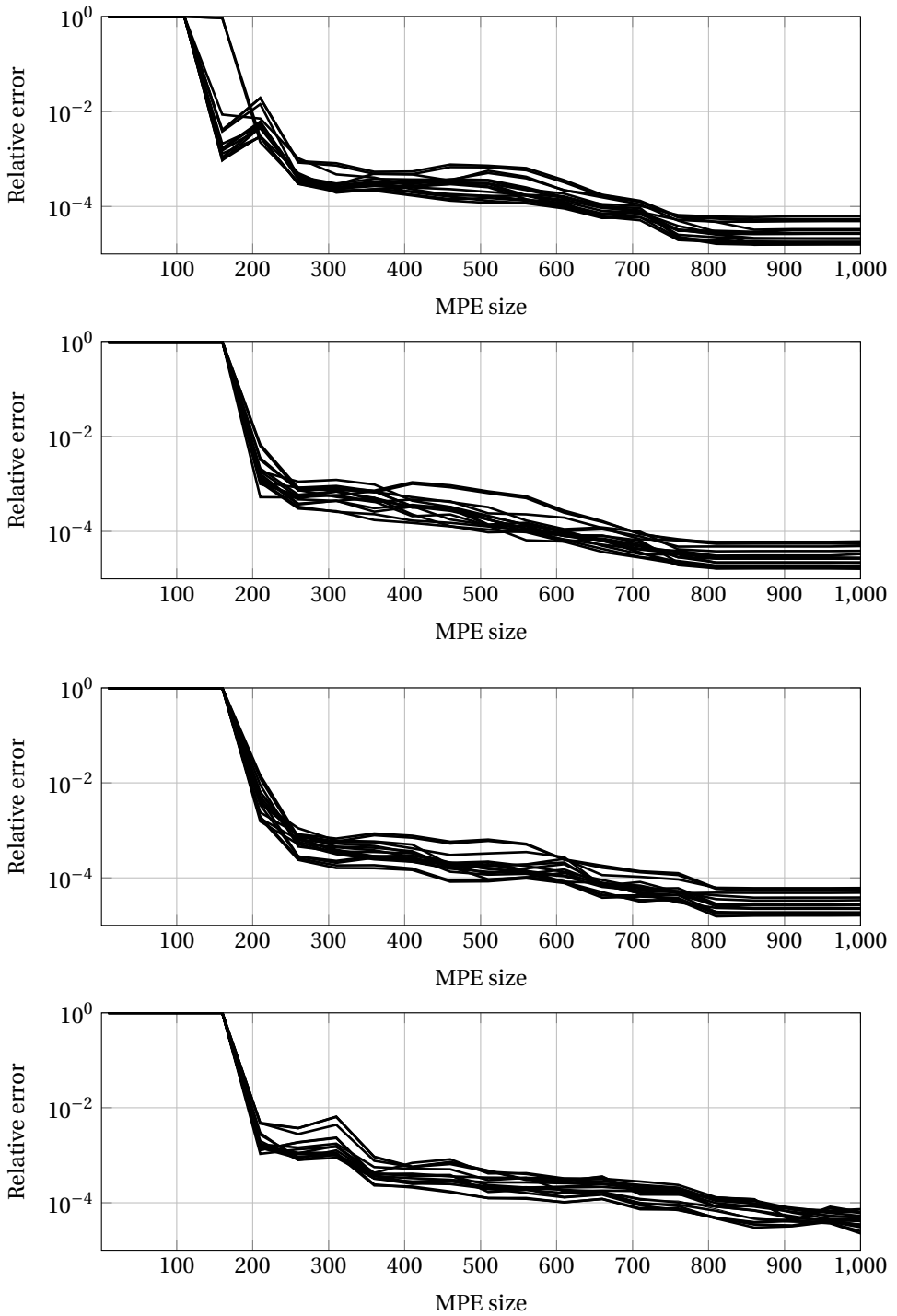
Figure 6.13: Relative error (all cases) vs MPE size for scenario 1, 2, 3 and 4.

Table 6.3: Synthesis of model order reduction results on the coupled three-phased voltage-driven power transformer.

Method	Robustness	Resolution reduction ratio	Assembly reduction ratio	Relative error	Speed-up
FULL	✓	/	/	/	/
POD coupled	✗	/	/	/	/
POD decoupled	✓	99%	0%	1e-4	0x
POD-MPE	✓	99%	97%	1e-3	~ 60x
POD-DEIM/DIME	✗	/	/	/	/

need of human knowledge and automatize design, optimisation and operational stages of electromagnetic energy conversion devices. However, those HFMs are described through discretization techniques, e.g. the FEM, and lead to expensive assemblies and resolutions both in time and in required resources. In order to cope with this limitation, model order reduction techniques have been a hot topic for the last two decades.

In this last chapter, the direct use of the POD on the original coupled problem leads to unstable and ill-conditioned systems–requiring another reduction methodology for such problems. A (novel) decoupled approach in magnetodynamics is developed by investigating several reduction techniques to efficiently and drastically reduce the complexity of a coupled parametric system by only curtailing the high fidelity formulation using the appropriate reduction mapping.

As an application, the HFM is made of a nonlinear magnetodynamic three-phase transformer coupled to three electric circuits (one input and two outputs). The obtained reduction ratios are higher than 97% for both resolution and assembly processes–allowing a theoretical speed-up around 350 for the "state of the art" logarithmic solvers. However, we showed that all reduction methods may not permit an efficient and/or reliable curtailment as the obtained relative errors may be too large—misleading the direct/general use of such methods for all problems and requiring particular investigation for each situation.

Table 6.3 lists the results from all the investigated approaches with a practical (engineer) error criterion—even if the method was not robust. As both stages are time consuming and scales logarithmically for the best solvers [43, 106, 107], the corresponding speed-up factor is the theoretical minimum achievable between the speed-ups from the resolution and the assembly reduction parts. In case of the solver scales in $\mathcal{O}(n^2)$, the speed-ups are in the order of $\mathcal{O}((1-\eta)^{-2})$ where η is the reduction ratio.

Conclusion

In this thesis, we investigated several model order reduction techniques to handle parametric electromagnetic models involving linear, nonlinear, dynamic and coupled aspects. The main achievements and conclusions, already presented at the end of each chapter, are summarized hereafter. Subsequently, an overview of future prospects are proposed.

Main achievements and conclusions

High fidelity modeling provides an outstanding accuracy compared to equivalent models, however the computational time required to solve them remains its biggest disadvantage. Creating robust and stable reduced order models of such systems to describe, optimize and operate electromagnetic applications is crucial for further developments. Therefore, a major part of this thesis was dedicated to the investigation of the available reduced order model techniques in several research areas.

First, we proposed several algorithms to automate the reduction procedure of linear electromagetics in both time and frequency domains. This allows to avoid any arbitrary choice as it is often the case with the selection of snapshots, their number, their spacing (in time or frequency), etc. The proposed algorithms have been tested on two applications: a transformer and a microwave antenna with two different linear reduced order model techniques: the Proper Orthogonal Decomposition and the Arnoldi Krylov-based method. The results show important reduction above 99% in all tested situations —in agreement with the intensive research for linear applications in the literature.

Then, the reduction of nonlinear magnetodynamics has been investigated by the means of the Missing Point Estimation and the Discrete Empirical Interpolation Method—two element sampling methods which only evaluate a reduced set of entries in nonlinear matrices. The results show significant stable and robust reduction of 95% in the assembly phase with the (preferred) MPE method regardless of the input values for a three-phase power transformer over the DEIM. Indeed, DEIM method suffers from a lack of robustness with regards to *a priori* independent parameters such as the time stepping discretisation or the conductivity value.

As the input and the output values change either in design or operational processes, building appropriate parametrized reduced order model is then necessary and two complementary philosophies have been investigated. The first one, consisting in building a global basis for all parameters, is a well-known method in electromagnetic reduction while the second one deals with nonlinear interpolation of reduced bases (generated at different parameter values) and has been first introduced in aeronautics. Although the

systematic investigation showed interesting results, the global basis approach remains the preferred one as it provides better results (*i.e.* one order of magnitude lower) and is easier to deal with for the limited parameter space considered in our applications.

Lastly, the coupling of the reduced model of a three-phase power transformer with external electric network presented issues by the direct use of the aforementioned linear methods and nonlinear sampling techniques. Indeed, the reduced system presents robustness problems—avoiding the brute force reduction concepts detailed up to now. To solve this instability problem, a decoupled approach has been detailed to only curtail the local variables coming from the high fidelity discretisation of the transformer, while preserving the global quantities intact. Although this approach may be simple, it has–to the best of our knowledge–never been explored in electromagnetic applications. The obtained results showed a reduction above 95% in both the resolution and the assembly processes during the online stage (i.e. without considering the training procedure)—allowing a speedup of a factor 60 with a relative error of 0.1%.

Future prospects

Several suggestions for future work are listed hereafter:

1. A better MPE (*a priori*) error criterion should be determined. While it showed promising accordance with the obtained results in thermodynamics, we have shown the limit of its general formulation in magnetodynamics. In a sense, an optimal algorithm could provide a better suited criterion than the greedy approach proposed in [15].

2. The DEIM/DIME method has been efficiently applied to 3D static applications [100]. However, it failed in our dynamic test applications. Further mathematical analysis is needed to explain this lack of robustness.

3. An electromagnetic specifically dedicated sampling method could be elaborated to outperform the results obtained with the POD-MPE approach. This method should be able to accurately determine the critical regions for electromagnetic applications with an important interest in nonlinear, dynamical, parametric and coupling considerations.

4. We considered the element sampling method as the best approach in contrast to the projection technique which implies numerous multiplications between the sampled matrices and the sampled POD basis—which can become rather costly in practice. However, a direct generation of the reduced nonlinear matrices with respect to the reduced states–by integrating this operator in the discretized generation of the nonlinear terms–would eliminate the need of the projection or the element sampling approaches. This prospect is worth investigating as a major potential breakthrough.

5. We determined the nonlinear interpolation on manifold as ineffective compared to the global basis method for parametric problems. However, the frequency variation in the applications we considered may be too limited to reveal the

advantage of the aforementioned approach. As our applications did not involve large variations of the parameter values, the global basis method works perfectly fine but other electromagnetic applications should investigate the nonlinear interpolation when the number of parameters and their intensity variations are larger than proposed in this dissertation.

6. We only considered balanced resistive loads in the coupled three-phase transformer. The following cases should be studied:

    a) Unbalanced resistive loads.

    b) Balanced complex loads (comprising capacitances and inductances).

    c) Unbalanced complex loads.

    d) Abrupt change in the input or output configurations.

    e) The appropriate training strategies for such systems.

    f) The coupling of multiple reduced models within a single electric circuit.

7. Lastly, we did not take movement (which is crucial for the modeling of e.g. rotating machines) into account in the energy conversion applications that we considered. The development of model order reduction techniques applied to the finite element method in this context remains an active research area, where the various methodologies to handle movement (remeshing, dynamic periodicity conditions, mortar methods, etc) need to be integrated. In the case of rotating machines, a possible alternative, which would be directly amenable to the methods proposed in this thesis, is the use of a multi-harmonic steady-state formulation for the period movement [92].

"During a PhD, we try to give answers but I think it's more about finding the right question." Prof. K. Willcox, Paris 2015.

List of Figures

List of Tables

List of Acronyms

AKS   Arnoldi Krylov Subspace

BT   Balanced Truncation

DEIM   Discrete Empirical Interpolation Method

FDM   Finite Difference Method

FE   Finite Element

FEM   Finite Element Method

FVM   Finite Volume Method

HFM   High Fidelity Model

KLD   Karhunen-Loeve Decomposition

LPM   Lumped Parameter Model

MOR   Model Order Reduction

MPE   Missing Point Estimation

ODE   Ordinary Differential Equation

PCA   Principal Component Analysis

PDE   Partial Differential Equation

PGD   Proper Generalized Decomposition

POD   Proper Orthogonal Decomposition

ROM   Reduced Order Model

SVD   Singular Value Decomposition

TPWL   Trajectory Piece-Wise Linear

TPWP   Trajectory Piece-Wise Polynomial

List of Symbols

Common symbols

$\mathbb{R}$	: Set of real numbers
$\mathbb{R}^n$	: Set of all vectors of dimension n with real numbers
$\mathbb{R}^{n \times m}$	: Set of all $n \times m$ matrices with real numbers

Operators

^{T}	: (Conjugate) Transpose
$\cdot$	: Scalar product
$\times$	: Vector product
$\|\boldsymbol{a}\|$	: 2-norm of a vector, equals to $\sqrt{\boldsymbol{a} \cdot \boldsymbol{a}}$
d_x	: First-order derivative
∂_x	: First-order partial derivative
$(\boldsymbol{a}, \boldsymbol{a}')_\Omega$	: Volume integral of $\boldsymbol{a} \cdot \boldsymbol{a}'$ over Ω
$\langle \boldsymbol{a}, \boldsymbol{a}' \rangle_\Gamma$	: Surface integral of $\boldsymbol{a} \cdot \boldsymbol{a}'$ over Γ

Specific symbols for electromagnetism

ε	: Electric permittivity (F/m)
ε_0	: Electric permittivity of vacuum ($\approx 8.854187817 \, 10^{-12}$ F/m)
μ	: Magnetic permeability [H/m]
μ_0	: Magnetic permeability of vacuum ($= 4\pi \, 10^{-7}$ H/m)
ν	: Magnetic reluctivity ($1/\mu$)
$\underline{\mathbf{a}}/\mathbf{a}$	: Continuous/Discrete Magnetic vector potential (Wb/m)
$\underline{\mathbf{b}}/\mathbf{b}$	: Continuous/Discrete Magnetic induction field (T)
$\underline{\mathbf{h}}/\mathbf{h}$	: Continuous/Discrete Magnetic field (A/m)
$\underline{\mathbf{d}}/\mathbf{d}$	: Continuous/Discrete Displacement current (C/m^2)
$\underline{\mathbf{e}}/\mathbf{e}$	: Continuous/Discrete Electric field (V/m)
$\mathbf{z}$	: Input impedance of antenna (Ω)
n	: Size of High Fidelity Model
r	: Resolution size
q	: Assembly size

Bibliography

[1] Y. Achdou and O. Pironneau. *Computational methods for option pricing*. SIAM, 2005.

[2] M. N. Albunni, V. Rischmuller, T. Fritzsche, and B. Lohmann. Model-order reduction of moving nonlinear electromagnetic devices. *IEEE Transactions on Magnetics*, 44(7):1822–1829, 2008.

[3] A. Ammar, B. Mokdad, F. Chinesta, and R. Keunings. A new family of solvers for some classes of multidimensional partial differential equations encountered in kinetic theory modeling of complex fluids. *Journal of Non-Newtonian Fluid Mechanics*, 139(3):153–176, 2006.

[4] D. Amsallem. *Interpolation on manifolds of CFD-based fluid and finite element-based structural reduced-order models for on-line aeroelastic predictions*. PhD thesis, Stanford University, 2010.

[5] D. Amsallem and C. Farhat. Interpolation method for adapting reduced-order models and application to aeroelasticity. *AIAA Journal*, 46(7):1803–1813, 2008.

[6] D. Amsallem and C. Farhat. An online method for interpolating linear parametric reduced-order models. *SIAM Journal on Scientific Computing*, 33(5):2169–2198, 2011.

[7] D. Amsallem, J. Cortial, K. Carlberg, and C. Farhat. A method for interpolating on manifolds structural dynamics reduced-order models. *International Journal for numerical methods in engineering*, 80(9):1241, 2009.

[8] D. Amsallem, J. Cortial, and C. Farhat. Towards real-time computational-fluid-dynamics-based aeroelastic computations using a database of reduced-order information. *AIAA Journal*, 48(9):2029–2037, 2010.

[9] D. Amsallem, M. J. Zahr, and C. Farhat. Nonlinear model order reduction based on local reduced-order bases. *International Journal for Numerical Methods in Engineering*, 92(10):891–916, 2012.

[10] A. C. Antoulas. *Approximation of large-scale dynamical systems*. SIAM, 2005.

[11] A. C. Antoulas and D. C. Sorensen. Approximation of large-scale dynamical systems: An overview. *Applied Mathematics and Computer Science*, 11(5):1093–1122, 2001.

[12] A. C. Antoulas, D. C. Sorensen, and S. Gugercin. A survey of model reduction methods for large-scale systems. *Contemporary mathematics*, 280:193–220, 2001.

[13]   P. Astrid and S. Weiland. On the construction of POD models from partial ob-
        servations. In *Proceedings of 44th IEEE Conference on Decision and Control and
        European Control Conference (CDC-ECC 2005)*, pages 2272–2277, Sevilla, Spain,
        2005.

[14]   P. Astrid, S. Weiland, and K. Willcox. On the acceleration of the POD-based
        model reduction technique. In *Proceedings of 16th International Symposium on
        Mathematical Theory of Network and Systems*, Leuven, Belgium, 2004.

[15]   P. Astrid, S. Weiland, K. Willcox, and T. Backx. Missing point estimation in models
        described by proper orthogonal decomposition. *IEEE Transactions on Automatic
        Control*, 53(10):2237–2251, 2008.

[16]   Z. Bai. Krylov subspace techniques for reduced-order modeling of large-scale
        dynamical systems. *Applied numerical mathematics*, 43(1-2):9–44, 2002.

[17]   Z. Bai and D. Skoogh. A projection method for model reduction of bilinear
        dynamical systems. *Linear Algebra and its Applications*, 415(2):406 – 425, 2006.

[18]   S. Barnett and C. Storey. Some applications of the lyapunov matrix equation. *IMA
        Journal of Applied Mathematics*, 4(1):33–42, 1968.

[19]   M. Barrault, Y. Maday, N. C. Nguyen, and A. T. Patera. An 'empirical interpo-
        lation'method: application to efficient reduced-basis discretization of partial
        differential equations. *Comptes Rendus Mathematique*, 339(9):667–672, 2004.

[20]   K.-J. Bathe and E. L. Wilson. *Numerical methods in finite element analysis*, volume
        197. Prentice-Hall Englewood Cliffs, NJ, 1976.

[21]   U. Baur, C. Beattie, P. Benner, and S. Gugercin. Interpolatory projection methods
        for parameterized model reduction. *SIAM Journal on Scientific Computing*, 33(5):
        2489–2518, 2011.

[22]   T. Bechtold, M. Striebel, K. Mohaghegh, and E. Ter Maten. Nonlinear model
        order reduction in nanoelectronics: combination of POD and TPWL. *PAMM*, 8(1):
        10057–10060, 2008.

[23]   Y. Bengio, I. J. Goodfellow, and A. Courville. Deep learning. *Nature*, 521:436–444,
        2015.

[24]   P. Benner, L. Feng, S. Li, and Y. Zhang. Reduced-order modeling and rom-based
        optimization of batch chromatography. In *Numerical Mathematics and Advanced
        Applications-ENUMATH 2013*, pages 427–435. Springer, 2015.

[25]   P. Benner, S. Gugercin, and K. Willcox. A survey of projection-based model
        reduction methods for parametric dynamical systems. *SIAM review*, 57(4):483–
        531, 2015.

[26]   J.-P. Berenger. A perfectly matched layer for the absorption of electromagnetic
        waves. *Journal of computational physics*, 114(2):185–200, 1994.

[27]   G. Berkooz, P. Holmes, and J. L. Lumley. The proper orthogonal decomposition in
        the analysis of turbulent flows. *Annual review of fluid mechanics*, 25(1):539–575,
        1993.

[28]   B. Besselink, U. Tabak, A. Lutowska, N. Van De Wouw, H. Nijmeijer, D. Rixen,
        M. Hochstenbach, and W. Schilders. A comparison of model reduction techniques

from structural dynamics, numerical mathematics and systems and control. *Journal of Sound and Vibration*, 332(19):4403–4422, 2013.

[29] O. Bíró, D. A. Lowther, P. Alotto, M. Clemens, S. Schöps, H. De Gersem, and A. Bartel. Decomposition and regularization of nonlinear anisotropic curl-curl DAEs. *COMPEL-The International Journal for computation and mathematics in electrical and electronic engineering*, 30(6):1701–1714, 2011.

[30] B. N. Bond and L. Daniel. A piecewise-linear moment-matching approach to parameterized model-order reduction for highly nonlinear systems. *IEEE Transactions on Computer-Aided Design of Integrated Circuits and Systems*, 26(12): 2116–2129, 2007.

[31] A. Bossavit. Whitney forms: A class of finite elements for three-dimensional computations in electromagnetism. *IEE Proceedings A (Physical Science, Measurement and Instrumentation, Management and Education, Reviews)*, 135(8): 493–500, 1988.

[32] A. Bossavit. *Electromagnetisme, en vue de la modelisation*, volume 14. Springer Science & Business Media, 2004.

[33] S. Boyd and L. Chua. Fading memory and the problem of approximating nonlinear operators with volterra series. *IEEE Transactions on Circuits and Systems*, 32(11): 1150–1161, 1985.

[34] S. Boyd, Y. Tang, and L. Chua. Measuring volterra kernels. *IEEE Transactions on Circuits and Systems*, 30(8):571–577, 1983.

[35] S. Boyd, L. O. Chua, and C. A. Desoer. Analytical foundations of volterra series. *IMA Journal of Mathematical Control and Information*, 1(3):243–282, 1984.

[36] R. W. Brockett. Volterra series and geometric control theory. *Automatica*, 12(2): 167 – 176, 1976.

[37] R. W. Brockett. Volterra series and geometric control theory. *Automatica*, 12(2): 167–176, 1976.

[38] A. Buffa, Y. Maday, A. T. Patera, C. Prud'homme, and G. Turinici. A priori convergence of the greedy algorithm for the parametrized reduced basis method. *ESAIM: Mathematical Modelling and Numerical Analysis*, 46(3):595–603, 2012.

[39] T. Bui-Thanh, M. Damodaran, and K. Willcox. Aerodynamic data reconstruction and inverse design using proper orthogonal decomposition. *AIAA Journal*, 42(8): 1505–1516, 2004.

[40] T. Bui-Thanh, K. Willcox, and O. Ghattas. Model reduction for large-scale systems with high-dimensional parametric input space. *SIAM Journal on Scientific Computing*, 30(6):3270–3288, 2008.

[41] H.-J. Bungartz and M. Griebel. Sparse grids. *Acta Numerica*, 13:147–269, 2004.

[42] K. Carlberg, C. Farhat, J. Cortial, and D. Amsallem. The gnat method for nonlinear model reduction: effective implementation and application to computational fluid dynamics and turbulent flows. *Journal of Computational Physics*, 242:623–647, 2013.

[43] C. Cecka, A. J. Lew, and E. Darve. Assembly of finite element methods on graphics

processors. *International Journal for Numerical Methods in Engineering*, 85(5): 640–669, 2011.

[44] M. Celanovic. A lumped parameter electromechanical model for describing the nonlinear behavior of piezoelectric actuators. *Journal of dynamic systems, measurement, and control*, 119:478–485, 1997.

[45] S. Chaturantabut and D. C. Sorensen. Discrete empirical interpolation for non-linear model reduction. In *Proceedings of 48th IEEE Conference on Decision and Control*, pages 4316–4321, Shanghai, China, 2009.

[46] S. Chaturantabut and D. C. Sorensen. Nonlinear model reduction via discrete empirical interpolation. *SIAM Journal on Scientific Computing*, 32(5):2737–2764, 2010.

[47] J. A. Cherry. *Distortion analysis of weakly nonlinear filters using volterra series*. PhD thesis, Faculty of Graduate Studies and Research in partial fulfillment of the requirements for the degree of Master of Engineering Ottawa-Carleton Institute for Electrical Engineering, Department of Electronics, Carleton University, Ottawa, 1994.

[48] F. Chinesta, A. Ammar, and E. Cueto. Recent advances and new challenges in the use of the proper generalized decomposition for solving multidimensional models. *Archives of Computational methods in Engineering*, 17(4):327–350, 2010.

[49] F. Chinesta, P. Ladeveze, and E. Cueto. A short review on model order reduction based on proper generalized decomposition. *Archives of Computational Methods in Engineering*, 18(4):395, 2011.

[50] D. Ciregan, U. Meier, and J. Schmidhuber. Multi-column deep neural networks for image classification. In *Proceedings of 2012 IEEE Conference on Computer Vision and Pattern Recognition (CVPR)*, pages 3642–3649, Providence, USA, 2012.

[51] S. Clenet, T. Henneron, and N. Ida. Reduction of a finite-element parametric model using adaptive POD methods—application to uncertainty quantification. *IEEE Transactions on Magnetics*, 52(3):7000704, 2016.

[52] P. Concus, G. H. Golub, and D. P. O'Leary. *A generalized conjugate gradient method for the numerical solution of elliptic partial differential equations*. Computer Science Department, School of Humanities and Sciences, Stanford University, 1976.

[53] P. Concus, G. Golub, and G. Meurant. Block preconditioning for the conjugate gradient method. *SIAM Journal on Scientific and Statistical Computing*, 6(1): 220–252, 1985.

[54] R. R. Craig and M. C. Bampton. Coupling of substructures for dynamic analysis. *AIAA Journal*, 6(7):1313–1319, 1968.

[55] R. Dautray and J.-L. Lions. Analyse mathématique et calcul numérique pour les sciences et les techniques. 1988.

[56] R. Dautray and J.-L. Lions. *Mathematical Analysis and Numerical Methods for Science and Technology: Volume 1 Physical Origins and Classical Methods*. Springer Science & Business Media, 2012.

[57] L. De Lathauwer, B. De Moor, and J. Vandewalle. A multilinear singular value decomposition. *SIAM journal on Matrix Analysis and Applications*, 21(4):1253–1278, 2000.

[58] J. Degroote, J. Vierendeels, and K. Willcox. Interpolation among reduced-order matrices to obtain parameterized models for design, optimization and probabilistic analysis. *International Journal for Numerical Methods in Fluids*, 63(2): 207–230, 2010.

[59] G. Dhatt and G. Touzot. *Une présentation de la méthode des éléments finis*. Presses Université Laval, 1981.

[60] N. Dong and J. Roychowdhury. Piecewise polynomial nonlinear model reduction. In *Proceedings of IEEE Design Automation Conference*, pages 484–489, Anaheim, USA, 2003.

[61] F. J. Doyle, B. A. Ogunnaike, and R. K. Pearson. Nonlinear model-based control using second-order volterra models. *Automatica*, 31(5):697–714, 1995.

[62] Z. Drmac and S. Gugercin. A new selection operator for the discrete empirical interpolation method—improved a priori error bound and extensions. *SIAM Journal on Scientific Computing*, 38(2):A631–A648, 2016.

[63] M. Drohmann, B. Haasdonk, M. Ohlberger, et al. Adaptive reduced basis methods for nonlinear convection-diffusion equations. *Finite Volumes for Complex Applications VI-Problems & Perspectives*, 1:369–377, 2011.

[64] P. Dular. *Modélisation du champ magnétique et des courants induits dans des systèmes tridimensionnels non linéaires*. PhD thesis, Université de Liège, Liège, Belgique, 1994.

[65] P. Dular, C. Geuzaine, F. Henrotte, and W. Legros. A general environment for the treatment of discrete problems and its application to the finite element method. *IEEE Transactions on Magnetics*, 34(5):3395–3398, 1998.

[66] P. Dular, W. Legros, and A. Nicolet. Coupling of local and global quantities in various finite element formulations and its application to electrostatics, magnetostatics and magnetodynamics. *IEEE Transactions on Magnetics*, 34(5):3078–3081, 1998.

[67] P. Dular, F. Henrotte, and W. Legros. A general and natural method to define circuit relations associated with magnetic vector potential formulations. *IEEE Transactions on Magnetics*, 35(3):1630–1633, 1999.

[68] P. Dular, P. Kuo-Peng, C. Geuzaine, N. Sadowski, and J. Bastos. Dual magnetodynamic formulations and their source fields associated with massive and stranded inductors. *IEEE Transactions on Magnetics*, 36(4):1293–1299, 2000.

[69] P. Dular, R. V. Sabariego, and P. Kuo-Peng. Three-dimensional finite element modeling of inductive and capacitive effects in micro-coils. *COMPEL-The International Journal for computation and mathematics in electrical and electronic engineering*, 25(3):642–651, 2006.

[70] J. L. Eftang and B. Stamm. Parameter multi-domain 'hp'empirical interpolation. *International Journal for Numerical Methods in Engineering*, 90(4):412–428, 2012.

[71] C. Emson and J. Simkin. An optimal method for 3-D eddy currents. *IEEE Transactions on Magnetics*, 19(6):2450–2452, 1983.

[72] B. Engquist and A. Majda. Absorbing boundary conditions for numerical simulation of waves. *Proceedings of the National Academy of Sciences*, 74(5):1765–1766, 1977.

[73] D. F. Enns. Model reduction with balanced realizations: An error bound and a frequency weighted generalization. In *Proceedings of 23rd IEEE Conference on Decision and Control*, volume 23, pages 127–132, Las Vegas, USA, 1984.

[74] R. Everson and L. Sirovich. Karhunen–loeve procedure for gappy data. *JOSA A*, 12 (8):1657–1664, 1995.

[75] R. W. Freund. Model reduction methods based on Krylov subspaces. *Acta Numerica*, 12:267–319, 2003.

[76] K. Fukunaga and W. L. Koontz. Application of the Karhunen-Loeve expansion to feature selection and ordering. *IEEE Transactions on Computers*, 100(4):311–318, 1970.

[77] N. Galoppo, N. K. Govindaraju, M. Henson, and D. Manocha. Lu-gpu: Efficient algorithms for solving dense linear systems on graphics hardware. In *Proceedings of 2005 ACM/IEEE conference on Supercomputing*, page 3, Seattle, USA, 2005.

[78] C. Geuzaine. High order hybrid finite element schemes for maxwell's equations taking thin structures and global quantities into account. *University of Liege Faculty of Applied Sciences, doctoral thesis*, 2001.

[79] C. Geuzaine, P. Dular, and W. Legros. A general environment for the treatment of discrete problems and its application to coupled finite element and boundary integral methods. In *Proceedings of 8th International IGTE Symposium on Numerical Field Calculation in Electrical Engineering*, Graz, Austria, 1998.

[80] M. Goldfarb and N. Celanovic. Modeling piezoelectric stack actuators for control of micromanipulation. *IEEE Control Systems Magazine*, 17(3):69–79, 1997.

[81] G. H. Golub and C. Reinsch. Singular value decomposition and least squares solutions. *Numerische mathematik*, 14(5):403–420, 1970.

[82] D. Gratton and K. Willcox. Reduced-order, trajectory piecewise-linear models for nonlinear computational fluid dynamics. In *Proceedings of 34th AIAA Fluid Dynamics Conference and Exhibit*, page 2329, Portland, USA, 2004.

[83] M. A. Grepl, Y. Maday, N. C. Nguyen, and A. T. Patera. Efficient reduced-basis treatment of nonaffine and nonlinear partial differential equations. *ESAIM: Mathematical Modelling and Numerical Analysis*, 41(3):575–605, 2007.

[84] E. J. Grimme. *Krylov projection methods for model reduction*. PhD thesis, Citeseer, 1997.

[85] C. Gu and J. Roychowdhury. Model reduction via projection onto nonlinear manifolds, with applications to analog circuits and biochemical systems. In *Proceedings of IEEE/ACM International Conference on Computer-Aided Design*, pages 85–92, San Jose, USA, 2008.

[86] S. Gugercin and A. C. Antoulas. A survey of model reduction by balanced trun-
      cation and some new results. *International Journal of Control*, 77(8):748–766,
      2004.

[87] S. Gugercin, D. C. Sorensen, and A. C. Antoulas. A modified low-rank smith
      method for large-scale Lyapunov equations. *Numerical Algorithms*, 32(1):27–55,
      2003.

[88] K. Gurney. *An introduction to neural networks.* CRC press, 1997.

[89] R. J. Guyan. Reduction of stiffness and mass matrices. *AIAA Journal*, 3(2):380,
      1965.

[90] J. Gyselinck. *Twee-dimensionale dynamische eindige-elementenmodellering van
      statische en roterende elektromagnetische energieomzetters.* PhD thesis, Univer-
      siteit Gent, 2000.

[91] J. Gyselinck, L. Vandevelde, J. Melkebeek, P. Dular, F. Henrotte, and W. Legros.
      Calculation of eddy currents and associated losses in electrical steel laminations.
      IEEE Transactions on Magnetics, 35(3):1191–1194, 1999.

[92] J. Gyselinck, L. Vandevelde, P. Dular, C. Geuzaine, and W. Legros. A general method
      for the frequency domain fe modeling of rotating electromagnetic devices. *IEEE
      Transactions on Magnetics*, 39(3):1147–1150, 2003.

[93] B. Haasdonk and M. Ohlberger. Reduced basis method for finite volume ap-
      proximations of parametrized linear evolution equations. *ESAIM: Mathematical
      Modelling and Numerical Analysis*, 42(2):277–302, 2008.

[94] B. Haasdonk, M. Dihlmann, and M. Ohlberger. A training set and multiple bases
      generation approach for parameterized model reduction based on adaptive grids
      in parameter space. *Mathematical and Computer Modelling of Dynamical Sys-
      tems*, 17(4):423–442, 2011.

[95] M. R. Hasan, R. V. Sabariego, C. Geuzaine, and Y. Paquay. Proper orthogonal de-
      composition versus Krylov subspace methods in reduced-order energy-converter
      models. In *Proceedings of 2016 IEEE International Energy Conference (ENERGY-
      CON)*, number 16156643, Leuven, Belgium, 2016.

[96] A. Hay, J. Borggaard, I. Akhtar, and D. Pelletier. Reduced-order models for pa-
      rameter dependent geometries based on shape sensitivity analysis. *Journal of
      Computational Physics*, 229(4):1327–1352, 2010.

[97] J. He and L. Durlofsky. Constraint reduction procedures for reduced-order sub-
      surface flow models based on POD-TPWL. *International Journal for Numerical
      Methods in Engineering*, 103(1):1–30, 2015.

[98] T. Henneron and S. Clénet. Model order reduction of quasi-static problems based
      on POD and PGD approaches. *The European Physical Journal Applied Physics*, 64
      (2):24514, 2013.

[99] T. Henneron and S. Clenet. Model order reduction of non-linear magnetostatic
      problems based on POD and DEI methods. *IEEE Transactions on Magnetics*, 50
      (2):33–36, 2014.

[100] T. Henneron and S. Clenet. Application of the PGD and DEIM to solve a 3-D

non-linear magnetostatic problem coupled with the circuit equations. *IEEE Transactions on Magnetics*, 52(3):7202104, 2016.

[101] T. Henneron, A. Benabou, and S. Clenet. Nonlinear proper generalized decomposition method applied to the magnetic simulation of a SMC microstructure. *IEEE Transactions on Magnetics*, 48(11):3242–3245, 2012.

[102] T. Henneron, H. Mac, and S. Clenet. Error estimation of a proper orthogonal decomposition reduced model of a permanent magnet synchronous machine. *IET Science, Measurement & Technology*, 9(2):172–177, 2015.

[103] D. Hickey, L. Masset, G. Kerschen, and O. Brüls. Proper orthogonal decomposition for nonlinear radiative heat transfer problems. In *Proceedings of ASME 2011 International Design Engineering Technical Conferences and Computers and Information in Engineering Conference*, pages 407–418, Washington DC, USA, 2011.

[104] D. A. Hill, J. G. Van Bladel, J. A. Stratton, L. Josefsson, P. Persson, Y. Zhu, and A. C. Cangellaris. Time-harmonic electromagnetic fields. 1961.

[105] G. Hinton, O. Vinyals, and J. Dean. Distilling the knowledge in a neural network. *arXiv preprint arXiv:1503.02531*, 2015.

[106] R. Hiptmair and J. Xu. Nodal auxiliary space preconditioning in H (curl) and H (div) spaces. *SIAM Journal on Numerical Analysis*, 45(6):2483–2509, 2007.

[107] R. Hiptmair and J. Xu. Auxiliary space preconditioning for edge elements. *IEEE Transactions on Magnetics*, 44(6):938–941, 2008.

[108] W. C. Hurty. Dynamic analysis of structural systems using component modes. *AIAA Journal*, 3(4):678–685, 1965.

[109] I. M. Jaimoukha and E. M. Kasenally. Krylov subspace methods for solving large lyapunov equations. *SIAM Journal on Numerical Analysis*, 31(1):227–251, 1994.

[110] C. Johnson. *Numerical solution of partial differential equations by the finite element method*. Courier Corporation, 2012.

[111] I. Jolliffe. *Principal component analysis*. Wiley Online Library, 2002.

[112] A. Kameari. Calculation of transient 3d eddy current using edge-elements. *IEEE Transactions on Magnetics*, 26(2):466–469, 1990.

[113] G. Kepler, H. Tran, and H. Banks. Reduced order model compensator control of species transport in a cvd reactor. *Optimal Control Applications and Methods*, 21 (4):143–160, 2000.

[114] G. M. Kepler, H. T. Tran, and H. Banks. Compensator control for chemical vapor deposition film growth using reduced-order design models. *IEEE Transactions on semiconductor manufacturing*, 14(3):231–241, 2001.

[115] G. M. Kepler, H. Banks, H. Tran, and S. Beeler. Reduced order modeling and control of thin film growth in an hpcvd reactor. *SIAM Journal on Applied Mathematics*, 62(4):1251–1280, 2002.

[116] G. Kerschen, J.-c. Golinval, A. F. Vakakis, and L. A. Bergman. The method of proper orthogonal decomposition for dynamical characterization and order reduction of mechanical systems: an overview. *Nonlinear dynamics*, 41(1):147–169, 2005.

[117] D. S. Kershaw. The incomplete cholesky—conjugate gradient method for the iterative solution of systems of linear equations. *Journal of Computational Physics*, 26(1):43–65, 1978.

[118] M. Kirby and L. Sirovich. Application of the Karhunen-Loeve procedure for the characterization of human faces. *IEEE Transactions on Pattern analysis and Machine intelligence*, 12(1):103–108, 1990.

[119] K. S. Kumar. *Electric circuits and networks*. Pearson Education India, 2009.

[120] K. S. Kunz and R. J. Luebbers. *The finite difference time domain method for electromagnetics*. CRC press, 1993.

[121] P. Ladeveze, J.-C. Passieux, and D. Néron. The latin multiscale computational method and the proper generalized decomposition. *Computer Methods in Applied Mechanics and Engineering*, 199(21):1287–1296, 2010.

[122] R. B. Laughlin and D. Pines. The theory of everything. *Proceedings of the National Academy of Sciences of the United States of America*, pages 28–31, 2000.

[123] Y. LeCun, L. Bottou, Y. Bengio, and P. Haffner. Gradient-based learning applied to document recognition. *Proceedings of the IEEE*, 86(11):2278–2324, 1998.

[124] Y. LeCun, Y. Bengio, and G. Hinton. Deep learning. *Nature*, 521(7553):436–444, 2015.

[125] J.-R. Li. *Model reduction of large linear systems via low rank system gramians*. PhD thesis, Massachusetts Institute of Technology, 2000.

[126] S. Li. *Fast algorithms for sparse matrix inverse computations*. PhD thesis, Citeseer, 2009.

[127] Y. Liang, W. Lin, H. Lee, S. Lim, K. Lee, and D. Feng. A neural-network-based method of model reduction for the dynamic simulation of MEMS. *Journal of Micromechanics and Microengineering*, 11(3):226, 2001.

[128] Y. Liang, W. Lin, H. Lee, S. Lim, K. Lee, and H. Sun. Proper orthogonal decomposition and its applications–part ii: Model reduction for MEMS dynamical analysis. *Journal of Sound and Vibration*, 256(3):515–532, 2002.

[129] H. Liu and N. Wong. Autonomous volterra algorithm for steady-state analysis of nonlinear circuits. *IEEE Transactions on Computer-Aided Design of Integrated Circuits and Systems*, 32(6):858–868, 2013.

[130] B. Lohmann and R. Eid. Efficient order reduction of parametric and nonlinear models by superposition of locally reduced models. In *Methoden und Anwendungen der Regelungstechnik. Erlangen-Münchener Workshops*, pages 27–36, 2007.

[131] E. C. Lovelace, T. M. Jahns, and J. H. Lang. A saturating lumped-parameter model for an interior pm synchronous machine. *IEEE Transactions on Industry Applications*, 38(3):645–650, 2002.

[132] A. M. Lyapunov. The general problem of the stability of motion. *International Journal of Control*, 55(3):531–534, 1992.

[133] X. Ma and J. De Abreu-Garcia. On the computation of reduced order models of nonlinear systems using balancing technique. In *Proceedings of 27th IEEE Conference on Decision and Control*, pages 1165–1166, Austin, USA, 1988.

[134] Y. Maday, A. Patera, and G. Turinici. Reliable real-time solution of parametrized partial differential equations: Reduced-basis output bound methods. *J. Fluids Eng*, 124(1):70–80, 2002.

[135] J. C. Maxwell. *A treatise on electricity and magnetism*, volume 1. Clarendon press, 1881.

[136] R. Melhem. Parallel gauss-jordan elimination for the solution of dense linear systems. *Parallel Computing*, 4(3):339–343, 1987.

[137] P. Mellor, D. Roberts, and D. Turner. Lumped parameter thermal model for electrical machines of TEFC design. 138(5):205–218, 1991.

[138] S. Mijalkovic. Truly nonlinear model-order reduction techniques. In *Proceedings of 7th IEEE International Conference on Thermal, Mechanical and Multiphysics Simulation and Experiments in Micro-Electronics and Micro-Systems*, pages 1–5, Como, Italy, 2006.

[139] A. R. Mitchell and D. F. Griffiths. *The finite difference method in partial differential equations*. John Wiley, 1980.

[140] e. a. Montier, Laurent. Robust model order reduction of a nonlinear electrical machine at start-up through reduction error estimation. In *10th International Symposium on Electric and Magnetic Fields*, 2015.

[141] B. Moore. Principal component analysis in linear systems: Controllability, observability, and model reduction. *IEEE Transactions on automatic control*, 26(1): 17–32, 1981.

[142] C. Mullis and R. Roberts. Synthesis of minimum roundoff noise fixed point digital filters. *IEEE Transactions on Circuits and Systems*, 23(9):551–562, 1976.

[143] G. Mur. Absorbing boundary conditions for the finite-difference approximation of the time-domain electromagnetic-field equations. *IEEE Transactions on Electromagnetic Compatibility*, (4):377–382, 1981.

[144] F. Negri, A. Manzoni, and D. Amsallem. Efficient model reduction of parametrized systems by matrix discrete empirical interpolation. *Journal of Computational Physics*, 303:431–454, 2015.

[145] A. Nouy. A priori model reduction through proper generalized decomposition for solving time-dependent partial differential equations. *Computer Methods in Applied Mechanics and Engineering*, 199(23):1603–1626, 2010.

[146] A. Odabasioglu, M. Celik, and L. T. Pileggi. Prima: Passive reduced-order interconnect macromodeling algorithm. In *Proceedings of 1997 IEEE/ACM international conference on Computer-aided design*, pages 58–65, San Jose, USA, 1997.

[147] H. Panzer, J. Mohring, R. Eid, and B. Lohmann. Parametric model order reduction by matrix interpolation. *at-Automatisierungstechnik Methoden und Anwendungen der Steuerungs-, Regelungs-und Informationstechnik*, 58(8):475–484, 2010.

[148] H. K. Panzer. *Model order reduction by Krylov subspace methods with global error bounds and automatic choice of parameters*. PhD thesis, Universität München, 2014.

[149] Y. Paquay, O. Brüls, and C. Geuzaine. Model order reduction of nonlinear magne-todynamics with manifold interpolation. In *MoRePaS 2015 - Model Reduction of Parametrized Systems III*, 2015.

[150] Y. Paquay, O. Brüls, and C. Geuzaine. Nonlinear interpolation on manifold of reduced-order models in magnetodynamic problems. *IEEE Transactions on Magnetics*, 52(3):7204804, 2016.

[151] Y. Paquay, C. Geuzaine, R. Hasan, and R. V. Sabariego. Reduced-order model accounting for high-frequency effects in power electronic components. *IEEE Transactions on Magnetics*, 52(3):7202904, 2016.

[152] A. T. Patera, G. Rozza, et al. Reduced basis approximation and a posteriori error estimation for parametrized partial differential equations, 2007.

[153] A. Paul-Dubois-Taine and D. Amsallem. An adaptive and efficient greedy proce-dure for the optimal training of parametric reduced-order models. *International Journal for Numerical Methods in Engineering*, 102(5):1262–1292, 2015.

[154] B. Peherstorfer, D. Butnaru, K. Willcox, and H.-J. Bungartz. Localized discrete empirical interpolation method. *SIAM Journal on Scientific Computing*, 36(1): A168–A192, 2014.

[155] S. D. Pekarek, O. Wasynczuk, E. A. Walters, J. V. Jatskevich, C. E. Lucas, N. Wu, and P. T. Lamm. An efficient multirate simulation technique for power-electronic-based systems. *IEEE Transactions on power systems*, 19(1):399–409, 2004.

[156] T. Penzl. A cyclic low-rank smith method for large sparse lyapunov equations. *SIAM Journal on Scientific Computing*, 21(4):1401–1418, 1999.

[157] T. Penzl. Algorithms for model reduction of large dynamical systems. *Linear Algebra and its Applications*, 415(2-3):322–343, 2006.

[158] L. Pernebo and L. Silverman. Model reduction via balanced state space represen-tations. *IEEE Transactions on Automatic Control*, 27(2):382–387, 1982.

[159] G. Peters and J. H. Wilkinson. On the stability of gauss-jordan elimination with pivoting. *Communications of the ACM*, 18(1):20–24, 1975.

[160] J. Phillips. A statistical perspective on nonlinear model reduction. In *Proceedings of 2003 IEEE International Workshop on Behavioral Modeling and Simulation*, pages 41–46, San Jose, USA, 2003.

[161] A. Pierquin, T. Henneron, S. Clénet, and S. Brisset. Model-order reduction of magnetoquasi-static problems based on POD and Arnoldi-based Krylov methods. *IEEE Transactions on Magnetics*, 51(3):7206204, 2015.

[162] F. Plumier, C. Geuzaine, and T. Van Cutsem. A multirate approach to combine electromagnetic transients and fundamental-frequency simulations. In *Proceed-ings of 10th International Conference on Power System Transients*, Vancouver, Canada, 2013.

[163] W. H. Press. *Numerical recipes 3rd edition: The art of scientific computing*. Cam-bridge university press, 2007.

[164] E. Pruliere, F. Chinesta, and A. Ammar. On the deterministic solution of multi-dimensional parametric models using the proper generalized decomposition.

Mathematics and Computers in Simulation, 81(4):791–810, 2010.

[165] M. A. Rahman and P. Zhou. Analysis of brushless permanent magnet synchronous motors. *IEEE Transactions on Industrial Electronics*, 43(2):256–267, 1996.

[166] G. Raithby and E. Chui. A finite-volume method for predicting a radiant heat transfer in enclosures with participating media. *Journal of Heat Transfer*, 112: 415–423, 1990.

[167] M. Rewienski and J. White. A trajectory piecewise-linear approach to model order reduction and fast simulation of nonlinear circuits and micromachined devices. *IEEE Transactions on Computer-Aided Design of Integrated Circuits and Systems*, 22(2):155–170, 2003.

[168] M. Rewieński and J. White. Model order reduction for nonlinear dynamical systems based on trajectory piecewise-linear approximations. *Linear algebra and its applications*, 415(2-3):426–454, 2006.

[169] G. Rozza, D. B. P. Huynh, and A. T. Patera. Reduced basis approximation and a posteriori error estimation for affinely parametrized elliptic coercive partial differential equations. *Archives of Computational Methods in Engineering*, 15(3): 229, 2008.

[170] W. J. Rugh. *Nonlinear system theory.* John Hopkins University Press Baltimore, 1981.

[171] D. Ryckelynck. A priori hyperreduction method: an adaptive approach. *Journal of computational physics*, 202(1):346–366, 2005.

[172] D. Ryckelynck. Hyper-reduction of mechanical models involving internal variables. *International Journal for Numerical Methods in Engineering*, 77(1):75–89, 2009.

[173] D. Ryckelynck, K. Lampoh, and S. Quilicy. Hyper-reduced predictions for lifetime assessment of elasto-plastic structures. *Meccanica*, 51(2):309–317, 2016.

[174] Y. Saad. Krylov subspace methods on supercomputers. *SIAM Journal on Scientific and Statistical Computing*, 10(6):1200–1232, 1989.

[175] B. Salimbahrami, B. Lohmann, and T. Bechtold. Two-sided arnoldi in order reduction of large scale mimo systems. *Sci. Report, IAT, Univ. Bremen*, 2002.

[176] S. B. Salimbahrami. *Structure preserving order reduction of large scale second order models.* PhD thesis, Universität München, 2005.

[177] I. Sandberg. Series expansions for nonlinear systems. *Circuits, Systems, and Signal Processing*, 2(1):77–87, 1983.

[178] I. Sandberg. Volterra-like expansions for solutions of nonlinear integral equations and nonlinear differential equations. *IEEE Transactions on Circuits and Systems*, 30(2):68–77, 1983.

[179] Y. Sato and H. Igarashi. Generation of equivalent circuit from finite-element model using model order reduction. *IEEE Transactions on Magnetics*, 52(3): 1100304, 2016.

[180] Y. Sato, T. Shimotani, and H. Igarashi. Synthesis of cauer-equivalent circuit based on model order reduction considering nonlinear magnetic property. *IEEE*

Transactions on Magnetics, 53(6):1100204, 2017.

[181] J. M. Scherpen. Balancing for nonlinear systems. *Systems & Control Letters*, 21(2): 143–153, 1993.

[182] M. Schetzen. The volterra and wiener theories of nonlinear systems. 1980.

[183] W. H. Schilders, H. A. Van der Vorst, and J. Rommes. *Model order reduction: theory, research aspects and applications*, volume 13. Springer, 2008.

[184] S. Schops, H. De Gersem, and A. Bartel. A cosimulation framework for multi-rate time integration of field/circuit coupled problems. *IEEE Transactions on Magnetics*, 46(8):3233–3236, 2010.

[185] P. Schwarz and P. Schneider. Model library and tool support for MEMS simulation. In *Conference on Microelectronic and MEMS technology*, volume 4407, pages 1–14, Edinburgh, Scotland, 2001.

[186] J. R. Shewchuk et al. An introduction to the conjugate gradient method without the agonizing pain, 1994.

[187] T. Shimotani, Y. Sato, and H. Igarashi. Equivalent-circuit generation from finite-element solution using proper orthogonal decomposition. *IEEE Transactions on Magnetics*, 52(3):7206804, 2016.

[188] J. Shlens. A tutorial on principal component analysis. *arXiv preprint arXiv:1404.1100*, 2014.

[189] D. Silver, A. Huang, C. J. Maddison, A. Guez, L. Sifre, G. Van Den Driessche, J. Schrittwieser, I. Antonoglou, V. Panneershelvam, M. Lanctot, et al. Mastering the game of go with deep neural networks and tree search. *Nature*, 529(7587): 484–489, 2016.

[190] L. Sirovich. Turbulence and the dynamics of coherent structures. i. coherent structures. *Quarterly of applied mathematics*, 45(3):561–571, 1987.

[191] M. Smith. *Neural networks for statistical modeling*. Thomson Learning, 1993.

[192] D. C. Sorensen. Private discussions, 2015.

[193] D. C. Sorensen and A. Antoulas. The sylvester equation and approximate balanced reduction. *Linear algebra and its applications*, 351:671–700, 2002.

[194] J. A. Stratton. *Electromagnetic theory*. John Wiley & Sons, 2007.

[195] T. Stykel. Numerical solution and perturbation theory for generalized lyapunov equations. *Linear Algebra and its Applications*, 349(1-3):155–185, 2002.

[196] A. Taflove and S. C. Hagness. *Computational electrodynamics: the finite-difference time-domain method*. Artech house, 2005.

[197] H. A. Tilmans. Equivalent circuit representation of electromechanical transducers: I. lumped-parameter systems. *Journal of Micromechanics and Microengineering*, 6(1):157, 1996.

[198] A. Verhoeven. Redundancy reduction of ic models by multirate time-integration and model order reduction. *Dept. of Mathematics and Computer Science, University of Technology, Eindhoven, The Netherlands*, 2008.

[199] H. K. Versteeg and W. Malalasekera. *An introduction to computational fluid dynamics: the finite volume method*. Pearson Education, 2007.

[200] D. V. Vranic, D. Saupe, and J. Richter. Tools for 3d-object retrieval: Karhunen-Loeve transform and spherical harmonics. In *Proceedings of 2001 IEEE Fourth Workshop on Multimedia Signal Processing*, pages 293–298, Cannes, France, 2001.

[201] M. E. Wall, A. Rechtsteiner, and L. M. Rocha. Singular value decomposition and principal component analysis. In *A practical approach to microarray data analysis*, pages 91–109. Springer, 2003.

[202] Z. Wang. Nonlinear model reduction based on the finite element method with interpolated coefficients: Semilinear parabolic equations. *Numerical Methods for Partial Differential Equations*, 31(6):1713–1741, 2015.

[203] K. Washabaugh, D. Amsallem, M. Zahr, and C. Farhat. Nonlinear model reduction for CFD problems using local reduced-order bases. In *Proceedings of 42nd AIAA Fluid Dynamics Conference and Exhibit*, volume 2686, pages 1–16, New Orleans, USA, 2012.

[204] H. Whitney. *Geometric integration theory*. Courier Corporation, 2012.

[205] K. Willcox. Unsteady flow sensing and estimation via the gappy proper orthogonal decomposition. *Computers & Fluids*, 35(2):208–226, 2006.

[206] E. L. Wilson. The static condensation algorithm. *International Journal for Numerical Methods in Engineering*, 8(1):198–203, 1974.

[207] S. Wold, K. Esbensen, and P. Geladi. Principal component analysis. *Chemometrics and intelligent laboratory systems*, 2(1-3):37–52, 1987.

[208] H. H. Woodson and J. R. Melcher. Electromechanical dynamics. 1968.

[209] J. Wray and G. G. Green. Calculation of the volterra kernels of non-linear dynamic systems using an artificial neural network. *Biological Cybernetics*, 71(3):187–195, 1994.

[210] X. Y. Xiong, L. J. Jiang, J. E. Schutt-Ainé, and W. C. Chew. Volterra series-based time-domain macromodeling of nonlinear circuits. *IEEE Transactions on Components, Packaging and Manufacturing Technology*, 7(1):39–49, 2017.

[211] G. H. Yoon. Structural topology optimization for frequency response problem using model reduction schemes. *Computer Methods in Applied Mechanics and Engineering*, 199(25):1744–1763, 2010.

[212] K. Zhou, J. C. Doyle, K. Glover, et al. *Robust and optimal control*, volume 40. Prentice hall New Jersey, 1996.

[213] A. Zhu and T. J. Brazil. Behavioral modeling of rf power amplifiers based on pruned volterra series. *IEEE Microwave and Wireless Components Letters*, 14(12): 563–565, 2004.

[214] Z. Zhu, Y. Pang, D. Howe, S. Iwasaki, R. Deodhar, and A. Pride. Analysis of electromagnetic performance of flux-switching permanent-magnet machines by nonlinear adaptive lumped parameter magnetic circuit model. *IEEE Transactions on Magnetics*, 41(11):4277–4287, 2005.

[215] O. C. Zienkiewicz and R. L. Taylor. *The finite element method: solid mechanics,* volume 2. Butterworth-heinemann, 2000.